RÉPUBLIQUE FRANÇAISE
Liberté Égalité Fraternité

Université de Toulouse

Doctorat de l'Université de Toulouse

préparé à l'ISAE-SUPAERO

Conception de formes d'onde basée sur l'information mutuelle pour des systèmes OFDM à double fonction radar-communication

---

Thèse présentée et soutenue, le 19 janvier 2026 par

Nadia BEKKALI

École doctorale
EDMITT - Ecole Doctorale Mathématiques, Informatique et Télécommunications de Toulouse

Spécialité
Informatique et Télécommunications

Unité de recherche
ISAE-ONERA SCANR Signal communication Antennes Navigation Radar

Thèse dirigée par
Stéphanie BIDON et Damien ROQUE

Composition du jury
M. Olivier RABASTE, Président, ONERA Palaiseau
M. Éric SIMON, Rapporteur, Université de Lille
M. Thierry CHONAVEL, Rapporteur, IMT Atlantique
M. Ronan COSQUER, Examinateur, DGA
Mme Stéphanie BIDON, Directrice de thèse, ISAE-SUPAERO
M. Damien ROQUE, Co-directeur de thèse, ISAE-SUPAERO

Membres invités
Mme Meryem BENAMMAR, Co-encadrante, ISAE-SUPAERO

Acknowledgments

I would like to express my deepest gratitude to everyone who contributed, in one way or another, to bringing this PhD thesis to life.

I would first like to acknowledge the DGA/AID for supporting this work through the NEWAVE2 project. I am also sincerely grateful to ISAE-SUPAERO for hosting me and for providing such a stimulating environment throughout my PhD. My sincere thanks also go to the members of my jury Olivier Rabaste, Éric Simon, Thierry Chonavel and Ronan Cosquer for accepting to be part of this committee and for dedicating their time to reading and evaluating my work.

I am profoundly grateful to my PhD supervisors, Stéphanie Bidon and Damien Roque, for their unwavering guidance, constant availability, and invaluable advice throughout these years. Their support and expertise have been the foundation of this work and I have learned immensely from both of them. I'm grateful too for the conference adventures we shared, which were as fun as they were instructive. I would also like to warmly thank my co-supervisor, Meryem Bennamar, who has been supportive from the very beginning and with whom it has always been a true pleasure to work (Orangina is in good hands.)

I am deeply grateful to all my DEOS colleagues, with whom I shared not only countless coffee breaks but also unforgettable moments during *soirées* and restaurant discoveries. A special shoutout to my ComIT colleagues, especially Agathe, Youness, Javier, and of course my fellow CrossFit enthusiast Thomas, our *pause café* conversations were the perfect blend of intellectual debate and complete nonsense, and they made work infinitely more fun. I also want to thank the former members: Leila, Steven, Fabio, Khaled, and Benjamin for showing me the ropes of ComIT life. And then there's the legendary *Bureau des génies*, my colleagues-turned-actual-friends. Cyril, thank you for being such a wonderful friend and for hosting our movie parties. Gastón, we shared an office for many years, through endless discussions and plenty of absurd conversations that had nothing to do with research. Somewhere in all of that, you became one of my dearest friends, and I meant that promise, I'll see you in Uruguay!

Beyond the lab, I want to thank my friends from school, especially Alexandra, Floriane, Augustin, and Bérénice, for reminding me there's life outside of research. And to my dear friend Saadia, thank you for the friendship that crosses oceans.

My deepest gratitude goes to my family. To my mother, I promise I will always be there for you, just as you have always been there for me, with a love and strength I can only hope to live up to. To my father, I can only wish to make you proud and, one day, to give back even a small part of all the sacrifices you have made for me. To my brother Simo, who is truly my best friend (even if he insists the feeling is not mutual), you've never let me down, not once. I'm incredibly proud of who you've become and I hope you know you can always count on me. And to my little brother Nizar who seems far more impressed by my teaching activities than by this thesis and whose curiosity about the world never fails to inspire me, I

look forward to continuing to impress you in the years to come.

Finally, I want to thank my boyfriend, Mathieu. Thank you for standing by my side throughout these three years of PhD and for supporting me through moments of complete despair (if you know, you know) as well as moments of pure joy. You have this rare ability to always put things into perspective and your way of helping me take a step back has carried me through more than you will ever know. I feel incredibly lucky to have you by my side. Here's to facing many more challenges, always together — preferably with a little less thesis panic.

Thank you all for being part of this journey.

Contents

List of Acronyms **xv**

Notations **xix**

Introduction **1**

1 State of the art: from spectrum sharing to MI-based design in OFDM-DFRC systems **5**

1.1 DFRC waveform design 5

1.1.1 Spectrum sharing between radar and communication systems 5

1.1.2 Fundamental trade-offs in DFRC 8

1.1.3 Waveform families for DFRC 10

1.2 Mutual information as an OFDM-DFRC performance metric 14

1.2.1 MI in communications 14

1.2.2 MI in radar 16

1.2.3 MI in DFRC systems 16

1.3 Identified research gaps and thesis positioning 17

2 OFDM-DFRC system model and performance metrics **19**

2.1 Transmitted and received signal models 19

2.1.1 CP-OFDM transmitter 20

2.1.2 Channel models 23

2.1.3 CP-OFDM receivers 28

2.1.4 System model summary and limitations 33

2.2 Performance metrics 34

2.2.1 Elements of information theory 34

2.2.2 Radar performance metrics 35
2.2.3 Communication performance metric: IR 38
2.3 Chapter summary 41

3 MI-based waveform optimization 43
3.1 Power allocation problem 43
3.1.1 Problem formulation 45
3.1.2 Intractability of the power allocation problem 46
3.2 Gaussian symbol model 46
3.2.1 Jensen's approximation 48
3.2.2 Jensen-Hadamard's approximation 50
3.2.3 Overview of Gaussian symbol modeling 52
3.3 Discrete symbol model 53
3.3.1 Jensen's approximation 54
3.3.2 Hadamard's approximation 55
3.3.3 Overview of discrete symbol modeling 59
3.4 Chapter summary 60

4 Comparative analysis of approaches 63
4.1 Simulation setup 63
4.1.1 Radar channel 64
4.1.2 Communication channel 65
4.1.3 Legend conventions 66
4.2 Analysis of power allocation strategies with Gaussian symbols 66
4.2.1 Communication-only waveform 67
4.2.2 Radar-only waveform 68
4.2.3 DFRC waveform 71

4.3 Impact of symbol randomness in OFDM-DFRC systems 76
4.3.1 Radar-only waveform 77
4.3.2 DFRC scenario 79
4.4 Analysis of power allocation strategies with discrete symbols 81
4.4.1 Communication-only waveform 82
4.4.2 Radar-only waveform 85
4.4.3 DFRC waveform 87
4.5 Chapter summary 91

5 Extension of OFDM waveform design to multi-block scenarios with Doppler robustness 93

5.1 Doppler effects and multi-block scenarios 94
5.1.1 Radar performance metrics in multi-block scenarios 94
5.1.2 Block-wise estimation structure and fast implementation 96
5.2 CMI-based waveform optimization 97
5.2.1 Power allocation problem 98
5.2.2 Intractability and approximation 98
5.3 Performance study of the radar-only waveform 99
5.3.1 Simulation setup 99
5.3.2 Numerical results 100
5.4 Waveform robustness to Doppler mismatch 102
5.4.1 Doppler mismatch 102
5.4.2 Numerical results 104
5.5 Chapter summary 105

Conclusion 107

A CP-OFDM radar received symbols for a Doppler-free scenario 111

A.1 Radar received-signal formulation 111

A.2 Frequency-domain radar symbols 112

B Derivation of radar CMI for a single-block Doppler-free OFDM-DFRC scenario 113

C Derivation of radar CMSE with matrix representations 115

C.1 CMSE expression using the observation matrix 115

C.2 CMSE expression for Doppler-free scenarios 116

D IR for discrete constellation symbols 117

D.1 Derivation of the IR 117

D.2 IR as a function of the power allocation 118

E Analysis of PAPR in OFDM-DFRC waveforms 121

E.1 PAPR expression 121

E.2 PAPR simulation setup 122

F Jensen-based approximation and power allocation 125

F.1 Application of Jensen's inequality 125

F.2 J allocation at very low and high power budget 127

F.2.1 Determinant of the radar objective 127

F.2.2 J allocation at very low power budget 128

F.2.3 J allocation at very high power budget 128

F.3 J allocation for a radar-only waveform and a fully-correlated channel 128

G Jensen-Hadamard-based approximation and power allocation 131

G.1 Application of Hadamard's inequality 131

G.2 Jensen-Hadamard's power allocation 132

G.2.1 Principle 132

G.2.2 Lagrangian and KKT conditions 132

G.2.3 Solution for a fixed λ 133

G.2.4 Unique solution and optimal $\lambda^\star$ 135

G.3 Asymptotic behavior of $p_k(\lambda^{-1})$ 135

G.4 Bisection search of $\lambda^\star$ 136

G.5 J and JH allocations for a radar-only waveform and an uncorrelated channel . 137

H Jensen gap analysis for radar CMI approximation **139**

I Optimal allocation for Gaussian transmitted symbols at very low power budget **145**

J Hadamard-based approximation and power allocation **147**

J.1 Proof of Hadamard's inequality applied to radar CMI 147

J.2 Lagrangian and KKT conditions 148

J.3 Solution for a fixed λ 149

J.4 Unique solution and optimal $\lambda^\star$ 150

K MMSE estimator under a well-designed CP **151**

K.1 Observation matrix under the range-unambiguous assumption 151

K.2 Exploiting CP-induced circularity 151

K.3 Fourier diagonalization of circulant matrices 152

References **162**

Abstract — English and French versions **163**

List of Figures

1.1 Continuum from coexistence to cooperation and co-design. 8

1.2 DFRC system. 9

1.3 Venn diagram of entropy and mutual information. 15

2.1 Block diagram of the discrete-time DFRC observation model. 20

2.2 Time–frequency grid showing OFDM symbols at coordinates (m, k) with spacing T_0 in time and F_0 in frequency. 21

2.3 Block diagram of the discrete-time OFDM-DFRC system model with radar and communication channels emphasizing a block-wise processing. The power profile of each transmitted symbol vector $\boldsymbol{x}_m$ on each block m is $\boldsymbol{p}$. 33

3.1 Radar CMI approximations depending on transmitted-symbol model. 47

3.2 Jensen–Hadamard's power allocation strategy. Scenario: $K = 2$, $\boldsymbol{a} = [50, 2]^{\mathsf{T}}$, $\boldsymbol{c} = [2, 50]^{\mathsf{T}}$, $w_{\mathrm{r}} = 0.9$ and $P_{\mathrm{T}} = 0.2$. 53

4.1 *Statistical radar channel in the subcarrier domain*: modulus of $\sigma_{n_{\mathrm{r}}}^{-2}\boldsymbol{K}_{\boldsymbol{g}_{\mathrm{r}}}$ for two levels of correlation ρ_{r} , diagonal elements are the radar SNRs a_k defined in (2.39). When $|\rho_{\mathrm{r}}| > 0$, ρ_{r} is taken as a complex value to avoid restrictive case of real-symmetric radar channel. 65

4.2 *Deterministic communication channel in the subcarrier domain*: communication SNRs c_k defined in (2.43) for two scenarios com #1 and com #2. Values of c_k for com #1 are obtained by a circular shift with respect to com #2. The degree of competition between radar and communication is assessed by comparing the communication SNRs c_k (shown here) with the radar SNRs a_k of Figure 4.1. In com #1, communication subcarriers are mostly *allied* with those of radar when $|\rho_{\mathrm{r}}| > 0$, i.e., highest-SNR subcarriers [#(0,1,2,4)] are common to both channels. In com #2, communication and radar subcarriers with high SNR are mostly in *competition*: communication subcarriers [#(5,6)] compete with radar channels [#(0,1,2)]. 65

4.3 Radar-only waveform design with $w_{\mathrm{r}} = 1$, assuming a frequency-flat radar channel $\rho_{\mathrm{r}} = 0$. Comparison of the power allocations strategies J, JH and EQ. 69

4.4 Radar-only waveform design with $w_{\mathrm{r}} = 1$ under frequency-selective radar channels. Top: normalized power allocations for J, JH, and EQ (4.3) strategies at three transmit power levels: very low, moderate, and very high P_{T}. Bottom: corresponding radar CMI values computed via Monte Carlo integration ($M_{\mathrm{c}} = 5E3$ runs), using (3.1). Left column: frequency-selective radar channel with $\rho_{\mathrm{r}} = 0.99e^{j2\pi/12}$. Right column: fully-correlated case ($|\rho_{\mathrm{r}}| = 1$). Zoomed views are shown where relevant. 70

4.5 DFRC waveform design with a frequency-flat radar channel ($\rho_{\mathrm{r}} = 0$) and a frequency-selective allied communication channel (com #1). Normalized power allocations p_k/P_{T} for J and JH strategies are shown at two transmit power levels: $P_{\mathrm{T}} = -40$ dB and $P_{\mathrm{T}} = -4$ dB. 72

4.6 DFRC waveform performance with a frequency-flat radar channel ($\rho_{\mathrm{r}} = 0$) and a frequency-selective allied communication channel (com #1). Curves are shown for J, JH, and EQ (4.3) strategies. 72

4.7 DFRC waveform design in selective channel scenarios, with $w_{\mathrm{r}} = w_{\mathrm{c}} = 0.5$ and channel settings from Figs. 4.1b and 4.2. Top: normalized power allocations for J, JH, and EQ (4.3) strategies at very low and moderate P_{T}. Bottom: corresponding radar CMI and communication IR, computed via (3.1) and (3.3). Zoomed views are included where relevant. The two scenarios differ in the degree of subcarrier competition between radar and communication. Results are compared to radar-only performance in Figure 4.4. 75

4.8 DFRC waveform design in selective channel scenarios, with radar and communication channels shown in Figs. 4.1b and 4.2. The communication IR (3.3) is plotted as a function of radar CMI (3.1), forming a parametric curve with $w_{\mathrm{r}} \in [0, 1]$. Markers indicate $w_{\mathrm{r}} \in \{0, 0.5, 1\}$, and w_{r} increases from left to right, as shown by the black arrow. Two scenarios are considered, differing in the level of subcarrier competition between radar and communication. . . . 76

4.9 Performance of optimized radar-only waveforms: radar MI (2.59) and MSE (2.62) for deterministic symbols $\boldsymbol{x}^{(\mathrm{OPT-R})}$ vs. radar CMI (3.1) and CMSE (3.4) for Gaussian and discrete constellations with power allocation J when $w_{\mathrm{r}} = 1$ in Problem J. CMI and CMSE are evaluated via Monte Carlo integration with $M_{\mathrm{c}} = 5E3$ runs. 78

4.10 Performance of optimized DFRC waveforms: radar CMI (3.1), radar CMSE (3.4), and communication IR (3.3) as a function of P_{T} for Gaussian and discrete constellations with power allocation J. Metrics evaluated via Monte Carlo integration with $M_{\mathrm{c}} = 5E3$ runs except for (3.3). 80

4.11 Trade-off between communication IR (3.3) and radar metrics (CMSE (3.4), CMI (3.1)) for varying $w_{\mathrm{r}} \in [0,1]$ at total power $P_{\mathrm{T}} = 0$ dB. Curve is parameterized by w_{r} increasing from left to right for the IR-CMI curve and from right to left for the IR-CMSE curve, as shown by the black arrow. 82

4.12 Communication-only waveform design with $w_{\mathrm{r}} = 0$ assuming the communication scenarios (com #1 and com #2). Communication IR (3.3) values computed via Monte Carlo integration ($M_{\mathrm{c}} = 5E3$ runs). 83

4.13 Radar-only waveform design with $w_{\mathrm{r}} = 1$ assuming a frequency-selective radar channel with strong correlation $\rho_{\mathrm{r}} = .99e^{j2\pi/12}$. Radar CMI and CMSE values computed via Monte Carlo integration with $M_{\mathrm{c}} = 5E3$ runs. 86

4.14 DFRC waveform design in selective radar ($\rho_{\mathrm{r}} = .99e^{j2\pi/12}$) and communication channels. For $P_{\mathrm{T}} = 0$ dB, the communication IR (3.3) is plotted as a function of radar CMI (3.1) and as a function of CMSE (3.4), forming a parametric curve with $w_{\mathrm{r}} \in [0,1]$. w_{r} increases from left to right for the IR-CMI curve and from right to left for the IR-CMSE curve, as shown by the black arrow. Two scenarios are considered, differing in the level of subcarrier competition between radar and communication: allied (com #1) vs competitive (com #2). 90

5.1 Radar channel in the subcarrier domain: modulus of $M\sigma_{n_{\mathrm{r}}}^{-2}\boldsymbol{B}_{\mathrm{r}}\boldsymbol{K}_{\boldsymbol{h}_{\mathrm{r}}}\boldsymbol{B}_{\mathrm{r}}^{\mathsf{H}}$ for $M \in \{1,16,128\}$. Radar subcarriers with SNR in decreasing order are [#(1,0,2,8,4,6,9,3,7,5)]. Note that subcarriers [#4] and [#8] are highly correlated with subcarriers [#(0,1,2)]. 101

5.2 Radar-only waveform design with a frequency-selective radar channel with M sweeps in the presence of radar Doppler. Normalized power allocations p_k/P_{T} for J-R strategy are shown at the total transmit power: $P_{\mathrm{T}} = -8$ dB and for $M \in \{1,16,128\}$. 102

5.3 Radar-only waveform design with $w_{\mathrm{r}} = 1$ assuming a frequency-selective radar channel with M sweeps in the presence of radar Doppler. Radar CMI and CMSE values computed via Monte Carlo integration with $M_{\mathrm{c}} = 5E3$ runs. Curves are shown for J-R and EQ (4.3) strategies. 103

5.4 Comparison of CMSE (5.2) (perfect Doppler knowledge) and $\overline{\mathrm{CMSE}}$ (5.19) (with Doppler mismatch) for Gaussian symbols, using J-R and EQ (4.3) power allocations with $M = 16$. Results are shown for different Doppler mismatches $\delta_{f_d} \in \{0, 1/8M, 1/4M\}$, with performance metrics estimated via Monte Carlo integration with $M_{\mathrm{c}} = 10E4$ runs. 105

5.5 Difference $\overline{\text{CMSE}} - \text{CMSE}$, where CMSE is given by (5.2) (perfect Doppler knowledge) and $\overline{\text{CMSE}}$ by (5.19) (with Doppler mismatch), for Gaussian symbols under Doppler mismatch, comparing J-R and EQ (4.3) power allocations with $M = 16$. Results are shown for $\delta_{f_d} \in \{1/8M, 1/4M\}$. Performance metrics are obtained via Monte Carlo integration with $M_c = 10E4$ runs. . . . 106

E.1 CCDF of the PAPR for $K = 10$ subcarriers and $P_T = -4$ dB with 4-PSK symbols. 123

List of Tables

1.1 Comparison of radar and communication waveform requirements and constraints. 10

3.1 Comparison of power allocation strategies. 61

4.1 Simulation parameters for a single-block OFDM-DFRC system with no Doppler. 64

List of Acronyms

AWGN	Additive White Gaussian Noise
BER	Bit Error Ratio
CBRS	Citizens Broadband Radio Service
CEPT	*Conférence Européenne des administrations des Postes et Télécommunications*
CCDF	Complementary Cumulative Distribution Function
CDM	Code-Division Multiplexing
CMI	Conditional Mutual Information
CMSE	Conditional Mean Squared Error
CP	Cyclic Prefix
CRLB	Cramér–Rao Lower Bound
CSI	Channel State Information
CSS	Chirp Spread Spectrum
CW	Continuous-Wave
DARPA	Defense Advanced Research Projects Agency
DFRC	Dual-Function Radar-Communication
DFT	Discrete Fourier Transform
DSA	Dynamic Spectrum Access
DSSS	Direct-Sequence Spread Spectrum
ETSI	European Telecommunications Standards Institute
FBMC	Filter Bank MultiCarrier
FCC	Federal Communications Commission
FFT	Fast Fourier Transform
FMCW	Frequency-Modulated Continuous-Wave
FSK	Frequency-Shift Keying
GMI	Generalized Mutual Information

IDFT	Inverse Discrete Fourier Transform
IFFT	Inverse Fast Fourier Transform
IoT	Internet of Things
IR	Information Rate
KKT	Karush–Kuhn–Tucker
LFM	Linear Frequency Modulated
MC	Monte Carlo
MI	Mutual Information
MIMO	Multiple-Input Multiple-Output
MMSE	Minimum Mean Squared Error
mmWave	Millimeter-Wave
MSE	Mean Squared Error
MWF	Mercury/Waterfilling
NTIA	National Telecommunications and Information Administration
OFDM	Orthogonal Frequency Division Multiplexing
OTFS	Orthogonal Time Frequency Space
PAPR	Peak-to-Average Power Ratio
PMEPR	Peak-to-Mean-Envelope Power Ratio
PDF	Probability Density Function
PRI	Pulse Repetition Interval
PSD	Power Spectral Density
P/S	Parallel-to-Serial (conversion)
PSK	Phase-Shift Keying
QAM	Quadrature Amplitude Modulation
RL	Reinforcement Learning
RF	Radio Frequency
RX	Receiver
SAS	Spectrum Access Systems

SIMO	Single-Input Multiple-Output
SNR	Signal-to-Noise Ratio
SS	Spectrum Sharing
SSPARC	Shared SPectrum Access for Radar and Communications
SU	Secondary User
S/P	Serial-to-Parallel (conversion)
TX	Transmitter
UAV	Unmanned Aerial Vehicle
WF	Waterfilling

Notations

Matrices and Vectors

Matrices are denoted by italic uppercase letters (e.g., $\boldsymbol{A}$) and vectors by bold italic lowercase letters (e.g., $\boldsymbol{x}$).

- $\boldsymbol{A}^{\mathsf{T}}$ denotes the transpose of matrix $\boldsymbol{A}$;
- $\boldsymbol{A}^{*}$ denotes the conjugate of matrix $\boldsymbol{A}$;
- $\boldsymbol{A}^{\mathsf{H}}$ denotes the Hermitian transpose (conjugate transpose) of matrix $\boldsymbol{A}$;
- $\det(\boldsymbol{A})$ denotes the determinant of matrix $\boldsymbol{A}$;
- $\boldsymbol{D}_{\boldsymbol{x}}$ denotes a square diagonal matrix with the elements of vector $\boldsymbol{x}$ on the main diagonal;
- $\operatorname{circ}\{\boldsymbol{x}\}$ denotes the circulant matrix generated by $\boldsymbol{x}$;
- $\operatorname{Toeplitz}\{\boldsymbol{x}\}$ denotes the (possibly asymmetric) $L \times L$ Toeplitz matrix built from the column vector $\boldsymbol{x} \triangleq [x_0, \ldots, x_{L-1}]^{\mathsf{T}}$ and the row vector $[x_0, 0, \ldots, 0]$;
- $\otimes$ is the Kronecker product;
- $\odot$ is the Hadamard (element-wise) product.

Sets

$\mathbb{N}$ the set of natural numbers;

$\mathbb{Z}$ the set of integers;

$\mathbb{R}$ the set of real numbers;

$\mathbb{C}$ the set of complex numbers;

$\mathcal{I}_N$ the set $\{0, \ldots, N-1\}$ for $N \in \mathbb{N} \setminus \{0\}$;

$\mathcal{S}_{++}^{K}(\mathbb{C})$ the set of positive definite matrices of size $K \times K$, i.e.,

$$\mathcal{S}_{++}^{K}(\mathbb{C}) \triangleq \{\, \boldsymbol{X} \in \mathbb{C}^{K \times K} \mid \boldsymbol{X} = \boldsymbol{X}^{\mathsf{H}},\ \boldsymbol{v}^{\mathsf{H}} \boldsymbol{X} \boldsymbol{v} > 0 \ \ \forall \boldsymbol{v} \in \mathbb{C}^{K} \setminus \{0\} \,\}.$$

Complex Numbers

j the imaginary unit such that $j^2 = -1$;

z^* the conjugate of $z \in \mathbb{C}$;

$\Re\{z\}$ the real part of $z \in \mathbb{C}$;

$\Im\{z\}$ the imaginary part of $z \in \mathbb{C}$;

$|z|$ the modulus of $z \in \mathbb{C}$.

Functions

$\log_2$ the binary logarithm;

$\delta_{\cdot,\cdot}$ the Kronecker delta function;

$\mathbb{I}_{\mathcal{A}}(x)$ the indicator function of a subset $\mathcal{A} \subseteq \mathcal{X}$, defined by

$$\mathbb{I}_{\mathcal{A}}(x) = \begin{cases} 1, & \text{if } x \in \mathcal{A}, \\ 0, & \text{otherwise.} \end{cases}$$

Statistics

$\mathcal{E}\{y\}$ denotes the expectation of y;

$\mathcal{N}(\boldsymbol{m}, \boldsymbol{K})$ the real-valued Gaussian distribution with mean vector $\boldsymbol{m}$ and covariance matrix $\boldsymbol{K}$;

$\mathcal{CN}(\boldsymbol{m}, \boldsymbol{K})$ the circularly-symmetric Gaussian distribution with mean vector $\boldsymbol{m}$ and covariance matrix $\boldsymbol{K}$.

Introduction

General context

At first glance, using the same signal for sensing and communications (also known as Dual-Function Radar-Communication (DFRC)[1] system) appears almost too good to be true: it promises spectral efficiency, cost savings, and better integration and coordination. Unsurprisingly, this idea has motivated an impressive research effort across academia, industry, and defense organizations over the last decade. However, as with most ideas that look simple on paper, the reality is less forgiving. In this case, a single waveform must satisfy two sets of requirements historically considered conflicting; radar favors deterministic, high-power signals with good ambiguity properties, while communications relies on waveforms that convey information, designed to maximize spectral or power efficiency under regulatory constraints[2]. Reconciling these two different technologies inevitably leads to complex scientific challenges. Waveform design is key in this quest for joint radar-communication systems. Among the many candidates, Orthogonal Frequency Division Multiplexing (OFDM) rapidly emerged as one of the most widely studied [2]. The reasons are clear: OFDM is used for several modern wireless standards; it naturally decomposes multipath channels into parallel single-tap sub-channels; and its natural Discrete Fourier Transform (DFT)-based structure makes implementation practical. In joint radar-communication systems, the same subcarrier structure used for high-rate data transmission can be exploited for radar range and Doppler estimation [3]. This combination of efficiency and flexibility explains why OFDM has become a reference waveform for joint sensing and communication. That said, continuous OFDM has constraints: it is ill-suited to long-range sensing, and its high Peak-to-Average Power Ratio (PAPR) lowers effective radiated power and thus range (see Chapter 1 for details). In practice, it is better suited to short-to-medium ranges.

The second critical question is: according to which performance metric should these joint radar-communication waveforms be optimized? Traditional performance metrics such as bit error ratio or detection probability remain specific to one function, and do not provide a unified way to describe the joint radar–communication behavior of a DFRC waveform. As a result, they may offer limited insight when analyzing the trade-offs between radar and communication performance. In recent years, information-theoretic criteria, particularly Mutual Information (MI), have been introduced as possibly unifying performance metrics. MI offers a fundamental way to quantify how much information a received signal carries about either the transmitted symbols (for communication) [4] or the target/environment (for radar) [5]. This double interpretation makes it an appealing tool to evaluate joint radar-communication systems, at least in theory.

However, our exploration of the literature revealed a lack of consensus on how to define

[1] In this PhD thesis, we adopt the definition of DFRC given in [1].

[2] The rules set by spectrum regulators that communication signals must obey.

and apply MI in DFRC scenarios, sometimes leading to contradictory formulations. In many works, radar MI is formulated under the assumption of deterministic waveforms, while communication MI assumes random inputs. This obscures the fundamental meaning of MI, and these ambiguities make establishing a stringent framework for MI-based joint radar-communication waveform design difficult.

This thesis aims to address this gap in the literature precisely. Our goal is to clarify how MI may be consistently defined and used as a performance metric for designing an OFDM-DFRC waveform, while also accounting for practical constraints such as transmitting random symbols from discrete constellations and Doppler effects. The central research problem addressed in this thesis is formulated in detail in Section 1.3.

Organization of the work

The remainder of this manuscript is structured to progressively build from context (Chapter 1) to system model (Chapter 2) and technical contributions and results (Chapter 3, 4 and 5). Each chapter develops a specific component of the study, from the state of the art to the proposed framework and its evaluation.

Chapter 1 sets the stage by reviewing existing literature along three axes: spectrum sharing and DFRC principles, the role of OFDM as a candidate waveform, and the use of MI as a design criterion. This provides the context and justification for the contributions developed in the remainder of the manuscript.

Chapter 2 introduces the OFDM-DFRC system models adopted in this thesis. It also defines the radar and communication performance metrics used to design and evaluate the optimized OFDM-DFRC waveforms [IntJrnl1, IntConf1, IntJrnl2].

Chapter 3 presents the proposed MI-based OFDM-DFRC optimization framework. It details the assumptions, simplifications, and approximations required to make the problem tractable, as well as the corresponding solution strategies [IntJrnl1, IntConf2, IntJrnl2].

Chapter 4 evaluates the power allocation strategies proposed in Chapter 3 for OFDM-DFRC systems. Numerical simulations are used to compare their radar and communication performance and to quantify the trade-offs induced by symbol constellations, allocation strategies, and channel conditions [IntJrnl1, IntConf3, IntJrnl2].

Chapter 5 extends the MI-based OFDM-DFRC waveform design to practical conditions such as multiple OFDM blocks (radar sweeps) and by assuming a narrowband scenario [IntConf1].

List of contributions

These contributions have resulted in publications in international conferences and submissions to peer-reviewed journals. The related articles are cited in the relevant chapters, where the material is extended and reorganized into a unified framework.

International conferences

[IntConf1] N. Bekkali, S. Bidon, and D. Roque. "OFDM-DFRC waveform design based on mutual information in presence of Doppler." In: *Proc. Int. Radar Conf.* 2024, pp. 1–6. DOI: 10.1109/RADAR58436.2024.10993945 (cit. on p. 2).

[IntConf2] N. Bekkali et al. "Optimal Power Allocation in Monostatic OFDM Joint Radar Communications Systems." In: *Proc. IEEE Radar Conf.* Mar. 2022, pp. 1–6. DOI: 10.1109/RadarConf2248738.2022.9764299 (cit. on p. 2).

[IntConf3] N. Bekkali et al. "The Price of Information in OFDM-DFRC Systems." In: *Proc. IEEE Radar Conf.* 2024, pp. 1–6. DOI: 10.1109/RadarConf2458775.2024.10548514 (cit. on p. 2).

Journal articles

[IntJrnl1] N. Bekkali et al. "Mutual Information-Driven Power Allocation in OFDM Dual-Function Radar-Communication Systems." In: *IEEE Trans. Radar Syst.* 1 (2023), pp. 605–622. DOI: 10.1109/TRS.2023.3322961 (cit. on p. 2).

[IntJrnl2] N. Bekkali et al. "Mutual Information-Driven Power Allocation in OFDM-DFRC Systems with Discrete Signaling." In: *IEEE Trans. Radar Syst.* (2026). Under review (cit. on p. 2).

Chapter 1

State of the art: from spectrum sharing to MI-based design in OFDM-DFRC systems

This chapter clarifies the context of this thesis work. We first define the concept of Spectrum Sharing (SS) between radar and communication systems, then focus on one specific approach: DFRC. Next, we justify the relevance of multi-carrier modulations such as OFDM for fulfilling both functions simultaneously. We then introduce the use of MI as a performance metric for both radar and communication, in order to guide the design of OFDM-DFRC waveforms. Finally, the chapter concludes by specifying the main objectives of this work, namely the investigation of suitable waveforms for MI-based OFDM-DFRC systems.

Contents

1.1 DFRC waveform design 5
1.1.1 Spectrum sharing between radar and communication systems 5
1.1.2 Fundamental trade-offs in DFRC 8
1.1.3 Waveform families for DFRC 10
1.2 Mutual information as an OFDM-DFRC performance metric 14
1.2.1 MI in communications 14
1.2.2 MI in radar 16
1.2.3 MI in DFRC systems 16
1.3 Identified research gaps and thesis positioning 17

1.1 DFRC waveform design

1.1.1 Spectrum sharing between radar and communication systems

The demand for wireless communication services has grown rapidly, driven by the proliferation of coordinated or uncoordinated cellular networks (e.g., 5G and below, WiFi), and the expansion of ad-hoc connected devices [6]. For instance, the radio spectrum has become increasingly crowded, as part of a long-running trend that has intensified in the past decade,

as services are increasingly placed closer together to accommodate growing demand [7]. This growth results in a severe congestion of the Radio Frequency (RF) spectrum, which is a finite resource that should serve at the same time the commercial, military, and public safety services. By contrast, radar systems have long enjoyed large spectrum allocations. These include both shared bands (HF, VHF, UHF) and exclusive allocations: L-band for long-range surveillance and air traffic control; S- and C-bands for air and missile defense, weather monitoring, and tracking; and X-, Ku-, and Ka-bands for fire control, navigation, terrain following, and high-resolution mapping [8]. These allocations ensure availability and reliability in defense, aviation, and weather applications. However, radar spectrum usage is often sparse in time, frequency, and geography. Beyond these utilization patterns, the more fundamental challenge is that radar applications lack short-term commercial viability compared with mainstream communication services.

This imbalance between the congested communication bands and underutilized radar spectrum has converged with a second trend: the increasing similarities in current technological development, radio frequency front-end architectures in radar and wireless communication technology [3]. Hardware functions are increasingly replaced by digital signal processing, and modern wireless standards now extend into microwave and Millimeter-Wave (mmWave) bands traditionally reserved for radar. Simultaneously, joint RF hardware platforms for communication and radar have become technically feasible, motivating extensive research on spectrum sharing to improve efficiency and meet future demand. The US Government agencies have also acted on this challenge. Defense Advanced Research Projects Agency (DARPA) launched the Shared SPectrum Access for Radar and Communications (SSPARC) initiative to ensure military radar performance while enabling spectrum access for communications [9]. In parallel, regulatory and policy initiatives also illustrate the trend toward spectrum sharing. For example, the Citizens Broadband Radio Service (CBRS) in the 3.5 GHz band used by military radar systems (mainly shipborne and coastal radars for surveillance and defense) introduces a three-tiered dynamic access model, where federal radar systems coexist with commercial cellular users under Spectrum Access Systems (SAS) traffic controller supervision [10]. In Europe, similar efforts are underway to institutionalize spectrum sharing between radar and communications. The European Telecommunications Standards Institute (ETSI) has released compatibility and coexistence studies [11] which analyze interference between automotive radar and the radio astronomy service and recommend technical mitigation measures. Beyond regulatory studies, the Horizon Europe[1] dedicates substantial funding to research on dynamic spectrum sharing and multi-system coexistence, including between radar and 5G/6G systems [12].

In parallel, the academic community has intensively studied spectrum sharing as a response to RF congestion. Early works emphasized the convergence of radar and communications as a way to improve spectrum efficiency [13]. Subsequent studies expanded this view with system proposals enabling simultaneous data exchange and target detection [14], while others focused on signal processing aspects such as waveform and transceiver design [15]. More recent surveys integrated these advances into a broader perspective on resource management, interference, and security [16]. Overall, as shown in Figure 1.1, the literature

[1]European Union scientific research initiative.

on spectrum sharing between radar and communication systems was commonly categorized into three levels:

- **Coexistence** (non-cooperative) refers to physically separate radar and communication systems that treat each other purely as interference sources [17]. No information is shared; instead, each system mitigates interference independently. Three main types of coexistence can be identified [18]: (i) communications act as a Secondary User (SU) transmitting only when radar is inactive, with interference controlled through interference-to-noise ratio limits or by independently characterizing the channel and adjusting transmissions without coordinating with radar [19, 20]; (ii) radar itself may operate as a SU by employing dynamic spectrum access, sensing and adapting in real time (often via cognitive radar perception–action cycle) to coexist with primary communication systems; (iii) dual-role radar alternates between primary and secondary status by dynamically adapting bandwidth and waveform, although this remains largely theoretical.

- **Cooperation** (cooperative coexistence) involves radar and communication systems that exchange limited information or coordinate spectrum access to jointly manage interference [18]. This often occurs through a control center or via shared signaling protocols. Key forms of cooperation include sharing Channel State Information (CSI), where both systems estimate the interference channel and exchange results to avoid disturbing each other and joint scheduling, where communication users are informed of radar transmissions to prevent collisions, and waveform coordination, where radar adapts its pulse shape if aware of the communication system's modulation, and vice versa.

- **Co-design** refers to approaches where radar and communication systems are jointly considered from the design stage, with performance trade-offs analyzed and optimized to meet application requirements. Within this framework, co-design approaches can be categorized by their level of integration. Joint hardware platforms reuse physical components such as antennas and RF chains to support both functions, irrespective of whether the waveform itself is dual-purpose. Joint resource management focuses on optimizing the allocation of time, frequency, power, and beams to balance communication quality and sensing performance from the design stage. Joint waveform design (namely DFRC systems) embeds both communication and radar functions within the same waveform [1].

While complexity and integration increase progressively from coexistence to cooperation to co-design, each paradigm faces inherent limitations that constrain its scalability and performance. Coexistence methods are often inefficient, and handling interference can be costly as explained in [21]. Coexistence is difficult to guarantee when systems have heterogeneous detection thresholds or incompatible signaling formats, leading to hidden or exposed node problems. Cooperative approaches require additional signaling overhead and strict time synchronization. Furthermore, the benefits diminish when observations across cooperating systems are highly correlated. In addition, cooperative approaches are vulnerable to security and

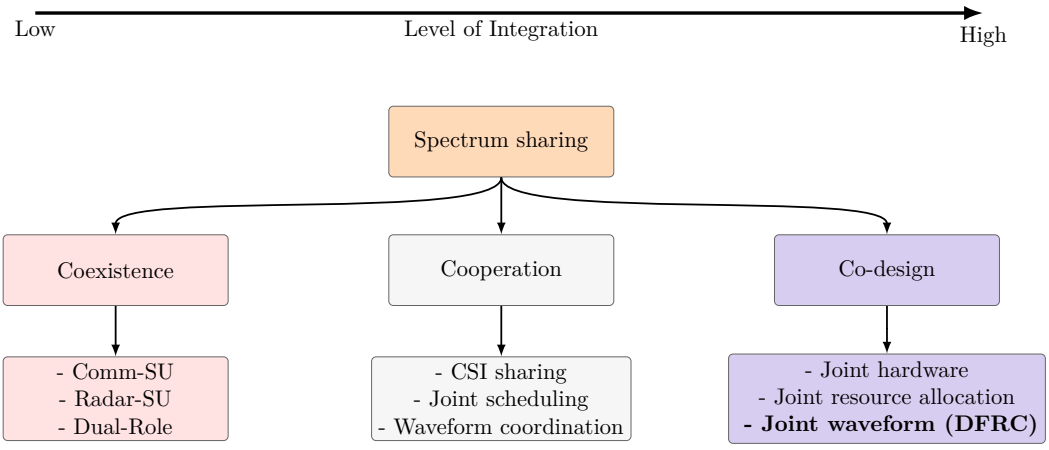


Figure 1.1: Continuum from coexistence to cooperation and co-design.

trust issues, such as spectrum sensing data falsification, where corrupted or faulty reports can significantly degrade system decisions [22].

These limitations of coexistence and cooperation approaches motivate the move toward co-design, where radar and communication are considered jointly from the design stage. By addressing both functions simultaneously, co-design offers improved spectral and hardware efficiency. The latter also aligns with the needs of emerging applications such as autonomous platforms, Unmanned Aerial Vehicle (UAV)s, and 6G networks. At the most integrated level, co-design leads to DFRC systems, which employ a single waveform to simultaneously sense and communicate as defined in [1]. These systems have been widely regarded as a promising solution to the RF spectrum congestion problem. Beyond spectrum efficiency, the joint waveform of DFRC systems also provides flexibility, enabling a tunable trade-off between radar and communication performance. However, this very flexibility highlights the central challenge of DFRC design: achieving the desired balance in practice is highly non-trivial. In the next section, we explain in more detail the basis of DFRC systems.

Remark 1.1.1. *It is worth noting that the taxonomy of the spectrum sharing approaches remains inconsistent in the literature, with no universally agreed-upon definition of a DFRC system for instance. In what follows, we adopt the above definitions.*

1.1.2 Fundamental trade-offs in DFRC

DFRC systems are defined as architectures in which a single transmitted waveform is exploited for both radar sensing and wireless communication [1]. Figure 1.2 illustrates the general principle: a transmitter (RadCom) generates a dual-use waveform $\boldsymbol{s}$, which propagates through two distinct channels: the radar channel $\boldsymbol{h}_{\mathrm{r}}$ toward the radar receiver and the communication channel $\boldsymbol{h}_{\mathrm{c}}$ toward the communication receiver. The radar receiver processes the echoes of $\boldsymbol{s}$ reflected by the target to detect it and/or estimate its parameters such as range or velocity, while the communication receiver decodes the same waveform to recover transmitted information symbols.

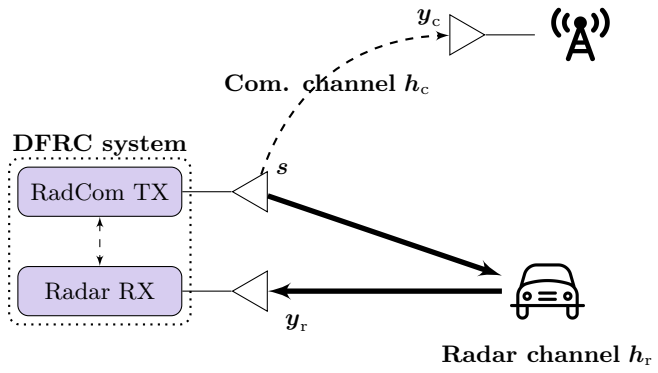


Figure 1.2: DFRC system.

This simple representation highlights the importance of the DFRC paradigm: the same waveform must serve two different objectives simultaneously. Consequently, waveform design has emerged as a central challenge in DFRC research, attracting significant attention in recent years [23, 24]. The main challenge lies in finding suitable waveforms simultaneously employed for information transmission and radar. This task requires carefully balancing the often conflicting requirements of the two functions. The following reviews the principal objectives and constraints guiding DFRC waveform choice. To illustrate the trade-offs, we first examine the performance criteria on the radar and communication sides. A brief comparison is summarized in Table 1.1.

When choosing a DFRC waveform, trade-offs are inevitable because radar and communication functions share the same waveform. What benefits one function often degrades the other, creating fundamental tensions that must be carefully managed [25]. A first dimension of conflict lies in bandwidth allocation. In pulsed radars, short pulses (hence of large bandwidth) are transmitted, followed by a silent period for the reception of the targets echoes. Radars that transmit continuous waveforms also typically cover an extensive range of frequencies. A large bandwidth is desired in radar signals to improve range resolution. On the other hand, communication systems usually operate in a bandwidth-restricted scenario prone to multiuser resource allocation leading to signals with much smaller bandwidths than radar waveforms. Another critical dimension concerns the transmission power, which is usually high for pulsed radars to support long-range operation, for example. Communication systems usually function on less power since their coverage range is much less than that of radars. Additionally, there is always the determinism-randomness dilemma between radar and communication waveforms. Radar benefits from transmitting the same deterministic pulse repeatedly to suppress clutter and enhance sensitivity, but this repetition conveys no new information. In contrast, communications require random, modulated symbol variation to transmit data, which degrades sensing performance.

As a result, DFRC design requires flexible strategies to balance radar and communication performance under varying operational contexts.

Table 1.1: Comparison of radar and communication waveform requirements and constraints.

Aspect	Radar	Communication
Primary goal	Accurate detection and estimation of target parameters (range, velocity, angle); reliable tracking and classification.	Reliable and efficient transmission of information under noise, fading, and interference.
Performance criteria	High range, Doppler, and angular resolution with low sidelobes; high probability of detection and low false alarm rate; sensitivity to weak targets; robustness against clutter, jamming, and interception; accurate parameter estimation (benchmarked by the Cramér–Rao Lower Bound (CRLB)) and multi-target resolution.	High spectral efficiency and achievable Information Rate (IR); low Bit Error Ratio (BER) and latency; tolerable PAPR; robustness against fading, interference, and synchronization errors; scalability to multi-user operation and coexistence with other systems.
System-specific constraints	Restricted waveform space due to resolution, ambiguity, and robustness needs.	Feedback and control overhead, latency, multi-user scheduling and resource allocations.
Shared constraints	Synchronization, spectrum regulations, and coexistence policies.	

1.1.3 Waveform families for DFRC

To effectively balance radar and communication performance, the design of waveforms plays a crucial role, as it directly influences the trade-off between these two functions. This motivates a closer look at the different candidate waveforms investigated in the literature for DFRC systems. Existing waveforms can be broadly grouped into radar-inspired families and communication-inspired families. Each family exhibits advantages and limitations in terms of ambiguity function, bandwidth use, hardware constraints, and implementation complexity. The following review outlines the main candidates from both perspectives, before converging toward OFDM as the reference waveform for this thesis.

1.1.3.1 Radar-inspired waveforms

Traditional radar systems have historically relied on well-established waveform families [26, p. 774], such as pulsed signals (e.g., Linear Frequency Modulated (LFM), also known as chirp, and phase-coded signals such as pseudorandom sequences) as well as Continuous-Wave (CW)

signals [26, p. 20]. In pulsed radar, short bursts of RF energy are transmitted, reflected by targets, and detected by the receiver; such systems are typically used for long-range operation and employ high peak transmit power. By contrast, CW radars transmit continuously and uniformly throughout the entire cycle[2], and are widely used for precise Doppler/velocity estimation; when modulated (e.g., Frequency-Modulated Continuous-Wave (FMCW)), they also provide range measurement.

Overall, these waveform families are favored in radar because when operated with large bandwidth (e.g., chirps/coded pulses or FMCW), they provide good range resolution and with long coherent observation (e.g., CW), they enable precise Doppler/velocity estimation; in addition, their favorable autocorrelation properties, characterized by sharp main peaks and low sidelobes, enhance target discrimination and enable the detection of multiple, closely spaced objects.

Building on these foundations, several radar-inspired waveform candidates have been investigated for DFRC applications. One of the earliest concepts was introduced in [27], where communication bits were embedded in the radar pulse interval. Subsequently, [28] proposed the first DFRC scheme exploiting chirp signals. Beyond basic chirps, Chirp Spread Spectrum (CSS) techniques were also explored in [28], with the goal of improving robustness against interference. More advanced designs have since emerged. For example, covert (hidden) communication strategies using LFM pulses were investigated in [29], while pseudorandom codes have been employed as both probing signals and information carriers [30].

Radar-centric waveforms used for DFRC are inherently robust to noise and interference owing to their favorable correlation properties. However, they suffer from poor spectral efficiency: traditional radar signals generally use constant-envelope waveforms which are typically incompatible with high-order modulation schemes, and they often occupy wide bandwidths. These limitations are particularly restrictive in sub-30 GHz bands, where spectrum is already scarce and must be shared with other communication and navigation services. To address this, several works have advocated operation at mmWave frequencies (> 30 GHz), where spectrum is more abundant [31]. At these higher bands, even bandwidth-hungry waveforms can be accommodated, enabling both high-resolution sensing and high data rate communication. For example, IEEE 802.11ad[3] systems have demonstrated centimeter-scale range resolution in parallel with multi-Gbps throughput [32, 33]. Nevertheless, mmWave operation introduces new challenges: high free-space path loss[4] limits radar range and necessitates large antenna arrays with beamforming. These considerations highlight that waveform design cannot be decoupled from spectrum allocation; the scarcity of bandwidth below 30 GHz continues to motivate exploration of mmWave operation for DFRC systems.

[2]In this PhD thesis, we use CW (continuous-wave) in this sense. We note that in the communication literature, sometimes continuous-wave may refer to an unmodulated sinusoid which is not the case here.

[3]The Wi-Fi amendment that defines wireless communication in the 60 GHz millimeter-wave band also known as WiGig.

[4]The decrease in signal strength of a signal traveling between two antennas on a line-of-sight path through free space.

1.1.3.2 Communication-inspired waveforms

In contrast to radar-centric designs, another approach is to adapt existing communication waveforms for sensing. Communication-inspired candidates for DFRC can be broadly grouped into single-carrier and multi-carrier families.

Single-carrier linearly modulated waveforms are attractive for DFRC because their typically low PAPR allows efficient use of power amplifiers [34, 35]. Additionally, single-carrier systems usually need simpler signal processing techniques, reducing the complexity of transmitter and receiver design. A key drawback of single-carrier transmission is its need for equalization in channels with delay spread, as it is more sensitive to such impairments. This adds nontrivial complexity and pilot design challenges, especially compared to multi-carrier systems.

Among multi-carrier approaches, Filter Bank MultiCarrier (FBMC) with offset-Quadrature Amplitude Modulation (QAM) has been studied in the context of 5G and beyond, but was not standardized. By combining offset-QAM signaling[5] with carefully designed prototype filters, FBMC pulse-shapes each subcarrier (via a frequency-shifted copy of the prototype), yielding cleaner spectra and reduced out-of-band emissions—an important feature in congested bands [36, 37]. These advantages come at the expense of increased implementation complexity, longer filter lengths that introduce latency, and stricter synchronization requirements, which complicate real-time DFRC deployment.

For this reason, much of the DFRC literature still gravitates toward OFDM. OFDM is a multi-carrier modulation scheme in which the available bandwidth is divided into many orthogonal subcarriers, each carrying a sequence of modulated symbols (refer to Chapter 2 for more details). It is widely used in communication systems as it offers high spectral efficiency and is robust to frequency-selective fading, provided the Cyclic Prefix (CP)[6] length exceeds the maximum delay spread (i.e., well-designed CP), and it admits efficient Fast Fourier Transform (FFT)-based implementation. Furthermore, OFDM underpins most modern wireless standards, including Wi-Fi, LTE, 5G NR, and vehicular standards such as IEEE 802.11p[7] and IEEE 802.11ad. Within DFRC, OFDM has attracted particular attention because the same symbol structure enabling high-rate communications can also be exploited for target parameter estimation. Under standard conditions: (i) a well-designed CP, and (ii) small normalized Doppler[8] (ensured in practice by choosing the subcarrier spacing larger than the expected Doppler spread), subcarrier-domain processing yields a separation of range and Doppler estimations. In this model, the range is estimated from the subcarrier grid (fast-time) and Doppler from coherent integration across symbols (slow time), typically via a single $2-$ D FFT, producing independent range and Doppler estimates [3]. These properties facilitate the construction of delay–Doppler maps that reveal target position and velocity with resolu-

[5] Offset-QAM signaling sends the real and imaginary parts of each QAM symbol separately, half a symbol apart, on each subcarrier so overlapping filters stay orthogonal and spill less into neighbors.

[6] The CP is an identical copy of the last portion of an OFDM symbol that is appended before the symbol

[7] The Wi-Fi standard designed for vehicular communications, also known as WAVE (Wireless Access in Vehicular Environments

[8] Doppler frequency divided by the actual transmitted frequency.

tions determined by the occupied bandwidth (for range) and observation time (for Doppler). Beyond technical performance, OFDM benefits from decades of standardization, optimized hardware, and pilot structures designed initially for channel estimation, all of which can be directly reused for radar sensing [38].

However, OFDM-based DFRC suffers from well-known limitations. First, its inherently high PAPR reduces power amplifier efficiency compared to constant-envelope signals. Second, its strict synchronization requirements make it highly sensitive to frequency offsets, quickly degrading performance. Third, standardized OFDM waveforms impose bandwidth constraints that limit radar resolution: for instance, IEEE 802.11p with 20 MHz bandwidth yields a rough range resolution of about 7.5 m. In contrast, IEEE 802.11ad at mmWave frequencies offers finer resolution but at the cost of severe propagation losses. In summary, OFDM remains one of the dominant choices for DFRC due to its proven technical efficiency (spectral efficiency, robustness to multipath, and FFT-based simplicity) and its maturity in terms of standardization, hardware availability, and interoperability. Nevertheless, its inherent limitations motivate active research into improved OFDM-based waveform designs for DFRC.

Another possible scheme is Orthogonal Time Frequency Space (OTFS) modulation [39] introduced initially to mitigate doubly dispersive wireless channels by mapping information symbols into the delay–Doppler domain [40] (practically, we can view OTFS as unitary 2− D DFT precoding of the symbols before standard OFDM transmission). For communications, OTFS allegedly offers strong Doppler tolerance and reduced inter-carrier interference [41] (with suitable equalization and practical pulse-shaping), while for radar it provides delay–Doppler estimation accuracy comparable to conventional waveforms and remains compatible with matched filtering techniques [42]. Within DFRC, OTFS is presented as an attractive option for high-mobility scenarios, where it can enable efficient spectrum reuse and robust hardware operation. Nevertheless, OTFS inherently produces velocity sidelobes in its ambiguity function, complicating sidelobe suppression (similarly to OFDM, although OFDM sidelobe behavior is well-studied). Furthermore, despite its promise, OTFS remains relatively new, with limited standardization and higher processing complexity than more established schemes. Overall, OTFS and CP–OFDM deliver similar DFRC sensing benefits and share the same core limitations (same resolution limits and similar 2-D processing), but OTFS incurs higher implementation complexity; we therefore retain CP–OFDM for this work.

Remark 1.1.2. *Traditional radar- and communication-inspired waveforms often fail in rapidly varying environments. Learning-based approaches, such as reinforcement learning for weak target detection in clutter or for dynamic resource allocation, can adapt waveforms dynamically and are especially relevant for autonomous platforms [43]. However, this topic lies outside the scope of this work.*

We established CP-OFDM as the waveform of interest for DFRC systems. With the waveform family fixed, *design* now refers to selecting its tunable parameters, not the waveform family itself. For CP-OFDM waveforms, several degrees of freedom remain such as subcarrier spacing, CP length, modulation order and most notably the *power allocation across subcarriers* under a total power constraint. We single out power allocation as the central theme

throughout this work, as it plays a crucial role in balancing the trade-off between radar and communications. Accordingly, the critical question becomes, according to which criteria do we design the OFDM waveform, i.e., determine the power profile of the transmitted OFDM symbols? Radar and communication systems traditionally rely on distinct performance metrics; in DFRC design, these metrics must be considered simultaneously, often under conflicting requirements. The following section introduces the performance metrics relevant to OFDM-based DFRC, which will serve as the foundation for subsequent optimization.

1.2 Mutual information as an OFDM-DFRC performance metric

Several approaches have been developed to optimize the performance of OFDM-DFRC waveform. However, conventional metrics such as BER (at a given Signal-to-Noise Ratio (SNR) and channel impulse response) or detection probability versus false-alarm probability are too specific to one system and not the other. To address this limitation, this thesis focuses on a metric that captures the performance of both radar and communication within a unified framework.

Among available candidates, information theory, and particularly MI, has recently gained attention [17, 44, 45]. MI measures how much useful information a received signal conveys about the transmitted signal or the environment. Let X and Y be two discrete random variables. The mutual information between them is defined as

$$I(X;Y) = H(X) - H(X|Y) \tag{1.1}$$
$$= H(Y) - H(Y|X) \tag{1.2}$$

where $H(X)$ is the entropy of X and $H(X|Y)$ is the conditional entropy of X given Y. The relationships among $H(X)$, $H(Y)$, $H(X|Y)$, $H(Y|X)$, and $H(X,Y)$ can be illustrated using a Venn diagram (see Figure 1.3). In this representation, the mutual information $I(X;Y)$ corresponds to the intersection of the information contained in X and in Y. More details, including the extension to continuous random variables, will be discussed later in Section 2.2.1.

MI can be interpreted both in terms of achievable data rate for communication systems [4], and in terms of target information extraction from the received radar symbols. In the following, we recall the role of MI in communication systems, then extend its interpretation to radar, before presenting its application as a performance metric in the DFRC context.

1.2.1 MI in communications

In digital communications, MI between the input and the output of a communication channel is a widely used measure of performance as it quantifies the information the received symbols convey about the transmitted ones. For a given input distribution (Gaussian or discrete

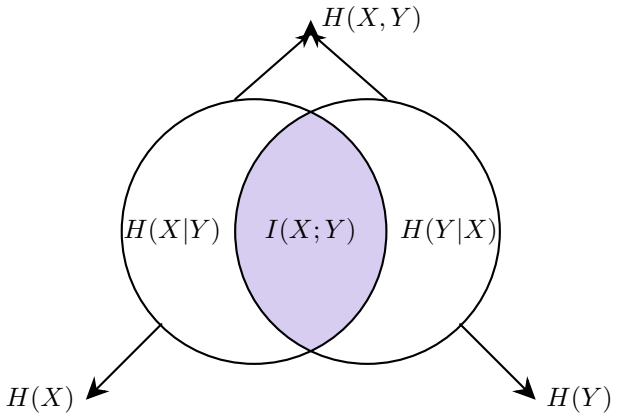


Figure 1.3: Venn diagram of entropy and mutual information.

constellation) and assuming optimal coding and decoding strategies, the MI equals the IR, i.e., the maximum reliable rate supported by that distribution. In practice, IR is often lower due to system constraints, but it remains an important metric for evaluating performance. Maximizing IR over all possible input distributions subject to a power constraint yields the channel capacity, which for the Additive White Gaussian Noise (AWGN) channel is attained with Gaussian inputs [4].

In multi-channel settings, such as parallel Gaussian channels with Gaussian inputs, IR maximization reduces to finding a power allocation across the subchannels. This leads the well-known optimal solution Waterfilling (WF), which allocates more power to subchannels with the strongest SNRs while reducing transmission over weaker ones (see Section 3.2 for more details). However, practical systems typically employ discrete constellations such as QAM or Phase-Shift Keying (PSK); hence WF is no longer optimal. The corresponding power allocation that maximizes the IR in this case is the so-called Mercury/Waterfilling (MWF) solution [46], where the *mercury* component accounts for the IR saturation effect introduced by discrete constellations (see Section 3.3 for more details). Thus, MWF generalizes WF by adapting the power allocation jointly to the channel state and the modulation format.

Returning to our OFDM-DFRC waveforms, OFDM is particularly suitable for this framework because, with a sufficiently long CP and negligible inter-carrier interference, a frequency-selective fading channel can be decomposed into independent parallel Gaussian subchannels [47, Sec. 11.2-5], the same applies to Multiple-Input Multiple-Output (MIMO) systems [48, Sec. 7.1]. This decomposition makes it natural to apply WF or MWF principles for power allocation across subcarriers. The same reasoning extends to MIMO-OFDM systems, where the spatial and frequency dimensions together create a larger set of parallel subchannels. In the multiuser setting, the problem generalizes further: instead of maximizing a single-user sum rate, the objective often becomes a weighted sum-rate maximization [49], these optimization problems may also incorporate constraints such as latency, or per-user quality of service; however these formulations remain rooted in IR but require more advanced optimization tools, such as convex relaxation and dual decomposition.

1.2.2 MI in radar

The use of MI in radar is less conventional than in communications, but it was first introduced in the seminal work of [5] as a principled criterion for waveform design targeting parameter estimation. In Bell's formulation, the objective was not pure detection, but improved estimation performance for tasks such as identification or classification. This estimation-oriented perspective was later reinforced by the theoretical results of [50, 51], which formally established the connection between estimation accuracy and mutual information.

A major step forward came with the extension to statistical MIMO radar in [52], which showed that the waveform maximizing radar MI coincides with the one minimizing the Mean Squared Error (MSE) in estimating the target's impulse response. This equivalence gave MI a concrete operational meaning and triggered a substantial line of follow-up work on MI-based waveform design. Within this framework, researchers progressively addressed increasingly complex environments: uncertainty in the target's second-order statistics [53], colored noise [54], adversarial or smart targets equipped with countermeasures [55], and the joint optimization of the radar receiver [56]. Other works extended the approach to multiple extended targets in coherent phased-array radar [57], to signal-dependent interference [58], and to Gaussian mixture-distributed target responses [59]. Collectively, these studies demonstrated the robustness of the MI criterion across diverse radar scenarios.

Alongside this mainstream line of work, an alternative use of MI was also proposed for waveform design [60, 61, 62, 63]. In this formulation, space-time codes for statistical MIMO radar are optimized using the MI between the target's complex amplitudes and the signals received on multiple antennas. While conceptually different, this approach was shown to be competitive with other information-theoretic criteria.

In summary, MI has evolved from a theoretical tool linking information and estimation to a versatile and widely adopted criterion for radar waveform and receiver design. Its demonstrated adaptability across environments, target models, and system architectures makes it a natural candidate for extension to DFRC.

1.2.3 MI in DFRC systems

In conventional formulations, MI is modeled differently for communication and radar systems.

- In communication systems, the transmitted waveform is assumed to be *stochastic* since it carries information-bearing (random) symbols.
- In radar systems, the transmitted waveform is assumed to be *deterministic*, designed solely to maximize sensing performance.

Under this modeling, one can directly formulate joint optimization problems in coexistence scenarios, where communication and radar signals remain distinct. For example, coexistence

designs have been studied for monostatic radar in [64] and in [65] for a colocated MIMO radar.

In contrast, DFRC systems employ a single joint waveform. Directly combining the classical definitions of MI leads to a theoretical inconsistency: the classical communication MI depends on the probability distribution of random transmitted symbols and the radar MI assumes fixed deterministic waveform. Thus, one would have to jointly optimize both a probability distribution and a single realization of the same waveform which is a conceptually intricate task. Several works attempted to address this challenge by reformulating the problem, but each approach entails some limitations.

- In [44] and [66], an MI-based compound objective function is considered to optimize an OFDM waveform. The information rate is replaced by the MI between the communication channel and the received signal, given the transmitted symbols. The resulting MI reduces thus to an estimation performance metric of the communication channel, which does not inform us about the maximum achievable data rate *per se*.
- In [67] and [45], colocated and statistical MIMO-DFRC systems are considered. The information rate is replaced by a metric that exchanges the transmit covariance matrix with the sample covariance matrix of the deterministic waveform. This metric is unconventional and does not clearly relate to the information rate.
- MI-based multi-carrier and OFDM waveforms are designed in [17], [68] and [69]. MIs are expressed in the frequency domain. To obtain the radar MI, the authors consider the waveform random and deterministic at the same time when deriving its Power Spectral Density (PSD). This dual treatment is conceptually inconsistent.

However, in DFRC scenarios, the same transmitted symbols are simultaneously exploited for radar sensing and communication. These symbols must therefore be information-bearing, and are naturally modeled as random. As a result, the classical radar MI assumption of a deterministic waveform is therefore incompatible with the communication perspective. To resolve this inconsistency and preserve the IR as a valid communication performance metric while capturing radar performance, we adopt the radar Conditional Mutual Information (CMI) as a radar performance metric. The radar CMI is defined as the radar MI averaged over all possible realizations of the transmitted signal. This metric accounts for the all possible realizations of the random transmitted symbols, thereby aligning the radar MI definition with the dual-use nature of DFRC waveform.

1.3 Identified research gaps and thesis positioning

In light of the literature, we formulate DFRC-OFDM waveform design as a power allocation problem, where the objective is to maximize a weighted sum of radar CMI and communication IR, subject to a total transmit power constraint (this formulation will be explained more in

details in Chapter 3). However, despite its theoretical soundness, such a stringent joint MI-based formulation is mostly absent from the existing literature. This lack of a unified and consistent framework constitutes this thesis's first significant research gap.

A second gap concerns the solvability of the optimization problem once the CMI–IR formulation is adopted. The exact communication IR with practical discrete constellations (e.g., QAM, PSK) is analytically intractable, which has led most prior works to bypass the issue by assuming Gaussian transmitted symbols. However, the radar CMI term remains analytically intractable even under this simplification. As a result, the optimization problem cannot be solved in closed form, and no solution strategies exist in the literature. This thesis precisely addresses this gap: it develops tractable solution methods based on approximation techniques under Gaussian input assumptions and discrete constellations.

A third gap lies in the lack of an analysis of radar CMI itself. In particular, the "cost of information," the performance degradation in sensing induced by transmitting information-bearing symbols, has not been studied in detail in the DFRC literature.

Finally, a fourth gap arises from the limited treatment of practical conditions in OFDM-DFRC systems. Existing MI-based studies typically focus on single-block OFDM under idealized assumptions, neglecting key aspects such as multi-block transmission structures and Doppler effects. These factors are important to real-world scenarios, yet remain insufficiently addressed in the current state of the art.

Within this landscape, the present thesis is positioned at the intersection of these gaps as it builds on the need for a precise MI-based problem formulation for an OFDM-DFRC waveform, explores approximation strategies that help solve this latter problem numerically or analytically, extends the discussion to practical scenarios, and deepens the understanding of radar CMI.

Chapter 2

OFDM-DFRC system model and performance metrics

This chapter introduces the notations and models related to the OFDM-DFRC system. We first present the OFDM-DFRC system model, which encompasses the transmitted signal, the propagation channels, and the received signals in both the time and frequency domains. Particular emphasis is placed on the fact that two distinct propagation channels are considered—one for the radar function and one for the communication function—leading to two different received signals. The second part is dedicated to the radar and communication performance metrics that we will use later, whether to formulate our waveform optimization problems or assess the performance of our results.

Contents

2.1 Transmitted and received signal models 19
2.1.1 CP-OFDM transmitter 20
2.1.2 Channel models 23
2.1.3 CP-OFDM receivers 28
2.1.4 System model summary and limitations 33
2.2 Performance metrics 34
2.2.1 Elements of information theory 34
2.2.2 Radar performance metrics 35
2.2.3 Communication performance metric: IR 38
2.3 Chapter summary 41

2.1 Transmitted and received signal models

We consider a cognitive scenario in which the transmitted waveform is adapted to improve the estimation of an already pre-detected target, assumed to be localized in range and Doppler, with a priori information available on its statistical characteristics. At the same time, the system must transmit a communication message. In this work, we concentrate on the waveform design at the transmission stage, while the adaptive cognitive loop itself lies outside the scope of this manuscript.

This section presents the signal models adopted in our DFRC scenario. It defines the unique transmitted waveform structure, channel propagation models, and receiver processing for radar and communication channels.

2.1.1 CP-OFDM transmitter

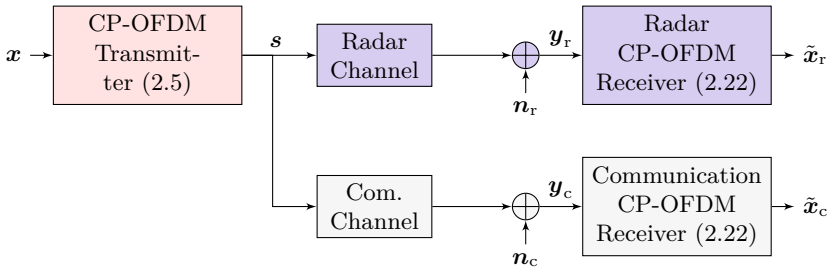


Figure 2.1: Block diagram of the discrete-time DFRC observation model.

We consider a multicarrier DFRC scenario as depicted in Figure 2.1 with a single transmitter responsible for transmitting a joint radar-communication waveform. We first present the CP-OFDM transmitted signal model in the time domain, followed by its discrete-time representation used in the DFRC context.

2.1.1.1 Time-domain signal model

We consider a scenario with a single transmitter emitting a RF signal $s_{\mathrm{RF}}(t)$ centered at carrier frequency F_c. The signal is assumed to be narrowband, i.e., $B \ll F_c$, which allows Doppler effects to be modeled as pure frequency shifts (see Section 2.1.2.1). It is convenient to describe it through its equivalent complex envelope $s(t)$, defined as [70, Sec. 2.1]

$$s_{\mathrm{RF}}(t) = \Re\{s(t)e^{j2\pi F_c t}\}. \tag{2.1}$$

Remark 2.1.1. *The complex envelope of a narrowband signal can be ideally recovered using an IQ receiver, and conversely, any narrowband RF signal can be reconstructed from its complex envelope using an IQ transmitter provided perfect synchronization.*

Let $x_{k,m}$ denote the complex data symbols to be transmitted on subcarrier $k \in \mathcal{I}_K$ and during block $m \in \mathcal{I}_M$ where K is the number of subcarriers and M the number of transmitted blocks (or radar sweeps). The single transmitter is responsible for generating these symbols, which are simultaneously directed towards the communication receiver and reflected by the radar target. Each symbol is placed at the coordinates (mT_0, kF_0) in the time–frequency plane and shaped by a rectangular pulse $g(t) = \mathbb{I}_{[0;T_0)}(t)$. Here, T_0 represents the block duration or Pulse Repetition Interval (PRI), and F_0 denotes the subcarrier spacing as illustrated in

Figure 2.2. The baseband complex envelope of the transmitted signal is written as [71]:

$$s(t) = \frac{1}{\sqrt{K}} \sum_{k \in \mathcal{I}_K} \sum_{m \in \mathcal{I}_M} x_{k,m} g(t - mT_0) e^{j2\pi k F_0 (t - mT_0)}. \tag{2.2}$$

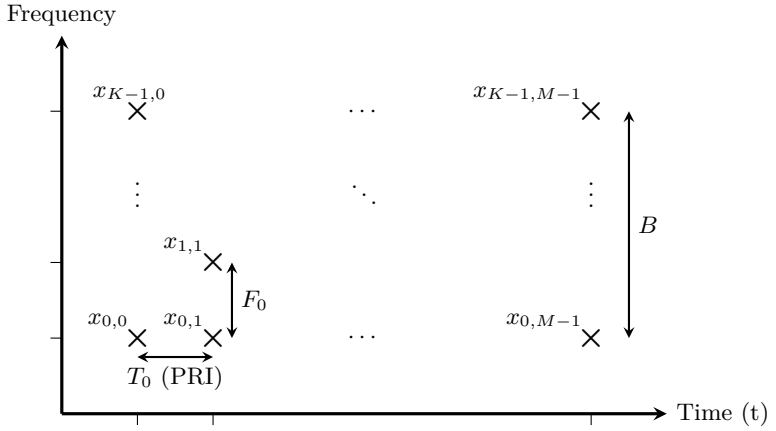


Figure 2.2: Time–frequency grid showing OFDM symbols at coordinates (m, k) with spacing T_0 in time and F_0 in frequency.

This continuous-time representation clarifies the signal's temporal multicarrier structure. In the following, we formalize the equivalent discrete-time baseband model used for algorithmic implementation and performance analysis.

2.1.1.2 Discrete-time and matrix model

We assume a large number of subcarriers ($K \gg 1$), so that the occupied bandwidth satisfies $B \approx KF_0$. We denote $L = T_0 B$ the number of time samples per symbol duration (or, PRI) T_0 and assume $L \in \mathbb{N}$ (this assumption avoids the need for interpolation when mapping the continuous-time signal to its discrete-time representation). We therefore sample the baseband multicarrier signal $s(t)$ given in (2.2) at the critical frequency $1/T_\mathrm{s} = B$ to obtain:

$$s[l] = \frac{1}{\sqrt{K}} \sum_{k \in \mathcal{I}_K} \sum_{m \in \mathcal{I}_M} x_{k,m} g[l - mL] e^{j2\pi \frac{k}{K}(l - mL)} \tag{2.3}$$

$$= \sum_{m \in \mathcal{I}_M} g[l - mL] \left(\frac{1}{\sqrt{K}} \sum_{k \in \mathcal{I}_K} x_{k,m} e^{j2\pi \frac{k}{K}(l - mL)} \right) \tag{2.4}$$

where we define $s[l] \triangleq s(lT_\mathrm{s})$ and $g[l] \triangleq g(lT_\mathrm{s})$. Here, $1/K$ represents the normalized version of the frequency spacing between two elementary symbols $x_{k,m}$.

In other words, at the discrete level (2.4), the CP-OFDM transmitter maps each block of symbols to subcarriers via an Inverse Discrete Fourier Transform (IDFT) and prepends a CP

of length $\Delta_{\mathrm{CP}} = L - K$ to each block to avoid inter-block interference [72, 73]. Each resulting block is of length $L = K + \Delta_{\mathrm{CP}}$, and the full transmitted signal consists of M time-disjoint blocks, because $g[l - mL]$ has support on $\{mL, \ldots, (m+1)L - 1\}$ for each m.

Remark 2.1.2 (Time-disjoint OFDM blocks under rectangular shaping)**.** *Let $g(t) = \mathbb{I}_{[0;T_0)}(t)$ so that $g(t - mT_0) = \mathbb{I}_{[mT_0,(m+1)T_0)}(t)$. Then, for $m \neq m' \in \mathcal{I}_M$, the supports $[mT_0, (m+1)T_0)$ and $[m'T_0, (m'+1)T_0)$ are disjoint; hence $s(t)$ in (2.2) is a concatenation of M non-overlapping blocks of duration T_0. In discrete time, with $T_{\mathrm{s}} = 1/B$, $L = T_0/T_{\mathrm{s}} \in \mathbb{N}$, and $g[l] \triangleq g(lT_{\mathrm{s}})$, we have $g[l] = \mathbb{I}_{\{0,\ldots,L-1\}}(l)$ and $g[l - mL] = \mathbb{I}_{\{mL,\ldots,(m+1)L-1\}}(l)$, so blocks are likewise time-disjoint over $\{mL, \ldots, (m+1)L - 1\}$.*

Consequently, in CP-OFDM each block occupies exactly one interval of length $L = K + \Delta_{\mathrm{CP}}$ samples, with no temporal overlap across blocks.

We introduce a matrix model for CP-OFDM to express the transmitted signal more compactly and facilitate efficient implementation. Thus, the overall transmitted discrete-time signal $\boldsymbol{s} \in \mathbb{C}^{LM}$ is given by:

$$\boldsymbol{s} \triangleq (\boldsymbol{I}_M \otimes \boldsymbol{T}_{\Delta_{\mathrm{CP}}} \boldsymbol{F}_K^{\mathsf{H}}) \boldsymbol{x} \tag{2.5}$$

where $\otimes$ is the Kronecker product and with

- $\boldsymbol{x} \triangleq [\boldsymbol{x}_0^{\mathsf{T}}, \ldots, \boldsymbol{x}_{M-1}^{\mathsf{T}}]^{\mathsf{T}}$ the full transmitted vector stacking all the blocks M such that the mth transmitted symbol block for $m \in \mathcal{I}_M$ is $\boldsymbol{x}_m \triangleq [x_{0,m}, \ldots, x_{K-1,m}]^{\mathsf{T}}$;
- $\boldsymbol{F}_K$ the $K \times K$ unitary DFT matrix with elements

$$[\boldsymbol{F}_K]_{k,k'} \triangleq (K)^{-1/2} \exp(-j2\pi kk'/K) \tag{2.6}$$

  for $k, k' \in \mathcal{I}_K$;
- $\boldsymbol{T}_{\Delta_{\mathrm{CP}}} \triangleq [\boldsymbol{0}_{\Delta_{\mathrm{CP}},K-\Delta_{\mathrm{CP}}}, \boldsymbol{I}_{\Delta_{\mathrm{CP}}}; \boldsymbol{I}_K]$ the $L \times K$ cyclic extension matrix. Multiplication by $\boldsymbol{T}_{\Delta_{\mathrm{CP}}}$ produces a $(K + \Delta_{\mathrm{CP}})$-length vector by replicating the last Δ_{CP} entries of the K-length input at its beginning, thereby implementing the cyclic prefix extension.

2.1.1.3 Statistical modeling of transmitted symbols

We assume that the transmitted symbols are random. This assumption is crucial to ensure that the DFRC waveform serves both radar and communication functions. While radar target detection typically does not require information-bearing signals, such a property is essential for transmitting information to the communication receiver.

At each OFDM block m, we recall that the transmitted symbol vector is denoted by $\boldsymbol{x}_m = [x_{0,m}, \ldots, x_{K-1,m}]^{\mathsf{T}}$ and is constructed as:

$$\boldsymbol{x}_m \triangleq \boldsymbol{v}_m \odot \sqrt{\boldsymbol{p}}, \tag{2.7}$$

where $\odot$ is the Hadamard (element-wise) product and

- $\boldsymbol{v}_m = [v_{0,m}, \ldots, v_{K-1}, m]^{\mathsf{T}}$ denotes a random symbol vector whose entries $\{v_{k,m}\}_{k=0}^{K-1}$ are mutually independent random variables with zero mean, $\mathcal{E}\{v_{k,m}\} = 0$, and unit variance, $\mathcal{E}\{|v_{k,m}|^2\} = 1$.
- $\boldsymbol{p} = [p_0, \ldots, p_{K-1}]^{\mathsf{T}}$ is the transmitted power allocation profile, with $p_k \triangleq \mathcal{E}_{x_{k,m}}\{|x_{k,m}|^2\}$ the transmitted power on subcarrier k. For each block m, the power p_k allocated to subcarrier k remains the same.

We distinguish two main cases based on the distribution of the symbols v_k.

Gaussian symbols Each $v_{k,m}$ is modeled as a complex Gaussian random variable with zero mean and unit variance. Hence, for each $m \in \mathcal{I}_M$, we have:

$$\boldsymbol{v}_m \sim \mathcal{CN}(\boldsymbol{0}, \boldsymbol{I}_K). \tag{2.8}$$

In this case, the transmitted symbol vector $\boldsymbol{x}$ follows a circular complex Gaussian distribution with diagonal covariance $\boldsymbol{D_p}$, namely:

$$\boldsymbol{x} \sim \mathcal{CN}(\boldsymbol{0}, \boldsymbol{D_p}). \tag{2.9}$$

Gaussian symbols do not carry information themselves; rather, this model is an idealized assumption adopted for mathematical tractability and performance benchmarking and is not used for practical scenarios. Moreover, such Gaussian-input assumptions are common in communications [74, 75].

Discrete constellation symbols Each $v_{k,m}$ takes values in a fixed discrete constellation $\mathcal{C}$, with zero mean and unit average power (e.g., PSK, QAM). The a priori probability of each symbol $v_{k,m}$ is denoted as $P(v_{k,m})$ (for PSK and QAM, this probability is fixed and is typically uniform over $\mathcal{C}$). This model captures typical practical constellations used in communication systems. The transmitted waveform propagates through distinct radar and communication channels. In the following two sections, we model separately both channels seen by the transmitted waveform.

2.1.2 Channel models

2.1.2.1 Received radar signal

As the transmitted signal propagates through free space at the speed of light c, it encounters various alterations. In particular, when the signal encounters obstacles, part of the electromagnetic wave is backscattered towards the radar receiver. The latter can then use these reflections to characterize its target. Below, we describe the signal model associated with the different contributions from the radar channel.

We consider a radar system in which the receiver is either collocated with the transmitter or otherwise knows the transmitted symbols $\boldsymbol{x}$ as is usually the case in radar processing. Our model presumes that the received signal consists of the transmitted signal reflected by a single target and additive white noise. This noise-limited radar model neglects potential contributions from environmental clutter, which may be significant in complex propagation environments (e.g., urban or indoor scenarios, weather clutter). Such effects are not considered here to maintain tractability and focus on the target response itself.

Target We consider a range-extended target that consists of L_r scatterers illuminated by the transmitted signal $\boldsymbol{s}$. Each scatterer i is assumed to be characterized by:

- a random non-zero complex amplitude $h_{\mathrm{r},i}$ constant over the duration of the transmitted signal, with $\boldsymbol{h}_\mathrm{r} = [h_{\mathrm{r},0}, \cdots, h_{\mathrm{r},L_\mathrm{r}-1}]^\mathsf{T}$;
- an initial distance $R_{\mathrm{r},i}$ to the RadCom system, associated with a round-trip signal propagation time $\tau_{\mathrm{r},i} = 2R_{\mathrm{r},i}/c$, with c the speed of light.
- a radial velocity relative to the radar, which is identical for all the scatterers, is denoted v. Hence, the Doppler effect of each scatterer manifests as a frequency shift $F_d = 2vF_c/c$.

Remark 2.1.3 (Common Doppler Assumption)**.** *Radar models often assume that all scatterers within a target share a common Doppler frequency. This assumption is valid when the target is compact and exhibits rigid-body motion, hence the internal motions within the target are negligible [76]. However, this assumption breaks down for articulated targets (e.g., pedestrians, animals, robotic systems) where individual scatterers exhibit differential motion and hence distinct Doppler shifts.*

Noise The received signal includes a noise component. We assume that it mainly results from the sum of the antenna noise contributions (including background radiation and thermal noise) generated by the thermal agitation of electrons within the electronic components of the receiver. The noise is classically modeled as a zero-mean white Gaussian process with power $\sigma^2_{n_\mathrm{r}}$.

Therefore, the complex envelope of the received signal can be written as

$$y_\mathrm{r}(t) = \sum_{i \in \mathcal{I}_{L_\mathrm{r}}} h_{\mathrm{r},i} e^{j2\pi F_d t} s(t - \tau_{\mathrm{r},i}) + n_\mathrm{r}(t)$$

with n_r the additive white Gaussian noise (AWGN).

The signal $y_\mathrm{r}(t)$ is then sampled at the critical sampling frequency $1/T_\mathrm{s} = B$.

- We assume, unless stated otherwise, that there is no range ambiguity meaning ultimately that the delay $\tau_{\mathrm{r},i}$ for any scatterer i is lower than the PRI, i.e., T_0 [26, p. 22]. We also assume that each $\tau_{\mathrm{r},i}$ is an integer multiple of T_s, i.e., $\tau_{\mathrm{r},i} = \ell_{\mathrm{r},i} T_s$ with $\ell_{\mathrm{r},i} \in \mathcal{I}_L$ the range bin of the scatterer i.

- We consider unambiguous Doppler shifts, so the measurable Doppler frequency satisfies $|F_d| \leq 1/(2T_0)$ [26, p. 24]. Accordingly, we model the target Doppler as $F_d = n_0/(MLT_\mathrm{s})$ with $n_0 \in [-M/2, M/2]$ the target's Doppler bin and M the number of radar sweeps. We also denote the normalized Doppler frequency $f_d \triangleq F_d L T_\mathrm{s} = n_0/M$.

Therefore, for $l \in \mathcal{I}_{LM}$, we denote $y_\mathrm{r}[l] = y_\mathrm{r}(lT_\mathrm{s})$, we obtain the following:

$$y_\mathrm{r}[l] = \sum_{i \in \mathcal{I}_{L_\mathrm{r}}} h_{\mathrm{r},i} e^{j2\pi l \frac{f_d}{L}} s[l - \ell^\mathrm{r}_{0,i}] + n_\mathrm{r}[l]. \tag{2.10}$$

The formulation (2.10) describes the radar echo as a superposition of delayed and Doppler-shifted copies of the transmitted signal, one per scatterer. The Doppler term introduces a time-varying phase, while the delay shifts the signal in time. The result is that each received sample contains overlapping reflections from different scatterers, which the radar receiver must resolve in range and velocity.

We now introduce a more compact vector notation to represent our signals (see Figure 2.1). We introduce the following LM-length received signal vector

$$\boldsymbol{y}_\mathrm{r} = \boldsymbol{D}_{\boldsymbol{v}_{f_d}}(\boldsymbol{P}_\mathrm{r}\boldsymbol{h}_\mathrm{r} * \boldsymbol{s}) + \boldsymbol{n}_\mathrm{r} \tag{2.11}$$

where $*$ denotes the linear convolution and

- $\boldsymbol{P}_\mathrm{r}$ is an $LM \times L_\mathrm{r}$ binary matrix indicating the scatterers positions such that

$$[\boldsymbol{P}_\mathrm{r}]_{i,j} = 1 \text{ if } j = \ell_{\mathrm{r},i} \text{ and 0 otherwise.} \tag{2.12}$$

  This means that the jth scatterer is located at delay index i (i.e., in the ith time slot).

- $\boldsymbol{D}_{\boldsymbol{v}_{f_d}}$ is the diagonal Doppler matrix given by

$$\boldsymbol{D}_{\boldsymbol{v}_{f_d}} = \mathrm{diag}\left\{ e^{j2\pi \frac{f_d}{L} 0}, \cdots, e^{j2\pi \frac{f_d}{L}(LM-1)} \right\}. \tag{2.13}$$

- $\boldsymbol{n}_\mathrm{r}$ is the AWGN vector $\boldsymbol{n}_\mathrm{r} \sim \mathcal{CN}\left(\boldsymbol{0}, \sigma^2_{n_\mathrm{r}} \boldsymbol{I}_{LM}\right)$.

Hence, the received block can thus be expressed as

$$\boldsymbol{y}_\mathrm{r} = \boldsymbol{D}_{\boldsymbol{v}_{f_d}} \boldsymbol{H}_\mathrm{r} \boldsymbol{s} + \boldsymbol{n}_\mathrm{r} \tag{2.14}$$

where we have $\boldsymbol{H}_\mathrm{r} = \text{Toeplitz}\{\boldsymbol{P}_\mathrm{r}\boldsymbol{h}_\mathrm{r}\}$. The structure in (2.14) can be interpreted as a block-wise linear mixing of the delayed and Doppler-shifted echoes from multiple scatterers, each contributing to distinct time samples of the received signal.

Alternatively, from the commutativity of the convolution product in Equation (2.11), we

can also rewrite the received radar vector as follows

$$\boldsymbol{y}_{\mathrm{r}} = \boldsymbol{D}_{\boldsymbol{v}_{f_d}} \boldsymbol{S} \boldsymbol{P}_{\mathrm{r}} \boldsymbol{h}_{\mathrm{r}} + \boldsymbol{n}_{\mathrm{r}} \tag{2.15}$$

where $\boldsymbol{S}$ is the $LM \times LM$ Toeplitz matrix constructed from the transmitted waveform $\boldsymbol{s}$ defined as:

$$\boldsymbol{S} = \text{Toeplitz}\left\{\boldsymbol{s}\right\}. \tag{2.16}$$

Remark 2.1.4 (Doppler Modeling under the Narrowband Assumption)**.** *The Doppler effect is modeled here as a pure frequency shift, which is valid under the narrowband assumption ($B \ll F_c$) [77, p. 336]. This simplifies the received signal model, as the Doppler manifests as a diagonal modulation matrix $\boldsymbol{D}_{\boldsymbol{v}_{f_d}}$. However, in wideband scenarios, Doppler induces both frequency and time distortion (i.e., a time-scaling effect), which would require a more sophisticated model beyond the scope of this work.*

2.1.2.2 Statistical modeling of the target response

We posit that the range-extended target has already been pre-detected in range and Doppler. Hence, its normalized Doppler frequency f_d and range bin positions $\ell_{0,i}$ (or, equivalently, the support of the extended target $\boldsymbol{P}_{\mathrm{r}}$) are known to the radar receiver. We further assume that a feedback mechanism (e.g., within a cognitive approach) collects information about the second-order statistics of the target amplitude vector, i.e., the target response $\boldsymbol{h}_{\mathrm{r}}$. To model it, we adopt a complex circular Gaussian prior:

$$\boldsymbol{h}_{\mathrm{r}} \sim \mathcal{CN}\left(\boldsymbol{0}, \boldsymbol{K}_{\boldsymbol{h}_{\mathrm{r}}}\right) \tag{2.17}$$

where $\boldsymbol{K}_{\boldsymbol{h}_{\mathrm{r}}}$ denotes the covariance matrix of $\boldsymbol{h}_{\mathrm{r}}$.

The radar target response $\boldsymbol{h}_{\mathrm{r}}$ is modeled as a zero-mean complex Gaussian vector. This assumption enables tractable derivations for estimation-theoretic metrics (e.g., Minimum Mean Squared Error (MMSE) estimator of the target response). While real-world scatterers amplitudes may follow more complex distributions (e.g., compound-Gaussian, K-distribution), the Gaussian model is a widely accepted first-order approximation, especially in cases with strong prior averaging or aggregation of many independent scatterers.

Moreover, the radar target response $\boldsymbol{h}_{\mathrm{r}}$ covariance matrix $\boldsymbol{K}_{\boldsymbol{h}_{\mathrm{r}}}$ is considered to be known. This assumption simplifies the analysis and enables the use of different radar estimation performance metrics (see Section 2.2.2). However, this assumption can have many limitations. First, we need accurate and reliable prior knowledge of the target's second-order statistics, which may not be available in practice. Second, the performance of the radar estimation metrics depends heavily on the knowledge $\boldsymbol{K}_{\boldsymbol{h}_{\mathrm{r}}}$. Thus, model mismatches may lead to suboptimal or biased performance. Nonetheless, this assumption may be reasonable in the cognitive radar approach, where a feedback mechanism can estimate and update $\boldsymbol{K}_{\boldsymbol{h}_{\mathrm{r}}}$ over time in applications with slowly varying environments. The estimation of this covariance matrix is not

addressed in this work.

2.1.2.3 Received communication signal

In addition to the radar reflections, the transmitted waveform propagates through a dedicated communication channel to a communication receiver. This section describes the propagation model for the communication channel and the resulting received signal.

We posit the communication receiver is located in a distinct position from the radar receiver and is subject to multipath propagation due to scattering by various reflectors in the environment. Let L_{c} be the number of multipath scatterers in the communication channel. Each scatterer $i \in \mathcal{I}_{L_{\mathrm{c}}}$ is characterized by:

- a complex path gain $h_{\mathrm{c},i}$, collected in the vector $\boldsymbol{h}_{\mathrm{c}} = [h_{\mathrm{c},0}, \ldots, h_{\mathrm{c},L_{\mathrm{c}}-1}]^{\mathsf{T}}$;
- a known delay $\tau_{\mathrm{c},i} = \ell_{\mathrm{c},i} T_s$, where $\ell_{\mathrm{c},i} \in \mathbb{N}$ denotes the discrete delay bin that align with the sampling grid;
- no Doppler shifts, assuming either static or slowly moving receiver relative to the transmitter.

The continuous-time received communication signal is then modeled as:

$$y_{\mathrm{c}}(t) = \sum_{i \in \mathcal{I}_{L_{\mathrm{c}}}} h_{\mathrm{c},i} s(t - \tau_{\mathrm{c},i}) + n_{\mathrm{c}}(t) \tag{2.18}$$

with $n_{\mathrm{c}}(t)$ denoting additive white Gaussian noise.

Sampling this signal at rate $1/T_s$, the discrete-time sampled signal is given by:

$$y_{\mathrm{c}}[l] = \sum_{i \in \mathcal{I}_{L_{\mathrm{c}}}} h_{\mathrm{c},i} s[l - \ell_{\mathrm{c},i}] + n_{\mathrm{c}}[l], \quad l \in \mathcal{I}_{LM}. \tag{2.19}$$

We then switch to matrix notation (see Figure 2.1). The LM-length received signal is:

$$\boldsymbol{y}_{\mathrm{c}} = \boldsymbol{H}_{\mathrm{c}} \boldsymbol{s} + \boldsymbol{n}_{\mathrm{c}} \tag{2.20}$$

with

- $\boldsymbol{H}_{\mathrm{c}} \triangleq \mathrm{Toeplitz}\{\boldsymbol{P}_{\mathrm{c}} \boldsymbol{h}_{\mathrm{c}}\}$ the $LM \times LM$ linear convolution matrix which captures the linear convolution between the channel impulse response and the transmitted signal $\boldsymbol{s}$. The discrete-time equivalent impulse response is denoted $\boldsymbol{P}_{\mathrm{c}} \boldsymbol{h}_{\mathrm{c}}$ where
  - $\boldsymbol{h}_{\mathrm{c}} \triangleq [h_{\mathrm{c},0}, \cdots, h_{\mathrm{c},L_{\mathrm{c}}-1}]^{\mathsf{T}}$ gathers the non-zero scatterers;

– $\boldsymbol{P}_{\mathrm{c}}$ is an $LM \times L_{\mathrm{c}}$ binary matrix indicating the communication scatterers positions such that

$$[\boldsymbol{P}_{\mathrm{c}}]_{i,j} = 1 \text{ if } j = \ell_{\mathrm{c},i} \text{ and 0 otherwise;} \tag{2.21}$$

- $\boldsymbol{n}_{\mathrm{c}} \sim \mathcal{CN}\left(\boldsymbol{0}, \sigma_{n_{\mathrm{c}}}^2 \boldsymbol{I}_{LM}\right)$ an additive white Gaussian noise with power $\sigma_{n_{\mathrm{c}}}^2$.

2.1.2.4 Deterministic modeling of the communication channel

The communication channel is considered to be Doppler-free, known and deterministic, unlike the radar channel. This reflects scenarios where the communication receiver is either static or moving slowly relative to the transmitter, and where channel state information (CSI) is available through feedback mechanisms, as commonly assumed in modern wireless systems (e.g., via pilot-based estimation) [48, p. 236].

2.1.3 CP-OFDM receivers

In this section, we describe the first and classical processing step of our assumed CP-OFDM radar and communication receivers, namely CP-OFDM demodulation. This initial operation does not represent the complete processing chain but rather provides the foundation for subsequent tasks such as estimation.

2.1.3.1 CP-OFDM receiver architecture

Usually, CP-OFDM communication receivers process the received signal in two main steps [78]. First, the CP is removed which discards the redundant samples added at transmission and, as long as the CP length exceeds the channel delay spread, converts the linear convolution with the channel into a circular convolution. This guarantees that inter-symbol and inter-carrier interference are avoided and that subcarrier orthogonality is preserved. Second, the signal is transformed by an FFT into the frequency domain. This operation diagonalizes the channel, so that each subcarrier experiences only a complex scalar gain.

We assume here that the radar receiver implements a similar architecture to benefit from the CP-OFDM waveform. Hence, the receiver processes the received signal block-wise by removing the CP and applying an FFT. This operation yields the following frequency-domain representation of the received signal:

$$\tilde{\boldsymbol{x}}_{\alpha} \triangleq (\boldsymbol{I}_M \otimes \boldsymbol{F}_K \boldsymbol{R}_{\Delta_{\mathrm{CP}}}) \boldsymbol{y}_{\alpha} \tag{2.22}$$

where the generic subscript $\alpha \in \{\mathrm{r}, \mathrm{c}\}$ refers either to radar or communication chan-

nels/receivers and

$$\boldsymbol{R}_{\Delta_{\mathrm{CP}}} \triangleq [\boldsymbol{0}_{K,\Delta_{\mathrm{CP}}}, \boldsymbol{I}_K] \tag{2.23}$$

is the CP removal matrix.

2.1.3.2 Radar CP-OFDM receiver

The radar receiver processes the signal in the frequency domain using the CP-OFDM structure. To express the received signal $\tilde{\boldsymbol{x}}_{\mathrm{r}}$ after CP removal and FFT, we introduce two equivalent notations depending on whether Doppler is treated as explicit modulation or folded into the channel matrix. Both notations are useful in different analysis contexts.

Notation 1: Radar channel matrix in the frequency domain This notation expresses the received vector as a linear function of the transmitted symbols and the radar channel matrix (see Figure 2.1). Starting from (2.14) and (2.5) and then applying the CP-OFDM receiver transformation (2.22), we obtain:

$$\begin{aligned}\tilde{\boldsymbol{x}}_{\mathrm{r}} &= (\boldsymbol{I}_M \otimes \boldsymbol{F}_K \boldsymbol{R}_{\Delta_{\mathrm{CP}}}) \left(\boldsymbol{D}_{\boldsymbol{v}_{f_d}} \boldsymbol{H}_{\mathrm{r}} \boldsymbol{s} + \boldsymbol{n}_{\mathrm{r}} \right) \\ &= (\boldsymbol{I}_M \otimes \boldsymbol{F}_K \boldsymbol{R}_{\Delta_{\mathrm{CP}}}) \boldsymbol{D}_{\boldsymbol{v}_{f_d}} \boldsymbol{H}_{\mathrm{r}} (\boldsymbol{I}_M \otimes \boldsymbol{T}_{\Delta_{\mathrm{CP}}} \boldsymbol{F}_K^{\mathsf{H}}) \boldsymbol{x} + \tilde{\boldsymbol{n}}_{\mathrm{r}} \\ &= \boldsymbol{G}_{\mathrm{r}} \boldsymbol{x} + \tilde{\boldsymbol{n}}_{\mathrm{r}}\end{aligned} \tag{2.24}$$

where $\boldsymbol{G}_{\mathrm{r}}$ is the $KM \times KM$ radar channel matrix in the frequency domain defined as:

$$\boldsymbol{G}_{\mathrm{r}} \triangleq (\boldsymbol{I}_M \otimes \boldsymbol{F}_K \boldsymbol{R}_{\Delta_{\mathrm{CP}}}) \boldsymbol{D}_{\boldsymbol{v}_{f_d}} \boldsymbol{H}_{\mathrm{r}} (\boldsymbol{I}_M \otimes \boldsymbol{T}_{\Delta_{\mathrm{CP}}} \boldsymbol{F}_K^{\mathsf{H}}) \tag{2.25}$$

and $\tilde{\boldsymbol{n}}_{\mathrm{r}}$ the AWGN vector in the frequency domain

$$\tilde{\boldsymbol{n}}_{\mathrm{r}} \triangleq (\boldsymbol{I}_M \otimes \boldsymbol{F}_K \boldsymbol{R}_{\Delta_{\mathrm{CP}}}) \boldsymbol{n}_{\mathrm{r}} \sim \mathcal{CN}\left(\boldsymbol{0}, \sigma_{n_{\mathrm{r}}}^2 \boldsymbol{I}_{KM}\right) \tag{2.26}$$

such that its power remains unchanged and equals that of $\boldsymbol{n}_{\mathrm{r}}$; this is easily proved by noticing that $\boldsymbol{R}_{\Delta_{\mathrm{CP}}} \boldsymbol{R}_{\Delta_{\mathrm{CP}}}^{\mathsf{H}} = \boldsymbol{I}_K$ and the unitarity of $\boldsymbol{F}_K$, so the map $(\boldsymbol{I}_M \otimes \boldsymbol{F}_K \boldsymbol{R}_{\Delta_{\mathrm{CP}}})$ preserves both noise power and whiteness.

Notation 2: Linear model for target response estimation An alternative and often more convenient notation expresses the received vector as a linear function of the target response $\boldsymbol{h}_{\mathrm{r}}$, using (2.15), we have:

$$\tilde{\boldsymbol{x}}_{\mathrm{r}} = (\boldsymbol{I}_M \otimes \boldsymbol{F}_K \boldsymbol{R}_{\Delta_{\mathrm{CP}}}) \left(\boldsymbol{D}_{\boldsymbol{v}_{f_d}} \boldsymbol{S} \boldsymbol{P}_{\mathrm{r}} \boldsymbol{h}_{\mathrm{r}} + \boldsymbol{n}_{\mathrm{r}} \right) \tag{2.27}$$

$$= \boldsymbol{A}_{\mathrm{r}} \boldsymbol{h}_{\mathrm{r}} + \tilde{\boldsymbol{n}}_{\mathrm{r}} \tag{2.28}$$

with $\boldsymbol{A}_{\mathrm{r}}$ the $KM \times L_{\mathrm{r}}$ matrix of $\boldsymbol{h}_{\mathrm{r}}$ defined as:

$$\boldsymbol{A}_{\mathrm{r}} \triangleq (\boldsymbol{I}_M \otimes \boldsymbol{F}_K \boldsymbol{R}_{\Delta_{\mathrm{CP}}}) \boldsymbol{D}_{\boldsymbol{v}_{f_d}} \boldsymbol{S} \boldsymbol{P}_{\mathrm{r}} \tag{2.29}$$

where $\boldsymbol{S} \triangleq \text{Toeplitz}\{\boldsymbol{s}\}$ is the Toeplitz matrix of the transmitted signal $\boldsymbol{s}$. This formulation is particularly well-suited for estimation-theoretic analysis (e.g., MMSE estimator of the target response).

Radar channel diagonalization under zero Doppler When the Doppler frequency F_d is zero (corresponding to stationary targets) the diagonal matrix $\boldsymbol{D}_{\boldsymbol{v}_{f_d}}$ (2.13) in the radar model (2.14) reduces to the identity matrix. In this case, the time-domain radar channel can be modeled as a pure linear convolution, unmodulated by any time-varying phase.
In the CP-OFDM framework, such linear convolution can be transformed into a circular convolution provided that the CP is sufficiently long to absorb the entire delay spread of the channel. This is known as the *well-designed* CP condition explained in the following definition.

Definition 2.1.1 (Well-designed CP)**.** The CP is said to be *well-designed*, if and only if its length equals or exceeds the channel's length $\ell_{\alpha,i}$:

$$\ell_{\alpha,i} \leq \Delta_{\mathrm{CP}}, \quad \text{for} \quad i \in \mathcal{I}_{L_\alpha} \tag{2.30}$$

with L_α the number of the non-zero scatterers for the α channel.

Using the expression of the frequency-domain radar channel matrix (2.25) and setting $\boldsymbol{D}_{\boldsymbol{v}_{f_d}} = \boldsymbol{I}_{LM}$, we obtain:

$$\boldsymbol{G}_{\mathrm{r}} \triangleq (\boldsymbol{I}_M \otimes \boldsymbol{F}_K \boldsymbol{R}_{\Delta_{\mathrm{CP}}}) \boldsymbol{H}_{\mathrm{r}} (\boldsymbol{I}_M \otimes \boldsymbol{T}_{\Delta_{\mathrm{CP}}} \boldsymbol{F}_K^{\mathsf{H}}). \tag{2.31}$$

When the CP is well designed, the radar channel matrix $\boldsymbol{H}_{\mathrm{r}}$ becomes block-circulant. As a result, the composition $\boldsymbol{R}_{\Delta_{\mathrm{CP}}} \boldsymbol{H}_{\mathrm{r}} \boldsymbol{T}_{\Delta_{\mathrm{CP}}}$ is circulant within each block and therefore diagonalizable by the DFT . Consequently, $\boldsymbol{G}_{\mathrm{r}}$ becomes diagonal and the elements along the diagonal are K-periodic, with each of the M blocks being a diagonal $K \times K$ submatrix, each corresponding to one OFDM block.
This diagonal structure reflects Transmitter (TX)/Receiver (RX) bi-orthogonality, i.e., there is no inter-carrier interference, and the radar receiver observes independent linear measurements per subcarrier. Under this structure, the received symbols simplify to:

$$\tilde{\boldsymbol{x}}_{\mathrm{r}} = \boldsymbol{D}_{\boldsymbol{x}} (\boldsymbol{1}_{M,1} \otimes \boldsymbol{I}_K) \boldsymbol{B}_{\mathrm{r}} \boldsymbol{h}_{\mathrm{r}} + \tilde{\boldsymbol{n}}_{\mathrm{r}} \tag{2.32}$$

$$= (\boldsymbol{I}_M \otimes \boldsymbol{D}_{\boldsymbol{g}_{\mathrm{r}}}) \boldsymbol{x} + \tilde{\boldsymbol{n}}_{\mathrm{r}}. \tag{2.33}$$

Here, the radar channel transfer function is defined by:

$$\boldsymbol{g}_{\mathrm{r}} \triangleq \boldsymbol{B}_{\mathrm{r}} \boldsymbol{h}_{\mathrm{r}} \tag{2.34}$$

with

$$\boldsymbol{B}_{\mathrm{r}} \triangleq \sqrt{K}\boldsymbol{F}_K\boldsymbol{Q}_{\Delta_{\mathrm{CP}}}\boldsymbol{P}_{\mathrm{r},1} \tag{2.35}$$

where

- $\boldsymbol{Q}_{\Delta_{\mathrm{CP}}}$ is the matrix defined as

$$\boldsymbol{Q}_{\Delta_{\mathrm{CP}}} \triangleq [\boldsymbol{I}_K, \boldsymbol{0}_{K,\Delta_{\mathrm{CP}}}]; \tag{2.36}$$

- $\boldsymbol{P}_{\mathrm{r},1}$ is an $L \times L_{\mathrm{r}}$ effective scatterer support matrix defined as:

$$\boldsymbol{P}_{\mathrm{r},1} = [\boldsymbol{P}_{\mathrm{r}}]_{1\leq i\leq L, 1\leq j\leq L_{\mathrm{r}}}. \tag{2.37}$$

The matrix $\boldsymbol{B}_{\mathrm{r}}$ maps the physical scatterer amplitudes (i.e., the target response $\boldsymbol{h}_{\mathrm{r}}$) into their contributions across frequency subcarriers. Its structure combines a DFT (via $\boldsymbol{F}_K$), a CP truncation operator ($\boldsymbol{Q}_{\Delta_{\mathrm{CP}}}$), and a delay-position mapping ($\boldsymbol{P}_{\mathrm{r},1}$) of the scatterers.

In contrast, when $F_d \neq 0$, the diagonal matrix $\boldsymbol{D}_{\boldsymbol{v}_{f_d}}$ introduces a time-varying phase across the received samples, which breaks the circular structure and induces inter-carrier interference. As a result, $\boldsymbol{G}_{\mathrm{r}}$ remains block-diagonal, but each block is not necessarily diagonal and subcarrier observations become coupled.

Proof. See Chapter A □

Definition 2.1.2 (Radar SNR per subcarrier)**.** With a sufficiently long CP and zero Doppler, the frequency-domain model (2.33) implies that the radar observation on each subcarrier can be written with a per-subcarrier gain $\boldsymbol{g}_{\mathrm{r}}$, which is a linear combination of the target's random impulse response $\boldsymbol{h}_{\mathrm{r}}$ (see (2.17)) and $\boldsymbol{B}_{\mathrm{r}}$ (2.35). Even if $\boldsymbol{x}$ is known, the randomness of $\boldsymbol{h}_{\mathrm{r}}$ induces fluctuations in $\boldsymbol{g}_{\mathrm{r}}$. To capture these second-order statistics directly in the subcarrier domain (where power per-subcarrier is typically measured and allocated) we therefore define the target's covariance matrix in the frequency domain (i.e., in the subcarrier domain) as follows:

$$\boldsymbol{K}_{\boldsymbol{g}_{\mathrm{r}}} = M\boldsymbol{B}_{\mathrm{r}}\boldsymbol{K}_{\boldsymbol{h}_{\mathrm{r}}}\boldsymbol{B}_{\mathrm{r}}^{\mathsf{H}} \tag{2.38}$$

where each entry $[\boldsymbol{K}_{\boldsymbol{g}_{\mathrm{r}}}]_{k,k'}$ quantifies the statistical correlation between two subcarriers k and k' induced by the range-extended target. Hence, the diagonal elements correspond to the signal power received on subcarrier k due to the reflection of the radar waveform from the range-extended target. The matrix $\boldsymbol{K}_{\boldsymbol{g}_{\mathrm{r}}}$ thus encapsulates how the target echoes manifest across the subcarrier dimension and serves as a foundational quantity in estimation-theoretic and information-theoretic radar performance metrics.

Therefore, we can introduce the dimensionless noise-normalized covariance matrix $\sigma_{n_{\mathrm{r}}}^{-2}\boldsymbol{K}_{\boldsymbol{g}_{\mathrm{r}}}$, which we interpret as "the radar channel in the subcarrier domain". Normalizing by $\sigma_{n_{\mathrm{r}}}^2$ expresses target-induced power and inter-subcarrier coupling directly in a SNR

way. In this formulation, the diagonal entries are the radar SNRs per subcarrier, defined as

$$a_k \triangleq \frac{[\boldsymbol{K}_{\boldsymbol{g}_\mathrm{r}}]_{k,k}}{\sigma_{n_\mathrm{r}}^2} \geq 0. \tag{2.39}$$

The off-diagonal elements of $\sigma_{n_\mathrm{r}}^{-2}\boldsymbol{K}_{\boldsymbol{g}_\mathrm{r}}$ indicate the correlation levels between subcarriers.

2.1.3.3 Communication CP-OFDM receiver

The communication receiver processes the signal in the frequency domain using the CP-OFDM structure. The communication channel is assumed to be Doppler free hence when the CP is well designed for the communication system (see Definition 2.1.1), we observe that $\boldsymbol{R}_{\Delta_\mathrm{CP}}\boldsymbol{H}_\mathrm{c}\boldsymbol{T}_{\Delta_\mathrm{CP}}$ is circulant. As a result, by applying the same diagonalization approach detailed in Chapter A as for the radar in the Doppler-free case, we obtain a diagonalized representation of the communication channel in the frequency domain. Specifically, the received communication symbols are given by

$$\tilde{\boldsymbol{x}}_\mathrm{c} = (\boldsymbol{I}_M \otimes \boldsymbol{D}_{\boldsymbol{g}_\mathrm{c}})\boldsymbol{x} + \tilde{\boldsymbol{n}}_\mathrm{c} \tag{2.40}$$

where

- $\boldsymbol{D}_{\boldsymbol{g}_\mathrm{c}}$ is the frequency-domain channel matrix where

  $$\boldsymbol{g}_\mathrm{c} = \sqrt{K}\boldsymbol{F}_K\boldsymbol{Q}_{\Delta_\mathrm{CP}}\boldsymbol{P}_\mathrm{c}\boldsymbol{h}_\mathrm{c} \tag{2.41}$$

  is the transfer function of the communication channel (which channel response is $\boldsymbol{h}_\mathrm{c}$), and $\boldsymbol{P}_\mathrm{c}$ defined in (2.21);

- $\tilde{\boldsymbol{n}}_\mathrm{c}$ is the AWGN in the frequency domain, *viz*

  $$\tilde{\boldsymbol{n}}_\mathrm{c} \triangleq (\boldsymbol{I}_M \otimes \boldsymbol{F}_K\boldsymbol{R}_{\Delta_\mathrm{CP}})\boldsymbol{n}_\mathrm{c} \sim \mathcal{CN}\left(\boldsymbol{0}, \sigma_{n_\mathrm{c}}^2\boldsymbol{I}_{KM}\right). \tag{2.42}$$

Definition 2.1.3 (Communication SNR per subcarrier)**.** We define the communication SNR on subcarrier k as

$$c_k \triangleq \frac{|g_{\mathrm{c},k}|^2}{\sigma_{n_\mathrm{c}}^2} \geq 0 \tag{2.43}$$

where $g_{\mathrm{c},k}$ is the complex communication channel gain (transfer function) in the subcarrier domain, and $\sigma_{n_\mathrm{c}}^2$ is the power of the AWGN at the communication receiver.
Each c_k quantifies the relative strength of the received signal to the background noise on subcarrier k. A higher value of c_k means better communication channel conditions and higher reliability for data transmission on that subcarrier.

2.1.4 System model summary and limitations

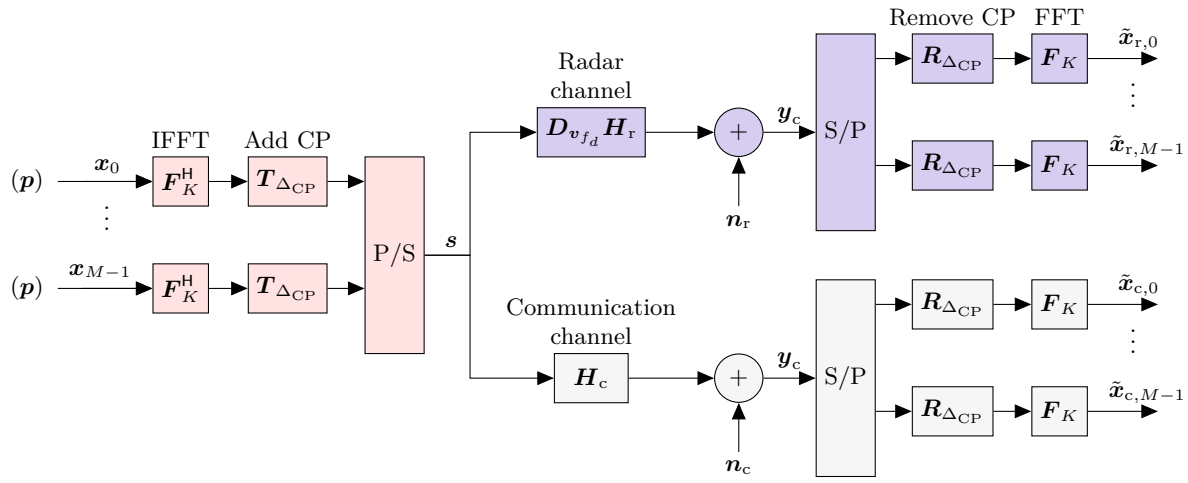


Figure 2.3: Block diagram of the discrete-time OFDM-DFRC system model with radar and communication channels emphasizing a block-wise processing. The power profile of each transmitted symbol vector $\boldsymbol{x}_m$ on each block m is $\boldsymbol{p}$.

Figure 2.3 presents a detailed block diagram of the discrete-time OFDM-DFRC system model described in this section. It can be seen as an expanded version of Figure 2.1, providing a more precise representation of the modules involved. A single transmitter sends a waveform that serves both radar and communication purposes. The multicarrier structure allows for flexible power allocation across subcarriers, and adding a CP maintains bi-orthogonality between TX and RX in the presence of linear time invariant channels by converting the linear convolution of the channel into circular convolution, enabling FFT-based diagonalization provided a well-designed CP.
The radar channel is modeled as a sum of delayed and Doppler-shifted reflections from a range-extended target composed of multiple scatterers. The communication channel is modeled as known, deterministic, multipath, and Doppler-free. Both channels are represented using Toeplitz matrices to capture their convolution components.

Although CP-OFDM enables low-complexity diagonalization, this structure has practical limitations. The primary weakness of CP-OFDM is its PAPR, a characteristic shared by all multicarrier modulation techniques. A high PAPR is undesirable because it reduces the efficiency of the transmitter's power amplifier as the latter must operate with a large back-off from saturation, which increases energy consumption. Moreover, if the amplifier is driven closer to saturation, the large peaks of the signal can induce nonlinear distortions, thereby degrading both radar and communication performance. The PAPR of our system using our proposed waveforms is studied in Chapter E. Additionally, the CP introduces a spectral efficiency loss, as a portion of each block carries redundant data. Furthermore, OFDM is particularly sensitive to carrier frequency offsets because any mismatch between the TX and RX oscillators destroys the orthogonality of the subcarriers. This loss of orthogonality causes inter-carrier interference necessitating complex frequency offset correction algorithms at the

OFDM receiver. Finally, in fast time-varying channels, the assumption of a quasi-static channel within an OFDM block breaks down, leading to loss of diagonalization and increased leakage across subcarriers. Usually, in this case, the OFDM block duration is selected shorter than the channel coherence time[1], ensuring that the channel remains approximately invariant within a block. These effects are not modeled in the scope of this work.

Having established the detailed models for both the transmitted and received signals, we can now assess the OFDM-DFRC system's performance. The following section introduces the radar and communication performance metrics this work considers and discusses how they relate to the earlier system design choices.

2.2 Performance metrics

We evaluate DFRC performance from two perspectives: radar estimation accuracy and communication information rate. For radar, we consider both an information-theoretic metric (radar mutual information) and an estimation-theoretic one (MSE of the MMSE estimator of the target response). For communication, we evaluate the information rate (IR), which measures the spectral efficiency (at fixed bandwidth) for communication systems.

However, before introducing the metrics, we need to recall some elements of information theory that will help us formulate the expressions of the MIs.

2.2.1 Elements of information theory

This section recalls elements of information theory [4]. Readers familiar with these concepts can proceed directly to the next subsection.

Definition 2.2.1 (Differential entropy)**.** The differential entropy of a continuous random variable $\boldsymbol{u}$ with density $f(\boldsymbol{u})$ is

$$h(\boldsymbol{u}) \triangleq \mathcal{E}_{\boldsymbol{u}} \left\{ -\log_2 \left(f(\boldsymbol{u}) \right) \right\}. \tag{2.44}$$

It measures the uncertainty about the possible outcomes of $\boldsymbol{u}$.

Theorem 2.2.1 (Differential entropy of a complex Gaussian distribution)**.** *If* $\boldsymbol{v} \sim \mathcal{CN}_K(\boldsymbol{m}, \boldsymbol{K})$*, its differential entropy is [4, Th. 8.4.1]*

$$h(\boldsymbol{v}) \triangleq \log_2 \left((\pi e)^K \det \{\boldsymbol{K}\} \right). \tag{2.45}$$

As is characteristic of an uncertainty measure, the entropy only depends on the covariance matrix $\boldsymbol{K}$*.*

[1] The time duration over which the channel impulse response is considered to be not varying

Definition 2.2.2 (Conditional differential entropy)**.** For two continuous random variables $\boldsymbol{u}$ and $\boldsymbol{v}$, the conditional differential entropy of $\boldsymbol{u}$ given $\boldsymbol{v}$ is

$$h(\boldsymbol{u}|\boldsymbol{v}) \triangleq \mathcal{E}_{\boldsymbol{v}} \left\{ h(\boldsymbol{u}|\boldsymbol{v} = .) \right\} \tag{2.46}$$

where $\boldsymbol{v} = .$ designates a realization of $\boldsymbol{v}$.

Definition 2.2.3 (Mutual information)**.** The mutual information (MI) between two continuous random variables $\boldsymbol{u}, \boldsymbol{v}$ can be formulated as a differential entropy difference

$$I(\boldsymbol{u}; \boldsymbol{v}) \triangleq h(\boldsymbol{u}) - h(\boldsymbol{u}|\boldsymbol{v}). \tag{2.47}$$

It measures the statistical dependence between $\boldsymbol{u}$ and $\boldsymbol{v}$. Equivalently, it is the reduction in uncertainty of $\boldsymbol{u}$ due to $\boldsymbol{v}$. The MI is a symmetric quantity.

Definition 2.2.4 (Conditional mutual information)**.** The CMI of random variables $\boldsymbol{u}, \boldsymbol{v}$ given $\boldsymbol{z}$ is

$$I(\boldsymbol{u}; \boldsymbol{v}|\boldsymbol{z}) \triangleq \mathcal{E}_{\boldsymbol{z}} \left\{ I(\boldsymbol{u}; \boldsymbol{v}|\boldsymbol{z} = .) \right\} \tag{2.48}$$

where $\boldsymbol{z} = .$ is a realization of $\boldsymbol{z}$. Using (2.46)–(2.47), the CMI can also be written as

$$I(\boldsymbol{u}; \boldsymbol{v}|\boldsymbol{z}) = h(\boldsymbol{u}|\boldsymbol{z}) - h(\boldsymbol{u}|\boldsymbol{v}, \boldsymbol{z}). \tag{2.49}$$

In the remainder, our mathematical developments use these definitions extensively. We draw attention to the specific use of the notation "$\boldsymbol{u}|\boldsymbol{v} = .$" in (2.46) and (2.48). Indeed, when defining *conditional entropy and MI*, a clear distinct notation between the random variable $\boldsymbol{v}$ and its realization $\boldsymbol{v} = .$ is necessary.

2.2.2 Radar performance metrics

In the following section, we present two radar performance metrics. The first metric is information-theoretic, i.e., the radar CMI; the second metric is a usual estimation-theoretic radar performance metric, i.e., the MSE of the MMSE estimator of the target response.

2.2.2.1 Radar MI and conditional MI

In our DFRC scenario, the radar target is pre-detected in range and Doppler. The radar receiver thus only focuses on estimating the response $\boldsymbol{h}_{\mathrm{r}}$ of the pre-detected range-extended target, over a set of known range bins (i.e., known support). The target response characterizes the reflectivity or scattering strength of the target at different delays. This setup corresponds to radar post-detection parameter estimation, which aims to recover target profiles, not detect their presence. This estimation task aligns with Bell's seminal works on information-theoretic radar waveform design [5], where radar MI–defined as the mutual information between the received radar symbols and the target response $\boldsymbol{h}_{\mathrm{r}}$–was proposed as a key criterion to optimize

radar performance for estimation purposes. Hence, although MI is not a conventional radar estimation metric, it may serve as a proxy that complements the more classical estimation-theoretic metric, namely the MMSE of the target response.

To tailor the metric more specifically to our setting, where the estimation is performed over random transmitted waveforms, we adopt the radar CMI as a performance metric. CMI quantifies the information between the received radar symbols and the target response $\boldsymbol{h}_{\mathrm{r}}$, knowing all the realizations of the random transmitted symbols $\boldsymbol{x}$, which reflects the estimation setting more accurately in DFRC systems. Therefore, combining (2.46)–(2.48), the radar CMI is given by

$$\begin{aligned}\mathrm{CMI} &\triangleq I(\tilde{\boldsymbol{x}}_{\mathrm{r}};\boldsymbol{h}_{\mathrm{r}}|\boldsymbol{x})\\ &\triangleq \mathcal{E}_{\boldsymbol{x}}\left\{h(\tilde{\boldsymbol{x}}_{\mathrm{r}}|\boldsymbol{x}=\cdot)\right\}-\mathcal{E}_{\boldsymbol{h}_{\mathrm{r}},\boldsymbol{x}}\left\{h(\tilde{\boldsymbol{x}}_{\mathrm{r}}|\boldsymbol{h}_{\mathrm{r}}=\cdot,\boldsymbol{x}=\cdot)\right\}. \end{aligned} \tag{2.50}$$

To evaluate (2.50) further, we need to determine the conditional and marginal distributions of $\tilde{\boldsymbol{x}}_{\mathrm{r}}|\boldsymbol{h}_{\mathrm{r}},\boldsymbol{x}$, and $\tilde{\boldsymbol{x}}_{\mathrm{r}}|\boldsymbol{x}$. From (2.28), we know that the received symbols are given by:

$$\tilde{\boldsymbol{x}}_{\mathrm{r}}=\boldsymbol{A}_{\mathrm{r}}\boldsymbol{h}_{\mathrm{r}}+\tilde{\boldsymbol{n}}_{\mathrm{r}}$$

and $\tilde{\boldsymbol{n}}_{\mathrm{r}}$ is an AWGN (2.26) and is given by

$$\tilde{\boldsymbol{n}}_{\mathrm{r}}\sim\mathcal{CN}\left(\boldsymbol{0},\sigma_{n_{\mathrm{r}}}^2\boldsymbol{I}_{KM}\right).$$

Hence, we easily conclude that

$$\tilde{\boldsymbol{x}}_{\mathrm{r}}|\boldsymbol{h}_{\mathrm{r}},\boldsymbol{x}\sim\mathcal{CN}_{KM}\left(\boldsymbol{A}_{\mathrm{r}}\boldsymbol{h}_{\mathrm{r}},\sigma_{n_{\mathrm{r}}}^2\boldsymbol{I}_{KM}\right). \tag{2.51}$$

The following Theorem helps to marginalize (2.51).

Theorem 2.2.2 (Marginalization of Gaussian distributions)**.** *If $\boldsymbol{v}|\boldsymbol{u}$ and $\boldsymbol{u}$ follow a complex Gaussian distribution as*

$$\boldsymbol{v}|\boldsymbol{u}\sim\mathcal{CN}\left(\boldsymbol{A}\boldsymbol{u},\boldsymbol{K}_{\boldsymbol{v}}\right) \tag{2.52}$$

$$\boldsymbol{u}\sim\mathcal{CN}\left(\boldsymbol{\mu},\boldsymbol{K}_{\boldsymbol{u}}\right), \tag{2.53}$$

then the marginal distribution of $\boldsymbol{v}$ is also Gaussian given by

$$\boldsymbol{v}\sim\mathcal{CN}\left(\boldsymbol{A}\boldsymbol{\mu},\boldsymbol{A}\boldsymbol{K}_{\boldsymbol{u}}\boldsymbol{A}^{\mathsf{H}}+\boldsymbol{K}_{\boldsymbol{v}}\right). \tag{2.54}$$

Proof. Proceeding as in [79, p. 93] with complex distributions leads to the result. □

Applying Theorem 2.2.2 to the Gaussian distributions (2.17) and (2.51) yields the marginal

$$\tilde{\boldsymbol{x}}_{\mathrm{r}}|\boldsymbol{x}\sim\mathcal{CN}_{KM}\left(\boldsymbol{0},\boldsymbol{A}_{\mathrm{r}}\boldsymbol{K}_{\boldsymbol{h}_{\mathrm{r}}}\boldsymbol{A}_{\mathrm{r}}^{\mathsf{H}}+\sigma_{n_{\mathrm{r}}}^2\boldsymbol{I}_{KM}\right). \tag{2.55}$$

As a result, we obtain the expressions of the conditional entropies required for evaluating

(2.50):

$$h(\tilde{\boldsymbol{x}}_{\mathrm{r}}|\boldsymbol{h}_{\mathrm{r}}=\cdot,\boldsymbol{x}=\cdot)=\log_2\left((\pi e)^{KM}\det\left\{\sigma_{n_{\mathrm{r}}}^2\boldsymbol{I}_K\right\}\right); \tag{2.56a}$$

$$h(\tilde{\boldsymbol{x}}_{\mathrm{r}}|\boldsymbol{x}=\cdot)=\log_2\left((\pi e)^{KM}\det\left\{\boldsymbol{A}_{\mathrm{r}}\boldsymbol{K}_{\boldsymbol{h}_{\mathrm{r}}}\boldsymbol{A}_{\mathrm{r}}^{\mathsf{H}}+\sigma_{n_{\mathrm{r}}}^2\boldsymbol{I}_{KM}\right\}\right). \tag{2.56b}$$

Consequently, using (2.50), the radar CMI in case of M transmitted CP-OFDM blocks becomes

$$\mathrm{CMI}=\mathcal{E}_{\boldsymbol{x}}\left\{\log_2\det\left(\sigma_{n_{\mathrm{r}}}^{-2}\boldsymbol{A}_{\mathrm{r}}\boldsymbol{K}_{\boldsymbol{h}_{\mathrm{r}}}\boldsymbol{A}_{\mathrm{r}}^{\mathsf{H}}+\boldsymbol{I}_{KM}\right)\right\}. \tag{2.57}$$

Although $\boldsymbol{x}$ does not appear explicitly in (2.57), it is embedded in the observation matrix $\boldsymbol{A}_{\mathrm{r}}$: by (2.29) together with (2.5), $\boldsymbol{A}_{\mathrm{r}}$ is a function of the transmitted symbols. Under the zero-Doppler assumption this dependence becomes explicit, (see (3.1) in Chapter 3).

Remark 2.2.1 (Radar MI with deterministic waveform)**.** *In a conventional radar scenario where the transmitted symbols are deterministic and known, the radar MI quantifies the information between the random extended target response* $\boldsymbol{h}_{\mathrm{r}}$ *and the received signal* $\tilde{\boldsymbol{x}}_{\mathrm{r}}$*. Using the definition* (2.47) *and a similar derivation approach to the radar CMI, we obtain:*

$$\begin{aligned} MI &\triangleq I(\tilde{\boldsymbol{x}}_{\mathrm{r}};\boldsymbol{h}_{\mathrm{r}}) \\ &= h(\tilde{\boldsymbol{x}}_{\mathrm{r}})-h(\tilde{\boldsymbol{x}}_{\mathrm{r}}|\boldsymbol{h}_{\mathrm{r}}) && (2.58)\\ &= \log_2\det\left(\sigma_{n_{\mathrm{r}}}^{-2}\boldsymbol{A}_{\mathrm{r}}\boldsymbol{K}_{\boldsymbol{h}_{\mathrm{r}}}\boldsymbol{A}_{\mathrm{r}}^{\mathsf{H}}+\boldsymbol{I}_{KM}\right) && (2.59)\end{aligned}$$

2.2.2.2 MSE and conditional MSE

We explicitly discuss the estimation of the target's echo using standard estimation techniques. Our interest is focused on the conventional MMSE estimator of $\boldsymbol{h}_{\mathrm{r}}$ given knowledge of the current transmitted waveform "$\boldsymbol{x}=.$". Using (2.17)–(2.26), its expression is obtained by extending [80, Th. 10.3]—stated for real-valued vectors—to the complex case via [80, Chap. 15]:

$$\begin{aligned}\boldsymbol{h}_{\mathrm{r}}^{\mathrm{MMSE}} &\triangleq \arg\min_{\hat{\boldsymbol{h}}_{\mathrm{r}}}\mathcal{E}_{\boldsymbol{h}_{\mathrm{r}}|\boldsymbol{x}}\left\{\left\|\boldsymbol{h}_{\mathrm{r}}-\hat{\boldsymbol{h}}_{\mathrm{r}}\right\|^2\right\} \\ &= \boldsymbol{K}_{\boldsymbol{h}_{\mathrm{r}}}\boldsymbol{A}_{\mathrm{r}}^{\mathsf{H}}\left(\boldsymbol{A}_{\mathrm{r}}\boldsymbol{K}_{\boldsymbol{h}_{\mathrm{r}}}\boldsymbol{A}_{\mathrm{r}}^{\mathsf{H}}+\sigma_{n_{\mathrm{r}}}^2\boldsymbol{I}_{KM}\right)\tilde{\boldsymbol{x}}_{\mathrm{r}}.\end{aligned} \tag{2.60}$$

The estimator (2.60) assumes a fixed value of $\boldsymbol{x}$ and can be applied regardless of whether the transmitted symbols are deterministic or random. We recall that the radar receiver has full knowledge of the transmitted symbols thus they do not need to be estimated or marginalized out to estimate the target.

When the transmitted symbols are random, the radar receiver cannot rely on a fixed waveform realization. We have to account for the varying realizations of $\boldsymbol{x}$ used at each transmission. In this case, the relevant performance metric is the Conditional Mean Squared Error (CMSE), defined as the expectation of the MSE of the MMSE estimator of the channel

response (2.60) with respect to the distribution of the random *variable* $\boldsymbol{x}$, namely

$$\begin{aligned}\text{CMSE} &\triangleq \mathcal{E}_{\boldsymbol{x}}\left\{\mathcal{E}_{\boldsymbol{h}_\text{r}|\boldsymbol{x}}\left\{\left\|\boldsymbol{h}_\text{r}-\boldsymbol{h}_\text{r}^{\text{MMSE}}\right\|^2\right\}\right\}\\ &= \mathcal{E}_{\boldsymbol{x}}\left\{\text{Tr}\left\{\left({\boldsymbol{K}_{\boldsymbol{h}_\text{r}}}^{-1}+\sigma_{n_\text{r}}^{-2}\boldsymbol{A}_\text{r}^{\mathsf{H}}\boldsymbol{A}_\text{r}\right)^{-1}\right\}\right\}. \end{aligned} \tag{2.61}$$

Proof. Section C.1. □

Remark 2.2.2 (Radar MSE with deterministic symbols)**.** *When the transmitted symbols are deterministic and known at the radar receiver, the MSE of the MMSE estimator of the channel response* (2.60) *is given in closed form in Section C.2:*

$$\begin{aligned}MSE &\triangleq \mathcal{E}_{\boldsymbol{h}_\text{r}|\boldsymbol{x}}\left\{\left\|\boldsymbol{h}_\text{r}-\boldsymbol{h}_\text{r}^{MMSE}\right\|^2\right\}\\ &= \text{Tr}\left\{\left({\boldsymbol{K}_{\boldsymbol{h}_\text{r}}}^{-1}+\sigma_{n_\text{r}}^{-2}\boldsymbol{A}_\text{r}^{\mathsf{H}}\boldsymbol{A}_\text{r}\right)^{-1}\right\}. \end{aligned} \tag{2.62}$$

2.2.3 Communication performance metric: IR

In DFRC systems, it is essential to evaluate how efficiently communication data is transmitted. The IR measures information rate, i.e., the theoretical data rate that can be reliably communicated over a given channel, given a specific distribution of transmitted symbols. We consider both Gaussian inputs and practical discrete constellations (e.g., PSK and QAM), and derive expressions for the IR under both models.

In general, communication IR is defined as the MI (2.47) between $\boldsymbol{x}$ and $\tilde{\boldsymbol{x}}_\text{c}$, and it is given by [81, Ch. 9],[4]:

$$\text{IR} \triangleq I(\tilde{\boldsymbol{x}}_\text{c};\boldsymbol{x}) \tag{2.63}$$

$$\triangleq h(\tilde{\boldsymbol{x}}_\text{c}) - h(\tilde{\boldsymbol{x}}_\text{c}|\boldsymbol{x}). \tag{2.64}$$

2.2.3.1 Gaussian symbols

Lemma 1. *When the transmitted symbols are Gaussian* $\boldsymbol{x}\sim\mathcal{CN}\left(\boldsymbol{0},\boldsymbol{D_p}\right)$*, the communication IR is given by*

$$IR = M\sum_{k\in\mathcal{I}_K}\log_2\left(1+c_k p_k\right). \tag{2.65}$$

Hence, the communication channel is equivalent to parallel Gaussian channels.

Proof. From the expression of the received communication symbols (2.40), and using the fact

that $\boldsymbol{g}_{\mathrm{c}}$ is deterministic, the conditional distribution of $\tilde{\boldsymbol{x}}_{\mathrm{c}}|\boldsymbol{x}$ is given by:

$$\tilde{\boldsymbol{x}}_{\mathrm{c}}|\boldsymbol{x} \sim \mathcal{CN}_{KM}\left(\left(\boldsymbol{I}_M \otimes \boldsymbol{D}_{\boldsymbol{g}_{\mathrm{c}}}\right)\boldsymbol{x}, \sigma_{n_{\mathrm{c}}}^2 \boldsymbol{I}_{KM}\right). \tag{2.66}$$

Applying Theorem 2.2.2 to the two Gaussian distributions (2.9) and (2.66) yields the marginal

$$\tilde{\boldsymbol{x}}_{\mathrm{c}} \sim \mathcal{CN}_{KM}\left(\boldsymbol{0}, \left(\boldsymbol{I}_M \otimes \boldsymbol{D}_{\boldsymbol{g}_{\mathrm{c}}}\right)\left(\boldsymbol{I}_M \otimes \boldsymbol{D}_{\boldsymbol{p}}\right)\left(\boldsymbol{I}_M \otimes \boldsymbol{D}_{\boldsymbol{g}_{\mathrm{c}}}\right)^{\mathsf{H}} + \sigma_{n_{\mathrm{c}}}^2 \boldsymbol{I}_{KM}\right). \tag{2.67}$$

Applying Theorem 2.2.1 to the Gaussian distributions (2.66) and (2.67) leads to the following entropies

$$h(\tilde{\boldsymbol{x}}_{\mathrm{c}}|\boldsymbol{x} = \cdot) = \log_2\left((\pi e)^{KM} \det\left\{\sigma_{n_{\mathrm{c}}}^2 \boldsymbol{I}_{KM}\right\}\right) \tag{2.68a}$$

$$h(\tilde{\boldsymbol{x}}_{\mathrm{c}}) = \log_2\left((\pi e)^{KM} \det\left\{\left(\boldsymbol{I}_M \otimes \boldsymbol{D}_{|\boldsymbol{g}_{\mathrm{c}}|^2}\boldsymbol{D}_{\boldsymbol{p}}\right) + \sigma_{n_{\mathrm{c}}}^2 \boldsymbol{I}_{KM}\right\}\right). \tag{2.68b}$$

Therefore, using the definition of the IR (2.64) and substituting (2.68), the communication IR is defined as:

$$\begin{aligned}\mathrm{IR} &= \log_2\left((\pi e)^{KM} \det\left\{\sigma_{n_{\mathrm{c}}}^2 \boldsymbol{I}_{KM}\right\}\right) - \log_2\left((\pi e)^{KM} \det\left\{\left(\boldsymbol{I}_M \otimes \boldsymbol{D}_{|\boldsymbol{g}_{\mathrm{c}}|^2}\boldsymbol{D}_{\boldsymbol{p}}\right) + \sigma_{n_{\mathrm{c}}}^2 \boldsymbol{I}_{KM}\right\}\right) \\ &= \log_2\left(\det\left\{\sigma_{n_{\mathrm{c}}}^{-2}\left(\boldsymbol{I}_M \otimes \boldsymbol{D}_{|\boldsymbol{g}_{\mathrm{c}}|^2}\boldsymbol{D}_{\boldsymbol{p}}\right) + \boldsymbol{I}_{KM}\right\}\right).\end{aligned}$$

We then use the fact that $\boldsymbol{I}_{KM} = \boldsymbol{I}_M \otimes \boldsymbol{I}_K$ and the property of the determinant of the Kronecker product of two matrices, we obtain

$$\begin{aligned}\mathrm{IR} &= \log_2\left(\det\left\{\sigma_{n_{\mathrm{c}}}^{-2}\left(\boldsymbol{I}_M \otimes \boldsymbol{D}_{|\boldsymbol{g}_{\mathrm{c}}|^2}\boldsymbol{D}_{\boldsymbol{p}}\right) + \left(\boldsymbol{I}_M \otimes \boldsymbol{I}_K\right)\right\}\right) \\ &= \log_2\left(\det\left\{\left(\boldsymbol{I}_M \otimes \left(\sigma_{n_{\mathrm{c}}}^{-2}\boldsymbol{D}_{|\boldsymbol{g}_{\mathrm{c}}|^2}\boldsymbol{D}_{\boldsymbol{p}} + \boldsymbol{I}_K\right)\right)\right\}\right) \\ &= \log_2\left(\det\left\{\boldsymbol{I}_M\right\}\det\left\{\left(\sigma_{n_{\mathrm{c}}}^{-2}\boldsymbol{D}_{|\boldsymbol{g}_{\mathrm{c}}|^2}\boldsymbol{D}_{\boldsymbol{p}} + \boldsymbol{I}_K\right)\right\}^M\right) \\ &= M\log_2\left(\det\left\{\left(\sigma_{n_{\mathrm{c}}}^{-2}\boldsymbol{D}_{|\boldsymbol{g}_{\mathrm{c}}|^2}\boldsymbol{D}_{\boldsymbol{p}} + \boldsymbol{I}_K\right)\right\}\right).\end{aligned}$$

The matrix inside the determinant is diagonal, so the determinant reduces to a product of scalar terms. Therefore, we obtain:

$$\begin{aligned}\mathrm{IR} &= M\sum_{k\in\mathcal{I}_K}\log_2\left(1 + \frac{|g_{\mathrm{c},k}|^2}{\sigma_{n_{\mathrm{c}}}^2}p_k\right) \\ &= M\sum_{k\in\mathcal{I}_K}\log_2\left(1 + c_k p_k\right).\end{aligned}$$

□

2.2.3.2 Discrete constellation symbols

We now extend the IR computation to the case of discrete input constellations, which better reflect practical modulation schemes. We recall from (2.7) that the transmitted symbols on

each OFDM block m follow the model $\boldsymbol{x}_m = \boldsymbol{v}_m \odot \sqrt{\boldsymbol{p}}$, where $\boldsymbol{v}_m$ contains i.i.d. zero-mean unit-variance symbols from a discrete constellation $\mathcal{C}$. Hence, by rewriting (2.40) for each block m, the received communication symbol on subcarrier $k \in \mathcal{I}_K$ is given by

$$\tilde{x}_{\mathrm{c},k,m} = g_{\mathrm{c},k}\sqrt{p_k}v_{k,m} + \tilde{n}_{\mathrm{c},k,m}$$

where we recall that p_k is the power allocated to the kth symbol of each block and $v_{k,m}$ is taken from a normalized centered constellation, the communication transfer function $g_{\mathrm{c},k}$ is deterministic and the noise is $\tilde{n}_{\mathrm{c},k,m} \sim \mathcal{CN}\left(0, \sigma_{n_\mathrm{c}}^2\right)$.

The communication IR under discrete constellations is defined by:

$$\mathrm{IR} = \sum_{m\in\mathcal{I}_M}\sum_{k\in\mathcal{I}_K} I_{\mathrm{c},k}^{(m)}(p_k) \tag{2.69}$$

where the per-subcarrier contribution $I_{\mathrm{c},k}(p_k)$ to the total IR is defined as:

$$I_{\mathrm{c},k}^{(m)}(p_k) \triangleq h(\tilde{x}_{\mathrm{c},k,m}) - \log\left(\pi e\sigma_{n_\mathrm{c}}^2\right) \tag{2.70}$$

$$= -\mathcal{E}_{\tilde{x}_{\mathrm{c},k,m}}\left\{\log\left(\sum_{v_{k,m}\in\mathcal{C}} P(v_{k,m})\mathrm{CN}\left(\tilde{x}_{\mathrm{c},k,m}|g_{\mathrm{c},k}\sqrt{p_k}v_{k,m}, \sigma_{n_\mathrm{c}}^2\right)\right)\right\} - \log\left(\pi e\sigma_{n_\mathrm{c}}^2\right) \tag{2.71}$$

with $\mathrm{CN}\left(x|\mu,\sigma^2\right) \triangleq e^{-|x-\mu|^2/\sigma^2}/(\pi\sigma^2)$ the complex Gaussian Probability Density Function (PDF) and $P(v_{k,m})$ the probability of each symbol $v_{k,m}$ (Section 2.1.1.3).

Proof. See Section D.1. □

Remark 2.2.3. *Assume that, for every subcarrier k, the probability of input symbols $v_{k,m}$ is identical across blocks; that is $P(v_{k,m})$ does not depend on m. Together with the block-invariant per-subcarrier power allocation $\boldsymbol{p}$ in (2.7), the quantity $I_{\mathrm{c},k}^{(m)}(p_k)$ is then independent of m. We may therefore write $I_{\mathrm{c},k}^{(m)}(p_k) \equiv I_{\mathrm{c},k}(p_k)$ for all m.*

This situation arises in particular when, in every block, the symbols $x_{k,m}$ are formed from the same discrete constellation (e.g., PSK or QAM) with the same (typically uniform) symbol probability over $\mathcal{C}$ and the same power allocation $\boldsymbol{p}$. Note that independence across blocks is not required, only identical per-block marginals.

This expression accounts for the randomness of the transmitted symbol and the Gaussian noise, integrating over all possible symbol realizations. It has no closed form but can be evaluated numerically. For most practical constellations, such as PSK and QAM, lookup tables or Monte Carlo simulations are commonly used for numerical evaluation [82, 83].

Remark 2.2.4 (IR as a function of the power allocation)**.** *For a given discrete constellation (e.g., PSK or QAM) and under a fixed communication channel c_k, IR* (2.69) *depends solely on the transmit power vector $\boldsymbol{p}$. This follows from the expression of the per-subcarrier contribution $I_{\mathrm{c},k}(p_k)$* (2.71)*. By using the phase invariance of the complex Gaussian distribution,*

performing a change of variable to polar coordinates, and rotating the integrating domain to absorb the phase of the channel coefficient, the dependence on the complex channel gain $g_{c,k}$ reduces to its magnitude. After simplification and averaging over the constellation, the resulting expression becomes a function of the product $c_k p_k$. The proof is detailed in Section D.2.

The discrete IR, as expressed in equation (2.69), plays a central role in optimizing OFDM-DFRC systems, especially when power allocation across subcarriers is a design variable. However, directly maximizing this quantity is generally intractable due to the lack of a closed-form expression for finite-input constellations (e.g., QAM, PSK).
In this context, understanding the sensitivity of the IR with respect to power allocation p_k becomes critical. In particular, the derivative $dI_{c,k}(p_k)/dp_k$ provides valuable insights into how the IR changes when more or less power is allocated to subcarrier k. This derivative is instrumental in optimizing algorithms and provides insight into power allocation strategies under communication constraints. A key result, initially established in [46], links this derivative to the MMSE of the input symbol estimation. This result is studied further in Section 3.3.2.1.

2.3 Chapter summary

This chapter establishes the system model and performance analysis framework for DFRC systems using CP-OFDM waveforms. It details the transmitted and received signal models, with a focus on discrete-time representations, and the matrix-based formulations useful for algorithmic implementation.

We introduced distinct propagation models for radar and communication channels, emphasizing their structural differences: the radar channel includes a pre-detected random range-extended target with known support and Doppler shifts, whereas the communication channel is deterministic and Doppler-free. The resulting received signals were formulated in both time and frequency domains, highlighting key mathematical structures such as linear and circular convolutions.

The chapter then presented performance metrics critical for evaluating and optimizing OFDM-DFRC systems. For radar, we introduced both information-theoretic (radar CMI) and estimation-theoretic (radar CMSE) metrics, applicable to scenarios with either deterministic or random transmitted symbols (Gaussian and discrete symbol constellations). The IR was derived for both Gaussian and discrete symbol constellations for communication.

Throughout the chapter, mathematical precision was maintained, and multiple equivalent formulations were provided where they serve different purposes (e.g., optimization or estimation). These models and metrics constitute the analytical backbone of waveform optimization and performance evaluation tasks developed in the subsequent chapters.

Chapter 3

MI-based waveform optimization

This chapter presents power allocation optimization strategies for OFDM-DFRC waveform design based on MI. Building on the system model and performance metrics established in the previous chapter, we aim to allocate transmit power across OFDM subcarriers to jointly optimize radar and communication objectives. Specifically, we focus on maximizing a weighted combination of radar CMI and communication IR under a total power constraint. Due to the intractability of exact formulations, particularly under discrete transmitted symbols, we introduce several approximations that yield analytically or numerically tractable problems. Gaussian and discrete symbol models are considered, and their impact on the resulting power allocation strategies is analyzed.

Contents

3.1 Power allocation problem 43
3.1.1 Problem formulation 45
3.1.2 Intractability of the power allocation problem 46
3.2 Gaussian symbol model 46
3.2.1 Jensen's approximation 48
3.2.2 Jensen-Hadamard's approximation 50
3.2.3 Overview of Gaussian symbol modeling 52
3.3 Discrete symbol model 53
3.3.1 Jensen's approximation 54
3.3.2 Hadamard's approximation 55
3.3.3 Overview of discrete symbol modeling 59
3.4 Chapter summary 60

3.1 Power allocation problem

In DFRC systems, the transmitted waveform must efficiently serve both radar sensing and communication tasks simultaneously. This dual function requires careful waveform design, especially in how power is distributed across the system's subcarriers. An unbalanced design risks unintentionally favoring one function at the expense of the other, degrading overall system performance.

MI provides a practical framework for optimizing OFDM-DFRC waveform performance. In radar systems, radar CMI quantifies how much information the received signal contains about the target's scattering profile. Hence, a higher radar MI suggests a more precise estimation of the target profile. In communication, the IR represents the maximum data rate that can be reliably transmitted over the channel. By optimizing MI-based metrics, it becomes possible to jointly shape the waveform for accurate radar estimation and high communication information rate. We thus formulate a joint optimization problem based on maximizing a weighted combination of radar CMI and communication IR under a total power constraint.

For the initial design stage, we simplify the problem by assuming that

- the waveform consists of a single block (or sweep), i.e., $M = 1$;
- the Doppler effect induced by the radar target is negligible (i.e., $F_d = 0$).

These assumptions allow us to derive analytical expressions and to isolate the core structure of the power-allocation problem, making the role of the transmitted symbols $\boldsymbol{x}$ explicit in the performance metrics. We therefore introduce the following definitions.

Definition 3.1.1 (Expression of radar CMI for a single block with $F_d = 0$)**.** When $M = 1$ (i.e., only one OFDM block (sweep) is transmitted) and $F_d = 0$ (no target Doppler), the radar CMI (2.57) can be easily written as follows

$$\begin{aligned} \mathrm{CMI} &= \mathcal{E}_{\boldsymbol{x}} \left\{ \log_2 \det \left(\sigma_{n_\mathrm{r}}^{-2} \boldsymbol{B}_\mathrm{r} \boldsymbol{K}_{\boldsymbol{h}_\mathrm{r}} \boldsymbol{B}_\mathrm{r}^{\mathsf{H}} \boldsymbol{D}_{|\boldsymbol{x}|^2} + \boldsymbol{I}_K \right) \right\} \\ &= \mathcal{E}_{\boldsymbol{x}} \left\{ \log_2 \det \left(\sigma_{n_\mathrm{r}}^{-2} \boldsymbol{K}_{\boldsymbol{g}_\mathrm{r}} \boldsymbol{D}_{|\boldsymbol{x}|^2} + \boldsymbol{I}_K \right) \right\}. \end{aligned} \tag{3.1}$$

Proof. Proof in Chapter B. □

Remark 3.1.1 (CMI as a function of the power allocation)**.** *By explicitly defining the discrete symbols as having unit average power, as specified in equation* (2.7) *into the radar CMI expression, we obtain:*

$$\mathit{CMI} = \mathcal{E}_{\boldsymbol{v}} \left\{ \log_2 \det \left(\sigma_{n_\mathrm{r}}^{-2} \boldsymbol{K}_{\boldsymbol{g}_\mathrm{r}} \boldsymbol{D}_{\boldsymbol{p}} \boldsymbol{D}_{|\boldsymbol{v}|^2} + \boldsymbol{I}_K \right) \right\} \tag{3.2}$$

This shows that, under fixed radar channel statistics and a fixed symbol distribution (either Gaussian or discrete), the radar CMI depends solely on the power allocation vector $\boldsymbol{p}$*. This property holds regardless of the specific distribution of the symbols.*

Definition 3.1.2 (Expression of communication IR for a single block)**.** When $M = 1$ (i.e., when only one OFDM block (sweep) is transmitted) the communication IR (2.69) is immediately given by

$$\mathrm{IR} = \sum_{k \in \mathcal{I}_K} \log_2 \left(1 + c_k p_k \right). \tag{3.3}$$

Even though it is not used as a waveform optimization metric we also recall the expression of the radar CMSE in case of $M = 1$ and $F_d = 0$ as it will be used further for numerical results and performance evaluation of the radar system.

Definition 3.1.3 (Expression of radar CMSE for a single block)**.** When $M = 1$, i.e., when only one OFDM block (sweep) is transmitted and $F_d = 0$, the radar CMSE can be easily written as follows

$$\mathrm{CMSE} = \mathcal{E}_{\boldsymbol{x}} \left\{ \mathrm{Tr} \left\{ \left(\boldsymbol{K}_{\boldsymbol{h}_\mathrm{r}}^{-1} + \sigma_{n_\mathrm{r}}^{-2} \boldsymbol{B}_\mathrm{r}^{\mathsf{H}} \boldsymbol{D}_{|\boldsymbol{x}|^2} \boldsymbol{B}_\mathrm{r} \right)^{-1} \right\} \right\}. \tag{3.4}$$

Proof. We start from the expression of the radar CMSE in (2.61), simplify it for Doppler-free scenarios using the method presented in Section C.2, and then set $M = 1$, which yields the simplified expression in (3.4). □

The more general case with $M > 1$ and nonzero Doppler shifts $F_d \neq 0$ is studied in Chapter 5 where we show that the problem structure remains amenable to similar techniques to the single-block $M = 1$ case.

3.1.1 Problem formulation

We consider an objective function defined as a weighted sum of the radar CMI (3.1) and the communication IR (2.69):

$$w_\mathrm{r}\mathrm{CMI} + w_\mathrm{c}\mathrm{IR} \tag{3.5}$$

where $(w_\mathrm{r}, w_\mathrm{c}) \in [0, 1]^2$ are weighting factors with $w_\mathrm{r} + w_\mathrm{c} = 1$. They determine the relative importance of radar and communication performance. We aim to maximize (3.5) under a total power constraint P_T.

Assuming fixed radar and communication channels, and known input symbol constellations, both radar CMI and communication IR depend solely on the power profile $\boldsymbol{p}$ of the transmitted symbols (see Remarks 3.1.1 and 2.2.4), leading to the following optimization problem:

Problem OPT (Optimal power allocation)**.**

$$\arg\max_{\boldsymbol{p}} \quad w_\mathrm{r} CMI + w_\mathrm{c} IR \tag{3.6}$$

$$\text{s.t.} \quad \sum_{k \in \mathcal{I}_K} p_k = P_\mathrm{T}, \tag{3.7}$$

$$\boldsymbol{p} \geq \boldsymbol{0}. \tag{3.8}$$

The goal is to determine optimal power allocation strategies for the transmitted symbols that maximize the objective function (3.6), while satisfying the total transmit power constraint (3.7).

3.1.2 Intractability of the power allocation problem

Solving Problem OPT exactly is generally intractable, except in certain very simplified scenarios. This intractability arises from two main factors:

- Radar CMI involves an expectation over a log-determinant function of the random input symbols. This structure lacks a closed-form solution for random transmitted symbols (discrete and Gaussian) which makes the radar CMI intractable in general and complicates both analytical and numerical integration.
- The IR for Gaussian symbols is given in closed form (2.65). However, the communication IR is particularly challenging under discrete symbol constraints as it has no closed-form expression (2.69). The IR depends on the exact constellation and input probabilities, and must often be evaluated via Monte Carlo simulations or numerical quadrature, which introduces substantial complexity and makes direct optimization impossible.

In the following sections, we propose tractable approximations of the radar CMI for both Gaussian and discrete constellation inputs based on classical inequalities in information theory:

- Jensen's inequality, which upper-bounds the expectation of a concave function [4, Th. 2.6.2];
- Hadamard's inequality, which bounds the determinant with a product of diagonal entries [4, Th. 17.9.2].

Figure 3.1 summarizes the approximations used in this work, which are explained in detail in the next sections. These approximations yield tractable reformulations of the original problem that preserve its core structure, admit efficient numerical solutions and in some cases, have closed-form expressions.

3.2 Gaussian symbol model

In this section, we assume that the transmitted symbols follow a complex Gaussian distribution. While practical systems use discrete constellations (e.g., QAM or PSK), modeling the input as Gaussian is a widely adopted assumption in communication theory, particularly for analyzing capacity and optimizing transmission strategies [75, 74]. This assumption offers key advantages: it ensures analytic tractability, preserves convexity in the resulting optimization problems, and provides useful upper bounds on achievable performance.

When the transmitted symbols are Gaussian, the CMI and the communication IR are given in (3.1) and (2.65); hence, the optimization problem can be formulated as follows.

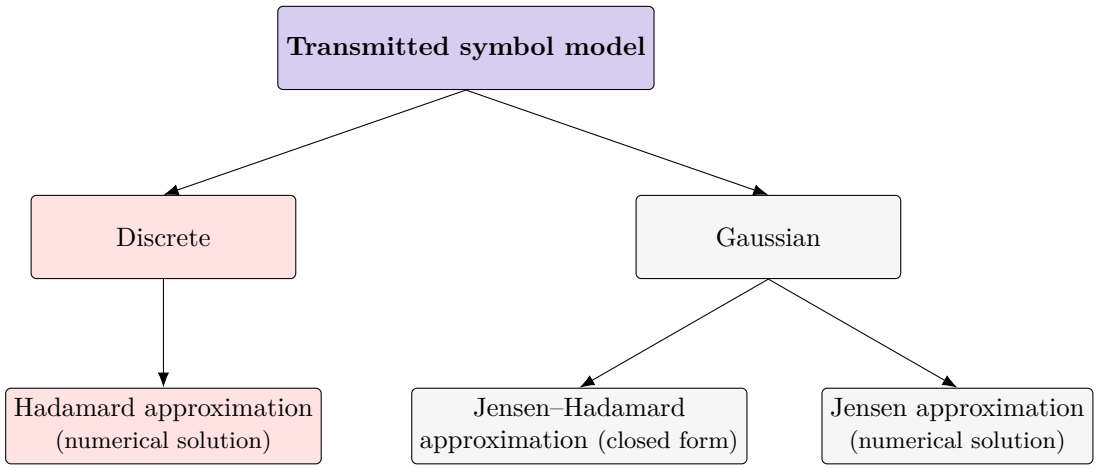


Figure 3.1: Radar CMI approximations depending on transmitted-symbol model.

Problem OPT-G (Optimal power allocation for Gaussian transmitted symbols)**.**

$$\arg\max_{\boldsymbol{p}} \quad w_{\mathrm{r}}\mathcal{E}_{\boldsymbol{x}}\left\{\log_2\det\left(\boldsymbol{I}_K+\frac{1}{\sigma_{n_{\mathrm{r}}}^2}\boldsymbol{K}_{\boldsymbol{g}_{\mathrm{r}}}\boldsymbol{D}_{|\boldsymbol{x}|^2}\right)\right\}+w_{\mathrm{c}}\sum_{k\in\mathcal{I}_K}\log_2\left(1+\frac{|g_{\mathrm{c},k}|^2}{\sigma_{n_{\mathrm{c}}}^2}p_k\right) \tag{3.9}$$

$$\text{s.t.} \quad \sum_{k\in\mathcal{I}_K} p_k = P_{\mathrm{T}}, \tag{3.10}$$

$$\boldsymbol{p}\geq\boldsymbol{0}. \tag{3.11}$$

where $x\sim\mathcal{CN}\left(\boldsymbol{0},\boldsymbol{D}_{\boldsymbol{p}}\right)$.

Remark 3.2.1. *Strictly speaking, Gaussian modeling posits* $\boldsymbol{p}>\boldsymbol{0}$*; hence, zero power would contradict the Gaussian assumption. However, this issue can be resolved by thresholding in practical implementations and can be discarded in high-SNR regimes.*

By assuming the transmitted symbols are Gaussian, the communication IR expression becomes analytically tractable and is available in closed form. Suppose the objective was limited to IR alone (i.e., in the absence of the radar CMI term with $w_{\mathrm{r}}=0$), the optimization problem would reduce to a classic WF formulation that is well known and widely studied in the communication literature [84, p. 245]. However, in the DFRC context, the presence of the radar CMI complicates the objective function (3.9). Specifically, the expectation over the random transmitted symbols in the radar CMI prevents a closed-form expression, making Problem OPT intractable even under Gaussian symbol assumptions.

To simplify our optimization problems, we transform Problem OPT-G into two tractable problems. To that end, we successively approximate the radar CMI in the objective function (3.9) using Jensen's and Hadamard's inequalities. Both inequalities are widely used in information theory and are the basis of many fundamental results [4]. We provide a detailed analysis of the resulting suboptimal Gaussian optimization problems in our article [85].

3.2.1 Jensen's approximation

Jensen's inequality offers an effective approximation of the radar CMI under the assumption of Gaussian transmitted symbols. Indeed, in our prior work [86], we observed that the Jensen-based approximation of radar CMI leads to an appropriate approximation on a wide range of transmitted power compared to other approximations based on low or high power regimes. Moreover, in Chapter H, we analyze the gap between the exact CMI and its Jensen's approximation, and show that this Jensen gap remains constant and depends only on the number of radar scatterers.

We begin by introducing Jensen's inequality in the following.

Definition 3.2.1 (Jensen's inequality)**.** Jensen's inequality is a crucial concept in information theory and is the basis of many fundamental results [4, Ch. 2]. It states that if $\boldsymbol{e}$ is a random variable and f is a real-valued concave function, the mean of the concave transformation is less than or equal to the concave transformation of the mean [4, Th. 2.6.2]. This relationship can be expressed mathematically as:

$$\mathcal{E}_{\boldsymbol{e}}\left\{f(\boldsymbol{e})\right\} \leq f(\mathcal{E}_{\boldsymbol{e}}\left\{\boldsymbol{e}\right\}). \tag{3.12}$$

We now apply Jensen's inequality to the radar CMI expression in (3.1) as reported in Lemma 2.

Lemma 2. *Jensen's inequality applied to the radar CMI* (3.1) *yields*

$$\begin{aligned} I(\tilde{\boldsymbol{x}}_{\mathrm{r}};\boldsymbol{h}_{\mathrm{r}}|\boldsymbol{x}) &\triangleq \mathcal{E}_{\boldsymbol{x}}\left\{\log_2\det\left(\boldsymbol{I}_K+\frac{1}{\sigma_{n_{\mathrm{r}}}^2}\boldsymbol{K}_{\boldsymbol{g}_{\mathrm{r}}}\boldsymbol{D}_{|\boldsymbol{x}|^2}\right)\right\} \\ &\leq \log_2\det\left(\boldsymbol{I}_K+\frac{1}{\sigma_{n_{\mathrm{r}}}^2}\boldsymbol{K}_{\boldsymbol{g}_{\mathrm{r}}}\boldsymbol{D}_{\boldsymbol{p}}\right) \qquad (3.13) \\ &\leq \log_2\det\left(\boldsymbol{I}_K+\frac{1}{\sigma_{n_{\mathrm{r}}}^2}\boldsymbol{K}_{\boldsymbol{g}_{\mathrm{r}}}^{1/2}\boldsymbol{D}_{\boldsymbol{p}}\boldsymbol{K}_{\boldsymbol{g}_{\mathrm{r}}}^{1/2}\right). \qquad (3.14) \end{aligned}$$

The final form in (3.14) *allows a more compact and symmetric expression, suitable for convex analysis and solver implementation.*

Proof. See Section F.1. □

Fortunately, in our case, the expectation involved in Jensen's inequality is tractable and preserves the functional form of the radar CMI. Therefore, we replace the radar CMI in (3.9) with Jensen's inequality in (3.14) and obtain a suboptimal yet tractable optimization problem as follows.

Problem J (Suboptimal power allocation based on Jensen's inequality for Gaussian symbols)**.**

$$\boldsymbol{p}^{(\mathrm{J})} = \arg\max_{\boldsymbol{p}} \quad w_{\mathrm{r}} \log_2 \det\left(\boldsymbol{I}_K + \frac{1}{\sigma_{n_{\mathrm{r}}}^2}\boldsymbol{K}_{\boldsymbol{g}_{\mathrm{r}}}^{1/2}\boldsymbol{D}_{\boldsymbol{p}}\boldsymbol{K}_{\boldsymbol{g}_{\mathrm{r}}}^{1/2}\right) + w_{\mathrm{c}} \sum_{k\in\mathcal{I}_K} \log_2\left(1 + \frac{|g_{\mathrm{c},k}|^2}{\sigma_{n_{\mathrm{c}}}^2} p_k\right) \tag{3.15}$$

$$\text{s.t.} \quad \sum_{k\in\mathcal{I}_K} p_k = P_{\mathrm{T}}, \tag{3.16}$$

$$\boldsymbol{p} \geq \boldsymbol{0}. \tag{3.17}$$

Problem J is a convex optimization problem. The objective function (3.15) to maximize is concave (cf. Theorem F.1.1 in Section F.1), and the functions (3.16) and (3.17) define convex constraints [84, Sec. 1.3]. This matters because convex problems can be efficiently solved and are guaranteed to have global optima. Hence, Problem J always has a solution that satisfies the Karush–Kuhn–Tucker (KKT) conditions, as discussed below.

Existence of a Solution to Problem J. *The objective function* (3.15) *is real and continuous, and the constraint set* $\mathcal{K} \triangleq \{\boldsymbol{p} \in \mathbb{R}_+^K | \sum_{k\in\mathcal{I}_K} p_k = P_{\mathrm{T}}\}$ *is compact (bounded and convex). Using Weierstrass theorem (also known as extreme-value Theorem), we conclude that Problem J attains a maximum on* $\mathcal{K}$ *[87, Th. 4.16]. In other words, it always has a solution.*

KKT Conditions to Problem J. *Problem J is convex with differentiable objective and constraint functions. The latter satisfy Slater's condition in the weak sense. Indeed, since the inequality constraint functions are linear, Slater's condition is verified if and only if the constraint set is nonempty, which is the case (for instance,* $p_k = P_{\mathrm{T}}/K$ *is a feasible point) [84, Sec. 5.2.3]. Hence, KKT conditions are sufficient and necessary conditions for optimality [84, Sec. 5.5.3].*

Unfortunately, solving the KKT conditions analytically appears tedious due to the functional form of the radar CMI (cf. the development in (F.5) in Section F.2). Nonetheless, since Problem J is convex, it can be solved numerically by various software programs. In this work, we use CVX, a widely used MATLAB-based modeling framework for convex optimization problems [88, 89].

Remark 3.2.2 (CVX use)**.** *CVX enables users to express convex objectives and constraints using a high-level, readable syntax resembling their mathematical formulation. It automatically verifies the convexity of the problem and translates the user-defined model into a standard form suitable for numerical solvers like SDPT3 or SeDuMi. These solvers use primal-dual interior-point algorithms, which iteratively update primal and dual variables to satisfy optimality conditions while maintaining feasibility.*
CVX is particularly well-suited for our purposes because it natively supports functions like the log-determinant of positive semidefinite matrices and affine constraints. These features allow us to directly encode the radar CMI and the communication IR expressions derived under the Gaussian and Jensen assumptions. Consequently, we can efficiently compute the optimal power allocation strategy without manually deriving the derivatives or the gradients.

To reduce complexity and avoid numerical inaccuracies, we recommend expressing Problem J 1) as a function of $\boldsymbol{K}_{\boldsymbol{h}_\mathrm{r}}^{1/2}$ *using an explicit Hermitian form in the radar objective of* (3.15)*; and 2) with specific problems when* $w_\mathrm{r} = 0$ *or* $w_\mathrm{r} = 1$.

Remark 3.2.3 (Unicity of solution to Problem J)**.** *The solution to Problem J is unique in certain cases, as discussed in Appendices F.2, F.3 and G.5. In the general case, uniqueness is not guaranteed. We treat the solution returned by CVX as* a *possible solution (a valid global optimum).*

3.2.2 Jensen-Hadamard's approximation

Although Problem J is convex and solvable via numerical methods, its lack of closed-form solution complicates interpretation of the resulting power allocation and increases computational complexity for large-scale scenarios. To address this, we approximate Problem J using Hadamard's inequality. This bound is useful as it diagonalizes the objective, leading to a fully separable form over subcarriers. Hence, this approach leads to an optimization problem that has a closed-form solution, which is both straightforward and easy to interpret, as discussed in the following sections.

Definition 3.2.2 (Hadamard's inequality)**.** Hadamard's inequality states that the determinant of any positive definite matrix $\boldsymbol{M} \in \mathcal{S}_{++}^{K}(\mathbb{C})$ is less than or equal to the product of its diagonal elements [4, Th. 17.9.2], namely

$$\det\{\boldsymbol{M}\} \leq \prod_{k \in \mathcal{I}_K} [\boldsymbol{M}]_{k,k}. \tag{3.18}$$

Equality holds if and only if the matrix is diagonal.

Applying Jensen's and Hadamard's inequalities successively to the radar CMI (2.57) leads to Lemma 3.

Lemma 3. *Hadamard's inequality applied to the right-hand side term of* (3.13) *yields*

$$\log_2 \det\left(\boldsymbol{I}_K + \frac{1}{\sigma_{n_\mathrm{r}}^2} \boldsymbol{K}_{\boldsymbol{g}_\mathrm{r}} \boldsymbol{D}_{\boldsymbol{p}}\right) \leq \sum_{k \in \mathcal{I}_K} \log_2\left(1 + \frac{[\boldsymbol{K}_{\boldsymbol{g}_\mathrm{r}}]_{k,k}}{\sigma_{n_\mathrm{r}}^2} p_k\right). \tag{3.19}$$

Proof. See Section G.1. □

Using Lemma 3 and (3.23), we formulate a third power allocation problem.

Problem JH (Suboptimal power allocation based on Jensen–Hadamard's inequality for

Gaussian symbols)**.**

$$\boldsymbol{p}^{(\mathrm{JH})} = \arg\max_{\boldsymbol{p}} \quad w_{\mathrm{r}} \sum_{k\in\mathcal{I}_K} \log_2\left(1 + a_k p_k\right) + w_{\mathrm{c}} \sum_{k\in\mathcal{I}_K} \log_2\left(1 + c_k p_k\right) \tag{3.20}$$

$$\text{s.t.} \quad \sum_{k\in\mathcal{I}_K} p_k = P_{\mathrm{T}}, \tag{3.21}$$

$$\boldsymbol{p} \geq \mathbf{0}. \tag{3.22}$$

Here, $\boldsymbol{a}$ (2.39) and $\boldsymbol{c}$ (2.43), denote the per-subcarrier SNRs for the statistical radar and deterministic communication channels, respectively. We recall the definition of their elements:

$$\forall k \in \mathcal{I}_K \quad a_k \triangleq \frac{[\boldsymbol{K}_{\boldsymbol{g}_{\mathrm{r}}}]_{k,k}}{\sigma^2_{n_{\mathrm{r}}}} \geq 0 \quad \text{and} \quad c_k \triangleq \frac{|g_{\mathrm{c},k}|^2}{\sigma^2_{n_{\mathrm{c}}}} \geq 0. \tag{3.23}$$

A similar optimization problem is discussed in [57], which focuses on designing a radar-only waveform for multiple extended targets. The objective function in that case is a weighted linear sum of the MIs related to each target response. This problem is solved numerically for any number of targets. In contrast, our problem is restricted to two MIs (related to the radar and communication functions), allowing us to derive a unique closed-form solution using the KKT conditions. A summary of this solution is provided below.

Unique Solution to Problem JH. *Problem JH always admits a unique solution given by*

$$[\boldsymbol{p}^{(\mathrm{JH})}]_k = p_k(\lambda^{\star -1}) \tag{3.24}$$

where, for $\lambda > 0$*,*

$$p_k(\lambda^{-1}) \triangleq \begin{cases} 0 & \text{if } \lambda_k^{th} = 0 \\ \begin{cases} 0 & \text{if } \lambda^{-1} \leq \lambda_k^{th\,-1} \\ p_k^{+}(\lambda^{-1}) & \text{if } \lambda^{-1} > \lambda_k^{th\,-1} \end{cases} & \text{if } \lambda_k^{th} > 0 \end{cases} \tag{3.25}$$

is a continuous function with

$$\lambda_k^{th} \triangleq (w_{\mathrm{r}} a_k + w_{\mathrm{c}} c_k) \tag{3.26}$$

$$p_k^{+}(\lambda^{-1}) \triangleq \begin{cases} \frac{1}{2}\left(-\beta_k + \sqrt{\Delta_k}\right) & \text{if } a_k, c_k > 0 \\ \lambda^{-1} w_{\mathrm{r}} - a_k^{-1} & \text{if } a_k > 0 \text{ and } c_k = 0 \\ \lambda^{-1} w_{\mathrm{c}} - c_k^{-1} & \text{if } a_k = 0 \text{ and } c_k > 0 \end{cases} \tag{3.27}$$

and, if $a_k, c_k > 0$*,*

$$\beta_k \triangleq -\lambda^{-1} + a_k^{-1} + c_k^{-1}$$

$$\Delta_k \triangleq \left[\lambda^{-1}\left(w_{\mathrm{r}} - w_{\mathrm{c}}\right) + \left(c_k^{-1} - a_k^{-1}\right)\right]^2 + 4\lambda^{-2} w_{\mathrm{r}} w_{\mathrm{c}}.$$

Finally, $\lambda^\star$ is the unique strictly positive solution to

$$\sum_{k\in\mathcal{I}_K} p_k(\lambda^{\star-1}) = P_{\mathrm{T}}. \tag{3.28}$$

In this work, we find $\lambda^\star$ using the bisection method [90].

Proof. See Section G.2. The bisection search is described in Appendices G.3–G.4. □

The solution is very similar to the WF method [84, p. 245] and becomes an exact one for special cases: e.g., when $w_{\mathrm{r}} = 0$ and $c_k > 0$, the activation function (3.25) boils down to

$$p_k(\lambda^{\star-1}) = \max(0, \lambda^{\star-1} - c_k^{-1}). \tag{3.29}$$

The solution to Problem JH is illustrated for a simplified scenario in Figure 3.2. In this scenario, the power for each subcarrier is allocated based on the activation function $p_k(\lambda^{-1})$, which is described in (3.25). This function is zero when the input is below the activation threshold ${\lambda_k^{\mathrm{th}}}^{-1}$ and non-zero when above it. Notably, λ_k^{th} defined in (3.26) represents a weighted SNR for the DFRC system. From (3.28), a unique $\lambda^{\star-1} > 0$ satisfies the total power budget allocation P_{T}. Therefore, all subcarriers with an activation threshold below $\lambda^{\star-1}$ are activated. Similar to the WF algorithm, power is allocated first to the subcarriers with the highest (DFRC) SNRs. Thus, only the subcarrier with the highest DFRC SNR is activated at very low power levels. In contrast, an equal power allocation is achieved at very high power levels. However, unlike the traditional WF approach, the subcarriers are not necessarily filled at the same rate when increasing P_{T}. This dissimilarity arises from the functional form of the activation functions (3.25) whose rate of change may differ between subcarriers (see Figure 3.2 and to be compared to the unitary slope for the WF method in (3.29)). Finally, it is noteworthy that, by construction, the JH allocation ignores the correlation between the subcarriers of the target's response. Instead, the J allocation uses this knowledge: if two of these subcarriers are highly correlated, no substantial information to estimate the target is retrieved by illuminating both. Consequently, the J solution activates fewer subcarriers, as illustrated in the next Section.

3.2.3 Overview of Gaussian symbol modeling

The Jensen's and Jensen–Hadamard's approximations are key techniques for simplifying the optimization problem under Gaussian symbol modeling. We began by introducing the Jensen's inequality, which approximated the radar CMI by moving the expectation outside the log-determinant. This yields an approximation of the radar CMI that preserves the functional form of the original problem. This enables efficient numerical optimization while still capturing the correlation structure in the radar channel. The approximation, therefore, offers a good balance between tractability and fidelity in modeling.

To further reduce complexity, we introduced the Jensen–Hadamard's approximation which

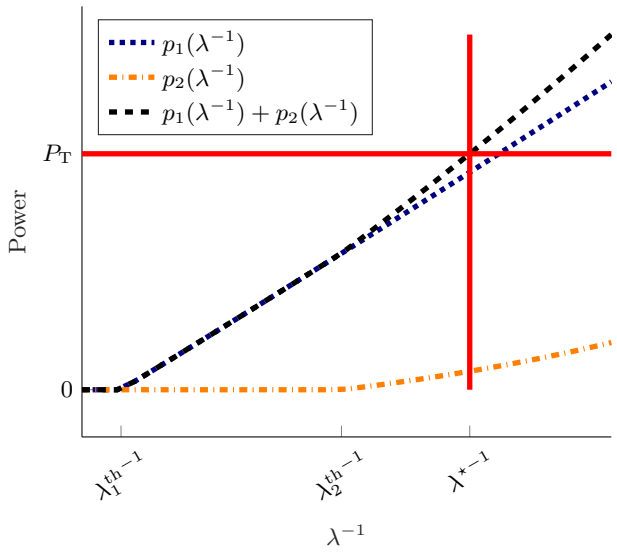


Figure 3.2: Jensen–Hadamard's power allocation strategy. Scenario: $K = 2$, $\boldsymbol{a} = [50, 2]^{\mathsf{T}}$, $\boldsymbol{c} = [2, 50]^{\mathsf{T}}$, $w_{\mathrm{r}} = 0.9$ and $P_{\mathrm{T}} = 0.2$.

adds a second layer of simplification by applying Hadamard's inequality to the matrix inside the determinant. This replaces the log-determinant term with a sum over log-scaled diagonal entries. As a result, the optimization problem becomes separable across subcarriers and admits a closed-form solution. While this formulation is highly interpretable and computationally efficient, it does not capture the correlations between subcarriers in the radar channel, which can degrade performance in correlated scenarios. This limitation will be illustrated through numerical results in Chapter 4.

Both approximations are valuable tools for deriving tractable solutions under Gaussian assumptions. However, they involve trade-offs: the Jensen's approximation is more accurate and does not neglect the correlation between radar subcarriers but lacks a closed-form solution, requiring numerical solvers. On the other hand, the Jensen–Hadamard's approximation provides a closed-form solution and enables low-complexity implementations, but at the cost of modeling accuracy.

Finally, it is important to note that these Gaussian-based models, while analytically convenient, do not fully reflect the behavior of practical systems using discrete symbol constellations. This limitation motivates the study of discrete-input models, which is the focus of the next section.

3.3 Discrete symbol model

In practical systems, transmitted symbols are drawn from finite constellations such as PSK or QAM. Although assuming Gaussian inputs facilitates the derivation of simplified closed-form solutions under certain approximations, this assumption tends to overestimate system

performance and fails to account for the constraint of practical modulation schemes. These limitations motivate the explicit modeling of discrete symbol constellations in our DFRC framework [91].

In this section, we reformulate the OFDM-DFRC power allocation problem to incorporate discrete symbol constraints from the design stage, yielding a more realistic optimization framework. The optimal power allocation for discrete symbols is given as follows.

Problem OPT-D (Optimal power allocation for discrete symbols)**.**

$$\arg\max_{\boldsymbol{p}} \quad w_{\mathrm{r}}\mathcal{E}_{\boldsymbol{x}}\left\{\log_2\det\left(\boldsymbol{I}_K+\frac{1}{\sigma_{n_{\mathrm{r}}}^2}\boldsymbol{K}_{\boldsymbol{g}_{\mathrm{r}}}\boldsymbol{D}_{|\boldsymbol{x}|^2}\right)\right\}+w_{\mathrm{c}}\sum_{k\in\mathcal{I}_K}I_{\mathrm{c},k}(p_k) \tag{3.30}$$

$$\text{s.t.} \quad \sum_{k\in\mathcal{I}_K}p_k=P_{\mathrm{T}}, \tag{3.31}$$

$$\boldsymbol{p}\geq\boldsymbol{0}. \tag{3.32}$$

where x is drawn from a finite discrete constellation.

In this formulation, the radar CMI and the communication IR are both evaluated under discrete input assumptions. However, neither term admits a closed-form expression, making direct optimization of Problem OPT-D computationally intractable.

To address this issue, we again consider approximating the radar CMI using the techniques introduced in Section 3.2 to simplify the radar CMI expression and derive suboptimal yet tractable power allocation strategies, as developed in the following sections.

3.3.1 Jensen's approximation

The primary idea is to apply once more Jensen's inequality to the radar CMI. This approach leads to the following optimization problem:

Problem D-J (Suboptimal power allocation based on Jensen's inequality for discrete symbols)**.**

$$\boldsymbol{p}^{(\mathrm{D-J})}=\arg\max_{\boldsymbol{p}} \quad w_{\mathrm{r}}\log_2\det\left(\boldsymbol{I}_K+\frac{1}{\sigma_{n_{\mathrm{r}}}^2}\boldsymbol{K}_{\boldsymbol{g}_{\mathrm{r}}}\boldsymbol{D}_{\boldsymbol{p}}\right)+w_{\mathrm{c}}\sum_{k\in\mathcal{I}_K}I_{\mathrm{c},k}(p_k) \tag{3.33}$$

$$s.t. \quad \sum_{k\in\mathcal{I}_K}p_k=P_{\mathrm{T}}, \tag{3.34}$$

$$\boldsymbol{p}\geq\boldsymbol{0}. \tag{3.35}$$

Here, it is important to distinguish between two modeling assumptions for the transmitted symbols: Gaussian and discrete. This difference is crucial because it directly affects our capability to solve the resulting optimization problem. In the Gaussian case, Jensen's inequality leads to an approximation of the radar CMI that preserves a closed-form log-determinant

structure. Additionally, the communication IR also admits a closed-form expression. Because both terms are concave and analytically tractable, the resulting optimization problem J is convex and can be efficiently solved using standard solvers such as CVX. In contrast, the discrete input causes a more significant challenge. While the radar CMI approximated using Jensen's inequality still keeps a closed-form log-determinant structure, the communication IR no longer has a closed-form expression. Instead, it must be computed numerically via Monte Carlo simulations or numerical integration methods. As a result, the optimization problem cannot be handled by solvers like CVX, which require symbolic closed-form expressions for the objective function.

3.3.2 Hadamard's approximation

In the Gaussian case, analytical tractability is further improved by applying the Jensen–Hadamard's approximation, which yields a fully closed-form and interpretable expression for the resulting power allocation strategies. This approximation facilitates efficient computation and analytical insight into the structure of the optimal solution.
However, the same approach does not apply in the discrete case. Even when Jensen–Hadamard's approximation is used, the IR term remains intractable due to the input's discrete nature. For this reason, we adopt a simplified strategy: we apply only the Hadamard's approximation to the radar CMI, bypassing the Jensen's inequality. While this results in a tighter approximation, it enables us to derive a practical and explicit suboptimal solution for power allocation under discrete modulation constraints.

We now formulate the resulting suboptimal power allocation problem. Here, Hadamard's inequality [4, Th. 17.9.2] provides a tractable approximation to the radar CMI (2.57), which will prove to be particularly useful when working with discrete modulation symbols. Hadamard's inequality is recalled below:

$$\begin{aligned} \mathrm{CMI} &\leq \mathcal{E}_{\boldsymbol{x}} \left\{ \sum_{k \in \mathcal{I}_K} \log_2 \det \left(\boldsymbol{I}_K + a_k |x_k|^2 \right) \right\} \\ &\leq \sum_{k \in \mathcal{I}_K} \mathcal{E}_{v_k} \left\{ \log_2 \left(1 + a_k |v_k|^2 p_k \right) \right\} \end{aligned} \tag{3.36}$$

where a_k is the per-subcarrier radar SNR defined in (2.39) and x_k denotes the OFDM symbol transmitted on subcarrier k in the (single) OFDM block considered here. In Chapter 2, we used the notation $x_{k,m}$ for the symbol sent on subcarrier k in OFDM block m. Since in this chapter we restrict our attention to a single block, the block index is always equal to 1 and we omit it for notational simplicity, i.e., $x_k \triangleq x_{k,1}$. Similarly, in the case $M = 1$, we write v_k instead of $v_{k,1}$ to simplify the notation (see Section 2.1.1.3 for the definitions of $\boldsymbol{x}$ and $\boldsymbol{v}$).

Proof. See Section J.1. □

This method enables optimization with respect to the actual discrete constellation of the

transmitted symbols, but it neglects subcarrier correlations in the radar channel because of Hadamard's inequality.

Problem H. *Suboptimal power allocation based on Hadamard's inequality for discrete symbols*

$$\boldsymbol{p}^{(\mathrm{H})} = \arg\max_{\boldsymbol{p}} \quad w_{\mathrm{r}} \sum_{k\in\mathcal{I}_K} \mathcal{E}_{v_k}\left\{\log_2\left(1+a_k|v_k|^2p_k\right)\right\} + w_{\mathrm{c}} \sum_{k\in\mathcal{I}_K} I_{\mathrm{c},k}(p_k) \tag{3.37}$$

$$s.t. \quad \sum_{k\in\mathcal{I}_K} p_k = P_{\mathrm{T}}, \tag{3.38}$$

$$\boldsymbol{p} \geq \mathbf{0}. \tag{3.39}$$

To solve this problem, we begin by analyzing key properties of the objective function in (3.37).

3.3.2.1 Analytical properties

The derivation of the optimal solution relies on the analytical structure of both terms in the objective: the approximated radar CMI (3.36) and the communication IR (2.69). In particular, we examine their first-order derivatives and monotonicity properties.

Properties of the radar CMI approximated via Hadamard's inequality

Lemma 4. *Let v_k be a discrete, unit-variance random variable with finite support. Hence, the derivative of the approximated radar CMI* (3.36) *with respect to p_k is given by:*

$$\frac{d}{dp_k}\mathcal{E}_{v_k}\left\{\log_2\left(1+a_k|v_k|^2p_k\right)\right\} = \mathcal{E}_{v_k}\left\{\frac{a_k|v_k|^2}{1+a_k|v_k|^2p_k}\right\}\log_2(e)\,. \tag{3.40}$$

Proof. Since v_k takes values in a finite discrete constellation, the expectation is a finite weighted sum. Therefore, differentiation and expectation operators can be interchanged term by term. □

Lemma 5. *Let v_k be a discrete symbol of unit variance variable. Then:*

- *the function $p_k \mapsto \mathcal{E}_{v_k}\{a_k|v_k|^2/(1+a_k|v_k|^2p_k)\}$ is strictly decreasing, continuous, and positive for $p_k \geq 0$;*
- *it satisfies the following limits*

$$\lim_{p_k\to 0} \mathcal{E}_{v_k}\left\{\frac{a_k|v_k|^2}{1+a_k|v_k|^2p_k}\right\} = a_k; \tag{3.41}$$

$$\lim_{p_k\to \infty} \mathcal{E}_{v_k}\left\{\frac{a_k|v_k|^2}{1+a_k|v_k|^2p_k}\right\} = 0. \tag{3.42}$$

Proof. Each term inside the expectation (i.e., $(a_k|v_k|^2) \,/\, (1 + a_k|v_k|^2 p_k)$) is strictly decreasing in p_k for fixed v_k. Since the expectation is a convex combination of such functions, the overall function preserves strict monotonicity. □

Properties of the IR We now analyze the behavior of the communication IR (2.69) with respect to the power allocation p_k, focusing on the derivative of the per-subcarrier term $I_{\mathrm{c},k}(p_k)$ as defined in (2.69). A central element in this analysis is the MMSE estimator of the transmitted unit-variance symbol v_k on subcarrier k.

Definition 3.3.1 (MMSE Estimator of v_k)**.** Let $x_k = \sqrt{p_k} v_k$ denote the transmitted symbol on subcarrier k (see (2.7)), where v_k is a discrete symbol with zero mean and unit variance. The communication receiver observes $\tilde{x}_{\mathrm{c},k}$ (2.40) and aims to estimate v_k. The MMSE estimator of v_k is given by:

$$\begin{aligned} v_k^{\mathrm{MMSE}} &\triangleq \arg\min_{\hat{v_k}} \mathcal{E}_{v_k} \left\{ |v_k - \hat{v_k}|^2 \right\} \\ &= \frac{\sum_{v_k \in \mathcal{C}} v_k P(v_k) \, \mathrm{CN}\left(\tilde{\boldsymbol{x}}_{\mathrm{c}} | g_{\mathrm{c},k} \sqrt{p_k} v_k, \sigma_{n_{\mathrm{c}}}^2\right)}{\sum_{v_k' \in \mathcal{C}} P(v_k') \, \mathrm{CN}\left(\tilde{\boldsymbol{x}}_{\mathrm{c}} | g_{\mathrm{c},k} \sqrt{p_k} v_k', \sigma_{n_{\mathrm{c}}}^2\right)}. \end{aligned} \tag{3.43}$$

The corresponding MSE is

$$\mathrm{MSE}_{\mathrm{c},k}(p_k) = \mathcal{E}_{v_k} \left\{ |v_k - v_k^{\mathrm{MMSE}}|^2 \right\}. \tag{3.44}$$

A fundamental result establishes a direct link between subcarrier contribution to the communication IR, i.e., $I_{\mathrm{c},k}(p_k)$ and the $\mathrm{MSE}_{\mathrm{c},k}$.

Theorem 3.3.1 (Derivative of $I_{\mathrm{c},k}(p_k)$)**.** *The derivative of $I_{\mathrm{c},k}(p_k)$ with respect to p_k is given by [50, 46]:*

$$\frac{dI_{\mathrm{c},k}(p_k)}{dp_k} = c_k MSE_{\mathrm{c},k}(p_k) \log_2(e). \tag{3.45}$$

This identity holds for any constellation. The functional form of $MSE_{\mathrm{c},k}(p_k)$, however, depends on the distribution of v_k.

Lemma 6. *Let v_k be a discrete symbol of unit variance and c_k the communication SNR on subcarrier k. Then:*

- *$MSE_{\mathrm{c},k}$ depends only on the product $c_k p_k$ [46, Eq. (24)];*
- *it satisfies the following limits [50, Sec. II-F]:*

$$\lim_{p_k \to 0} MSE_{\mathrm{c},k}(p_k) = 1, \quad \lim_{p_k \to \infty} MSE_{\mathrm{c},k}(p_k) = 0; \tag{3.46}$$

- *$MSE_{\mathrm{c},k}$ is a strictly decreasing, continuous function of p_k [50, Sec. II-C].*

Problem H is convex, as 1) the objective function in (3.37) is concave as the derivative of both terms in (3.37) are strictly decreasing as shown in Appendix J 2) the constraints in (3.39) define a convex feasible set [84, Sec. 1.3]. In addition, Problem H always has a solution that satisfies the KKT conditions.

Unique Solution to Problem H. *Problem H always admits a unique solution given by*

$$[\boldsymbol{p}^{(\mathrm{H})}]_k = p_k(\lambda^\star)$$

where, for $\lambda > 0$*,*

$$p_k(\lambda) \triangleq \begin{cases} 0 & \text{if } \lambda_k^{th} = 0 \\ \begin{cases} 0 & \text{if } \lambda \geq \lambda_k^{th} \\ (\ell_k)^{-1}(\lambda) & \text{if } \lambda < \lambda_k^{th} \end{cases} & \text{if } \lambda_k^{th} > 0 \end{cases}$$

is a continuous function with

$$\lambda_k^{th} \triangleq (w_{\mathrm{r}} a_k + w_{\mathrm{c}} c_k) \tag{3.47}$$

$$\ell_k(p_k) \triangleq w_{\mathrm{r}} \mathcal{E}_{v_k} \left\{ \frac{a_k |v_k|^2}{1 + a_k |v_k|^2 p_k} \right\} + w_{\mathrm{c}} c_k MSE_{\mathrm{c},k}(p_k) \tag{3.48}$$

where $MSE_{\mathrm{c},k}$ *is the MSE of the MMSE estimator of* v_k *(see Lemma 3.3.1). Finally,* $\lambda^\star$ *is the unique strictly positive solution to*

$$\sum_{k \in \mathcal{I}_K} p_k(\lambda^\star) = P_{\mathrm{T}}. \tag{3.49}$$

Proof. The result follows from the KKT optimality conditions. A detailed derivation is provided in Chapter J. □

To efficiently compute $\boldsymbol{p}^{(\mathrm{H})}$, we proceed as follows. For a given DFRC scenario, i.e., fixed radar and communication SNR values a_k and c_k, fixed weights w_{r} and w_{c}, and a total transmitted power P_{T}, we follow these steps:

1. Tabulate, for each subcarrier k, the functions mapping the power to the objective's gradient, i.e., $\ell_k(p_k)$. In practice, we define a power grid $\{p^{(0)}, \ldots, p^{(N_g-1)}\}$ with $p^{(0)} = 0$ and $p^{(N_g-1)} = P_{\mathrm{T}}$. The step size $P_{\mathrm{T}}/(N_g - 1)$ is chosen sufficiently small. We then compute the value of $\ell_k(p_k)$ at each point of the grid.

2. Specify the search interval $[\lambda_{\min}, \lambda_{\max}]$ for the Lagrange multiplier λ. The values $\lambda_{\min}$ and $\lambda_{\max}$ are simply the minimum and maximum of $\ell_k(p_k)$ over the power grid. The optimal $\lambda^\star$ necessarily lies in this range.

3. Define the function that assigns the tentative power allocation

$$\lambda \longmapsto \tilde{\boldsymbol{p}}(\lambda) = [\tilde{p}_0(\lambda), \ldots, \tilde{p}_{K-1}(\lambda)]^{\mathsf{T}} \tag{3.50}$$

   as follows. For each subcarrier k:

- scan the precomputed table of $\ell_k(p_k)$;
- select from the predefined power grid the value p_k whose tabulated gradient $\ell_k(p_k)$ is closest to λ;
- apply the threshold rule: set this power to zero whenever $\lambda \geq \lambda_k^{\text{th}}$.

4. Compute the resulting total power $\sum_{k\in\mathcal{I}_K} \tilde{p}_k(\lambda)$ and define the root function

$$f(\lambda) = \sum_{k\in\mathcal{I}_K} \tilde{p}_k(\lambda) - P_{\text{T}}. \tag{3.51}$$

This function indicates whether the tentative power profile uses too much power ($f(\lambda) > 0$), too little power ($f(\lambda) < 0$), or exactly the right amount ($f(\lambda) = 0$).

5. Apply a bisection method [90] over $[\lambda_{\min}, \lambda_{\max}]$ to identify the unique $\lambda^\star$ such that $f(\lambda^\star) = 0$ (i.e., the power constraint is met). Because the mapping $\tilde{p}_k(\lambda)$ is monotone in λ, the function $f(\lambda)$ is strictly decreasing, and a unique $\lambda^\star$ exists.

6. Evaluate the final power allocation $\boldsymbol{p}^{(\text{H})}$ using $\tilde{\boldsymbol{p}}(\lambda^\star)$, and return it.

We note that the resulting solution resembles the MWF strategy [46]. However, in the MWF, the tabulated function depends only on the modulation constellation and can therefore be reused for all subcarriers. Since $\text{MSE}_{c,k}$ depends only on the product $c_k p_k$ (see Lemma 6), it can be tabulated once as a function of this generic product term and reused independently of the channel gains. In the proposed algorithm, the gradient of the objective (3.48) also includes a radar term that depends explicitly on the radar SNR a_k and cannot be reduced to a function of the product $a_k p_k$ alone. Consequently, the tabulated function differs across subcarriers, and a separate table is required for each k. Hence, the proposed method requires more preprocessing time and memory, since the tabulation becomes channel-dependent rather than only constellation-dependent.

3.3.3 Overview of discrete symbol modeling

Discrete symbol modeling provides a more accurate representation of real-world systems than Gaussian assumptions, as it explicitly captures the actual structure of modulation schemes like PSK and QAM. This advantage is particularly relevant for small constellations, where the discrepancy from a Gaussian model is significant, whereas for large-order QAM constellations, the symbol distribution already approaches Gaussian behavior, and the Gaussian approximation remains accurate. The discrete symbol modeling approach thus accurately reflects the discrete nature of transmitted symbols but introduces significant complexity, as both the radar CMI and communication IR lack closed-form expressions. Consequently, optimization becomes intractable without suitable approximations. While Jensen's approximation simplifies the Gaussian case, its application to discrete models remains complex, and the resulting suboptimal problem is not tractable. By contrast, the Hadamard approximation provides a more interpretable solution, but it neglects the correlations between subcarriers in the radar channel. Thus, this modeling approach comes with trade-offs in terms of accuracy.

3.4 Chapter summary

This chapter addressed the problem of waveform optimization for OFDM-DFRC systems using MI-based metrics. We first introduced the power allocation problem, which was formulated as the joint maximization of radar CMI and communication IR. The focus is on optimizing power allocation across OFDM subcarriers to jointly improve radar and communication performance under a total power constraint. Depending on the radar and communication channels, this framework can highlight a trade-off between radar estimation accuracy and communication information rate. However, the resulting problem is generally intractable, primarily due to the radar CMI's structure and the non-closed-form IR's expression for discrete constellations.

In the case of Gaussian symbol modeling, where the transmitted symbols are assumed to follow a Gaussian distribution, the optimization problem becomes tractable albeit some approximations. Applying Jensen's and Hadamard's inequalities to approximate the radar CMI renders the problem convex and solvable. These approximations offer different trade-offs between computational complexity and accuracy: Jensen's inequality preserves the correlation structure between radar subcarriers but lacks a closed-form solution, whereas the Jensen–Hadamard approximation provides a closed-form expression at the cost of neglecting subcarrier correlations.

We then considered discrete symbol modeling, which reflects practical modulation schemes such as PSK and QAM. Although this approach captures the real-world behavior of communication systems more accurately, it introduces significant analytical intractability. In this setting, neither the radar CMI nor the communication IR admits a closed-form expression, making optimization considerably more challenging. As a result, we relied on the Hadamard approximation to obtain a tractable formulation. While this method supports discrete constellations, it also requires numerical techniques (e.g., Monte Carlo simulations) to estimate key quantities such as the MSE of the MMSE estimator of the input symbols, and it sacrifices the modeling of the correlations between subcarriers in the radar channel.

Overall, this chapter provided a comparative analysis of optimization strategies for DFRC systems under both Gaussian and discrete symbol assumptions, offering theoretical insights and practical methods for efficient power allocation. The results were summarized in Table 3.1.

Table 3.1: Comparison of power allocation strategies.

Strategy	Advantages	Disadvantages
$\boldsymbol{p}^{(\mathrm{J})}$	Simplifies the radar CMI term Preserves subcarrier correlation structure Convex and solvable with numerical tools	Only valid for Gaussian input symbols Lack of closed-form solution
$\boldsymbol{p}^{(\mathrm{JH})}$	Fully closed-form solution Fast to compute Easy to interpret	Only valid for Gaussian input symbols Ignores correlations between radar subcarriers
$\boldsymbol{p}^{(\mathrm{H})}$	Supports discrete input constellations Reflects practical system constraints, particularly for small constellations Interpretable solution	Ignores correlations between subcarriers Requires numerical approximations Higher computational complexity

Chapter 4

Comparative analysis of approaches

This chapter presents a numerical evaluation of the power allocation strategies introduced in Chapter 3 for OFDM-DFRC systems. Our objective is to compare their performance under a range of radar and communication scenarios, and to assess the impact of key design choices such as transmitted symbol constellations and power allocation methods on radar estimation accuracy and communication information rate. Through numerical simulations, we explore the trade-offs that emerge across varying channel and operating conditions, thereby providing practical insight into the benefits and limitations of each strategy. Parts of this chapter are based on results published in [85, 92, 91].

Contents

4.1 Simulation setup 63
4.1.1 Radar channel 64
4.1.2 Communication channel 65
4.1.3 Legend conventions 66
4.2 Analysis of power allocation strategies with Gaussian symbols 66
4.2.1 Communication-only waveform 67
4.2.2 Radar-only waveform 68
4.2.3 DFRC waveform 71
4.3 Impact of symbol randomness in OFDM-DFRC systems 76
4.3.1 Radar-only waveform 77
4.3.2 DFRC scenario 79
4.4 Analysis of power allocation strategies with discrete symbols 81
4.4.1 Communication-only waveform 82
4.4.2 Radar-only waveform 85
4.4.3 DFRC waveform 87
4.5 Chapter summary 91

4.1 Simulation setup

This section details the simulation setup used to evaluate the performance of the proposed power allocation strategies in OFDM-DFRC systems for one block (sweep) $M = 1$, focusing

on frequency-selective radar channels under varying subcarrier correlation conditions and diverse communication channel configurations.

Table 4.1 summarizes the parameters used throughout our simulations. The parameter values are chosen to highlight the behavior of the proposed power allocation strategies, rather than to replicate a specific real-world system. In particular, we set $K = 10$ subcarriers to make the trends easy to interpret. In a practical OFDM system, the number of subcarriers K would typically be larger to support the band-limited assumption and exploit entirely the coherence time of the channel.

Table 4.1: Simulation parameters for a single-block OFDM-DFRC system with no Doppler.

Parameter	**Variable**	**Value**
Number of range cells	L	15
Number of subcarriers	K	10
Number of nonzero radar scatterers	L_{r}	5
Radar channel	$\mathcal{E}\{\lvert\boldsymbol{h}_{\mathrm{r}}\rvert^2\}$	$[8, 9.6, 7.2, 8.8, 8]^{\mathsf{T}}$
Radar scatterers position matrix	$\boldsymbol{V}_{\mathrm{r}}$	$[\boldsymbol{I}_{L_{\mathrm{r}}}; \boldsymbol{0}_{L-L_{\mathrm{r}},L_{\mathrm{r}}}]$
Noise power in the radar channel	σ_{r}^2	1
Number of nonzero communication scatterers	L_{c}	5
Communication impulse resp.	$\Re(\boldsymbol{h}_{\mathrm{c}})$ $\Im(\boldsymbol{h}_{\mathrm{c}})$	$[8.4, -5.8, 7.2, -6.6, 5.9]^{\mathsf{T}}$ $[0.6, -6.3, 3.3, -5.2, 6]^{\mathsf{T}}$
Communication scatterers position matrix	$\boldsymbol{V}_{\mathrm{c}}$	$[\boldsymbol{I}_{L_{\mathrm{c}}}; \boldsymbol{0}_{L-L_{\mathrm{c}},L_{\mathrm{c}}}]$
Noise power in the communication channel	σ_{c}^2	1

4.1.1 Radar channel

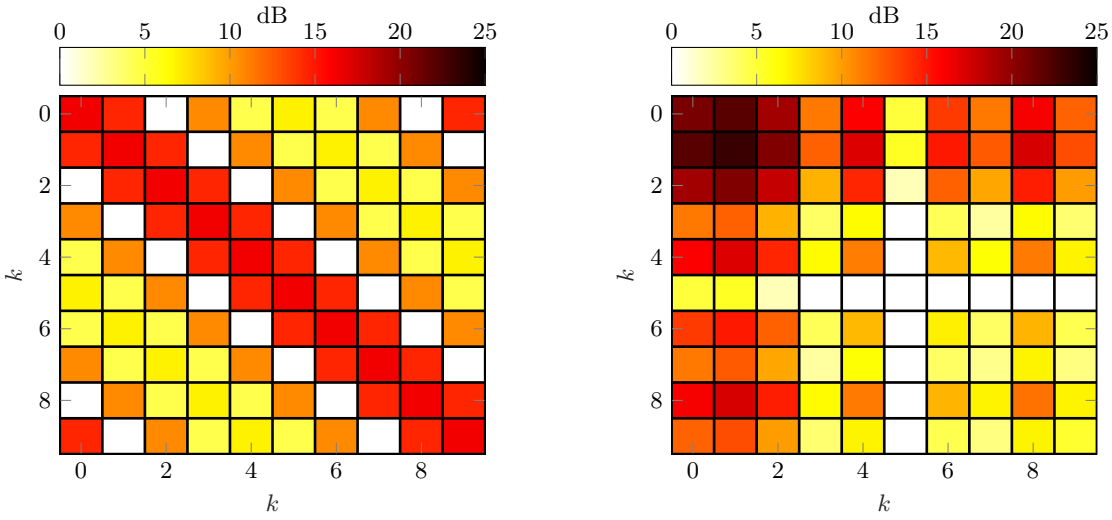
As introduced in Section 2.1.2.2, the radar target is assumed range-extended with random response vector $\boldsymbol{h}_{\mathrm{r}} \sim \mathcal{CN}(\boldsymbol{0}, \boldsymbol{K}_{\boldsymbol{h}_{\mathrm{r}}})$ (see (2.17)). In this setting, the second-order statistics of $\boldsymbol{h}_{\mathrm{r}}$ are fully characterized by the radar target covariance matrix $\boldsymbol{K}_{\boldsymbol{h}_{\mathrm{r}}}$. The latter is Hermitian, hence, to simplify notation, only the upper triangular part of the matrix is explicitly defined, and the full matrix is obtained by symmetry. Specifically, for $l > l'$, the (l, l')-th element is chosen as:

$$[\boldsymbol{K}_{\boldsymbol{h}_{\mathrm{r}}}]_{l,l'} = \rho_{\mathrm{r}}^{l-l'} \sqrt{\mathcal{E}\{|[\boldsymbol{h}_{\mathrm{r}}]_l|^2\}\, \mathcal{E}\{|[\boldsymbol{h}_{\mathrm{r}}]_{l'}|^2\}}, \tag{4.1}$$

where ρ_{r} is the complex correlation coefficient, constrained by $|\rho_{\mathrm{r}}| < 1$.

The corresponding target covariance matrix in the subcarrier domain is then obtained as $\boldsymbol{K}_{\boldsymbol{g}_{\mathrm{r}}} = \boldsymbol{B}_{\mathrm{r}} \boldsymbol{K}_{\boldsymbol{h}_{\mathrm{r}}} \boldsymbol{B}_{\mathrm{r}}^{\mathsf{H}}$, as defined in (2.38). Figure 4.1 illustrates $\boldsymbol{K}_{\boldsymbol{g}_{\mathrm{r}}}$ when the correlation in range is either null or very high, i.e., when $\rho_{\mathrm{r}} = 0$ and $|\rho_r| = .99$, respectively. The display for $|\rho_r| = 1$ is very similar to that of $|\rho_r| = .99$ and is not added (also, this is a limiting case

that leads to a non-invertible covariance matrix, which makes the Gaussian distribution not well-defined). Looking at the diagonal of $\boldsymbol{K}_{\boldsymbol{g}_\mathrm{r}}$, the radar channel *becomes frequency selective* when $|\rho_\mathrm{r}| > 0$; otherwise, when $\rho_\mathrm{r} = 0$ it is *frequency-flat*.



(a) Radar Flat ($\rho_\mathrm{r} = 0$)

(b) Radar Selective ($\rho_\mathrm{r} = .99e^{j2\pi/12}$)

Figure 4.1: *Statistical radar channel in the subcarrier domain*: modulus of $\sigma_{n_\mathrm{r}}^{-2}\boldsymbol{K}_{\boldsymbol{g}_\mathrm{r}}$ for two levels of correlation ρ_r , diagonal elements are the radar SNRs a_k defined in (2.39). When $|\rho_\mathrm{r}| > 0$, ρ_r is taken as a complex value to avoid restrictive case of real-symmetric radar channel.

4.1.2 Communication channel



(a) Com. Selective com #1 (SNR-allied scenario)

(b) Com. Selective com #2 (SNR-competitive scenario)

Figure 4.2: *Deterministic communication channel in the subcarrier domain*: communication SNRs c_k defined in (2.43) for two scenarios com #1 and com #2. Values of c_k for com #1 are obtained by a circular shift with respect to com #2. The degree of competition between radar and communication is assessed by comparing the communication SNRs c_k (shown here) with the radar SNRs a_k of Figure 4.1. In com #1, communication subcarriers are mostly *allied* with those of radar when $|\rho_\mathrm{r}| > 0$, i.e., highest-SNR subcarriers [#(0,1,2,4)] are common to both channels. In com #2, communication and radar subcarriers with high SNR are mostly in *competition*: communication subcarriers [#(5,6)] compete with radar channels [#(0,1,2)].

The communication channel is deterministic and defined via the SNR per subcarrier:

$$c_k \triangleq \sigma_{n_\mathrm{c}}^{-2}|g_{\mathrm{c},k}|^2, \tag{4.2}$$

as given in (2.43). Two communication scenarios are considered, both frequency-selective. In the first one (com #1), the values of c_k are those obtained using the values of the communication impulse response $\boldsymbol{h}_{\mathrm{c}}$ and the noise power reported in Table 4.1. The second scenario (com #2) is obtained by applying a circular shift of the c_k values from com #1. The difference lies in whether the high-SNR communication subcarriers align with those of the radar channel when the radar channel is frequency-selective ($|\rho_{\mathrm{r}}| > 0$). These configurations are shown in Figure 4.2.

4.1.3 Legend conventions

In all subsequent figures in Chapter 4, each curve is identified by a label of the form:

$$\texttt{[Design method]}, \ [w_r = \cdot], \ \texttt{[Evaluation constellation]}.$$

This shorthand contains three key elements:

1. `[Design method]`: the optimization problem used to obtain the power profile of the transmitted symbols: either J, JH, or when the H problem is optimized using a specific design constellation (e.g., 4-PSK or 16-QAM), we denote the resulting power allocation strategies by $\mathrm{H}^{\text{4-PSK}}$ and $\mathrm{H}^{\text{16-QAM}}$, respectively. As a baseline, we also consider EQ (equal power).

2. $[w_r = \cdot]$: the radar weight used in the multi-objective cost function, with $w_c = 1 - w_r$ implicitly assigned to the communication rate.

3. `[Evaluation constellation]`: the actual symbols used when computing radar CMI/CMSE and communication IR, e.g., Gaussian, 4-PSK, or 16-QAM, evaluated with the power profile produced by the chosen `[Design method]`.

Thus, for example, the legend [J, $w_r = 0.5$, 4-PSK] denotes a Jensen-based power allocation under a Gaussian assumption (solution to Problem J) with radar/communication weights 0.5/0.5, but whose performance (CMI, CMSE, IR) is evaluated assuming 4-PSK transmitted symbols. This systematic notation ensures that each curve can be traced back to its design hypothesis, weighting choice, and evaluation model. All figures in the sequel follow this convention consistently.

4.2 Analysis of power allocation strategies with Gaussian symbols

This section evaluates the performance of our two proposed power allocation strategies, Jensen-based (see Problem J) and Jensen–Hadamard-based (see Problem JH), across a range

of DFRC scenarios. We also include the equal power (EQ) baseline, defined as:

$$[\boldsymbol{p}^{(\mathrm{EQ})}]_k \triangleq \frac{P_{\mathrm{T}}}{K} \tag{4.3}$$

with P_{T} the total transmitted power and K the number of subcarriers. The EQ strategy (4.3) belongs to the feasible sets of both Problems J and JH and serves as a baseline for comparison. While suboptimal in most scenarios, the EQ strategy becomes optimal in certain limiting cases. Its inclusion allows us to assess whether the performance gains achieved by optimized power profiles (J and JH) justify their additional computational complexity. All results assume Gaussian transmitted symbols.

We focus on analyzing the impact of the radar and communication channel structures, specifically the correlation between target scatterers and the alignment of the communication SNRs with the radar ones, on the resulting power profiles. To this end, we consider three radar scenarios corresponding to increasing levels of correlation in the radar covariance matrix $\boldsymbol{K}_{\boldsymbol{h}_{\mathrm{r}}}$: uncorrelated, correlated, and fully correlated (see Figure 4.1) and two communication scenarios: SNR-allied (com #1) and SNR-competitive (com #2) (see Figure 4.2).

We assess the performance and the power allocation strategies using two metrics: the CMI for radar (defined in (3.1)) and the IR for communication (defined in (3.3)). Importantly, the expressions used in the plots correspond to the exact formulas of the metrics valid in the Gaussian case, not approximations. Radar CMI values are computed via Monte Carlo integration [93, Chap. 3]. All results in this section are plotted on a logarithmic scale (base 10) to better highlight differences between the curves, especially in regions where the performance gap is small.

To better understand the trade-offs in DFRC waveform design, we begin by analyzing communication-only and radar-only cases (i.e., $w_{\mathrm{r}} = 0$ and $w_{\mathrm{r}} = 1$, respectively), before turning to the joint DFRC case where both goals are balanced.

4.2.1 Communication-only waveform

Herein, we consider the communication-only case, corresponding to a radar weight $w_{\mathrm{r}} = 0$ (i.e., $w_{\mathrm{c}} = 1$) in the objective function. In this setting, the waveform design is entirely driven by communication objectives and is independent of the radar channel characteristics.

Under this assumption, Problems J and JH, and even the optimal Gaussian optimization Problem OPT-G, become equivalent. They all reduce to a classical communication power allocation problem assuming Gaussian symbols, whose optimal solution is given by the well-known WF strategy as described in (3.29):

$$p_k(\lambda^{\star -1}) = \max(0, \lambda^{\star -1} - c_k^{-1}).$$

with $\lambda^\star$ the unique strictly positive solution to

$$\sum_{k\in\mathcal{I}_K} p_k(\lambda^{\star-1}) = P_{\mathrm{T}}.$$

The WF solution allocates more power to subcarriers with stronger communication channels, i.e., higher values of the communication SNRs c_k (2.43), thereby maximizing the total communication IR. This approach is optimal assuming Gaussian transmitted symbols and has been widely studied in the literature on communication theory and convex optimization. For further details and derivations, we refer the reader to [84, 4, 94].

4.2.2 Radar-only waveform

We now examine the radar-only case, corresponding to a weight $w_{\mathrm{r}} = 1$, where the waveform design exclusively targets radar performance and is unaffected by the communication channel. In this setting, the JH allocation reduces to a classical WF solution, as given in (3.29):

$$p_k(\lambda^{\star-1}) = \max(0, \lambda^{\star-1} - a_k^{-1}).$$

with $\lambda^\star$ the unique strictly positive solution to

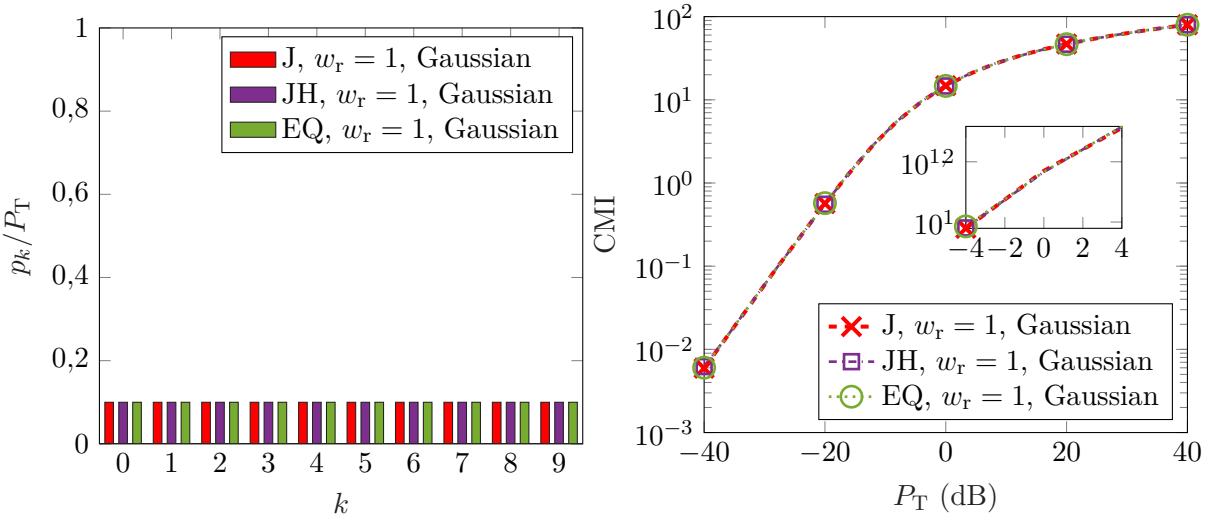
$$\sum_{k\in\mathcal{I}_K} p_k(\lambda^{\star-1}) = P_{\mathrm{T}}.$$

where the per-subcarrier radar SNRs a_k serve as the effective channel gains guiding the power distribution.

In contrast, the J allocation, obtained via convex optimization (e.g., using CVX), may diverge from the JH solution, particularly when strong subcarrier correlations are present. This difference arises because the J formulation accounts for inter-subcarrier dependencies in the radar channel covariance, while the JH formulation treats subcarriers independently through a separable bound. The differences between these two approaches are illustrated and discussed in detail in the following subsections and in Figs. 4.3 and 4.4.

4.2.2.1 Frequency-flat radar channel

When the radar channel $\boldsymbol{h}_{\mathrm{r}}$ is uncorrelated in range, i.e., $\rho_{\mathrm{r}} = 0$, its covariance matrix $\boldsymbol{K}_{\boldsymbol{h}_{\mathrm{r}}}$ is diagonal and hence the matrix $\boldsymbol{K}_{\boldsymbol{g}_{\mathrm{r}}}$ becomes a circulant matrix with a constant diagonal as illustrated in Figure 4.1a. In this case, we prove that the EQ allocation (4.3) is the unique solution to Problems J and JH (see Appendix G.5). This result is illustrated in Figure 4.3 with $\rho_{\mathrm{r}} = 0$.



(a) Power profiles with $P_T = -4$ dB

(b) CMI vs. P_T

Figure 4.3: Radar-only waveform design with $w_r = 1$, assuming a frequency-flat radar channel $\rho_r = 0$. Comparison of the power allocations strategies J, JH and EQ.

4.2.2.2 Frequency-selective radar channel

When the radar channel $\boldsymbol{h}_r$ is correlated in range, the J allocation varies significantly according to the power budget P_T, as shown in Figure 4.4 with $|\rho_r| \in (0, 1)$.

- At very low P_T, only the subcarrier with the highest radar SNR a_k is activated (similarly to the JH allocation). A formal proof is given in Appendix F.2.
- At moderate P_T, the power is allocated among the subcarriers with the highest SNRs. A distinguished feature compared to the JH allocation is that if some of these subcarriers are strongly correlated, not all are activated. (This feature has already been observed in a different context [95].) The resulting radar CMI is slightly higher with the J allocation. We have extensively observed this trend in simulations.
- At very high P_T, all subcarriers are activated and tend to have an EQ allocation (4.3) (similarly to the JH allocation), except in specific scenarios. A discussion is provided in Appendix F.2.

4.2.2.3 Frequency-selective radar channel: the fully-correlated case

When the radar channel $\boldsymbol{h}_r$ is fully-correlated in range, the J allocation activates only the highest-SNR subcarrier independently of the power P_T, as proved in Section F.3. It is shown in the right column of Figure 4.4 with $|\rho_r| = 1$. Strictly speaking, this fully correlated case violates the assumption that $\boldsymbol{K}_{\boldsymbol{h}_r}$ is positive definite (2.17), but it remains an instructive

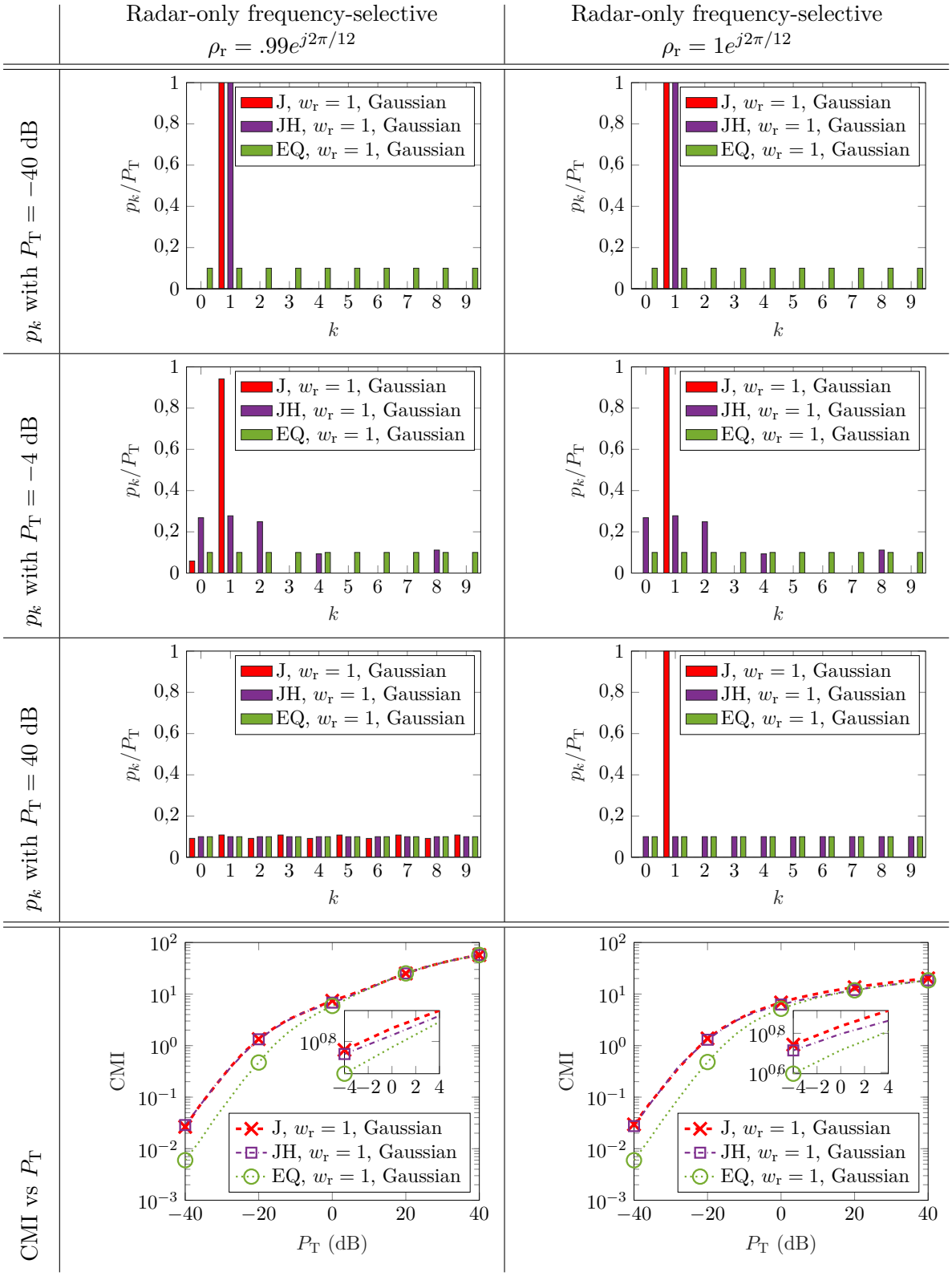


Figure 4.4: Radar-only waveform design with $w_r = 1$ under frequency-selective radar channels. Top: normalized power allocations for J, JH, and EQ (4.3) strategies at three transmit power levels: very low, moderate, and very high P_T. Bottom: corresponding radar CMI values computed via Monte Carlo integration ($M_c = 5E3$ runs), using (3.1). Left column: frequency-selective radar channel with $\rho_r = 0.99e^{j2\pi/12}$. Right column: fully-correlated case ($|\rho_r| = 1$). Zoomed views are shown where relevant.

example. Notably, the J allocation provides, at moderate power, a higher radar CMI than the JH allocation.

Summary of radar-only waveform performance

In practice, J and JH allocations differ only at moderate power when the radar channel is correlated in range. The J allocation tends to activate fewer subcarriers than the JH allocation when correlation exists between the latter. We observed that the J allocation results in a moderately higher radar CMI than the JH allocation, while both J and JH waveforms have higher radar CMI than the EQ waveform (4.3).

4.2.3 DFRC waveform

Herein, we consider DFRC waveforms (i.e., $w_{\mathrm{r}} \in (0,1)$) whose design is impacted by both the radar and communication channels. We discard in our discussion 1) the asymptotic case of a frequency-selective radar channel fully correlated in range; and 2) the case of a joint flat radar and communication channel (obviously, the EQ allocation (4.3) is then optimal). We study three DFRC scenarios formed by a combination of radar and communication channels introduced in Figure 4.1 and Figure 4.2.

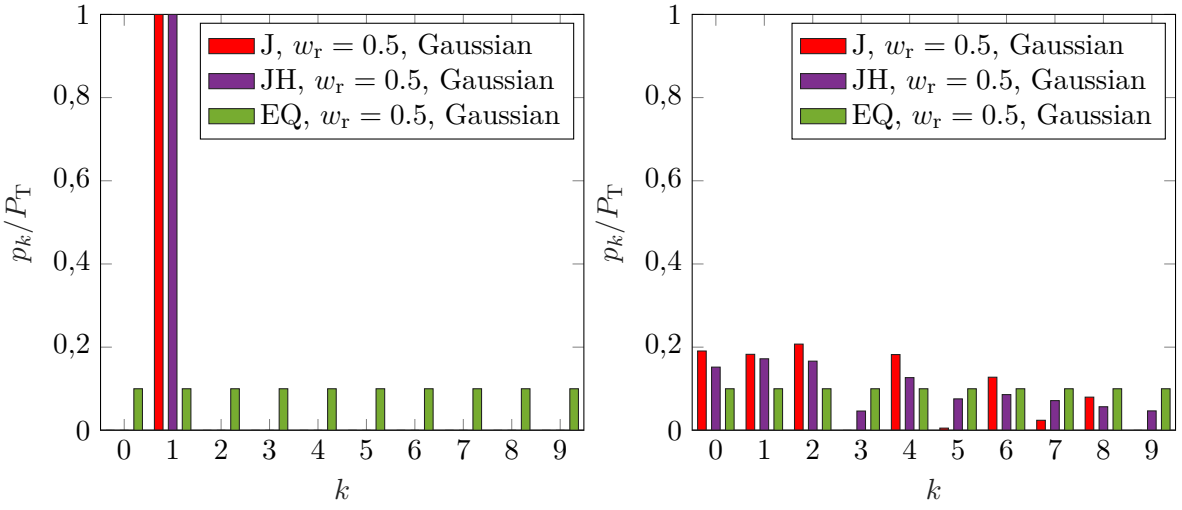
4.2.3.1 DFRC Flat&Selective scenario

In the DFRC Flat&Selective scenario with equal priority weights ($w_{\mathrm{r}} = w_{\mathrm{c}} = 0.5$), the radar channel is frequency-flat ($\rho_{\mathrm{r}} = 0$), whereas the communication channel is frequency-selective (scenario com #1). The main observations are summarized below:

- **Low power:** At very low total transmitted power P_{T}, both J and JH activate only the subcarrier with the highest DFRC SNR λ_k^{th}, as shown in Figure 4.5a and proven in Appendix I. Since their allocations coincide, their radar CMIs are identical. Although these power allocation profiles differ from EQ, J and JH still yield nearly the same radar CMI, as shown in Appendix I. In contrast, by prioritizing subcarriers with higher communication SNR, J and JH can achieve a higher communication IR than the EQ allocation (4.3).

- **Moderate power:** When the total transmitted power P_{T} is moderate, the J and JH allocations diverge. Both favor communication subcarriers with high SNRs (notably [#(0,1,2,4)]). The J allocation avoids allocating power to radar subcarriers correlated with those already selected (e.g., [#3] and [#9]), while JH, which ignores inter-subcarrier correlation, allocates power more uniformly across them. These allocation strategies are illustrated in Figure 4.5b. As a result, JH yields a radar CMI closer to EQ but with slightly degraded communication performance compared to J (see Figure 4.6).

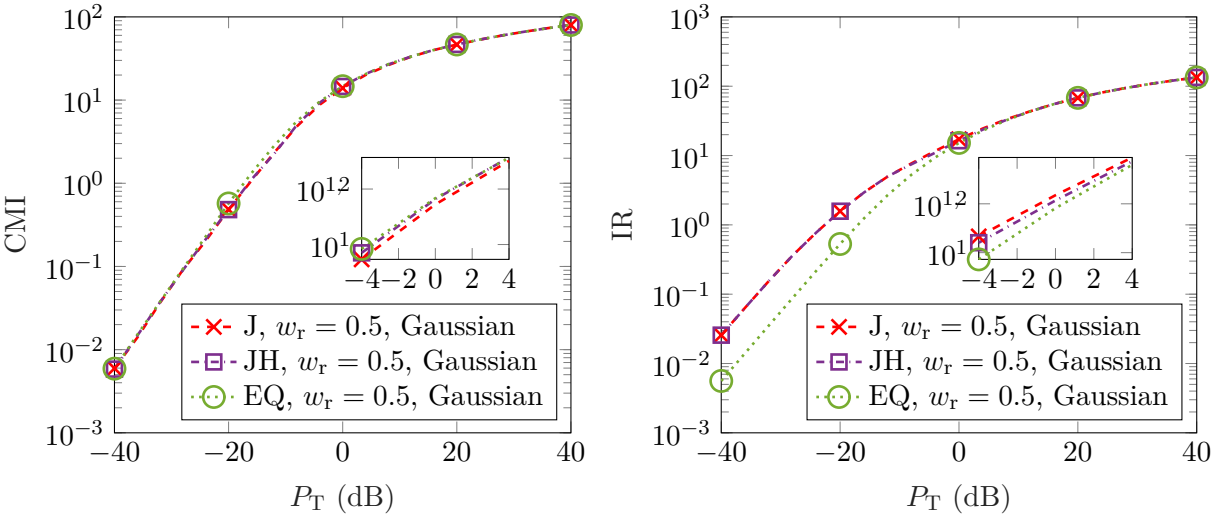
These observations show that J activates a sparser set of subcarriers by exploiting the radar channel structure, whereas H is less selective as it neglects the radar inter-subcarrier correlation, resulting in a more diffuse allocation across them.



(a) Power profiles with $P_T = -40$ dB

(b) Power profiles with $P_T = -4$ dB

Figure 4.5: DFRC waveform design with a frequency-flat radar channel ($\rho_r = 0$) and a frequency-selective allied communication channel (com #1). Normalized power allocations p_k/P_T for J and JH strategies are shown at two transmit power levels: $P_T = -40$ dB and $P_T = -4$ dB.



(a) Radar CMI vs. P_T

(b) Communication IR vs. P_T

Figure 4.6: DFRC waveform performance with a frequency-flat radar channel ($\rho_r = 0$) and a frequency-selective allied communication channel (com #1). Curves are shown for J, JH, and EQ (4.3) strategies.

4.2.3.2 DFRC frequency-selective scenario: allied vs competitive channels

We now examine DFRC waveform design in frequency-selective channels, focusing on two contrasting scenarios:

- DFRC Allied: the radar and communication channels share the highest-SNR subcarriers (com #1);
- DFRC Competitive: the highest-SNR subcarriers differ between the radar and communication channels, (com #2), creating potential conflict in power allocation.

Both scenarios use a radar correlation coefficient of $\rho_{\mathrm{r}} = 0.99e^{j2\pi/12}$ and assume equal priority weights ($w_{\mathrm{r}} = w_{\mathrm{c}} = 0.5$). The following results analyze the impact of this alignment on power allocation strategies, radar CMI, and communication IR across a range of total transmitted power values P_{T}. Several results are formally proven.

Influence of total power budget

- **Low power:** At very low total transmitted power P_{T}, the J and JH allocation strategies activate only the subcarrier with the highest DFRC SNR $\lambda_k^{\mathrm{th}} \triangleq (w_{\mathrm{r}} a_k + w_{\mathrm{c}} c_k)$ (3.26). This behavior is formally proven in Section F.2. This case is illustrated in the first row of Figure 4.7 where subcarrier [#1] has the highest DFRC SNR.

  Since the J and JH allocations are identical, they also have identical radar CMIs and communication IRs. However, their performance relative to the EQ allocation (4.3) depends on the scenario; J and JH may outperform, match, or underperform EQ depending on the DFRC scenario, specifically the radar and communication channels alignment. In Figure 4.7, we observe:

  - DFRC Allied: The J and JH allocations similarly benefit from this cooperative scenario and have higher radar CMIs and communication IRs than the EQ allocation (4.3).
  - DFRC Competitive: The J and JH allocations have a higher radar CMI than the EQ allocation but have, in contrast, a lower communication IR. The power is fully assigned to subcarrier [#1], which has the highest radar SNR but a low communication SNR. CMIs and IRs trends can be opposite depending on which subcarrier is activated.

- **Moderate power:** At moderate P_{T}, the J and JH allocations may differ significantly depending on the DFRC scenario. In Figure 4.7, we observe:

  - DFRC Allied: Trends are similar to those observed at very low total transmitted power P_{T}.

  - DFRC Competitive: Both J and JH allocations preferentially activate radar and communication subcarriers with a high SNR [#(0,1) and #(4,5,6,8), respectively]. The J allocation does not allocate power to radar subcarriers [#2] that are correlated to the former [#(0,1,4,6,8)]. The JH allocation cannot use this correlation and activates more subcarriers with high radar SNR such as [#2]. In the competitive scenario, subcarrier [#2] is a not a high communication-SNR one which explains why the JH allocation has a slightly higher radar CMI but a lower communication IR than the J allocation. Radar CMIs and communication IRs trends can be opposite if we increase the radar system weight w_{r} (cf. Figure 4.8 and as already described for a radar-only waveform).

  Finally, both J and JH allocations have higher radar CMIs and communication IRs than the EQ allocation (4.3) (except when the radar channel is uncorrelated in range, as discussed in Section 4.2.3.1).

- **Very high power** At very high P_{T}, the J allocation has an equal-power distribution (similarly to the JH allocation), except in specific scenarios. A discussion is provided in Section F.2. Radar CMIs and communication IRs thus match for all the strategies.

Influence of weights in the objective We finally represent the achievable CMI-IR region of our optimized waveforms by plotting the communication IR as a function of the radar CMI with a varying weight $w_{\mathrm{r}} \in [0, 1]$ but fixed power budget P_{T}. Any waveform with a curve above another from the right-hand side offers a better compromise between radar and communication. From our previous observations, we focus only on the case of a moderate P_{T}.

Results are depicted in Figure 4.8 for the two studied DFRC Selective scenarios. When the radar channel is correlated in range, the J allocation can offer a better compromise than the JH allocation between radar and communication. Though, the difference in radar CMIs and IRs may remain moderate. In addition, the weight w_{r} needs to be chosen carefully [e.g., w_{r} somewhere in $(0.5, 1)$ in the DFRC Competitive scenario]. In any event, the J and JH allocations offer an additional degree of freedom compared to the EQ allocation (4.3) to compromise between radar and communication functions.

Summary of DFRC waveform performance Similar to the radar-only case, the differences between the J and JH allocation strategies appear primarily at moderate total transmitted power levels P_{T}, when the radar or the communication channel is frequency-selective. The J allocation tends to activate fewer subcarriers than the JH allocation when a significant correlation exists between the latter. Nonetheless, this does not necessarily lead to a higher radar CMI compared to the JH allocation. It is mostly observed when communication subcarriers do not compete with radar subcarriers. In addition, for very low transmitted power P_{T}, the radar CMI and communication IR obtained with the J and JH allocations do not consistently outperform the EQ allocation (4.3). Instead, they result from a compromise driven by the dual objective function.

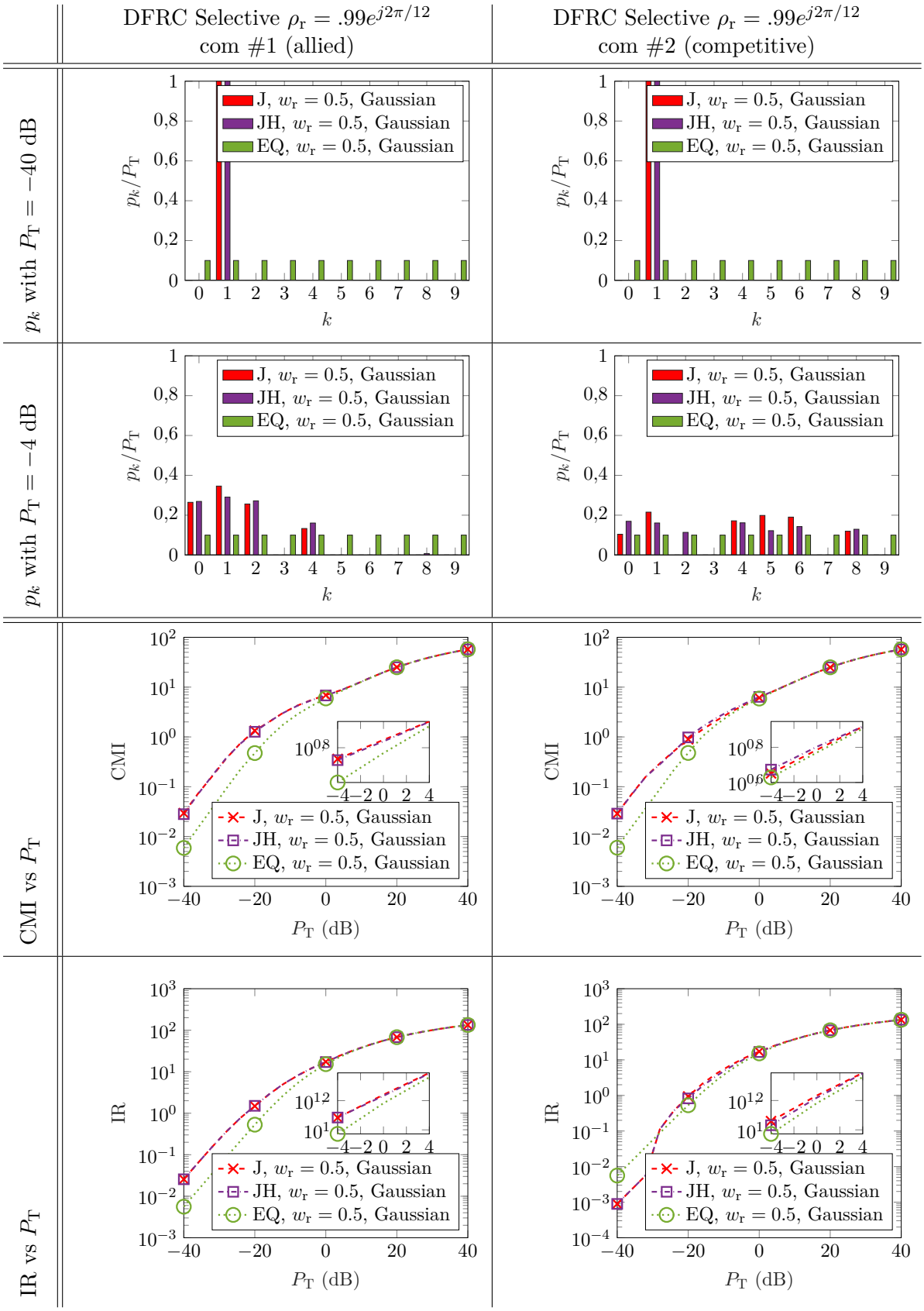


Figure 4.7: DFRC waveform design in selective channel scenarios, with $w_r = w_c = 0.5$ and channel settings from Figs. 4.1b and 4.2. Top: normalized power allocations for J, JH, and EQ (4.3) strategies at very low and moderate P_T. Bottom: corresponding radar CMI and communication IR, computed via (3.1) and (3.3). Zoomed views are included where relevant. The two scenarios differ in the degree of subcarrier competition between radar and communication. Results are compared to radar-only performance in Figure 4.4.

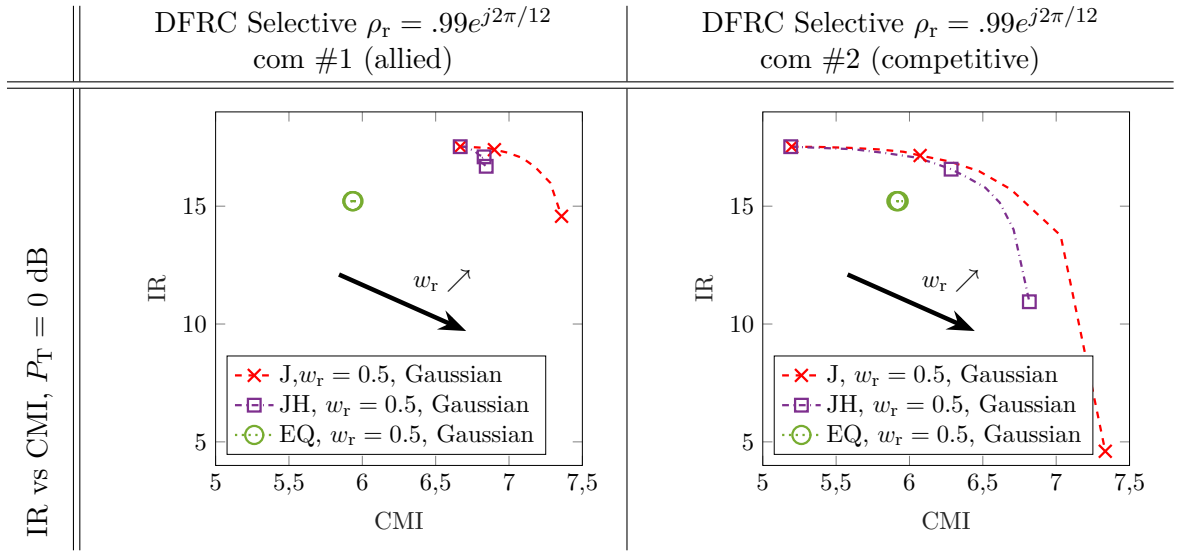


Figure 4.8: DFRC waveform design in selective channel scenarios, with radar and communication channels shown in Figs. 4.1b and 4.2. The communication IR (3.3) is plotted as a function of radar CMI (3.1), forming a parametric curve with $w_r \in [0, 1]$. Markers indicate $w_r \in \{0, 0.5, 1\}$, and w_r increases from left to right, as shown by the black arrow. Two scenarios are considered, differing in the level of subcarrier competition between radar and communication.

4.3 Impact of symbol randomness in OFDM-DFRC systems

In DFRC systems, the transmitted waveform must simultaneously serve sensing and communication functions. To enable communication functionality, information-bearing symbols from a constellation are embedded into the waveform, thereby inducing a random structure in the transmitted signal. While such randomness is fundamental to communication systems, its implications for radar estimation performance are not yet fully studied. In particular, the influence of various symbol constellations, ranging from discrete to Gaussian, on radar metrics such as CMI and the CMSE associated with the MMSE estimator of the target response require additional investigation [92].

It is important to stress that in this section, the constellation is not taken into account at the design stage: the power allocations still rely on the Gaussian-based designs (J and JH), but the resulting waveforms are then evaluated under different symbol constellations (Gaussian, 16-PSK and 16-QAM). Our analysis therefore focuses primarily on radar performance. We proceed in two steps. First, we assess the radar-only performance ($w_r = 1$), i.e., without communication design constraints, to isolate the impact of symbol randomness on radar metrics. Then, we examine the DFRC setting ($w_r = 0.5$), where both radar and communication performances are impacted.

4.3.1 Radar-only waveform

Our objective is to quantify the performance degradation–in terms of radar CMI and CMSE of the MMSE estimator of the target response–that occurs when radar waveforms are constrained to carry information. To this end, we compare information-bearing random waveforms to a purely radar-optimized deterministic waveform (optimized under an information-theoretic criterion i.e., radar MI). In this former case, communication performance is not considered; the focus is strictly on radar metrics.

4.3.1.1 Optimal deterministic radar waveform

We now return to the general optimization Problem OPT introduced earlier in Chapter 3, and focus on a conventional radar scenario. In this case, two simplifications are made: communication constraints are not taken into account, since we aim to isolate the radar performance, and the transmitted radar symbols are assumed deterministic, as in traditional radar systems. Under these assumptions, the CMI in Problem OPT reduces to the MI given in (2.59). The resulting formulation defines the deterministic radar optimization problem OPT-R, which may stem from OPT but specializes it to the radar-only, deterministic-symbol setting.

Problem OPT-R (Optimal power allocation for a deterministic radar waveform)**.**

$$\begin{aligned} \boldsymbol{x}^{(\mathrm{OPT-R})} = \arg\max_{\boldsymbol{x}} \quad & \log_2 \det\left(\boldsymbol{I}_K + \sigma_{n_\mathrm{r}}^{-2} \boldsymbol{K}_{\boldsymbol{g}_\mathrm{r}} \boldsymbol{D}_{|\boldsymbol{x}|^2}\right) \\ \text{s.t.} \quad & \sum_{k \in \mathcal{I}_K} |x_k|^2 = P_\mathrm{T}. \end{aligned}$$

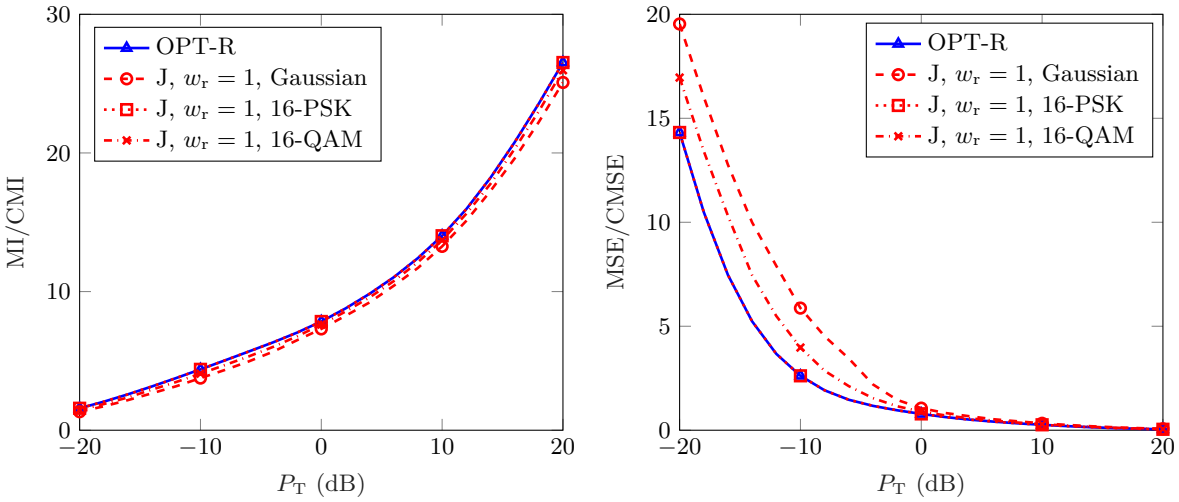
The problem OPT-R only depends on the power $|\boldsymbol{x}|^2$ of the deterministic symbols and is convex with respect to the latter, this can be proved using a similar proof used for Theorem F.1.2 and in [85, Th. 4]. We use the same toolbox CVX as we did for Problem J, to determine the optimal power allocation. Any waveform with such a power profile is thus a solution to problem OPT-R: an arbitrary phase offset can be appended to each symbol but remains unchanged along transmission. This optimal waveform is unable to convey information but is helpful to assess later the loss incurred by DFRC waveform.

4.3.1.2 Radar performance under symbol randomness

We aim first to assess the loss a CP-OFDM radar receiver endures when the transmitted symbols convey information. To that end, we recall that when ($w_\mathrm{r} = 1$), the optimization problems OPT and J yield the same solution in terms of the power allocation vector $\boldsymbol{p} = |\boldsymbol{x}|^2$. We therefore consider two radar-only waveforms based on: 1) the deterministic symbols solution to Problem OPT-R and 2) the random symbols drawn from three distributions: Gaussian, 16-PSK, and 16-QAM. The latter waveforms are assigned the same power profile J computed by solving Problem J with $w_\mathrm{r} = 1$ (i.e., radar-only optimization so there is no attempt to

optimize the communication IR though information-bearing symbols are transmitted).

For the deterministic-symbol waveform of Problem OPT-R (case 1), radar performance is evaluated using the MI (2.59) and the MSE (2.62). For the random-symbol waveforms (case 2), we instead compute the radar CMI (3.1) and CMSE (3.4) under each constellation (Gaussian, 16-PSK, 16-QAM). The deterministic MI and MSE values thus serve as a baseline reference against which the estimation loss due to symbol randomness can be quantified.



(a) Radar CMI

(b) Radar CMSE

Figure 4.9: Performance of optimized radar-only waveforms: radar MI (2.59) and MSE (2.62) for deterministic symbols $\boldsymbol{x}^{(\mathrm{OPT-R})}$ vs. radar CMI (3.1) and CMSE (3.4) for Gaussian and discrete constellations with power allocation J when $w_r = 1$ in Problem J. CMI and CMSE are evaluated via Monte Carlo integration with $M_c = 5E3$ runs.

MI and CMI In Figure 4.9a, the radar MI of the deterministic waveform OPT-R is consistently higher than the radar CMI of the random waveforms.

Notably, the 16-PSK constellation yields no CMI-loss compared to the deterministic waveform. This behavior is explained by the structure of the radar CMI (3.1), which reduces to the radar MI (2.59) when the transmitted symbols have constant modulus and deterministic power. More specifically, we recall the expression of the radar CMI:

$$\mathrm{CMI} = \mathcal{E}_{\boldsymbol{x}} \left\{ \log_2 \det \left(\boldsymbol{I}_K + \frac{1}{\sigma_{n_r}^2} \boldsymbol{K}_{\boldsymbol{g}_r} \boldsymbol{D}_{|\boldsymbol{x}|^2} \right) \right\}$$

where $|\boldsymbol{x}|^2$ denotes the squared amplitude of the transmitted symbols. For PSK constellations, all symbols have constant squared amplitude and $|\boldsymbol{x}|^2$ is fixed across realizations. Hence, the random phase does not affect the radar CMI, which explains why the radar CMI for 16-PSK is equal to the deterministic MI. In other words, introducing an information-bearing phase on each subcarrier of a deterministic CP-OFDM waveform does not affect the quantity of

information the received radar signal entails about a Gaussian target amid AWGN.

On the other hand, when non-constant modulus symbols are used, such as in 16-QAM or Gaussian signaling, the randomness introduced in $|\boldsymbol{x}|^2$ degrades the radar CMI. These fluctuations in symbol amplitudes lower the information the received radar signal entails about the target's echo. The degradation is more significant for Gaussian symbols, as they exhibit the highest amplitude variability.

MSE and CMSE As seen in Figure 4.9b, the ordering of the MSE and CMSE curves is inverted compared to the radar MI and CMI. This observation suggests an important insight: the waveform that maximizes radar MI or CMI also tends to minimize the MSE or CMSE of the MMSE estimator of the target response. While we do not yet have rigorous proof for this behavior, the consistent trend across simulations strongly indicates this dual relationship.

In particular, the estimation error is minimal for the optimal deterministic waveform and matches that of the 16-PSK waveform. This can again be understood by examining the expression of the radar CMSE:

$$\mathrm{CMSE} = \mathcal{E}_{\boldsymbol{x}} \left\{ \mathrm{Tr} \left\{ \left({\boldsymbol{K}_{\boldsymbol{h}_\mathrm{r}}}^{-1} + \sigma_{n_\mathrm{r}}^{-2} \boldsymbol{B}_\mathrm{r}^{\mathsf{H}} \boldsymbol{D}_{|\boldsymbol{x}|^2} \boldsymbol{B}_\mathrm{r} \right)^{-1} \right\} \right\}.$$

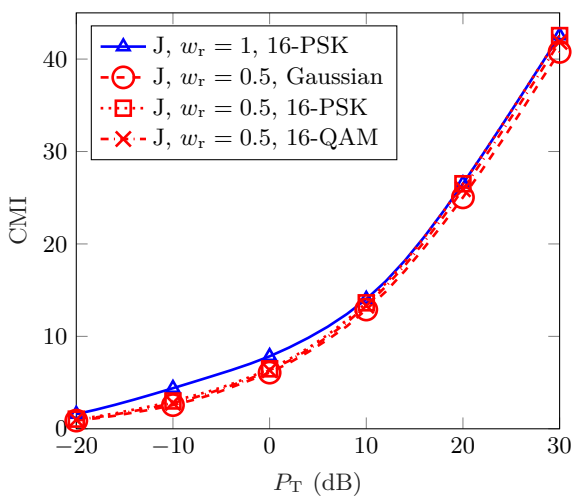
This expression shows that, similar to the radar CMI, the CMSE depends only on the squared amplitude $|\boldsymbol{x}|^2$ of the transmitted symbols. For constant modulus constellations such as PSK, the symbols squared amplitude $|\boldsymbol{x}|^2$ remain fixed across realizations. As a result, the CMSE reduces to the same value as the MSE achieved by the deterministic waveform. In contrast, here again, the target estimation is worsened for the random waveforms with 16-QAM followed by Gaussian symbols, especially at low transmitted power P_T.

To summarize, this radar-only scenario informs us that adding an information-bearing phase on each subcarrier of a CP-OFDM waveform incurs no radar estimation loss. On the contrary, adding randomness to the waveform using non-constant modulus symbols (e.g., with QAM or Gaussian constellations) degrades the target's estimation. This is in accordance with the recent results in [96, 97] showing that radar sensing is generally favored by "low-randomness" waveforms.

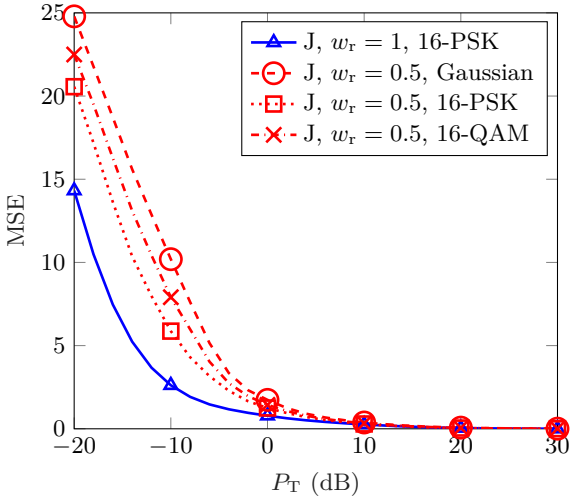
4.3.2 DFRC scenario

We further investigate the loss a CP-OFDM radar receiver endures when transmitting information within an actual DFRC scenario. In contrast to the radar-only case, the symbols power optimizes not only the radar CMI but also the communication IR as formulated in Problem J with $w_\mathrm{r} \in (0, 1)$. To isolate the loss induced by the communication constraint, the radar-only (i.e., $w_\mathrm{r} = 1$) J waveform is also displayed with 16-PSK symbols (this is the waveform that gave us the same radar performance as the deterministic waveform OPT-R). We focus on a competitive channel scenario (com #2), where high-SNR subcarriers compete

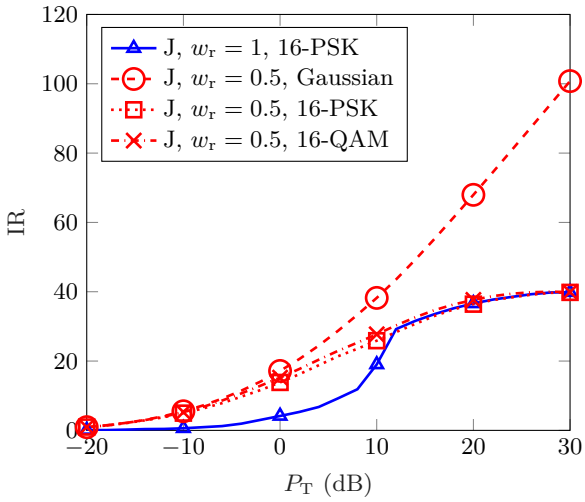
between the radar and communication channels. This setting is illustrated in Figs. 4.1b and 4.2b.



(a) CMI with respect to P_T



(b) CMSE with respect to P_T



(c) IR with respect to P_T

Figure 4.10: Performance of optimized DFRC waveforms: radar CMI (3.1), radar CMSE (3.4), and communication IR (3.3) as a function of P_T for Gaussian and discrete constellations with power allocation J. Metrics evaluated via Monte Carlo integration with $M_c = 5E3$ runs except for (3.3).

4.3.2.1 Radar CMI

In Figure 4.10a, the optimized radar-only waveform consistently achieves the highest radar CMI compared to the other DFRC waveforms, especially at low total transmitted power P_T. This is expected as in DFRC scenarios, power must also be allocated to subcarriers that favor

communication, even if they are suboptimal for radar, since the symbols are jointly adapted to the communication channel. In the competitive setting considered here, the radar and communication channels differ significantly, exacerbating this trade-off.

Among the DFRC waveforms, PSK symbols once again prove advantageous for radar sensing. Their constant-modulus structure enables higher information between the received radar signal and the target's response than QAM and Gaussian symbols.

4.3.2.2 Radar CMSE

In Figure 4.10b, the ordering of the CMSE curves is also inverted which confirms once again that the estimation accuracy (as measured by CMSE) follows a similar trend to radar CMI. At low power P_{T}, the target estimation is strongly degraded with symbols optimized to achieve the dual function whatever the constellation considered. Nonetheless, PSK symbols endure less degradation than QAM and Gaussian symbols.

4.3.2.3 Communication IR

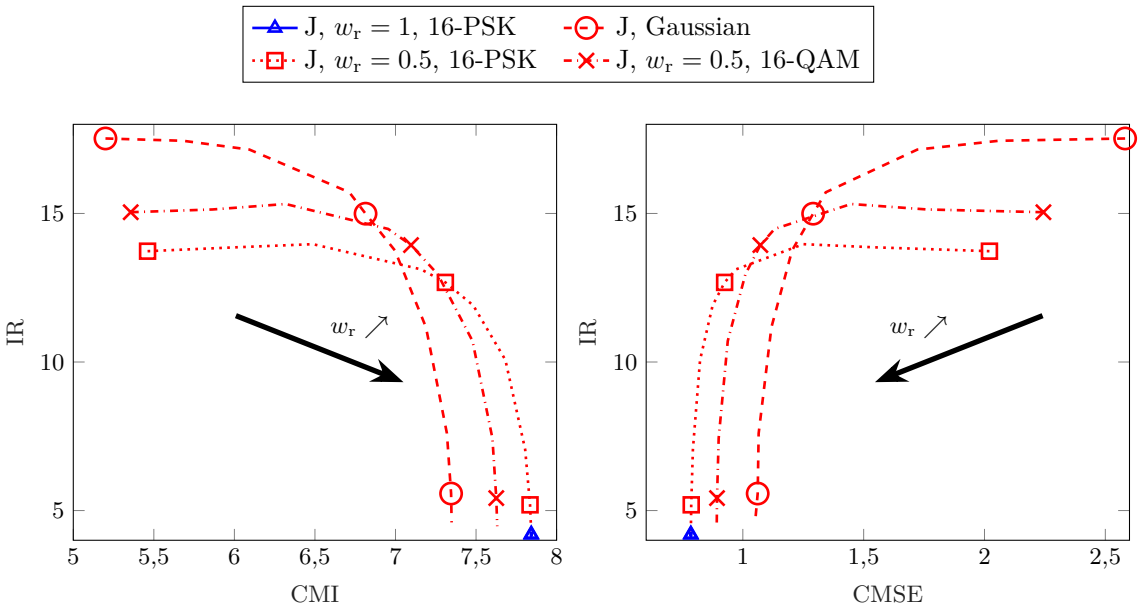
In Figure 4.10c, the communication IR of the radar-only waveform ($w_{\mathrm{r}} = 1$) is the poorest among those depicted. This result is to be expected since 1) this waveform does not optimize any communication objective; 2) radar and communication channels strongly compete here for the resource allocation. For the three other DFRC waveforms, well-known results are recovered [47, Sec. 4.6]. The IR is maximum for (non-practical) Gaussian symbols, and higher-order QAM constellations are more spectrally efficient[1] than their PSK counterparts. In addition, IRs obtained with (practical) discrete constellations reach a common, finite asymptote for an increasing power P_{T} unlike with Gaussian symbols.

To summarize, this DFRC scenario informs us that radar estimation can be highly degraded in the case of competitive DFRC channels. In addition, choosing a constellation results from a compromise between the radar and communication performance. Though PSK is favorable for the radar estimation, it is detrimental to the communication IR that, instead, requires high-randomness waveforms (e.g., QAM or the non-practical Gaussian symbols). This trade-off clearly appears when plotting the communication IR as a function of radar CMSE or as a function of radar CMI (see Figure 4.11).

4.4 Analysis of power allocation strategies with discrete symbols

This section extends the previous analysis by considering practical discrete modulation schemes, specifically PSK and QAM constellations, from the design stage. Unlike the Gaus-

[1]The IR that can be transmitted over a given bandwidth in a specific communication system.



(a) CMI with respect to P_T

(b) CMSE with respect to P_T

Figure 4.11: Trade-off between communication IR (3.3) and radar metrics (CMSE (3.4), CMI (3.1)) for varying $w_r \in [0, 1]$ at total power $P_T = 0$ dB. Curve is parameterized by w_r increasing from left to right for the IR-CMI curve and from right to left for the IR-CMSE curve, as shown by the black arrow.

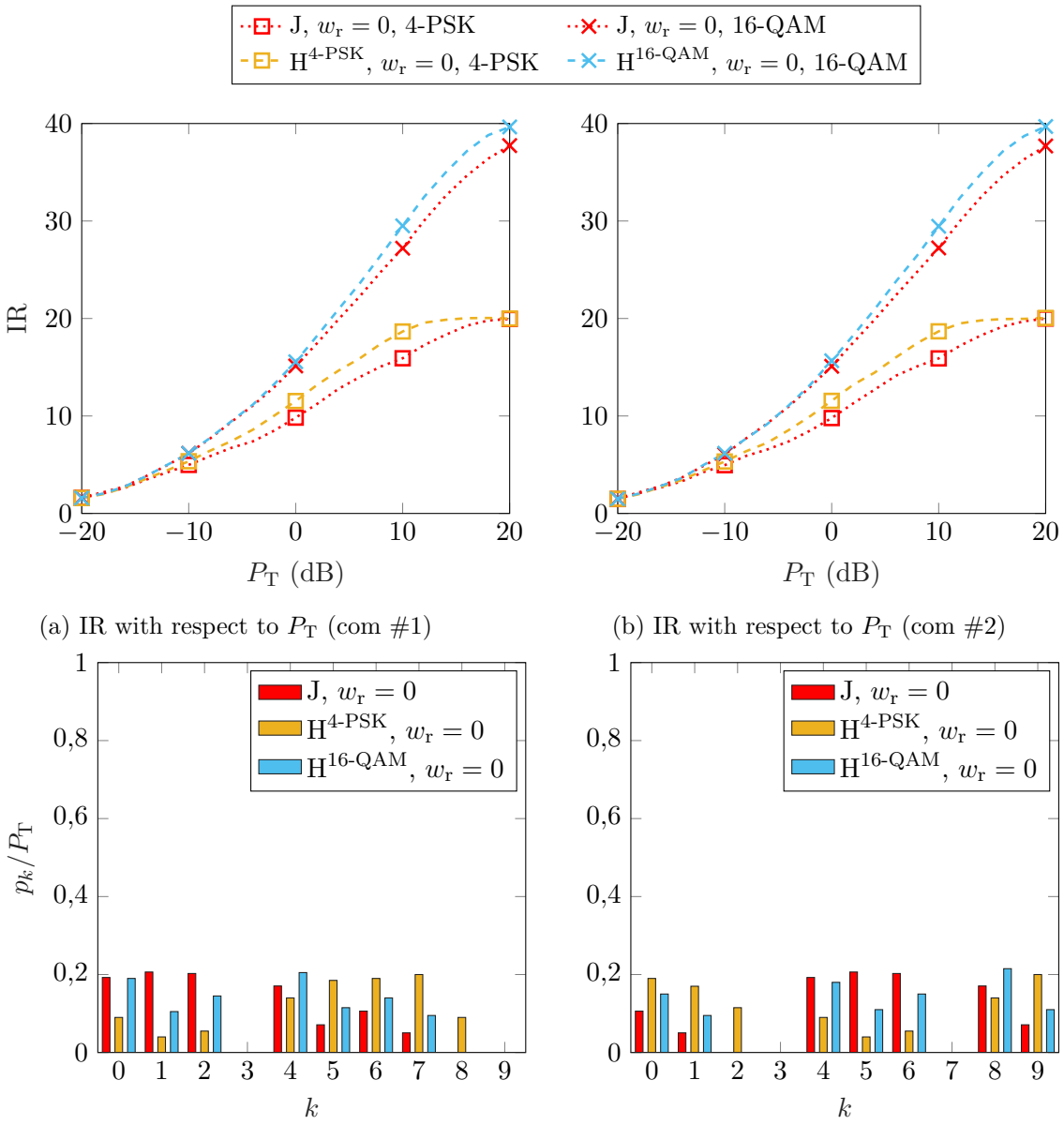
sian assumption at the design stage (adopted in previous sections), discrete constellations introduce additional challenges in waveform optimization as explained in Section 3.3.

We compare two power allocation strategies introduced previously: (i) the J power profile, obtained via a Jensen approximation under Gaussian input symbols (Problem J), and (ii) the H power profile, based on a Hadamard approximation for discrete input constellations. The H strategy is constellation-dependent; therefore, when using a 4-PSK constellation during design for instance, we denote the resulting allocation strategy $\mathrm{H}^{\text{4-PSK}}$, and similarly, $\mathrm{H}^{\text{16-QAM}}$ for 16-QAM, to avoid confusion.

The performance of the power profiles is evaluated in communication-only ($w_r = 0$), radar-only ($w_r = 1$), and DFRC scenarios, focusing on performance trade-offs and implementation complexity. The formulas for IR (3.3), the radar CMI (3.1), and CMSE (3.4) used in the plots are all tailored for discrete symbols.

4.4.1 Communication-only waveform

In the communication-only scenario, Problem H and OPT are equivalent since the radar CMI is not considered and no approximation is made on the communication IR. Moreover, in this setting H follows the MWF solution, which is the optimal power allocation strategy for parallel discrete-input memoryless channels under a total power constraint [46]. Unlike clas-



(a) IR with respect to P_T (com #1)

(b) IR with respect to P_T (com #2)

(c) Power profiles with $P_T = 0$ dB (com #1)

(d) Power profiles with $P_T = 0$ dB (com #2)

Figure 4.12: Communication-only waveform design with $w_r = 0$ assuming the communication scenarios (com #1 and com #2). Communication IR (3.3) values computed via Monte Carlo integration ($M_c = 5E3$ runs).

sical WF, which assumes Gaussian inputs and allocates more power to channels with higher communication SNRs (2.43), MWF accounts for the discrete nature of the input practical constellations (e.g., PSK or QAM). It uses the mercury function, which captures the performance gap between discrete and Gaussian inputs. In other words, MWF can be interpreted as filling water (power) into containers (channels) that may already contain some *mercury*. The mercury represents the penalty caused by the mismatch between the discrete input and the channel's ideal capacity. Power is allocated only to the *space above the mercury*, meaning channels with a larger gap receive less power even if their SNR is high. This mechanism allows MWF to optimally balance power across channels by considering both the channel capacity and the input distribution, thereby maximizing the communication IR.

One key implication of MWF is the phenomenon of saturation. For discrete inputs, the IR in each subchannel cannot grow unbounded with increasing power. Moreover, additional power becomes less and less effective once the constellation's capacity limit is approached. This saturation effect contrasts sharply with the Gaussian case, where the IR increases logarithmically with power without bound. MWF naturally captures this behavior by cutting off power allocation to subchannels whose IR gain has already saturated, reallocating power where it remains effective.

To illustrate this behavior, we consider a communication-only scenario with $w_{\mathrm{r}} = 0$ and the communication channel setups com #1 (allied) and com #2 (competitive) (see Figure 4.2). For a fixed total transmit power of $P_{\mathrm{T}} = 0$ dB, Figure 4.12 displays the resulting power allocations:

- **Jensen-based allocation (J)**: Assumes Gaussian inputs and hence is a WF solution.
- **Hadamard-based allocation (H)**: Tailored for discrete symbols from the design stage (for 4-PSK and 16-QAM constellations in our setting) and is an MWF solution.

For the com #1 scenario, we observe that J allocates power to subcarriers [#(0, 1, 2, 4, 5, 6, 7)], as expected from classical WF, as they are the subcarriers with the highest communication SNRs (see Figure 4.2a). The power profile $\mathrm{H}^{\text{16-QAM}}$ (tailored for 16-QAM symbols) follows a similar trend to J (tailored for Gaussian symbols); from an IR standpoint, this is consistent with the fact that high-order constellations are well approximated by a Gaussian-input model. However, compared to J, the $\mathrm{H}^{\text{16-QAM}}$ allocation tends to favor specific subcarriers more strongly, such as subcarrier [#6].
In contrast, the $\mathrm{H}^{\text{4-PSK}}$ allocation (tailored for 4-PSK, solution to H) exhibits a different behavior. It assigns less power to the strongest-SNR subcarriers and distributes power more broadly, notably including weaker subcarriers such as [#5] and [#7]. This redistribution is a direct consequence of MWF because PSK inputs saturate in IR more rapidly, high-SNR subcarriers with PSK inputs quickly become inefficient for additional power, leading to a more balanced (yet non-intuitive) allocation across available subcarriers.

Since com #2 is just a circular shift of com #1 (see Figure 4.2), and the communication IR used as objective function in both J and H decomposes into per-subcarrier IR contributions

each depending on the communication SNR, the resulting power allocation profiles for com #2 are simply circular shifts of those for com #1. We therefore omit further comments on com #2. The resulting IRs are exactly identical in both scenarios for the same reason, as shown in Figure 4.12.

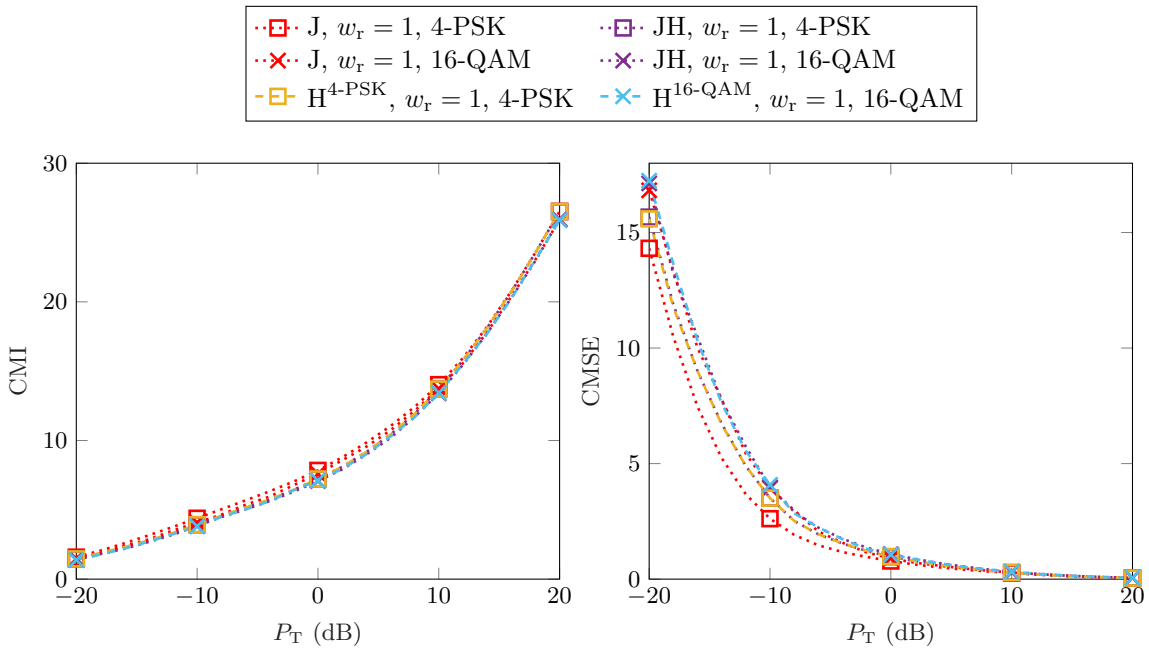
Hence, we evaluate the resulting communication IR, assuming that the transmitted symbols are drawn from 4-PSK and 16-QAM constellations, under two power allocation strategies: H and J (although the J allocation is designed based on Gaussian input assumptions, we still incorporate it into the expression of a discrete-input IR to assess its performance). As shown in Figure 4.12, the simulation results confirm H consistently outperforms J in terms of IR, which was derived under Gaussian input assumptions and is thus suboptimal in this context. This performance gap is observed for both 4-PSK and 16-QAM constellations.

4.4.2 Radar-only waveform

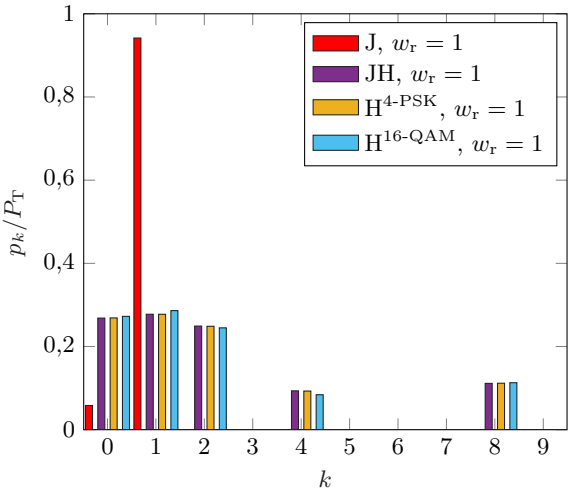
In this section, we evaluate the radar performance of our proposed power profiles using discrete constellation under a radar-only design objective (i.e., $w_{\mathrm{r}} = 1$). We compare three formerly introduced power allocation strategies, each based on a different approximation of radar CMI:

- **Jensen-based allocation (J)**: Applies Jensen's inequality to radar CMI. It captures radar channel correlations but ignores symbol randomness. The power profile is obtained via numerical tools (MATLAB toolbox CVX).
- **Hadamard-based allocation (H)**: Preserves the discrete randomness of transmitted symbols in the radar CMI (see (3.36)), but neglects inter-subcarrier channel correlations. The solution is obtained numerically as explained in the paragraph following Section 3.3.2.1.
- **Jensen–Hadamard-based allocation (JH)**: Corresponds to the Jensen–Hadamard-based allocation applied in the radar-only setting. It serves as a reference, as its results should coincide with those of the $\mathrm{H}^{\text{4-PSK}}$ waveform as we will explain in the following. We have a closed-form expression for the JH power profiles given in (3.24).

The main goal of this analysis is to assess how the two different approximations (J vs H) of the radar CMI used during waveform optimization affect the resulting radar CMI and CMSE (JH is used as a reference power profile). Simulations are conducted using 4-PSK and 16-QAM constellations and the radar channel is modeled as frequency-selective with strong correlation in range (see Figure 4.1b). We plot in Figure 4.13 the resulting CMI and CMSE computed assuming random discrete transmitted symbols. For a given specific constellation, CMI and CMSE exhibit opposite trends; we therefore focus on CMSE, which is a more conventional metric for radar estimation accuracy. When comparing CMI and CMSE trends, it is important to compare the trends of the CMI and CMSE within the same constellation, since their relative behavior may differ between modulation schemes.



(a) Radar CMI vs. total transmit power P_T (b) Radar CMSE vs. total transmit power P_T



(c) Power profiles with $P_T = -4$ dB

Figure 4.13: Radar-only waveform design with $w_r = 1$ assuming a frequency-selective radar channel with strong correlation $\rho_r = .99e^{j2\pi/12}$. Radar CMI and CMSE values computed via Monte Carlo integration with $M_c = 5E3$ runs.

Power-allocation profiles. First, as shown in Figure 4.13c, JH profile coincides with that of $H^{4\text{-PSK}}$. To explain this result, recall that with constant-modulus constellations such as PSK, the symbol amplitude is fixed (e.g., $|v_k| = 1$). The radar objectives considered in (3.37), namely $\sum_{k\in\mathcal{I}_K} \mathcal{E}_{v_k}\{\log_2(1 + a_k|v_k|^2 p_k)\}$, depend only on the transmit power and not on the symbol phase (see Section 4.3.1.2). Since $|v_k|^2 = 1$, this expression reduces to $\sum_{k\in\mathcal{I}_K} \log_2(1 + a_k p_k)$. Consequently, the radar objective of Problem H reduces to that

of Problem JH, and $\mathrm{H}^{\text{4-PSK}}$ and JH yield the same allocation and radar performance in this regime. Second, we note $\mathrm{H}^{\text{4-PSK}}$ and $\mathrm{H}^{\text{16-QAM}}$ are nearly identical, as observed in Figure 4.13c. This similarity may suggest that the radar metrics (CMI and CMSE) depend little on the constellations considered, unlike the IR metric. Moreover, H has a fundamentally different policy for allocating power than J. As H ignores the correlation between radar subcarriers, it allocates power first to high-SNR radar subcarriers [in descending order, #(1,0,2,8,4,6)]. Dissimilarly, J allocates less power to radar subcarriers [#(8,4,6)] highly correlated with strong ones [#(1,0,2)], as already observed in [85].

Radar CMSE. We observe in Figure 4.13b that radar estimation performance improves (i.e., CMSE decreases) with increasing power across all power profiles, without apparent saturation, as observed for IR. In our setting, for each constellation, the H strategy has degraded estimation performance (i.e., higher CMSE) compared to J in the low and moderate power regions, especially for the 4-PSK. Hence, at the design stage, accounting for the correlation among radar subcarriers is more beneficial for radar estimation than assuming an exact symbol distribution. As such, the J strategy should be favored over H in this regime (i.e., $w_{\mathrm{r}} = 1$), particularly for low-order modulation. Finally, for a fixed strategy (H or J) and opposite to IR, low-order modulation is more favorable to radar estimation, a trend already observed in Section 4.3.1.2.

4.4.3 DFRC waveform

We now analyze the performance of the proposed power allocation strategies in the joint radar–communication (DFRC) scenario, where both radar CMI and communication IR must be simultaneously optimized. Specifically, we evaluate the trade-off between radar CMI (or CMSE) and communication IR as a function of the total transmit power P_{T} and the radar–communication weighting factor w_{r}. Because the Jensen-based (J) and Hadamard-based (H) allocations rely on fundamentally different approximations (J uses radar channel correlations but assumes Gaussian transmitted symbols, while H captures the real discrete symbol behavior but ignores subcarrier correlation), their resulting performance is not always directly comparable on an absolute scale.

To provide a useful reference between these two extremes, we also consider a hybrid JH allocation previously introduced and analyzed, which serves as a bridge between the Jensen- and Hadamard-based approaches. When $w_{\mathrm{r}} = 1$ (radar-only regime), JH behaves similarly to H (see Section 4.4.2) and when $w_{\mathrm{r}} = 0$ (communication-only regime), JH converges to J as the objective will be optimized. Hence, JH offers a useful reference to interpret performance trends.

In the following analysis, rather than looking for a single dominant strategy, we focus on the key performance trends and trade-offs that emerge across different operating regimes. In particular, we investigate when and why one method outperforms the other, how their behavior depends on modulation order (e.g., 4-PSK vs. 16-QAM), and how their relative

performance evolves across radar-only, communication-only, and balanced DFRC configurations.

4.4.3.1 General IR–CMSE behavior

In our scenario, for $P_{\mathrm{T}} = 0$ dB, the IR -CMSE and IR -CMI curves depicted in Figure 4.14 exhibit smooth, concave transitions. The IR-CMSE and the IR-CMI curves exhibit exactly opposite trends, we focus here on the IR-CMSE as the CMSE metric is more conventional in radar scenarios. The general trend is as follows: the more weight we give to the communication function, the higher the IR at the expense of radar estimation; the more weight we give to the radar function, the better is the radar estimation at the expense of IR.

In general, a power allocation strategy can be considered superior if its IR–CMSE trade-off curve dominates the other, i.e., lies entirely above and to the left, achieving higher IR and lower CMSE across all weighting factors w_{r}. However, in our results, no such dominance is observed between strategies J and H. Hence, strategy H does not offer a better DFRC trade-off than strategy J, and vice versa. For a fixed constellation, strategy H achieves the highest IR when communication performance is prioritized, but results in the poorest radar estimation performance when the radar function is favored. The gap between the maximum IR achieved by H (achieved by H when the power allocation reduces to the MWF) and the maximum IR obtained by J at $w_{\mathrm{r}} = 0$ appears larger for low-order constellations (4-PSK) than for higher-order ones (16-QAM). However, this behavior may change depending on the transmit power (see Figs. 4.12a and 4.12b). The difference between the minimum CMSE, always reached by J in our simulations, and the CMSE of H at $w_{\mathrm{r}} = 1$ does not appear to be much influenced by the cardinality of the constellations. However, the difference becomes distinct for low-order modulations in low-power regions, showingthe advantage of J over H in terms of radar estimation (see Figure 4.13b).

Finally, for a fixed strategy (H or J), curves shift upward and to the right from 4-PSK to 16-QAM. This is a reflection of QAM's increased randomness, which improves communication performance (i.e., IR) at the expense of radar estimation accuracy (CMSE). It illustrates the price to be paid to transmit information, as already observed for J in Section 4.3.1.2 and also confirmed here for H. This result thus highlights again the deterministic-random trade-off recently unveiled in [97].

4.4.3.2 Surprising behavior of the IR-CMSE curves

The IR saturation inherent for the proposed H strategy induces behaviors in DFRC scenarios that may appear counterintuitive at first glance, yet remain predictible. Notably in Fig 4.14, when the communication function is favored, H exhibits a poorer DFRC trade-off in the SNR-allied scenario rather than in the competitive one, especially for 4-PSK. In this regime (i.e., small w_{r}), the H strategy allocates power mainly to maximize the IR (the true expression of IR for discrete symbols without any approximation). As a result, power is assigned not

only to the high-SNR communication subcarriers but, due to saturation, also to the weaker ones. In the SNR-allied scenario (see Figure 4.2a), these weaker subcarriers actually receive most of the allocated power [#(5,6,7)] (see Figure 4.12c). Since they do not correspond to the highest-SNR radar subcarriers [#(1,0,2)] (see Figure 4.1b), the radar CMSE increases significantly despite the apparent allied structure. Conversely, in the SNR-competitive scenario (see Figure 4.2a), the weak communication subcarriers coincide with the strong radar subcarriers (see Figure 4.1b), which helps limit the CMSE increase.

On the other hand, Figure 4.14d illustrates another peculiar behavior of the IR-CMSE curve. This time, the effect is due to *not* considering IR saturation at the design stage, as is the case when assuming Gaussian inputs. The IR achieved by J with 4-PSK decreases after a certain point as more weight is given to the communication function. As J ignores the saturation effect, it tends to overallocate power to high-SNR communication subcarriers. J with 4-PSK appears thus clearly IR-suboptimal in the communication-only regime at this transmit power (see Figure 4.12b with $P_{\mathrm{T}} = 0$ dB). When some weight is given back to the radar function (i.e., w_{r} small), J reallocates some power to high-SNR radar subcarriers. In the SNR-competitive scenario, the latter correspond to weaker communication subcarriers. It mimics thus the saturation effect, leading locally to an increased IR. A similar effect is not seen for 16-QAM, since J is almost IR-optimal at $w_{\mathrm{r}} = 0$ with this constellation at this transmit power (see Figs. 4.12a and 4.12b with $P_{\mathrm{T}} = 0$ dB).

4.4.3.3 Impact of modulation type

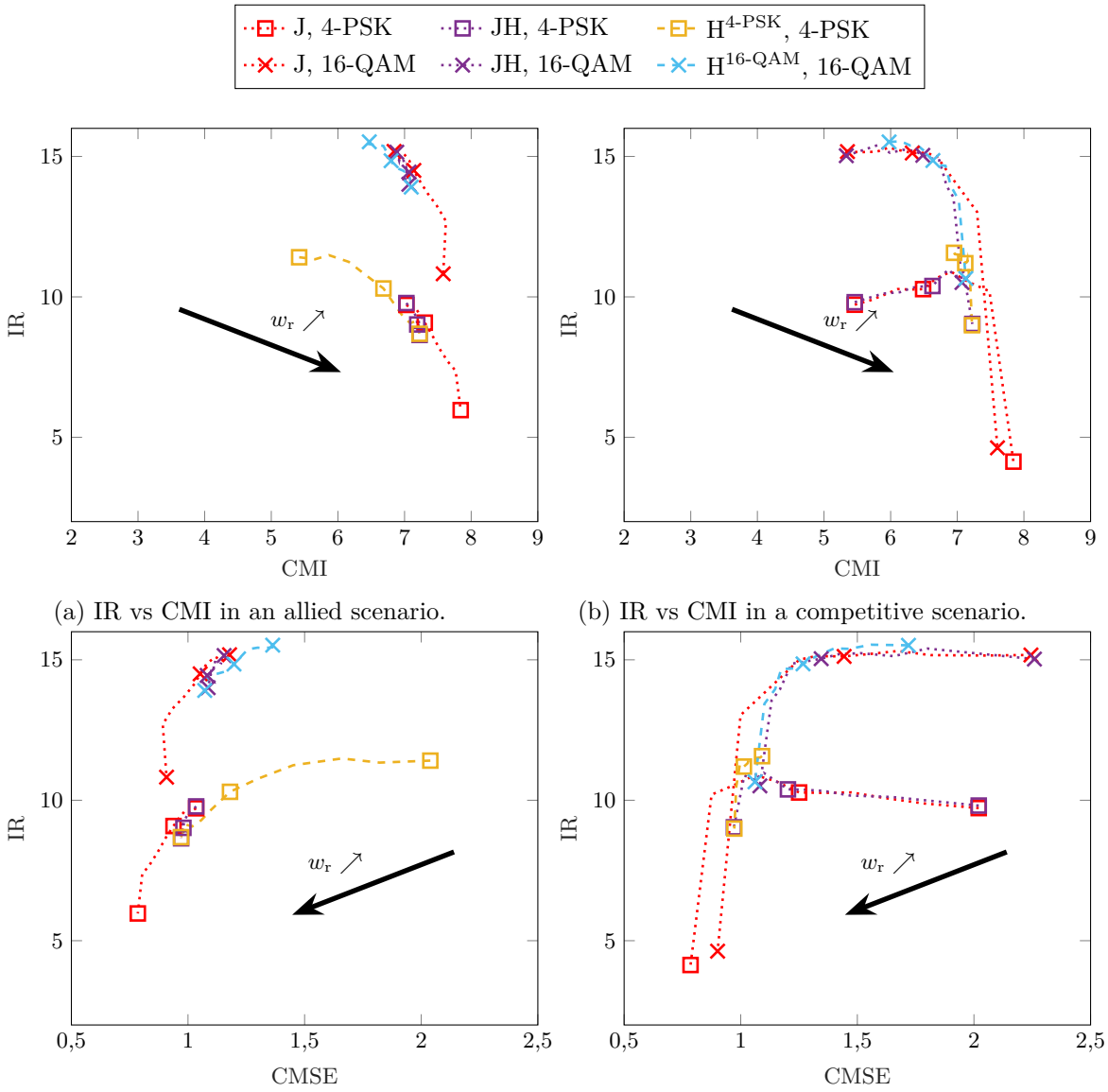
For a given constellation (either 4-PSK or 16-QAM), in our setting, the relative positioning of J and H remains similar. In the case of 16-QAM, the curves shift upward and to the right, a reflection of QAM's increased randomness, which benefits communication performance (IR) at the expense of radar estimation accuracy (CMSE).

4.4.3.4 Computational Complexity

In addition to performance, J offers a practical advantage regarding computational efficiency. It relies on a convex log-det formulation that can be quickly solved with standard solvers (e.g., CVX). Meanwhile, H requires iterative bisection and constellation-dependent evaluations, resulting in higher runtime and scalability issues, especially with large K or higher-order modulations like 16-QAM.

4.4.3.5 Performance summary

The results show that the proposed Hadamard- and Jensen-based approximations focus on complementary aspects of DFRC design. If radar performance is the main goal, it is preferable to ignore the discrete nature of the transmitted symbols and instead exploit the correlation structure of the radar channel subcarriers, as done in the Jensen-based approach J. On the



(a) IR vs CMI in an allied scenario.

(b) IR vs CMI in a competitive scenario.

(c) IR vs CMSE in an allied scenario.

(d) IR vs CMSE in a competitive scenario.

Figure 4.14: DFRC waveform design in selective radar ($\rho_r = .99e^{j2\pi/12}$) and communication channels. For $P_T = 0$ dB, the communication IR (3.3) is plotted as a function of radar CMI (3.1) and as a function of CMSE (3.4), forming a parametric curve with $w_r \in [0, 1]$. w_r increases from left to right for the IR-CMI curve and from right to left for the IR-CMSE curve, as shown by the black arrow. Two scenarios are considered, differing in the level of subcarrier competition between radar and communication: allied (com #1) vs competitive (com #2).

other hand, if the goal is to maximize communication performance (IR), the Hadamard-based method H is more suitable, especially in moderate-power regimes. This is because H accounts for the discreteness of the transmitted symbols, even though it ignores radar subcarrier correlations. However, this improved performance comes comes at the cost of significantly higher computational complexity. Overall, these results offer practical guidance for designing DFRC systems.

Nonetheless, in both allocations, the usual WF policy, where stronger channels receive more power, is not strictly followed. This was shown in this section with the H strategy and also seen in Section 4.2 with OPT-G, radar subcarriers that are highly correlated with stronger ones are often not given power. Moreover, as shown in this section, the IR-saturation phenomenon captured by H can lead to unexpected behaviors in DFRC regimes. For instance, an SNR-competitive scenario may achieve a better DFRC trade-off than an SNR-allied one. Therefore, such effects need to be carefully studied for each specific scenario.

Finally, to the best of our knowledge, there is currently no practical method that considers both symbol discreteness and radar subcarrier correlation at the same time. Developing such a waveform design would allow for a truly optimal DFRC trade-off.

4.5 Chapter summary

This chapter provided a detailed comparative analysis of the power allocation strategies in OFDM-DFRC systems that we proposed in Chapter 3, emphasizing their impact on radar estimation accuracy and communication information rate across diverse operating scenarios. Section 4.1 outlined the simulation setup and parameters, highlighting the influence of radar channel correlation and the alignment of radar and communication subcarriers.

In Section 4.2, we focused on Gaussian-modeled symbols for solving optimization problems introduced in Section 3.2. We introduced three power allocation strategies: our proposed Jensen-based J and Jensen–Hadamard-based JH, and the EQ baseline (4.3). We analyzed their behavior under communication-only, radar-only, and joint DFRC scenarios. Notably, the J strategy exploited radar subcarrier correlation to outperform JH at moderate power levels, particularly in radar-only configurations. In general, J and JH always outperform EQ (4.3) when they are not equal to it. Moreover, the DFRC performance depended heavily on the alignment (allied vs competitive) between radar and communication per-subcarrier SNRs.

In Section 4.3, we studied the effect of symbol randomness on radar estimation accuracy and the performance of our DFRC system. Using PSK, QAM, and Gaussian constellations, we evaluated the radar CMI and CMSE. We showed that, in the radar-only regime, constant-modulus symbols such as PSK do not degrade radar estimation compared to deterministic waveforms; they achieve the same performance. In DFRC scenarios, transmitting random symbols induces some loss; however, PSK degrades radar performance less than non-constant-modulus symbols (e.g., QAM, Gaussian). We noted the opposite effect of the communication

IR when used in DFRC systems, as the latter prefers high randomness modulations compared to radars.

Section 4.4 extended the analysis to discrete constellations at the design stage, comparing a Jensen-based power allocation strategy tailored for Gaussian symbols (J) and a Hadamard-based allocation strategy for discrete symbols (H). When radar performance dominates, exploiting subcarrier correlation using the J power allocation is more effective than modeling symbol discreteness. For communication-only settings, accounting for the real discrete constellation of the transmitted symbols by using the H allocation can improve the communication IR, but adds complexity and, as currently formulated in our design, ignores correlation between radar subcarriers.

Throughout the chapter, we emphasized how the interaction between waveform design, radar and communication channel characteristics, and symbol randomness governs DFRC system performance. These findings may support future work for waveform selection and power allocation in practical DFRC deployments.

Chapter 5

Extension of OFDM waveform design to multi-block scenarios with Doppler robustness

This chapter extends the MI-based OFDM-DFRC waveform design to practical conditions such as multiple OFDM blocks (radar sweeps) and by assuming radar scatterers experience Doppler shifts within a narrowband scenario. These practical conditions arise in scenarios with relative motion between transmitter and target. Building on the single-block, Doppler-free framework of Chapters 3 and 4, we analyze the impact of Doppler in a multi-block transmission on waveform optimization and on the radar MMSE estimation of the target response. We revisit the radar observation model for the multi-block case, derive the corresponding radar performance metrics, and identify conditions for extending the single-block power allocation optimization strategy to our new scenario. Finally, we address implementation aspects, including block-wise processing, and we assess robustness to Doppler mismatch through numerical simulations.

Contents

5.1 Doppler effects and multi-block scenarios 94
5.1.1 Radar performance metrics in multi-block scenarios 94
5.1.2 Block-wise estimation structure and fast implementation 96
5.2 CMI-based waveform optimization 97
5.2.1 Power allocation problem 98
5.2.2 Intractability and approximation 98
5.3 Performance study of the radar-only waveform 99
5.3.1 Simulation setup 99
5.3.2 Numerical results 100
5.4 Waveform robustness to Doppler mismatch 102
5.4.1 Doppler mismatch 102
5.4.2 Numerical results 104
5.5 Chapter summary 105

5.1 Doppler effects and multi-block scenarios

We now return to the general OFDM-DFRC model introduced in the system model chapter of the manuscript (see Section 2.1), which already accounts for M OFDM blocks (radar sweeps) and target-induced Doppler. In Chapters 3 and 4, we designed and analyzed waveforms in the simplified setting ($M = 1$ and $F_d = 0$). In this section, we lift these restrictions and consider $F_d \neq 0$ and $M \geq 1$ as required in practical DFRC scenarios. In practice, radar operates in dynamic environments where the target's relative motion induces Doppler shifts that must be considered in the waveform design stage; moreover, high-resolution radar systems often transmit multiple OFDM blocks to enhance estimation accuracy and robustness (multiple sweeps make the radar more robust because performance depends less on a single noisy, mismatched, or interfered measurement). Assuming a narrowband scenario, this section analyzes how the target's Doppler and multi-block transmission influence the performance of OFDM-DFRC waveforms, focusing on the radar performance metrics CMI and CMSE [98].

We briefly review the necessary background established in the system model chapter (see Section 2.1.3.2) to fix notation.

We adopt a narrowband scenario in which each target scatterer induces a constant normalized Doppler shift f_d identical across all subcarriers and blocks. Under these conditions, the radar received symbol vector in the frequency domain over M OFDM blocks is (see (2.28))

$$\tilde{\boldsymbol{x}}_{\mathrm{r}} = \boldsymbol{A}_{\mathrm{r}}\boldsymbol{h}_{\mathrm{r}} + \tilde{\boldsymbol{n}}_{\mathrm{r}},$$

where we recall that

- $\boldsymbol{A}_{\mathrm{r}}$ is the frequency-domain radar observation matrix that encapsulates both the waveform structure and the Doppler through $\boldsymbol{A}_{\mathrm{r}} = (\boldsymbol{I}_M \otimes \boldsymbol{F}_K \boldsymbol{R}_{\Delta_{\mathrm{CP}}})\boldsymbol{D}_{\boldsymbol{v}_{f_d}} \boldsymbol{S}\boldsymbol{P}_{\mathrm{r}}$ (2.29). We recall that $\boldsymbol{D}_{\boldsymbol{v}_{f_d}}$ is the diagonal Doppler shift matrix (2.13) and $\boldsymbol{S} = \text{Toeplitz}\{\boldsymbol{s}\}$ with $\boldsymbol{s}$ the transmitted signal (2.5);
- $\boldsymbol{h}_{\mathrm{r}}$ is the radar target response (2.17);
- $\tilde{\boldsymbol{n}}_{\mathrm{r}}$ denotes the AWGN vector in the frequency domain (2.26).

5.1.1 Radar performance metrics in multi-block scenarios

In this section, we restate the radar performance metrics used throughout—CMI and the CMSE of the MMSE estimator—within the multi-block narrowband-Doppler setting. These expressions were established earlier (see Section 2.2.2) and are gathered here for convenience. We evaluate whether Doppler shifts induced by the target's scatterers affect the quality of radar estimation and demonstrate that these expressions are Doppler-independent.

CMI expression. The radar CMI for the multi-block and narrowband Doppler case follows from the following expression (2.57):

$$\mathrm{CMI} = \mathcal{E}_{\boldsymbol{x}} \left\{ \log_2 \det \left(\boldsymbol{I}_{L_\mathrm{r}} + \sigma_{n_\mathrm{r}}^{-2} \boldsymbol{K}_{\boldsymbol{h}_\mathrm{r}} \boldsymbol{A}_\mathrm{r}^{\mathsf{H}} \boldsymbol{A}_\mathrm{r} \right) \right\} \tag{5.1}$$

with $\boldsymbol{K}_{\boldsymbol{h}_\mathrm{r}}$ the covariance matrix of the target response $\boldsymbol{h}_\mathrm{r}$ introduced in (2.17).

Minimum MSE and CMSE expressions. We assume the radar receiver has complete knowledge of the transmitted symbols $\boldsymbol{x}$. Therefore, $\boldsymbol{x}$ does not need to be estimated or marginalized when estimating the target. We also assume the radar receiver has perfect knowledge of the target Doppler (e.g., from a pre-detection stage). Consequently, the observation matrix $\boldsymbol{A}_\mathrm{r}$ in (2.29), which embeds both the transmitted symbols and the Doppler, is known at the radar receiver. The conventional MMSE estimator of the target response $\boldsymbol{h}_\mathrm{r}$ given by (2.60)

$$\begin{aligned} \boldsymbol{h}_\mathrm{r}^{\mathrm{MMSE}} &\triangleq \arg\min_{\hat{\boldsymbol{h}}_\mathrm{r}} \mathcal{E}_{\boldsymbol{h}_\mathrm{r}|\boldsymbol{x}} \left\{ \left\| \boldsymbol{h}_\mathrm{r} - \hat{\boldsymbol{h}}_\mathrm{r} \right\|^2 \right\} \\ &= \sigma_{n_\mathrm{r}}^{-2} \left(\boldsymbol{K}_{\boldsymbol{h}_\mathrm{r}}^{-1} + \sigma_{n_\mathrm{r}}^{-2} \boldsymbol{A}_\mathrm{r}^{\mathsf{H}} \boldsymbol{A}_\mathrm{r} \right)^{-1} \boldsymbol{A}_\mathrm{r}^{\mathsf{H}} \tilde{\boldsymbol{x}}_\mathrm{r}. \end{aligned}$$

We recall here that the corresponding CMSE of the MMSE estimator is given by (2.61)

$$\mathrm{CMSE} = \mathcal{E}_{\boldsymbol{x}} \left\{ \mathrm{Tr} \left\{ \left(\boldsymbol{K}_{\boldsymbol{h}_\mathrm{r}}^{-1} + \sigma_{n_\mathrm{r}}^{-2} \boldsymbol{A}_\mathrm{r}^{\mathsf{H}} \boldsymbol{A}_\mathrm{r} \right)^{-1} \right\} \right\}. \tag{5.2}$$

5.1.1.1 Doppler independence in radar CMI and CMSE

We now state a key result showing that the Doppler term cancels in $\boldsymbol{A}_\mathrm{r}^{\mathsf{H}} \boldsymbol{A}_\mathrm{r}$, leading to Doppler-independent radar performance metrics.

Lemma 7. *Under the narrowband Doppler assumption, the matrix $\boldsymbol{A}_\mathrm{r}^{\mathsf{H}} \boldsymbol{A}_\mathrm{r}$ can be simplified and rewritten as*

$$\boldsymbol{A}_\mathrm{r}^{\mathsf{H}} \boldsymbol{A}_\mathrm{r} = \boldsymbol{P}_\mathrm{r}^{\mathsf{H}} \boldsymbol{S}^{\mathsf{H}} (\boldsymbol{I}_M \otimes \boldsymbol{R}_{\Delta_{\mathrm{CP}}}^{\mathsf{H}} \boldsymbol{R}_{\Delta_{\mathrm{CP}}}) \boldsymbol{S} \boldsymbol{P}_\mathrm{r}. \tag{5.3}$$

One can clearly see that the Doppler term disappeared from the above expression. Hence, under the narrowband Doppler assumption, the matrix $\boldsymbol{A}_\mathrm{r}^{\mathsf{H}} \boldsymbol{A}_\mathrm{r}$ is independent of Doppler.

Proof. Doppler appears in $\boldsymbol{A}_\mathrm{r}$ via the diagonal Doppler matrix $\boldsymbol{D}_{\boldsymbol{v}_{f_d}}$, which introduces frequency shifts across time indices. However, when forming $\boldsymbol{A}_\mathrm{r}^{\mathsf{H}} \boldsymbol{A}_\mathrm{r}$, the phase terms introduced by $\boldsymbol{D}_{\boldsymbol{v}_{f_d}}$ cancel upon multiplication by their conjugate transpose. This result follows from the narrowband assumption, which models Doppler as a pure frequency shift. Hence, using (2.29), we first develop the Hermitian product of interest:

$$\begin{aligned} \boldsymbol{A}_\mathrm{r}^{\mathsf{H}} \boldsymbol{A}_\mathrm{r} &= \boldsymbol{P}_\mathrm{r}^{\mathsf{H}} \boldsymbol{S}^{\mathsf{H}} \boldsymbol{D}_{\boldsymbol{v}_{f_d}}^{\mathsf{H}} (\boldsymbol{I}_M \otimes \boldsymbol{R}_{\Delta_{\mathrm{CP}}}^{\mathsf{H}} \boldsymbol{R}_{\Delta_{\mathrm{CP}}}) \boldsymbol{D}_{\boldsymbol{v}_{f_d}} \boldsymbol{S} \boldsymbol{P}_\mathrm{r} \\ &= \boldsymbol{P}_\mathrm{r}^{\mathsf{H}} \boldsymbol{S}^{\mathsf{H}} \boldsymbol{D}_{\boldsymbol{v}_{f_d}}^{\mathsf{H}} \boldsymbol{D}_{\boldsymbol{v}_{f_d}} (\boldsymbol{I}_M \otimes \boldsymbol{R}_{\Delta_{\mathrm{CP}}}^{\mathsf{H}} \boldsymbol{R}_{\Delta_{\mathrm{CP}}}) \boldsymbol{S} \boldsymbol{P}_\mathrm{r} \end{aligned}$$

where, in the last line, we have noticed that $\boldsymbol{R}_{\Delta_{\mathrm{CP}}}^{\mathsf{H}}\boldsymbol{R}_{\Delta_{\mathrm{CP}}} = [\boldsymbol{0}_{\Delta_{\mathrm{CP}},L}; \boldsymbol{0}_{K,\Delta_{\mathrm{CP}}}, \boldsymbol{I}_K]$ is diagonal and used the commutativity of diagonal matrices. Observing that $\boldsymbol{D}_{\boldsymbol{v}_{f_d}}^{\mathsf{H}}\boldsymbol{D}_{\boldsymbol{v}_{f_d}} = \boldsymbol{I}_{LM}$ finally proves that $\boldsymbol{A}_{\mathrm{r}}^{\mathsf{H}}\boldsymbol{A}_{\mathrm{r}}$ has the form (5.3), independent of the Doppler frequency f_d. □

Under the narrowband Doppler assumption (constant frequency shift that is the same across all subcarriers), Lemma 7 implies that the radar CMSE (5.2) and CMI (2.57) are invariant to Doppler shifts. Intuitively, this can be explained because Doppler is a constant phase rotation per sample within each block in the narrowband model, so energy terms (norms of received signals) are unaffected provided the radar receiver perfectly compensates for the true Doppler shift. From an optimization perspective, this invariance means that the CMI-based waveform design problem does not depend on the target Doppler, simplifying the power allocation design process. However, for radar estimation (i.e., the MMSE of the target estimate (2.60)), perfect knowledge of the target Doppler is still required at the receiver in order to correctly compensate the Doppler-induced phase rotations in $\boldsymbol{A}_{\mathrm{r}}^{\mathsf{H}}\tilde{\boldsymbol{x}}_{\mathrm{r}}$. In practice, this Doppler knowledge may be imperfect, which motivates the robustness analysis presented in Section 5.4.

5.1.2 Block-wise estimation structure and fast implementation

Exploiting the block structure of the CP-OFDM waveform is important for real-time DFRC processing and for reducing the computational complexity of the MMSE estimator. In this section, we show how a *well-designed* CP ensures the channel's circularity and enables a block-wise implementation of the MMSE estimator of the target response $\boldsymbol{h}_{\mathrm{r}}$.

5.1.2.1 Block-wise estimation structure

In practice, the MMSE estimator (2.60) and its CMSE (5.2) can be implemented in an efficient way provided the CP is *well-designed*. For the block-wise implementation to be valid, the CP must be long enough to preserve circular convolution within each block and the absence of inter-block-interference. The condition is formalized in Definition 2.1.1.
In that case, removing each block's first Δ_{CP} samples in (2.28) allows block-wise processing, as formalized in the following lemma.

Lemma 8. *Under the* well-designed *CP condition (Definition 2.1.1), the expression for* $\boldsymbol{A}_{\mathrm{r}}^{\mathsf{H}}\boldsymbol{A}_{\mathrm{r}}$ *in* (5.3) *simplifies to*

$$\boldsymbol{A}_{\mathrm{r}}^{\mathsf{H}}\boldsymbol{A}_{\mathrm{r}} = \boldsymbol{B}_{\mathrm{r}}^{\mathsf{H}}\boldsymbol{D}_{\sum_{m=0}^{M-1}|\boldsymbol{x}_m|^2}\boldsymbol{B}_{\mathrm{r}} \tag{5.4}$$

where $\boldsymbol{B}_{\mathrm{r}}$ *is the position matrix in the subcarrier domain defined in* (2.35) *as:*

$$\boldsymbol{B}_{\mathrm{r}} \triangleq \sqrt{K}\boldsymbol{F}_K\boldsymbol{Q}_{\Delta_{\mathrm{CP}}}\boldsymbol{P}_{\mathrm{r},1} \tag{5.5}$$

In addition, we have:

$$\boldsymbol{A}_{\mathrm{r}}^{\mathsf{H}}\tilde{\boldsymbol{x}}_{\mathrm{r}} = \boldsymbol{B}_{\mathrm{r}}^{\mathsf{H}} \sum_{m=0}^{M-1} \boldsymbol{D}_{\boldsymbol{x}_m}^{\mathsf{H}} \boldsymbol{F}_K \boldsymbol{D}_{\boldsymbol{w}_{f_d}}^{\mathsf{H}} \boldsymbol{R}_{\Delta_{\mathrm{CP}}} \boldsymbol{y}_{\mathrm{r},m} e^{-j2\pi f_d m} \tag{5.6}$$

where $m \in 0, \ldots, M-1$ indexes the OFDM blocks and $\boldsymbol{y}_{\mathrm{r},m}$ is the mth L-length block of $\boldsymbol{y}_{\mathrm{r}}$ in (2.14) *and $\boldsymbol{w}_{f_d}$ is a length-K phase vector accounting for Doppler-induced shifts after CP removal and is defined as*

$$\boldsymbol{w}_{f_d} \triangleq [e^{2j\pi \frac{f_d}{L}\Delta_{\mathrm{CP}}}, \cdots, e^{2j\pi \frac{f_d}{L}(L-1)}]^{\mathsf{T}}. \tag{5.7}$$

Proof. The proof is provided in Chapter K. □

5.1.2.2 Complexity analysis

The expressions in (5.4)–(5.6) show that, under a *well-designed* CP, the block-wise structure enables most operations in the MMSE estimator (2.60) to be carried out in the frequency domain noting that (i) the transform $\boldsymbol{F}_K$ can be efficiently computed using the FFT algorithm, (ii) the Fourier transform for a single frequency (i.e., f_d) is rapidly computed, for instance, via the Goertzel algorithm [99], (iii) $\boldsymbol{Q}_{\Delta_{\mathrm{CP}}}$ (2.36) and $\boldsymbol{R}_{\Delta_{\mathrm{CP}}}$ (2.23) are selection matrices that extract the relevant coefficients, (iv) multiplying a vector by a diagonal matrix scales each vector element by the corresponding diagonal entry.

5.2 CMI-based waveform optimization

In this section, we build upon the MI-based optimal power allocation framework introduced in Chapter 3 (namely Problem OPT) and extend it to a more general setting that accounts for Doppler effects over multiple OFDM blocks. While the earlier formulation focused on the single-block, Doppler-free case, our objective here is to adapt and generalize it to the multi-block narrowband scenario under the Doppler assumption, i.e., where each scatterer induces a constant frequency shift f_d identical across all subcarriers K and blocks M.

We deliberately adopt a radar-only perspective: the optimization is performed solely on the radar performance metric, without introducing explicit constraints related to the communication system. This choice allows us to derive tractable formulations that enable efficient radar-only waveform design, while isolating and highlighting the impact of Doppler on the optimization problem.

5.2.1 Power allocation problem

The objective is to design a power allocation vector $\boldsymbol{p}$ that maximizes the radar CMI (5.1) across M blocks under a total transmitted power constraint P_{T}. We assume that the radar channel (i.e., the target covariance matrix) remains constant from block to block, so the same allocation $\boldsymbol{p}$ is applied identically to each transmitted OFDM block. Under the narrowband model, Doppler manifests as a block-wise phase rotation that cancels in the performance metrics. Consequently, the radar CMI is invariant to f_d, and we can use Doppler-free formulations in the objective function of our optimization problem. This extends the single-block Doppler-free framework of Section 3.1 to the multi-block radar-only setting.

Problem OPT-MR (Radar-only optimal power allocation for M blocks)**.**

$$\boldsymbol{p}^{(\mathrm{OPT-MR})} = \arg\max_{\boldsymbol{p}} \quad \mathcal{E}_{\boldsymbol{x}} \left\{ \log_2 \det \left(\boldsymbol{I}_{L_{\mathrm{r}}} + \sigma_{n_{\mathrm{r}}}^{-2} \boldsymbol{K}_{\boldsymbol{h}_{\mathrm{r}}} \boldsymbol{A}_{\mathrm{r}}^{\mathsf{H}} \boldsymbol{A}_{\mathrm{r}} \right) \right\} \tag{5.8}$$

$$\text{s.t.} \quad \sum_{k \in \mathcal{I}_K} p_k = P_{\mathrm{T}}, \tag{5.9}$$

$$\boldsymbol{p} \geq \boldsymbol{0}. \tag{5.10}$$

5.2.2 Intractability and approximation

Direct optimization of Problem OPT-MR with respect to the power allocation $\boldsymbol{p}$ is not feasible because of two main reasons. First, the observation matrix $\boldsymbol{A}_{\mathrm{r}}$ (2.29) depends on the random transmit symbol vector $\boldsymbol{x}$ through (2.5) and (2.29) in an intricate way. Second, the radar CMI (5.1) involves an expectation over a log-determinant function of the random input symbols $\boldsymbol{x}$. This structure generally lacks a closed-form solution for random transmitted symbols.

5.2.2.1 Structural simplification with a well-designed CP

A *well-designed* CP (Definition 2.1.1) guarantees that the channel convolution becomes circular within each block. This property enables the block-wise factorization of $\boldsymbol{A}_{\mathrm{r}}^{\mathsf{H}} \boldsymbol{A}_{\mathrm{r}}$ described in Lemma 8. In this case, the radar CMI reduces to

$$\mathrm{CMI} = \mathcal{E}_{\boldsymbol{x}} \left\{ \log_2 \det \left(\boldsymbol{I}_{L_{\mathrm{r}}} + \sigma_{n_{\mathrm{r}}}^{-2} \boldsymbol{K}_{\boldsymbol{h}_{\mathrm{r}}} \boldsymbol{B}_{\mathrm{r}}^{\mathsf{H}} \boldsymbol{D}_{\sum_{m=0}^{M-1} |\boldsymbol{x}_m|^2} \boldsymbol{B}_{\mathrm{r}} \right) \right\}. \tag{5.11}$$

Here, $\boldsymbol{D}_{\sum_{m=0}^{M-1} |\boldsymbol{x}_m|^2}$ denotes a diagonal matrix whose kth diagonal entry equals the total transmit energy allocated to subcarrier k across all M blocks, i.e., $\sum_{m=0}^{M-1} |x_{k,m}|^2$. This block-diagonal structure simplifies the expression of the radar CMI (5.1), but the expectation over $\boldsymbol{x}$ remains intractable.

5.2.2.2 Jensen's approximation

In the single-block case, Jensen's inequality was shown in Section 3.2 to provide a tractable approximation for the radar CMI. The same challenge arises here: the multi-block radar CMI in (5.11) remains analytically intractable. Since the log-determinant is concave, Jensen's inequality (3.12) can be applied to the multi-block radar CMI (5.11) yielding

$$\mathrm{CMI} \leq \log_2 \det\left(\boldsymbol{I}_{L_\mathrm{r}} + \sigma_{n_\mathrm{r}}^{-2}\boldsymbol{K}_{\boldsymbol{h}_\mathrm{r}}\boldsymbol{B}_\mathrm{r}^{\mathsf{H}}\boldsymbol{D}_{M\boldsymbol{p}}\boldsymbol{B}_\mathrm{r}\right) = \log_2 \det\left(\boldsymbol{I}_{L_\mathrm{r}} + M\sigma_{n_\mathrm{r}}^{-2}\boldsymbol{K}_{\boldsymbol{h}_\mathrm{r}}\boldsymbol{B}_\mathrm{r}^{\mathsf{H}}\boldsymbol{D}_{\boldsymbol{p}}\boldsymbol{B}_\mathrm{r}\right), \tag{5.12}$$

where $\mathcal{E}\left\{|x_{m,k}|^2\right\} = p_k$ denotes the power on subcarrier k. We recall that for each block m, the power p_k allocated to subcarrier k remains the same (see Section 2.1.1.3).

Hence, the radar-only power allocation problem based on Jensen's inequality for M blocks can be written as follows.

Problem J-R (Radar-only suboptimal power allocation based on Jensen's inequality for M blocks)**.**

$$\boldsymbol{p}^{(\mathrm{J-R})} = \arg\max_{\boldsymbol{p}} \quad \log_2 \det\left(\boldsymbol{I}_{L_\mathrm{r}} + M\sigma_{n_\mathrm{r}}^{-2}\boldsymbol{K}_{\boldsymbol{h}_\mathrm{r}}\boldsymbol{B}_\mathrm{r}^{\mathsf{H}}\boldsymbol{D}_{\boldsymbol{p}}\boldsymbol{B}_\mathrm{r}\right) \tag{5.13}$$

$$\text{s.t.} \quad \sum_{k\in\mathcal{I}_K} p_k = P_\mathrm{T}, \tag{5.14}$$

$$\boldsymbol{p} \geq \boldsymbol{0}. \tag{5.15}$$

Under a *well-designed* CP, Problem J-R is structurally identical to the single-block Doppler-free Jensen formulation (Problem prob:optimal-problem-gauss-jensen with $w_\mathrm{r} = 1$), except that the total transmitted power is scaled by M. This equivalence implies that all solution methods and properties derived in the single-block case apply here directly. In practice, Problem J-R can be solved efficiently using convex optimization tools such as CVX [88, 89].

5.3 Performance study of the radar-only waveform

Having derived a tractable Jensen-based formulation for the radar-only power allocation problem denoted J-R, we now validate its performance through numerical simulations and compare its performance against standard baseline approaches such as equal-power allocation.

5.3.1 Simulation setup

We now evaluate the proposed radar-only power allocation strategy for an OFDM-DFRC system with M sweeps in the presence of radar Doppler effects. The simulation parameters are identical to those summarized in Table 4.1. The normalized Doppler frequency is set to

$f_d = 2/M$. The target covariance matrix adopts the same structure as the one introduced in Chapter 3 and is defined in (4.1). We recall that the corresponding target covariance matrix in the subcarrier domain is given by (2.38):

$$\boldsymbol{K}_{\boldsymbol{g}_\mathrm{r}} = M\boldsymbol{B}_\mathrm{r}\boldsymbol{K}_{\boldsymbol{h}_\mathrm{r}}\boldsymbol{B}_\mathrm{r}^\mathsf{H}.$$

This matrix defines "the radar channel in the subcarrier domain", $\sigma_{n_\mathrm{r}}^{-2}\boldsymbol{K}_{\boldsymbol{g}_\mathrm{r}}$, whose diagonal entries correspond to per-subcarrier radar SNRs, while off-diagonal terms capture inter-subcarrier correlations (see Definition 2.1.2). From the structure of $\boldsymbol{K}_{\boldsymbol{g}_\mathrm{r}}$, it can be observed that, for any value of M, the subcarriers offering the highest radar SNRs as well as those exhibiting the strongest inter-subcarrier correlations remain unchanged. This is because $\boldsymbol{K}_{\boldsymbol{g}_\mathrm{r}}$ scales linearly with the number of radar sweeps M, i.e., each element is multiplied by M without altering the underlying correlation pattern. The radar channel for $M = 1$ was already shown in Figure 4.1b, while the corresponding channels for $M = 16$ and $M = 128$ are illustrated in Figure 5.1.

5.3.2 Numerical results

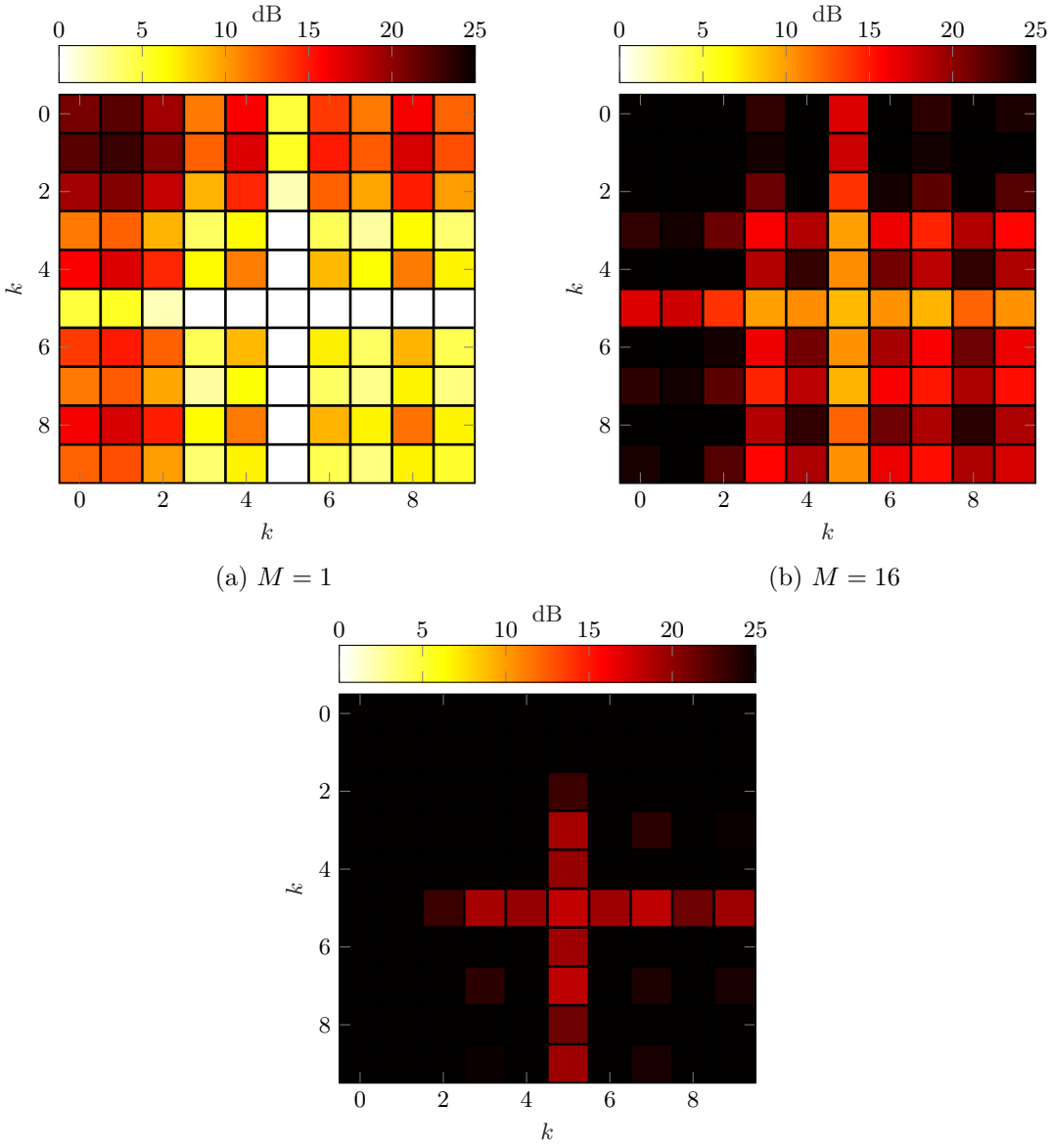
The goal of this section is to investigate the influence of the number of transmitted blocks M on radar performance, and in particular to assess the gain obtained when extending beyond the single-block case ($M = 1$). As a reference, we also display the EQ baseline (4.3) alongside the radar-only Jensen-based allocation (Problem J-R). Radar performance is evaluated using two metrics: the radar CMI (5.1), which measures the information content of the received signal, and the CMSE (5.2), which evaluates estimation accuracy.

We investigate how the optimal radar-only allocation adapts to the available transmit power when multiple OFDM blocks (M sweeps) are transmitted. In particular, we evaluate the behavior predicted by Problem J-R, namely that subcarriers with higher radar SNRs should be prioritized at low power, while the allocation gradually spreads across more subcarriers as MP_T increases.

We consider a radar-only scenario and solve Problem J-R for different values of M. The resulting allocations, shown in Figure 5.2, demonstrate how the power profile varies with the total transmitted power MP_T:

- at very low MP_T, only the subcarrier with the highest SNR is illuminated [#1] (e.g., $M = 1$);
- for moderate MP_T, power progressively extends to other strong subcarriers, except those highly correlated with already-illuminated ones [#(0,1,2,9)] (e.g., $M = 16$);
- at high MP_T, the allocation J-R converges toward equal-power across all subcarriers (e.g., $M = 128$).

These observations are consistent with the single-block results of Section 3.2, where varying



(a) $M = 1$

(b) $M = 16$

(c) $M = 128$

Figure 5.1: Radar channel in the subcarrier domain: modulus of $M\sigma_{n_\mathrm{r}}^{-2}\boldsymbol{B}_\mathrm{r}\boldsymbol{K}_{\boldsymbol{h}_\mathrm{r}}\boldsymbol{B}_\mathrm{r}^\mathsf{H}$ for $M \in \{1, 16, 128\}$. Radar subcarriers with SNR in decreasing order are [#(1,0,2,8,4,6,9,3,7,5)]. Note that subcarriers [#4] and [#8] are highly correlated with subcarriers [#(0,1,2)].

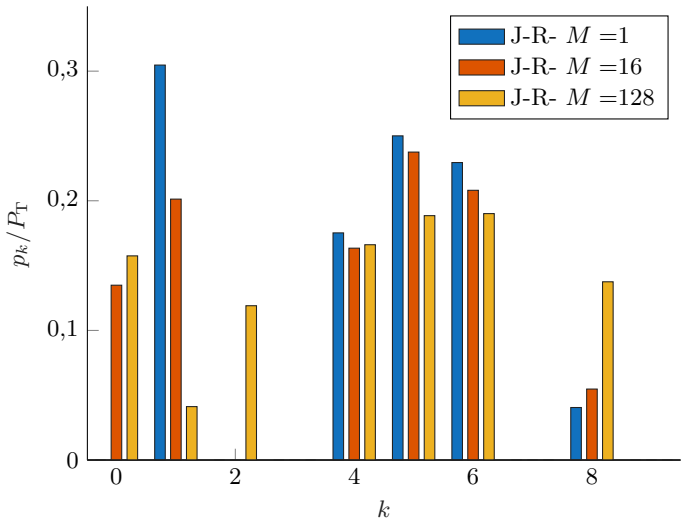


Figure 5.2: Radar-only waveform design with a frequency-selective radar channel with M sweeps in the presence of radar Doppler. Normalized power allocations p_k/P_T for J-R strategy are shown at the total transmit power: $P_\mathrm{T} = -8$ dB and for $M \in \{1, 16, 128\}$.

P_T produces the same trends. The J-R allocation adapts to the radar channel according to the available power MP_T. As seen in Figure 5.3, it leads to a higher CMI and lower CMSE than the EQ allocation (4.3), particularly for small MP_T. For high MP_T, the J-R allocation converges to an EQ allocation and thus tends to perform similarly. Finally, increasing MP_T augments the CMI and lowers the CMSE for both allocations.

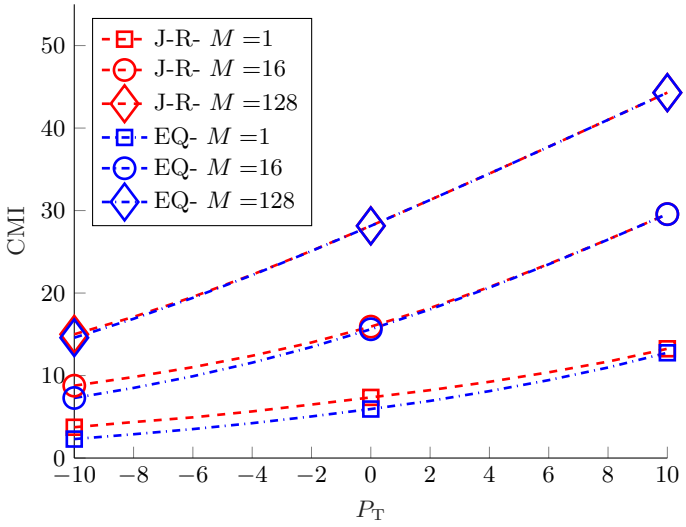
In summary, the optimized allocation J-R enhances the information the received radar signal shares with the target's response and the estimation performance, with the most significant gains observed at low and moderate transmitted power.

5.4 Waveform robustness to Doppler mismatch

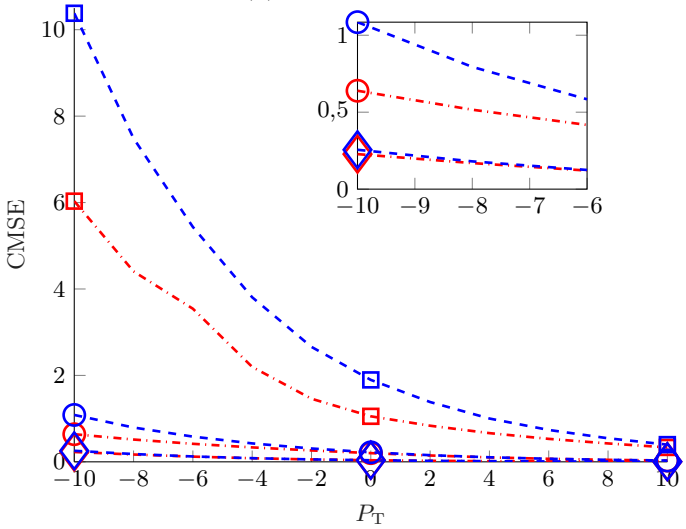
The previous simulations assumed that the radar receiver has perfect knowledge of the target Doppler—in particular for computing the MMSE estimator of the target response (see Section 5.1.1). In practice, however, Doppler estimates at the receiver may be imperfect. This section aims to investigate the robustness of the proposed power allocation strategy when Doppler mismatches occur and quantify the resulting impact on radar estimation performance.

5.4.1 Doppler mismatch

We investigate the robustness of the radar-only Jensen-based allocation J-R when the Doppler frequency used in the receiver processing is slightly mismatched from the actual target



(a) Radar CMI



(b) Radar CMSE

Figure 5.3: Radar-only waveform design with $w_{\mathrm{r}} = 1$ assuming a frequency-selective radar channel with M sweeps in the presence of radar Doppler. Radar CMI and CMSE values computed via Monte Carlo integration with $M_{\mathrm{c}} = 5E3$ runs. Curves are shown for J-R and EQ (4.3) strategies.

Doppler.

In practice, the target's Doppler frequency estimated at the pre-detection stage, denoted $\bar{f}_d$, may differ slightly from the true target Doppler f_d. We define the Doppler mismatch δ_{f_d} as:

$$\delta_{f_d} \triangleq \bar{f}_d - f_d.$$

The corresponding mismatched MMSE estimator is

$$\bar{\boldsymbol{h}}_{\mathrm{r}}^{\mathrm{MMSE}} = \sigma_{n_{\mathrm{r}}}^{-2} \left(\boldsymbol{K}_{\boldsymbol{h}_{\mathrm{r}}}^{-1} + \sigma_{n_{\mathrm{r}}}^{-2} \boldsymbol{A}_{\mathrm{r}}^{\mathsf{H}} \boldsymbol{A}_{\mathrm{r}} \right)^{-1} \bar{\boldsymbol{A}}^{\mathsf{H}} \tilde{\boldsymbol{x}}_{\mathrm{r}} \tag{5.16}$$

with

$$\bar{\boldsymbol{A}} \triangleq (\boldsymbol{I}_M \otimes \boldsymbol{F}_K \boldsymbol{R}_{\Delta_{\mathrm{CP}}}) \boldsymbol{D}_{\boldsymbol{v}(\bar{f}_d)} \boldsymbol{S} \boldsymbol{P}_{\mathrm{r}} \tag{5.17}$$

and where we have used $\bar{\boldsymbol{A}}^{\mathsf{H}} \bar{\boldsymbol{A}} = \boldsymbol{A}_{\mathrm{r}}^{\mathsf{H}} \boldsymbol{A}_{\mathrm{r}}$ according to Lemma 7, which allows simplifying later performance analysis.

Our simulation results indicate that, for small Doppler mismatches δ_{f_d}, the estimation loss endured by (5.16) compared to (2.60) remains moderate for the modulus and relative phases of its elements. Nonetheless, a residual phase remains on all its elements and equals the rotation induced by δ_{f_d} at mid-transmission.
To explain this, we neglect the noise in (2.28), so the mismatched estimator (5.16) becomes roughly

$$\bar{\boldsymbol{h}}_{\mathrm{r}}^{\mathrm{MMSE}} \approx \sigma_{n_{\mathrm{r}}}^{-2} \left(\boldsymbol{K}_{\boldsymbol{h}_{\mathrm{r}}}^{-1} + \sigma_{n_{\mathrm{r}}}^{-2} \boldsymbol{A}_{\mathrm{r}}^{\mathsf{H}} \boldsymbol{A}_{\mathrm{r}} \right)^{-1} \bar{\boldsymbol{A}}^{\mathsf{H}} \boldsymbol{A}_{\mathrm{r}} \boldsymbol{h}_{\mathrm{r}}.$$

Assuming δ_{f_d} is small and induces an averaged constant phase rotation, $\bar{\boldsymbol{A}}^{\mathsf{H}} \boldsymbol{A}_{\mathrm{r}}$ can be approximated by a constant phase factor

$$\bar{\boldsymbol{A}}^{\mathsf{H}} \boldsymbol{A}_{\mathrm{r}} \approx e^{-j2\pi \frac{\delta_{f_d}}{L} \frac{LM}{2}} \boldsymbol{A}_{\mathrm{r}}^{\mathsf{H}} \boldsymbol{A}_{\mathrm{r}}$$

which leads to

$$\bar{\boldsymbol{h}}_{\mathrm{r}}^{\mathrm{MMSE}} \approx e^{-j\pi\delta_{f_d} M} \boldsymbol{h}_{\mathrm{r}}^{\mathrm{MMSE}}. \tag{5.18}$$

Hence, a small Doppler mismatch introduces mainly a phase rotation $e^{-j\pi\delta_{f_d} M}$, without significantly altering the magnitude structure of the estimate.

In practice, the residual phase $-\pi\delta_{f_d} M$ may be of no interest in terms of estimation performance but still increases drastically the MSE.
To isolate the effect of Doppler mismatch (5.16), we define a modified CMSE as

$$\overline{\mathrm{CMSE}} \triangleq \mathcal{E}_{\boldsymbol{x}} \left\{ \mathcal{E}_{\boldsymbol{h}_{\mathrm{r}}|\boldsymbol{x}} \left\{ \left\| \boldsymbol{h}_{\mathrm{r}} - e^{j\pi\delta_{f_d} M} \bar{\boldsymbol{h}}_{\mathrm{r}}^{\mathrm{MMSE}} \right\|^2 \right\} \right\} \tag{5.19}$$

which compensates for the global phase shift in (5.18). Thus, $\overline{\mathrm{CMSE}}$ can be seen as a metric to separate the meaningful estimation performance degradation (magnitude) from this uninformative global phase rotation.

5.4.2 Numerical results

We now assess the robustness of CP-OFDM waveforms to Doppler mismatch δ_{f_d} that may arise at the pre-detection stage (see Section 5.4.1). The mismatch δ_{f_d} is kept below the length of one Doppler bin, consistent with practical pre-detection uncertainty.

Figure 5.4 compares the standard CMSE (5.2) (perfect Doppler knowledge) with the modified $\overline{\text{CMSE}}$ (5.19) (mismatched Doppler) for Gaussian symbols, using both the optimized allocation of Problem J-R and the EQ (4.3) baseline with $M = 16$, under three Doppler mismatch levels $\delta_{f_d} \in \{0, 1/8M, 1/4M\}$. As expected, CMSE (5.2) is always lower than $\overline{\text{CMSE}}$ (5.19) for $\delta_{f_d} > 0$. The degradation remains moderate for small mismatches.

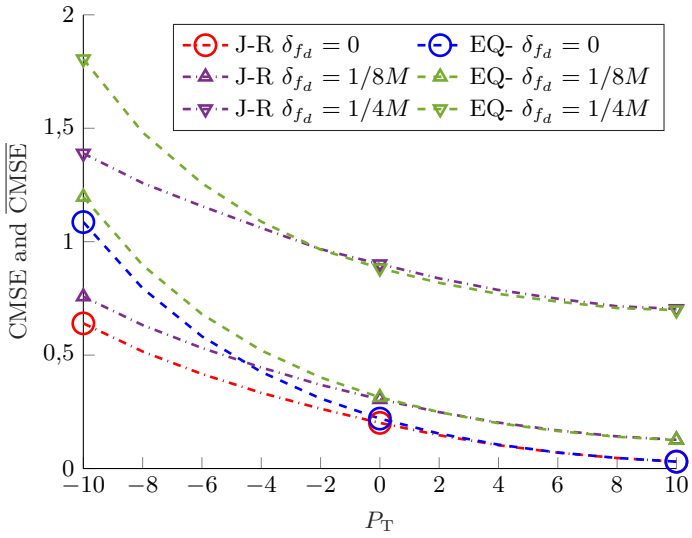


Figure 5.4: Comparison of CMSE (5.2) (perfect Doppler knowledge) and $\overline{\text{CMSE}}$ (5.19) (with Doppler mismatch) for Gaussian symbols, using J-R and EQ (4.3) power allocations with $M = 16$. Results are shown for different Doppler mismatches $\delta_{f_d} \in \{0, 1/8M, 1/4M\}$, with performance metrics estimated via Monte Carlo integration with $M_{\text{c}} = 10E4$ runs.

To further quantify the effect of Doppler mismatch, Figure 5.5 plots the difference $\overline{\text{CMSE}}-$ CMSE for $\delta_{f_d} \in \{1/8M, 1/4M\}$. The optimized allocation J-R is slightly more sensitive to mismatch, as it concentrates power on a few dominant subcarriers, but still provides superior estimation accuracy compared to EQ (4.3). For larger mismatches, however, both strategies will suffer severe degradation, highlighting the importance of accurate Doppler estimation.

5.5 Chapter summary

This chapter extended the MI-based waveform design for OFDM-DFRC systems to more realistic conditions, namely narrowband Doppler effects and multi-block transmission. In Section 5.1, we proved that under the narrowband assumption, both radar CMI and CMSE are invariant to target Doppler shifts. This invariance justifies reusing Doppler-free optimization strategies in narrowband Doppler scenarios.

Building on this invariance, a block-wise MMSE estimator was derived by using the circularity induced by a *well-designed* CP, enabling efficient FFT-based implementations well suited to real-time radar processing. The MI-based radar-only power allocation problem for a narrowband Doppler multi-block OFDM-DFRC scenario was then revisited. The intractabil-

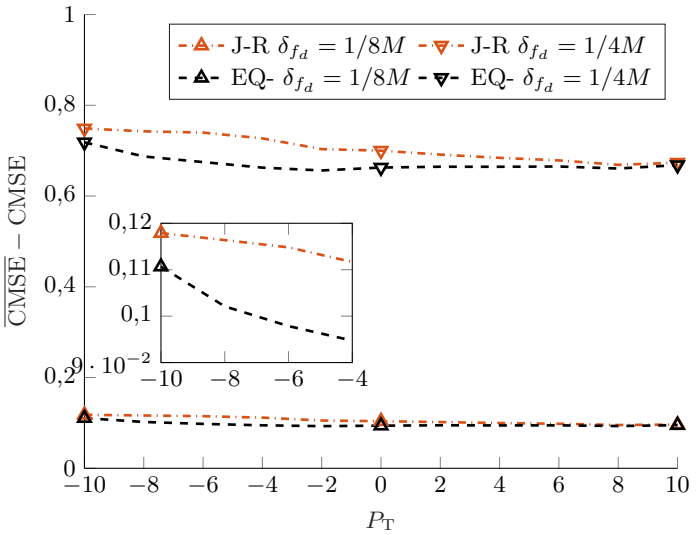


Figure 5.5: Difference $\overline{\text{CMSE}} - \text{CMSE}$, where CMSE is given by (5.2) (perfect Doppler knowledge) and $\overline{\text{CMSE}}$ by (5.19) (with Doppler mismatch), for Gaussian symbols under Doppler mismatch, comparing J-R and EQ (4.3) power allocations with $M = 16$. Results are shown for $\delta_{f_d} \in \{1/8M, 1/4M\}$. Performance metrics are obtained via Monte Carlo integration with $M_{\text{c}} = 10E4$ runs.

ity of directly maximizing the radar CMI was addressed through Jensen's inequality, leading to a convex formulation whose solution distributes power across subcarriers according to the radar channel structure, the number of OFDM blocks (or radar sweeps), and the total transmitted power.

Numerical simulations confirmed these theoretical insights. The proposed allocation strategy improved both radar CMI and CMSE compared to equal-power baselines at low and moderate transmit power, while naturally converging to equal-power performance in the high-power regime. Finally, robustness analysis demonstrated that the MMSE estimator was robust to small Doppler mismatches, which induce only a residual phase rotation and moderate CMSE degradation.

Overall, this chapter established both theoretical and numerical results supporting MI-based radar-only waveform design under Doppler and multi-block conditions for OFDM-DFRC systems.

Conclusion and future work

Conclusion

This PhD thesis aims to apply the MI framework for OFDM-based DFRC waveform design. In Chapter 2, we present the system model that specifies the transmit and receive signals including the assumptions on radar and communication channels, and the associated performance metrics, making all ingredients for the waveform design explicit. The core challenge we addressed is conceptual: conventional radar systems treat the transmitted waveform as deterministic, whereas communication requires random transmitted symbols. Combining the two concepts naively leads to inconsistencies and makes it harder to understand the design trade-offs. We resolved this by adopting radar CMI, which is the radar MI averaged over the possible realizations of the information-bearing transmitted symbols. This approach enables the evaluation of both radar and communication performance within a coherent information-theoretic framework, thereby restoring interpretability to the design objectives.

Building on that foundation, we develop an optimization approach for OFDM-DFRC by treating it as a power allocation problem in Chapter 3. The goal was to find the power profile of the joint transmitted waveform that maximizes a weighted sum of radar CMI and communication IR, the latter being also defined by an MI, under a total transmit power constraint. To overcome analytical intractability and address the complexity of the obtained problem, we first propose approximation strategies under Gaussian-input assumptions and then with practical discrete constellations, leading to closed-form solutions, numerical solutions or allocation profiles that can be interpreted as classic WF or MWF-like sometimes.

Within this framework, we also defined and quantified the "price of information", which refers to the loss in the radar estimation performance caused by transmitting information-bearing symbols. We provided practical options for users: constellation choice and weights between CMI and IR. This perspective enables us to clearly measure and adjust the trade-offs between radar and communication functions. We then moved beyond single-block OFDM models to incorporate elements essential in practical scenarios; we extended the optimization problem in Chapter 5 to handle target Doppler and multi-block (multi-sweep) waveform design in a narrowband radar-only scenario, preserving the same objective structure and solution pathway.

Throughout the thesis, simulation validated the proposed framework in Chapter 4 and Chapter 5. The power allocation strategies derived from the CMI–IR objective produced a trade-off frontier, and characterized how the trade-off point moves with the chosen weights, each channel's SNR and the degree of competition between radar and communication functions. Together, these results support an MI-based allocation formulation that is clear, interpretable, and practical for implementation.

Perspectives

While this thesis has primarily focused on theoretical analysis and optimization of MI-based DFRC waveform design, numerous complementary directions remain open. The following perspectives highlight potential ways for extending and applying this work in future studies.

Linking radar information and estimation. As a perspective, we can investigate the relationship between maximizing radar MI and minimizing radar MSE in our CP-OFDM framework. We will begin with deterministic transmitted symbols to establish clear baselines, then extend to random, information-bearing inputs suited to DFRC, using CMI and CMSE. In both regimes, we will pose power-constrained optimization problems (MI maximization and MSE minimization), seek closed-form structure where possible, and otherwise employ efficient iterative solvers with deeper analytical study as needed. Numerical experiments will map if and when MI- and MSE-optimal allocations coincide, quantify any gaps, and boil down the findings into practical design rules for OFDM-DFRC power allocation optimization, notably investigating whether the waveform that maximizes radar CMI also minimizes radar CMSE, as suggested by our numerical trends. This work is already underway.

Cognitive DFRC. In considering future research directions, it would be beneficial to explore a cognitive radar setup that moves beyond the assumption of a known covariance matrix for target responses. In this thesis, we modeled the radar target response as a zero-mean complex Gaussian vector with a *known* covariance matrix. In realistic scenarios, the second-order statistics of the target may be unknown or influenced by the environment. Transitioning to a cognitive framework that enables learning the target covariance online and adapting the radar waveform accordingly could yield significant advantages. In practice, this process follows the cognitive radar loop "sense, learn, and act" as introduced in the cognitive-radar literature [100]. In such a cognitive DFRC, the system would initialize with rough prior for the target covariance, such as an uncorrelated or structured model (e.g., Toeplitz). Then it could select an initial waveform or power allocation strategy, for instance, an equal-power allocation. After transmitting this waveform and receiving the echoes, the radar estimates the target response vector from the received data (as in this thesis). This estimated response provides empirical second-order information that can be used to update the covariance matrix estimate, either through a recursive averaging rule or via a Bayesian update using, for instance, an inverse-Wishart prior [101]. The updated covariance would represent the system's improved belief about the target statistics. Based on this refined covariance, the next waveform or power allocation profile would be computed by re-solving the same MI-based optimization problem developed in this thesis, balancing communication IR and radar CMI. This closes the cognitive loop as each new transmission is supposed to refine the model of the environment, and each refinement is supposed to lead to a power profile better adapted to our specific pre-detected target (in practice, estimation error and model mismatch would need to be accounted for). Over time, the system may converge to a stable point where both sensing accuracy and communication information rate are jointly optimized. This learning–control

structure could make the proposed DFRC framework adaptive and directly aligned with the principles of cognitive radar.

Hardware and implementation aspects. A natural continuation of this work is to validate the proposed DFRC framework under realistic hardware conditions. As a first step, we will implement a CP–OFDM-DFRC chain in a software-defined radio (SDR) testbed following the same power allocation and waveform design rules developed in this PhD work. The experiment will include (i) tests with real radar and communication channels (over-the-air), (ii) experiments with clutter-free conditions (e.g., using short-range line-of-sight and absorbers) and static channels, and (iii) comparisons between cooperative and allied scenarios configurations to assess performance limits. Second, we will investigate the impact of hardware impairments on system performance with emphasis on power amplifier nonlinearity. In particular, we will study how clipping[1] events degrade radar and communications performance [102]. Beyond the nonlinearities, we can also analyze the effect of oscillator phase noise which induces phase fluctuation across subcarriers on the performance of our waveform. These studies will quantify how such imperfections affect the joint CMI–IR trade-off. Third, we will address implementability: real-time complexity, update latency of the cognitive loop and coexistence constraints. Overall, this laboratory experiment will involve extensive development and validation.

Clutter-aware DFRC waveform design Another perspective is to treat clutter (i.e., the unwanted interference such as echoes from the environment) as part of the radar environment rather than ignore it. In this thesis, we assumed a radar scenario with only AWGN (see Section 2.1.2.1), we derived the corresponding radar CMI (3.1), and solved the power allocation problem using Jensen and/or Hadamard approximations. A simple extension is to assume the clutter is present and modeled as zero-mean circular complex Gaussian with a general (not necessarily diagonal) covariance matrix (which must be estimated); we can therefore explicitly model interference-plus-noise (clutter plus thermal noise) with its own covariance. In this setting, "the radar channel matrix in the subcarrier domain" that appears in the radar CMI (3.1) will be the target covariance matrix in the subcarrier domain (see Definition 2.1.2) pre-whitened with respect to the interference-plus-noise covariance matrix (i.e., the target covariance pre and post-multiplied by the inverse square root of the interference-plus-noise covariance matrix). With this change, the same approximation methods will still apply, but the interpretation will shift from a per-subcarrier SNR to a signal-to-interference-plus-noise view. This directly shapes how the radar power profile is spread across subcarriers (favoring regions with weaker clutter), while the communication system will continue to use its usual per-subcarrier communication SNR.

[1] An amplifier is said to be clipping when it cannot supply enough output power for large input signals, causing the signal peaks to be truncated.

Appendix A

CP-OFDM radar received symbols for a Doppler-free scenario

This appendix derives the expression of the radar received symbols in the CP-OFDM framework under the simplifying assumption of a Doppler-free scenario, providing the analytical basis for subsequent radar channel diagonalization.

A.1 Radar received-signal formulation

The received signal from radar echoes when $f_d = 0$ (2.15) is given by

$$\boldsymbol{y}_{\mathrm{r}} = \boldsymbol{S}\boldsymbol{P}_{\mathrm{r}}\boldsymbol{h}_{\mathrm{r}} + \boldsymbol{n}_{\mathrm{r}} \tag{A.1}$$

where $\boldsymbol{S} = \text{Toeplitz}\{\boldsymbol{s}\}$ (see (2.16)). $\boldsymbol{P}_{\mathrm{r}}$ is the binary matrix indicating the scatterers' position defined in (2.12).

We now exploit the structure induced by the well-designed-CP assumptions. Every scatterer delay lies in the interval $0, \ldots, L-1$, where L denotes the useful symbol length. As a consequence, the entries of the vector $\boldsymbol{P}_r\boldsymbol{h}_{\mathrm{r}}$ associated with delays outside this range are equal to zero, and the corresponding columns of $\boldsymbol{P}_r$ have no effect after multiplication by S. For this reason, we keep only the columns of $\boldsymbol{P}_{\mathrm{r}}$ associated with delays $0, \ldots, L-1$ and group them into the reduced matrix $\boldsymbol{P}_{\mathrm{r},1}$. The remaining columns do not affect the received signal and can be removed. Hence, in all subsequent derivations, we replace $\boldsymbol{P}_{\mathrm{r}}$ by its effective version $\boldsymbol{P}_{\mathrm{r},1}$ defined in (2.37), which restricts the model to the active channel support. With this reduction, we obtain

$$\boldsymbol{S}\boldsymbol{P}_{\mathrm{r}} = \begin{pmatrix} \boldsymbol{S}_0\boldsymbol{P}_{\mathrm{r},1} \\ \vdots \\ \boldsymbol{S}_{M-1}\boldsymbol{P}_{\mathrm{r},1} \end{pmatrix} \tag{A.2}$$

with

$$\boldsymbol{S}_m \triangleq [\boldsymbol{S}]_{mL \le i \le (m+1)L-1, 1 \le j \le L}. \tag{A.3}$$

A.2 Frequency-domain radar symbols

We recall that the radar receiver processes the received time-domain signal using CP removal and a DFT. Hence, using (2.22), the receiver radar symbols are given:

$$\tilde{\boldsymbol{x}}_{\mathrm{r}} = (\boldsymbol{I}_M \otimes \boldsymbol{F}_K \boldsymbol{R}_{\Delta_{\mathrm{CP}}}) \boldsymbol{y}_{\mathrm{r}} \tag{A.4}$$

$$= (\boldsymbol{I}_M \otimes \boldsymbol{F}_K \boldsymbol{R}_{\Delta_{\mathrm{CP}}}) \left(\boldsymbol{S}\boldsymbol{P}_{\mathrm{r}} \boldsymbol{h}_{\mathrm{r}} + \boldsymbol{n}_{\mathrm{r}}\right). \tag{A.5}$$

The latter simplifies to

$$\tilde{\boldsymbol{x}}_{\mathrm{r}} = \begin{pmatrix} \boldsymbol{F}_K \boldsymbol{R}_{\Delta_{\mathrm{CP}}} \boldsymbol{S}_0 \boldsymbol{P}_{\mathrm{r},1} \\ \vdots \\ \boldsymbol{F}_K \boldsymbol{R}_{\Delta_{\mathrm{CP}}} \boldsymbol{S}_{M-1} \boldsymbol{P}_{\mathrm{r},1} \end{pmatrix} \boldsymbol{h}_{\mathrm{r}} + \tilde{\boldsymbol{n}}_{\mathrm{r}}.$$

Let us denote $\boldsymbol{s}_m$ the mth L-length block of $\boldsymbol{s}$ in (2.5), i.e.,

$$\boldsymbol{s}_m = \boldsymbol{T}_{\Delta_{\mathrm{CP}}} \boldsymbol{F}_K^{\mathsf{H}} \boldsymbol{x}_m. \tag{A.6}$$

Considering now a well-designed CP (see Definition 2.1.1) leads to, for $m \in \mathcal{I}_M$:

$$\boldsymbol{F}_K \boldsymbol{R}_{\Delta_{\mathrm{CP}}} \boldsymbol{S}_m \boldsymbol{P}_{\mathrm{r},1} = \boldsymbol{F}_K \operatorname{circ}\left\{\boldsymbol{R}_{\Delta_{\mathrm{CP}}} \boldsymbol{s}_m\right\} \boldsymbol{Q}_{\Delta_{\mathrm{CP}}} \boldsymbol{P}_{\mathrm{r},1} \tag{A.7}$$

with $\boldsymbol{Q}_{\Delta_{\mathrm{CP}}}$ defined in (2.36) and where we have used that the Δ_{CP} first and last elements of $\boldsymbol{s}_m$ are equal by design. Injecting (A.6) in (A.7) and observing $\boldsymbol{R}_{\Delta_{\mathrm{CP}}} \boldsymbol{T}_{\Delta_{\mathrm{CP}}} = \boldsymbol{I}_K$ yields

$$\boldsymbol{F}_K \boldsymbol{R}_{\Delta_{\mathrm{CP}}} \boldsymbol{S}_m \boldsymbol{P}_{\mathrm{r},1} = \boldsymbol{F}_K \operatorname{circ}\left\{\boldsymbol{F}_K^{\mathsf{H}} \boldsymbol{x}_m\right\} \boldsymbol{Q}_{\Delta_{\mathrm{CP}}} \boldsymbol{P}_{\mathrm{r},1}. \tag{A.8}$$

Since any circulant matrix is diagonal in the Fourier basis, (K.5) results in

$$\begin{aligned} \boldsymbol{F}_K \boldsymbol{R}_{\Delta_{\mathrm{CP}}} \boldsymbol{S}_m \boldsymbol{P}_{\mathrm{r},1} &= \sqrt{K} \boldsymbol{F}_K \boldsymbol{F}_K^{\mathsf{H}} \boldsymbol{D}_{\boldsymbol{x}_m} \boldsymbol{F}_K \boldsymbol{Q}_{\Delta_{\mathrm{CP}}} \boldsymbol{P}_{\mathrm{r},1} \\ &= \boldsymbol{D}_{\boldsymbol{x}_m} \boldsymbol{B}_{\mathrm{r}} \end{aligned} \tag{A.9}$$

with $\boldsymbol{B}_{\mathrm{r}} \triangleq \sqrt{K} \boldsymbol{F}_K \boldsymbol{Q}_{\Delta_{\mathrm{CP}}} \boldsymbol{P}_{\mathrm{r},1}$ As a result,

$$\begin{aligned} \tilde{\boldsymbol{x}}_{\mathrm{r}} &= (\boldsymbol{I}_M \otimes \boldsymbol{D}_{\boldsymbol{x}_m} \boldsymbol{B}_{\mathrm{r}}) \boldsymbol{h}_{\mathrm{r}} + \tilde{\boldsymbol{n}}_{\mathrm{r}} \\ &= \begin{pmatrix} \boldsymbol{D}_{\boldsymbol{x}_0} \boldsymbol{B}_{\mathrm{r}} \\ \vdots \\ \boldsymbol{D}_{\boldsymbol{x}_{M-1}} \boldsymbol{B}_{\mathrm{r}} \end{pmatrix} \boldsymbol{h}_{\mathrm{r}} + \tilde{\boldsymbol{n}}_{\mathrm{r}} \\ &= \boldsymbol{D}_x (\boldsymbol{1}_{M,1} \otimes \boldsymbol{I}_K) \boldsymbol{B}_{\mathrm{r}} \boldsymbol{h}_{\mathrm{r}} + \tilde{\boldsymbol{n}}_{\mathrm{r}} \\ &= \boldsymbol{D}_x (\boldsymbol{1}_{M,1} \otimes \boldsymbol{I}_K) \boldsymbol{g}_{\mathrm{r}} + \tilde{\boldsymbol{n}}_{\mathrm{r}} \end{aligned}$$

where $\boldsymbol{g}_{\mathrm{r}} \triangleq \boldsymbol{B}_{\mathrm{r}} \boldsymbol{h}_{\mathrm{r}}$.

Appendix B

Derivation of radar CMI for a single-block Doppler-free OFDM-DFRC scenario

This appendix presents the detailed derivation of the radar CMI expression for a single-block OFDM-DFRC system without Doppler, starting from the signal model and information-theoretic definitions.

From (2.33) with $M = 1$, we obtain the following

$$\tilde{\boldsymbol{x}}_{\mathrm{r}} = \boldsymbol{D}_{\boldsymbol{x}} \boldsymbol{B}_{\mathrm{r}} \boldsymbol{h}_{\mathrm{r}} + \tilde{\boldsymbol{n}}_{\mathrm{r}} \tag{B.1}$$

$$= \boldsymbol{D}_{\boldsymbol{g}_{\mathrm{r}}} \boldsymbol{x} + \tilde{\boldsymbol{n}}_{\mathrm{r}}. \tag{B.2}$$

Here, recall that the radar channel transfer function is (2.34)

$$\boldsymbol{g}_{\mathrm{r}} \triangleq \boldsymbol{B}_{\mathrm{r}} \boldsymbol{h}_{\mathrm{r}}$$

with

$$\boldsymbol{B}_{\mathrm{r}} \triangleq \sqrt{K} \boldsymbol{F}_K \boldsymbol{Q}_{\Delta_{\mathrm{CP}}} \boldsymbol{P}_{\mathrm{r},1}.$$

We recall that the radar CMI is given by (2.50)

$$\begin{aligned} I(\tilde{\boldsymbol{x}}_{\mathrm{r}}; \boldsymbol{h}_{\mathrm{r}} | \boldsymbol{x}) = \mathcal{E}_{\boldsymbol{x}} \left\{ h(\tilde{\boldsymbol{x}}_{\mathrm{r}} | \boldsymbol{x} = \cdot) \right\} \\ - \mathcal{E}_{\boldsymbol{h}_{\mathrm{r}}, \boldsymbol{x}} \left\{ h(\tilde{\boldsymbol{x}}_{\mathrm{r}} | \boldsymbol{h}_{\mathrm{r}} = \cdot, \boldsymbol{x} = \cdot) \right\} \end{aligned}$$

To proceed, we determine the conditional and marginal distributions of $\tilde{\boldsymbol{x}}_{\mathrm{r}} | \boldsymbol{h}_{\mathrm{r}}, \boldsymbol{x}$ and $\tilde{\boldsymbol{x}}_{\mathrm{r}} | \boldsymbol{x}$. Using the same method as in Section 2.2.2.1, we obtain

$$\tilde{\boldsymbol{x}}_{\mathrm{r}} | \boldsymbol{h}_{\mathrm{r}}, \boldsymbol{x} \sim \mathcal{CN}_K \left(\boldsymbol{D}_{\boldsymbol{x}} \boldsymbol{g}_{\mathrm{r}}, \sigma_{n_{\mathrm{r}}}^2 \boldsymbol{I}_K \right) \tag{B.3}$$

where—by (2.34)—the mean is given as

$$\boldsymbol{D}_{\boldsymbol{x}} \boldsymbol{g}_{\mathrm{r}} = \boldsymbol{D}_{\boldsymbol{g}_{\mathrm{r}}} \boldsymbol{x} = \sqrt{K} \boldsymbol{D}_{\boldsymbol{x}} \boldsymbol{F}_K \boldsymbol{Q}_{\Delta_{\mathrm{CP}}} \boldsymbol{V}_{\mathrm{r}} \boldsymbol{h}_{\mathrm{r}}. \tag{B.4}$$

Applying Theorem 2.2.2 to (2.17) and (B.3)–(B.4) yields the marginal distribution reported

above

$$\tilde{\boldsymbol{x}}_{\mathrm{r}}|\boldsymbol{x} \sim \mathcal{CN}_K\left(\boldsymbol{0}, \boldsymbol{D}_{\boldsymbol{x}}\boldsymbol{K}_{\boldsymbol{g}_{\mathrm{r}}}\boldsymbol{D}_{\boldsymbol{x}}^{\mathsf{H}} + \sigma_{n_{\mathrm{r}}}^2\boldsymbol{I}_K\right) \tag{B.5}$$

where $\boldsymbol{K}_{\boldsymbol{g}_{\mathrm{r}}}$ denotes the covariance of the radar channel transfer function defined in (2.38). Next, invoking Theorem 2.2.1 on (B.3) and (B.5) gives the following entropy expressions

$$h(\tilde{\boldsymbol{x}}_{\mathrm{r}}|\boldsymbol{h}_{\mathrm{r}} = \cdot, \boldsymbol{x} = \cdot) = \log_2\left((\pi e)^K \det\left\{\sigma_{n_{\mathrm{r}}}^2\boldsymbol{I}_K\right\}\right) \tag{B.6a}$$

$$h(\tilde{\boldsymbol{x}}_{\mathrm{r}}|\boldsymbol{x} = \cdot) = \log_2\left((\pi e)^K \det\left\{\boldsymbol{K}_{\boldsymbol{g}_{\mathrm{r}}}\boldsymbol{D}_{|\boldsymbol{x}|^2} + \sigma_{n_{\mathrm{r}}}^2\boldsymbol{I}_K\right\}\right) \tag{B.6b}$$

where we have used, in the last line, $\det(\boldsymbol{I} + \boldsymbol{AB}) = \det(\boldsymbol{I} + \boldsymbol{BA})$ to have a more compact expression. Finally, the radar CMI is obtained while injecting (B.6) in (2.50), i.e.,

$$I(\tilde{\boldsymbol{x}}_{\mathrm{r}}; \boldsymbol{h}_{\mathrm{r}}|\boldsymbol{x}) = \mathcal{E}_{\boldsymbol{x}}\left\{\log_2\det\left(\boldsymbol{I}_K + \sigma_{n_{\mathrm{r}}}^{-2}\boldsymbol{K}_{\boldsymbol{g}_{\mathrm{r}}}\boldsymbol{D}_{|\boldsymbol{x}|^2}\right)\right\}.$$

Appendix C

Derivation of radar CMSE with matrix representations

This appendix derives the analytical expression of the radar CMSE of the MMSE estimator of the target response $\boldsymbol{h}_{\mathrm{r}}$. Two equivalent forms are obtained: one involving the sensing matrix $\boldsymbol{A}_{\mathrm{r}}$ (suited for narrowband Doppler scenarios) and another involving the block structure $\boldsymbol{B}_{\mathrm{r}}$ (suited for Doppler-free scenarios).

C.1 CMSE expression using the observation matrix

We adopt a narrowband Doppler model in which the received symbols are given by (2.28):

$$\tilde{\boldsymbol{x}}_{\mathrm{r}} = \boldsymbol{A}_{\mathrm{r}}\boldsymbol{h}_{\mathrm{r}} + \tilde{\boldsymbol{n}}_{\mathrm{r}}.$$

Given the known transmitted symbols $\boldsymbol{x}$, the MMSE estimator of the channel response is the conditional mean of $\boldsymbol{h}_{\mathrm{r}}$ given the received vector $\tilde{\boldsymbol{x}}_{\mathrm{r}}$, i.e., [80, Eq. (12.6)],

$$\begin{aligned}\boldsymbol{h}_{\mathrm{r}}^{\mathrm{MMSE}} &\triangleq \mathcal{E}_{\boldsymbol{h}_{\mathrm{r}}|\tilde{\boldsymbol{x}}_{\mathrm{r}},\boldsymbol{x}}\left\{\boldsymbol{h}_{\mathrm{r}}|\tilde{\boldsymbol{x}}_{\mathrm{r}},\boldsymbol{x}\right\} \\ &= \boldsymbol{K}_{\boldsymbol{h}_{\mathrm{r}}}\boldsymbol{A}_{\mathrm{r}}^{\mathsf{H}}\left(\boldsymbol{A}_{\mathrm{r}}\boldsymbol{K}_{\boldsymbol{h}_{\mathrm{r}}}\boldsymbol{A}_{\mathrm{r}}^{\mathsf{H}} + \sigma_{n_{\mathrm{r}}}^2\boldsymbol{I}_K\right)^{-1}\tilde{\boldsymbol{x}}_{\mathrm{r}}.\end{aligned}$$

The corresponding MSE is [80, Eq. (12.29)]

$$\begin{aligned}\mathrm{MSE} &= \mathrm{Tr}\left\{\mathcal{E}\left\{\left(\boldsymbol{h}_{\mathrm{r}}^{\mathrm{MMSE}} - \boldsymbol{h}_{\mathrm{r}}\right)\left(\boldsymbol{h}_{\mathrm{r}}^{\mathrm{MMSE}} - \boldsymbol{h}_{\mathrm{r}}\right)^{\mathsf{H}}\right\}\right\} \\ &= \mathrm{Tr}\left\{\left(\boldsymbol{K}_{\boldsymbol{h}_{\mathrm{r}}}{}^{-1} + \sigma_{n_{\mathrm{r}}}^{-2}\boldsymbol{A}_{\mathrm{r}}^{\mathsf{H}}\boldsymbol{A}_{\mathrm{r}}\right)^{-1}\right\}.\end{aligned}$$

The CMSE is defined as the expectation of the MSE over all possible realizations of the transmitted symbols $\boldsymbol{x}$, namely

$$\mathrm{CMSE} \triangleq \mathcal{E}_{\boldsymbol{x}}\left\{\mathrm{Tr}\left\{\left(\boldsymbol{K}_{\boldsymbol{h}_{\mathrm{r}}}^{-1} + \sigma_{n_{\mathrm{r}}}^{-2}\boldsymbol{A}_{\mathrm{r}}^{\mathsf{H}}\boldsymbol{A}_{\mathrm{r}}\right)^{-1}\right\}\right\}.$$

C.2 CMSE expression for Doppler-free scenarios

When Doppler effects on the radar target are neglected, the received signal reduces to (2.32):

$$\tilde{\boldsymbol{x}}_{\mathrm{r}} = \boldsymbol{D}_{\boldsymbol{x}}(\mathbf{1}_{M,1} \otimes \boldsymbol{I}_K)\boldsymbol{B}_{\mathrm{r}}\boldsymbol{h}_{\mathrm{r}} + \tilde{\boldsymbol{n}}_{\mathrm{r}}.$$

Following the same steps as above, the MMSE estimator is [80, Eq. (12.6)],

$$\begin{aligned}\boldsymbol{h}_{\mathrm{r}}^{\mathrm{MMSE}} &\triangleq \mathcal{E}_{\boldsymbol{h}_{\mathrm{r}}|\tilde{\boldsymbol{x}}_{\mathrm{r}},\boldsymbol{x}}\left\{\boldsymbol{h}_{\mathrm{r}}|\tilde{\boldsymbol{x}}_{\mathrm{r}},\boldsymbol{x}\right\} \\ &= \boldsymbol{K}_{\boldsymbol{h}_{\mathrm{r}}}\left(\boldsymbol{D}_{\boldsymbol{x}}(\mathbf{1}_{M,1} \otimes \boldsymbol{I}_K)\boldsymbol{B}_{\mathrm{r}}\right)^{\mathsf{H}}\left(\left(\boldsymbol{D}_{\boldsymbol{x}}(\mathbf{1}_{M,1} \otimes \boldsymbol{I}_K)\boldsymbol{B}_{\mathrm{r}}\right)\boldsymbol{K}_{\boldsymbol{h}_{\mathrm{r}}}\left(\boldsymbol{D}_{\boldsymbol{x}}(\mathbf{1}_{M,1} \otimes \boldsymbol{I}_K)\boldsymbol{B}_{\mathrm{r}}\right)^{\mathsf{H}} + \sigma_{n_{\mathrm{r}}}^2\boldsymbol{I}_K\right)^{-1}\tilde{\boldsymbol{x}}_{\mathrm{r}}.\end{aligned}$$

The associated MSE is

$$\mathrm{MSE} \triangleq \mathrm{Tr}\left\{\left(\boldsymbol{K}_{\boldsymbol{h}_{\mathrm{r}}}^{-1} + \sigma_{n_{\mathrm{r}}}^{-2}\left(\boldsymbol{D}_{\boldsymbol{x}}(\mathbf{1}_{M,1} \otimes \boldsymbol{I}_K)\boldsymbol{B}_{\mathrm{r}}\right)^{\mathsf{H}}\left(\boldsymbol{D}_{\boldsymbol{x}}(\mathbf{1}_{M,1} \otimes \boldsymbol{I}_K)\boldsymbol{B}_{\mathrm{r}}\right)\right)^{-1}\right\},$$

and averaging over all the possible realizations of the transmitted symbols $\boldsymbol{x}$ gives the CMSE:

$$\mathrm{CMSE} \triangleq \mathcal{E}_{\boldsymbol{x}}\left\{\mathrm{Tr}\left\{\left(\boldsymbol{K}_{\boldsymbol{h}_{\mathrm{r}}}^{-1} + \sigma_{n_{\mathrm{r}}}^{-2}\left(\boldsymbol{D}_{\boldsymbol{x}}(\mathbf{1}_{M,1} \otimes \boldsymbol{I}_K)\boldsymbol{B}_{\mathrm{r}}\right)^{\mathsf{H}}\left(\boldsymbol{D}_{\boldsymbol{x}}(\mathbf{1}_{M,1} \otimes \boldsymbol{I}_K)\boldsymbol{B}_{\mathrm{r}}\right)\right)^{-1}\right\}\right\}.$$

Appendix D

IR for discrete constellation symbols

This appendix details the derivation of the communication IR when discrete input constellations (e.g., PSK or QAM) are employed and analyzes its dependency on power allocation.

D.1 Derivation of the IR

The communication IR is defined as the difference between two entropy terms (2.64). Using the expression of the communication received symbols (2.40), we can clearly see that the MI decomposes additively (first over blocks, then over subcarriers) to obtain

$$\begin{aligned}\mathrm{IR} = I(\tilde{\boldsymbol{x}}_{\mathrm{c}}; \boldsymbol{x}) &= h(\tilde{\boldsymbol{x}}_{\mathrm{c}}) - h(\tilde{\boldsymbol{x}}_{\mathrm{c}}|\boldsymbol{x}) \\ &= \sum_{m\in\mathcal{I}_M} h(\tilde{\boldsymbol{x}}_{\mathrm{c},m}) - h(\tilde{\boldsymbol{x}}_{\mathrm{c},m}|\boldsymbol{x}_m) \\ &= \sum_{m\in\mathcal{I}_M}\sum_{k\in\mathcal{I}_K} \left(h(\tilde{x}_{\mathrm{c},k,m}) - \log\left(\pi e \sigma^2_{n_{\mathrm{c}}}\right)\right)\end{aligned}$$

where we used $h(\tilde{x}_{c,k,m} \mid x_{k,m}) = \log_2(\pi e\, \sigma^2_{n_{\mathrm{c}}})$ and where the entropy of the received symbol is given by:

$$h(\tilde{x}_{\mathrm{c},k,m}) = -\mathcal{E}_{\tilde{x}_{\mathrm{c},k,m}}\left\{\log\left(\sum_{v_{k,m}\in\mathcal{C}} P(v_{k,m})\mathrm{CN}\left(\tilde{x}_{\mathrm{c},k,m}|g_{\mathrm{c},k}\sqrt{p_k}v_{k,m},\sigma^2_{n_{\mathrm{c}}}\right)\right)\right\}. \tag{D.1}$$

Since no closed-form solution exists for IR, we introduce the per-subcarrier contribution $I^{(m)}_{\mathrm{c},k}(p_k)$ to the total IR for each block m, defined as:

$$I^{(m)}_{\mathrm{c},k}(p_k) \triangleq -\mathcal{E}_{\tilde{x}_{\mathrm{c},k,m}}\left\{\log\left(\sum_{v_{k,m}\in\mathcal{C}} P(v_{k,m})\mathrm{CN}\left(\tilde{x}_{\mathrm{c},k,m}|g_{\mathrm{c},k}\sqrt{p_k}v_{k,m},\sigma^2_{n_{\mathrm{c}}}\right)\right)\right\} - \log\left(\pi e\sigma^2_{n_{\mathrm{c}}}\right).$$

Thus, the IR can be rewritten equivalently as:

$$\mathrm{IR} = \sum_{m\in\mathcal{I}_M}\sum_{k\in\mathcal{I}_K} I^{(m)}_{\mathrm{c},k}(p_k).$$

D.2 IR as a function of the power allocation

We now prove that for a fixed constellation, the IR expression (2.69) depends only on the communication SNR per subcarrier (2.43) and the power profile of the transmitted symbols, i.e., $c_k p_k$. First, we focus on simplifying the expression of (2.71). In particular, the received symbol (per block and per subcarrier) entropy (D.1) that appears in the expression of (2.70) can be rewritten as:

$$\begin{aligned} h(\tilde{x}_{\mathrm{c},k,m}) &= -\mathcal{E}_{\tilde{x}_{\mathrm{c},k,m}} \left\{ \log_2 \sum_{v_{k,m}\in\mathcal{C}} P(v_{k,m}) \mathrm{CN}\left(\tilde{x}_{\mathrm{c},k,m} | g_{\mathrm{c},k}\sqrt{p_k} v_{k,m}, \sigma^2_{n_\mathrm{c}}\right) \right\} \\ &= -\int_{y\in\mathbb{C}} \log \left(\sum_{v_{k,m}\in\mathcal{C}} P(v_{k,m}) \frac{e^{-\frac{|y-|g_{\mathrm{c},k}|e^{i\phi_k}\sqrt{p_k}v_{k,m}|^2}{\sigma^2_{n_\mathrm{c}}}}}{\pi\sigma^2_{n_\mathrm{c}}} \right) \\ &\quad \times \sum_{v_{k,m}\in\mathcal{C}} P(v_{k,m}) \frac{e^{-\frac{|y-|g_{\mathrm{c},k}|e^{i\phi_k}\sqrt{p_k}v_{k,m}|^2}{\sigma^2_{n_\mathrm{c}}}}}{\pi\sigma^2_{n_\mathrm{c}}} \, dy \end{aligned}$$

where we used $g_{\mathrm{c},k} = |g_{\mathrm{c},k}|e^{i\phi_k}$. We denote

$$|y - \underbrace{|g_{\mathrm{c},k}|e^{i\phi_k}}_{g_{\mathrm{c},k}} \sqrt{p_k} v_{k,m}| = |y e^{-i\phi_k} - |g_{\mathrm{c},k}|\sqrt{p_k} v_{k,m}|.$$

Hence, (D.1) becomes

$$\begin{aligned} h(\tilde{x}_{\mathrm{c},k,m}) &= -\int_{r\in\mathbb{R}} \int_{\psi=0}^{2\pi} \log \left(\sum_{v_{k,m}\in\mathcal{C}} \frac{P(v_{k,m}) e^{-\frac{|re^{-i(-\psi+\phi_k)} - |g_{\mathrm{c},k}|\sqrt{p_k}v_{k,m}|^2}{\sigma^2_{n_\mathrm{c}}}}}{\pi\sigma^2_{n_\mathrm{c}}} \right) \\ &\quad \times \sum_{v_{k,m}\in\mathcal{C}} \frac{P(v_{k,m}) e^{-\frac{|re^{-i(-\psi+\phi_k)} - |g_{\mathrm{c},k}|\sqrt{p_k}v_{k,m}|^2}{\sigma^2_{n_\mathrm{c}}}}}{\pi\sigma^2_{n_\mathrm{c}}} r\, dr\, d\psi \\ &= -\int_{r'\in\mathbb{R}} \int_{\theta=\phi}^{2\pi+\phi} \log \left(\sum_{v_{k,m}\in\mathcal{C}} \frac{P(v_{k,m}) e^{-\frac{|r'e^{-i\theta} - \sqrt{c_k}\sqrt{p_k}v_{k,m}|^2}{\sigma^2_{n_\mathrm{c}}}}}{\pi\sigma^2_{n_\mathrm{c}}} \right) \\ &\quad \times \sum_{v_{k,m}\in\mathcal{C}} \frac{P(v_{k,m}) e^{-\frac{|r'e^{-i\theta} - \sqrt{c_k}\sqrt{p_k}v_{k,m}|^2}{\sigma^2_{n_\mathrm{c}}}}}{\pi\sigma^2_{n_\mathrm{c}}} r'\, dr'\, d\theta \\ &= -\int_{y\in\mathbb{C}} \log \left(\sum_{v_{k,m}\in\mathcal{C}} P(v_{k,m}) e^{-|y-\sqrt{c_k}\sqrt{p_k}v_{k,m}|^2} \right) \sum_{v_{k,m}\in\mathcal{C}} P(v_{k,m}) \frac{e^{-|y-\sqrt{c_k}\sqrt{p_k}v_{k,m}|^2}}{\pi\sigma^2_{n_\mathrm{c}}} \, dy \\ &\quad + \log_2 \pi\sigma^2_{n_\mathrm{c}}. \end{aligned} \tag{D.2}$$

Consequently, substituting the entropy in (2.70) with (D.2), we obtain:

$$\mathrm{IR} = \sum_{m\in\mathcal{I}_M}\sum_{k\in\mathcal{I}_K}\int_{y\in\mathbb{C}} \log_2 \sum_{v_{k,m}\in\mathcal{C}} P(v_{k,m}) e^{-|y-\sqrt{c_k}\sqrt{p_k}v_{k,m}|^2} \sum_{v_{k,m}\in\mathcal{C}} P(v_{k,m}) \frac{e^{-|y-\sqrt{c_k}\sqrt{p_k}v_{k,m}|^2}}{\pi\sigma^2_{n_\mathrm{c}}}\, dy. \tag{D.3}$$

This result confirms that for a fixed input constellation, the IR depends only on the communication SNR, c_k, and the power profile of the transmitted symbols, p_k.

Appendix E

Analysis of PAPR in OFDM-DFRC waveforms

While this work primarily optimizes waveform power allocation, high PAPR remains a known issue in OFDM-based systems. This appendix evaluates how the proposed power-allocation strategies affect PAPR, without targeting explicit PAPR reduction.

E.1 PAPR expression

We focus on short-range applications where the information throughput is more important than energy efficiency (e.g., Wi-Fi-based sensing [103]). We report PAPR distributions only for practically relevant cases. We exclude the trivial case where a single subcarrier is active. We measure PAPR over one block of the complex baseband envelope (this is sometimes called the Peak-to-Mean-Envelope Power Ratio (PMEPR)). It is given by

$$\mathrm{PAPR} \triangleq \frac{\max_{i\in\{0,\ldots,LN_\mathrm{s}-1\}} |[\boldsymbol{s}_{N_\mathrm{s}}]_i|^2}{\mathcal{E}_{\boldsymbol{x}}\left\{\frac{1}{LN_\mathrm{s}} \|\boldsymbol{s}_{N_\mathrm{s}}\|_2^2\right\}}. \tag{E.1}$$

where $\boldsymbol{s}_{N_\mathrm{s}}$ represents a sinc-interpolated version of (2.5) by a factor N_s. As prescribed in [104], we fix $N_\mathrm{s} = 4$ in the following.

Closed-form Complementary Cumulative Distribution Function (CCDF) of PAPR approximations for unequal power allocation with many subcarriers are given in [105, Eq. (22)]. These do not apply to our setting with only $K = 10$ subcarriers.

We therefore estimate the CCDF of the PAPR via Monte Carlo, we:

- Generate $1E6$ independent OFDM blocks of 4-PSK symbols;
- Compute PAPR per block;
- Fit the resulting maxima with a generalized extreme-value distribution [105].

E.2 PAPR simulation setup

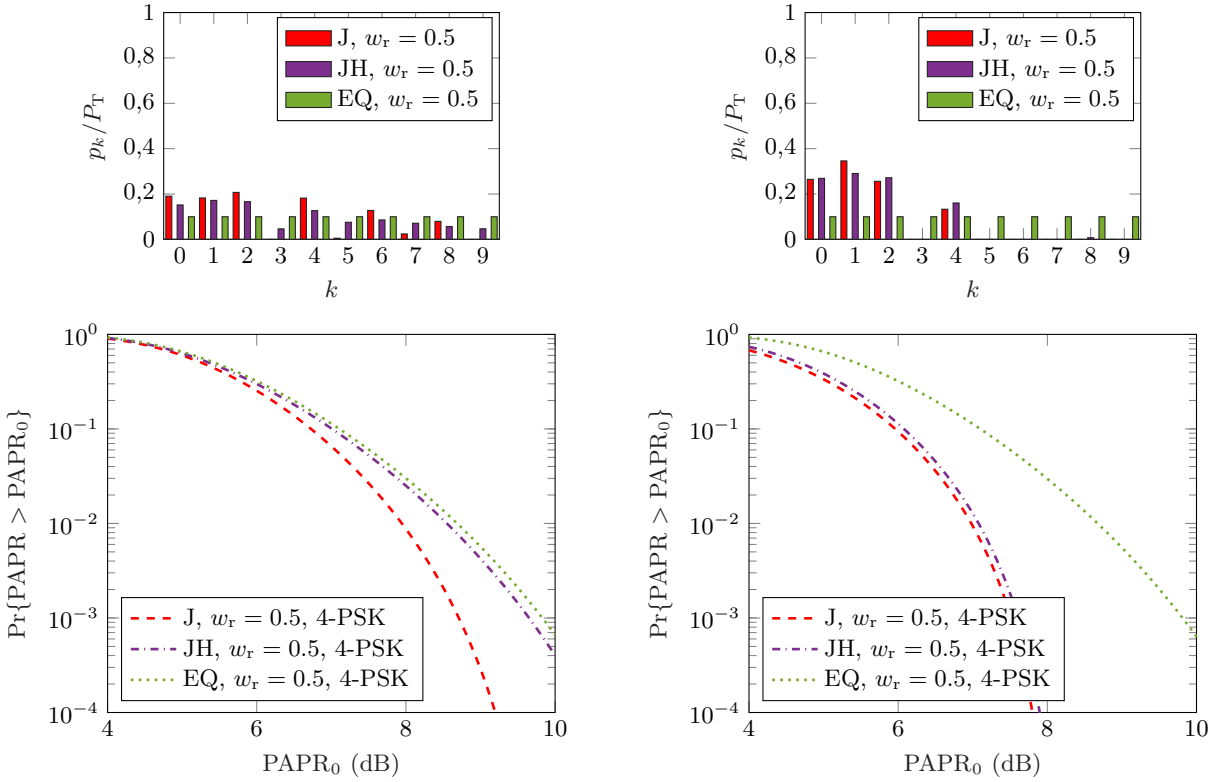
We reuse the parameters of Table 4.1 (DFRC scenario with $K = 10$ subcarriers, $w_{\mathrm{r}} = 0.5$) and consider three different scenarios:

- Frequency flat radar channel $\rho = 0$ and com #1 (see Figure 4.2a);
- Frequency-selective radar channel $\rho = 0.99e^{j2\pi/12}$, com #1 (see Figure 4.2a), i.e., an allied scenario;
- Frequency-selective radar channel $\rho = 0.99e^{j2\pi/12}$, com #2 (see Figure 4.2b), i.e., a competitive scenario.

For each scenario, we compare three power-allocation strategies: J, JH , EQ.

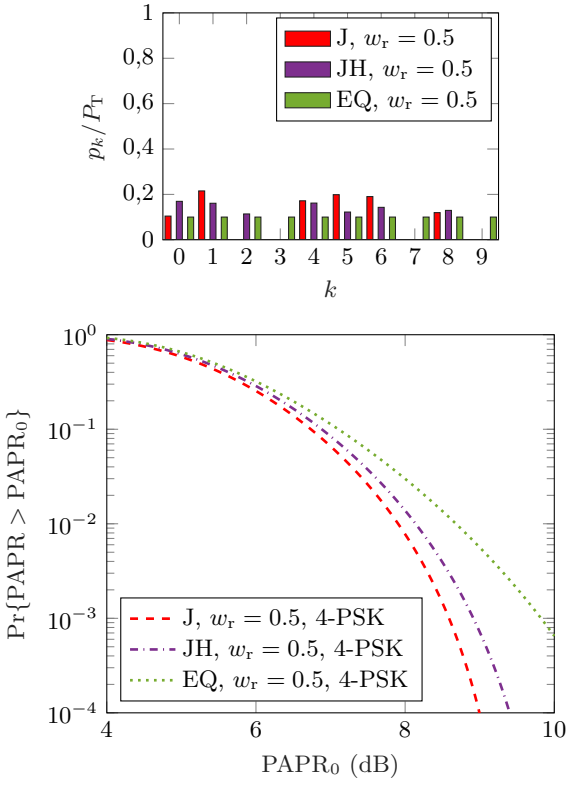
Across all simulated cases, we note that the solution of Problem J consistently activates a smaller subset of subcarriers compared to the solution of Problem JH. The corresponding CCDF curves (shown together with the equal-power allocation baseline, EQ) hence confirm that the PAPR tends to decrease (i) as the number of active subcarriers is reduced, and (ii) for a fixed number of active subcarriers, when the power distribution is non-uniform. This behavior aligns with the property that the peak magnitude (and hence the PAPR) of a superposition of independent subcarriers increases with both the number of activated subcarriers and the degree of amplitude homogeneity among them [106].

Based on the observations above, an intuitive approach would be to target an *a posteriori* PAPR reduction by 1) deactivating the weakest subcarriers from J or JH solutions, 2) reinvesting the underlying power budget to the benefit of active subcarriers. This would concentrate energy on fewer subcarriers and typically reduce the likelihood of large peaks. However, PAPR management also interacts with other elements of the transmission chain and could be more complicated. For instance, if bit-loading techniques (i.e., per-subcarrier optimal constellation design) are considered this may influence the resulting PAPR. Also, if the channel coding is included, it produces structured bit sequences, hence, scrambling or interleaving may be used to restore an approximately independent and identically distributed symbol sequence. As for traditional PAPR mitigation strategies (e.g., [107, 108]), a performance/complexity trade-off is expected.



(a) Scenario $\rho = 0$, com #1

(b) Scenario $\rho = 0.99e^{j2\pi/12}$, com #2



(c) Scenario $\rho = 0.99e^{j2\pi/12}$, com #1

Figure E.1: CCDF of the PAPR for $K = 10$ subcarriers and $P_T = -4$ dB with 4-PSK symbols.

Appendix F

Jensen-based approximation and power allocation

This appendix develops a Jensen-based approximation of the radar CMI under the assumption of Gaussian transmitted symbols. This approximation leads to a tractable formulation of the J allocation strategy introduced in Chapter 3. We begin by justifying the use of Jensen's inequality by expressing the radar CMI as the expectation of a concave function, which establishes the validity of the Jensen's approximation used in the J strategy. We then analyze the behavior of this allocation strategy in both low and high power regimes. Finally, we derive closed-form solutions in radar-only configurations for two special cases: fully correlated and uncorrelated radar channels.

F.1 Application of Jensen's inequality

In this section, we derive the approximation of the radar CMI using Jensen's inequality, assuming Gaussian transmitted symbols. The key idea is to express the radar CMI as the expectation of a concave function, thereby justifying the application of Jensen's inequality (see Lemma 2). Then, starting from (2.9), we apply a polar transformation to the radar CMI expression (3.1) under Gaussian inputs, leading to:

$$\begin{aligned} I(\tilde{\boldsymbol{x}}_{\mathrm{r}};\boldsymbol{h}_{\mathrm{r}}|\boldsymbol{x}) &= \int_{\boldsymbol{x}\in\mathbb{C}^K} \log_2\det\left(\boldsymbol{I}_K+\sigma_{n_{\mathrm{r}}}^{-2}\boldsymbol{K}_{\boldsymbol{g}_{\mathrm{r}}}\boldsymbol{D}_{|\boldsymbol{x}|^2}\right)\times\frac{1}{\pi^K\prod_{k\in\mathcal{I}_K}p_k}\exp\left(-\sum_{k\in\mathcal{I}_K}\frac{|x_k|^2}{p_k}\right)\mathrm{d}\boldsymbol{x}\\ &= \int_{\boldsymbol{\theta}\in[0,2\pi]^K}\int_{\boldsymbol{r}\in\mathbb{R}_+^K}\log_2\det\left(\boldsymbol{I}_K+\sigma_{n_{\mathrm{r}}}^{-2}\boldsymbol{K}_{\boldsymbol{g}_{\mathrm{r}}}\boldsymbol{D}_{\boldsymbol{p}}\boldsymbol{D}_{\frac{\boldsymbol{r}^2}{\boldsymbol{p}}}\right)\\ &\times\frac{\exp\left(-\sum_{k\in\mathcal{I}_K}\frac{r_k^2}{p_k}\right)}{\pi^K\prod_{k\in\mathcal{I}_K}p_k}\left(\prod_{k\in\mathcal{I}_K}r_k\right)\mathrm{d}\boldsymbol{r}\mathrm{d}\boldsymbol{\theta}. \end{aligned}$$

The change of variable $e_k=r_k^2/p_k$ allows us to express the radar CMI further as

$$I(\tilde{\boldsymbol{x}}_{\mathrm{r}};\boldsymbol{h}_{\mathrm{r}}|\boldsymbol{x})=\int_{\boldsymbol{e}\in\mathbb{R}_+^K}\log_2\det\left(\boldsymbol{I}_K+\sigma_{n_{\mathrm{r}}}^{-2}\boldsymbol{K}_{\boldsymbol{g}_{\mathrm{r}}}\boldsymbol{D}_{\boldsymbol{p}}\boldsymbol{D}_{\boldsymbol{e}}\right)\times\exp\left(-\sum_{k\in\mathcal{I}_K}e_k\right)\mathrm{d}\boldsymbol{e}. \tag{F.1}$$

An equivalent formulation is

$$I(\tilde{\boldsymbol{x}}_{\mathrm{r}};\boldsymbol{h}_{\mathrm{r}}|\boldsymbol{x}) = \mathcal{E}_{\boldsymbol{e}}\left\{\log_2\det\left(\boldsymbol{I}_K + \left(\sigma_{n_{\mathrm{r}}}^{-1}\boldsymbol{K}_{\boldsymbol{g}_{\mathrm{r}}}^{1/2}\boldsymbol{D}_{\boldsymbol{p}^{1/2}}\right)\boldsymbol{D}_{\boldsymbol{e}}\left(\sigma_{n_{\mathrm{r}}}^{-1}\boldsymbol{K}_{\boldsymbol{g}_{\mathrm{r}}}^{1/2}\boldsymbol{D}_{\boldsymbol{p}^{1/2}}\right)^{\mathsf{H}}\right)\right\} \tag{F.2}$$

where the elements of $\boldsymbol{e}$ are independent and follow an exponential distribution with a unit rate parameter, i.e.,

$$e_k \sim \mathcal{E}xp\,(1)\,. \tag{F.3}$$

We further recognize a concave function of $\boldsymbol{e}$ involved in (F.2) as follows.

Theorem F.1.1. *Consider the function*

$$\begin{aligned} f : \mathbb{R}_+^K &\to \mathbb{R} \\ \boldsymbol{e} &\mapsto \log_2\det\left(g(\boldsymbol{e})\right) \end{aligned}$$

where

$$\begin{aligned} g : \mathbb{R}_+^K &\to \mathcal{S}_{++}^K(\mathbb{C}) \\ \boldsymbol{e} &\mapsto \boldsymbol{I}_K + \left(\sigma_{n_{\mathrm{r}}}^{-1}\boldsymbol{K}_{\boldsymbol{g}_{\mathrm{r}}}^{1/2}\boldsymbol{D}_{\boldsymbol{p}^{1/2}}\right)\boldsymbol{D}_{\boldsymbol{e}}\left(\sigma_{n_{\mathrm{r}}}^{-1}\boldsymbol{K}_{\boldsymbol{g}_{\mathrm{r}}}^{1/2}\boldsymbol{D}_{\boldsymbol{p}^{1/2}}\right)^{\mathsf{H}}. \end{aligned} \tag{F.4}$$

f is concave on $\mathbb{R}_+^K$.

Proof. Consider $\lambda \in [0,1]$, and $\boldsymbol{e}_1, \boldsymbol{e}_2 \in \mathbb{R}_+^K$. We obtain

$$\begin{aligned} f(\lambda\boldsymbol{e}_1 + (1-\lambda)\boldsymbol{e}_2)) &= \log_2\det\left(g(\lambda\boldsymbol{e}_1 + (1-\lambda)\boldsymbol{e}_2))\right) \\ &= \log_2\det\left(\lambda g(\boldsymbol{e}_1) + (1-\lambda)g(\boldsymbol{e}_2)\right) \quad \text{[using (F.4)]} \\ &\geq \lambda\log_2\det\left(g(\boldsymbol{e}_1)\right) + (1-\lambda)\log_2\det\left(g(\boldsymbol{e}_2)\right) \end{aligned}$$

where the last line stems from the concavity of the log-determinant, as recalled in Theorem F.1.2. In addition, $\mathbb{R}_+^K$ is a convex set. Hence, f is concave. □

Theorem F.1.2 (Concavity of log-determinant)**.** *The function*

$$\begin{aligned} \mathcal{S}_{++}^K(\mathbb{C}) &\to \mathbb{R} \\ \boldsymbol{M} &\mapsto \log_2\det\left(\boldsymbol{M}\right) \end{aligned}$$

is concave.

Proof. We use a similar proof as in [84, p. 74] albeit for Hermitian matrices. □

From Theorem F.1.1, the conditions for applying Jensen's inequality are verified. Apply-

ing (3.12) to (F.2) yields

$$\begin{aligned} I(\tilde{\boldsymbol{x}}_{\mathrm{r}};\boldsymbol{h}_{\mathrm{r}}|\boldsymbol{x}) &= \mathcal{E}_{\boldsymbol{e}}\left\{\log_2\det\left(\boldsymbol{I}_K+\left(\sigma_{n_{\mathrm{r}}}^{-1}\boldsymbol{K}_{\boldsymbol{g}_{\mathrm{r}}}^{1/2}\boldsymbol{D}_{\boldsymbol{p}^{1/2}}\right)\boldsymbol{D}_{\boldsymbol{e}}\left(\sigma_{n_{\mathrm{r}}}^{-1}\boldsymbol{K}_{\boldsymbol{g}_{\mathrm{r}}}^{1/2}\boldsymbol{D}_{\boldsymbol{p}^{1/2}}\right)^{\mathsf{H}}\right)\right\} \\ &\leq \log_2\det\left(\boldsymbol{I}_K+\left(\sigma_{n_{\mathrm{r}}}^{-1}\boldsymbol{K}_{\boldsymbol{g}_{\mathrm{r}}}^{1/2}\boldsymbol{D}_{\boldsymbol{p}^{1/2}}\right)\boldsymbol{D}_{\mathcal{E}_{\boldsymbol{e}}\{\boldsymbol{e}\}}\left(\sigma_{n_{\mathrm{r}}}^{-1}\boldsymbol{K}_{\boldsymbol{g}_{\mathrm{r}}}^{1/2}\boldsymbol{D}_{\boldsymbol{p}^{1/2}}\right)^{\mathsf{H}}\right) \\ &\leq \log_2\det\left(\boldsymbol{I}_K+\sigma_{n_{\mathrm{r}}}^{-2}\boldsymbol{K}_{\boldsymbol{g}_{\mathrm{r}}}^{\frac{1}{2}}\boldsymbol{D}_{\boldsymbol{p}}\boldsymbol{K}_{\boldsymbol{g}_{\mathrm{r}}}^{\frac{1}{2}}\right) \end{aligned}$$

where, in the last line, we have used (F.3).

F.2 J allocation at very low and high power budget

In this section, we derive the J allocation solution to Problem J at very low power budgets and discuss it at high power budgets.

F.2.1 Determinant of the radar objective

Let us denote $\boldsymbol{i}_k$ and $\boldsymbol{\kappa}_k$ the column vectors of $\boldsymbol{I}_K$ and $\sigma_{n_{\mathrm{r}}}^{-2}\boldsymbol{K}_{\boldsymbol{g}_{\mathrm{r}}}$, respectively. Using multilinearity, the determinant of the radar objective in (3.15) is reformulated as

$$\begin{aligned} &\det\{\boldsymbol{I}_K+\frac{1}{\sigma_{n_{\mathrm{r}}}^2}\boldsymbol{K}_{\boldsymbol{g}_{\mathrm{r}}}\boldsymbol{D}_{\boldsymbol{p}}\} \\ =&\det\{[\boldsymbol{i}_0,\ldots,\boldsymbol{i}_{K-1}]\} \\ &+p_0\det\{[\boldsymbol{\kappa}_0,\boldsymbol{i}_1,\ldots,\boldsymbol{i}_{K-1}]\}+\ldots && \text{(one-}p_k\text{ terms)} \\ &+p_0p_1\det\{[\boldsymbol{\kappa}_0,\boldsymbol{\kappa}_1,\boldsymbol{i}_2,\ldots,\boldsymbol{i}_{K-1}]\}+\ldots && \text{(two-}p_k\text{ terms)} \\ &\vdots \\ &+p_0p_1\ldots p_{K-1}\det\{[\boldsymbol{\kappa}_0,\ldots,\boldsymbol{\kappa}_{K-1}]\} && (K\text{-}p_k\text{ terms}). \\ =&1 \\ &+p_0a_0+\ldots \\ &+p_0p_1\det\{[\boldsymbol{\kappa}_0,\boldsymbol{\kappa}_1,\boldsymbol{i}_2,\ldots,\boldsymbol{i}_{K-1}]\}+\ldots \\ &\vdots \\ &+p_0p_1\ldots p_{K-1}\det\left\{\sigma_{n_{\mathrm{r}}}^{-2}\boldsymbol{K}_{\boldsymbol{g}_{\mathrm{r}}}\right\}. \end{aligned} \tag{F.5}$$

We have used $\det\{[\boldsymbol{i}_0,\ldots,\boldsymbol{i}_{k-1},\boldsymbol{\kappa}_k,\boldsymbol{i}_{k+1},\ldots,\boldsymbol{i}_{K-1}]\} = a_k$ since by definition $[\boldsymbol{\kappa}_k]_k = a_k$. In addition, using Laplace expansion [109, Th. 4.1], we observe that a term like $\det\{[\boldsymbol{\kappa}_0,\boldsymbol{\kappa}_1,\boldsymbol{i}_2,\ldots,\boldsymbol{i}_{K-1}]\}$ is the determinant of the minor matrix $\sigma_{n_{\mathrm{r}}}^{-2}[\boldsymbol{K}_{\boldsymbol{g}_{\mathrm{r}}}]_{0:1,0:1}$ that reflects the correlation between the subcarriers 0 and 1. Finally, since the rank of $\boldsymbol{K}_{\boldsymbol{g}_{\mathrm{r}}}$ is equal to L_{r} by construction, all determinants in (F.5) having more than L_{r} columns $\boldsymbol{\kappa}_k$ are null.

F.2.2 J allocation at very low power budget

The equality constraint (3.16) implies $p_k \leq P_\mathrm{T}$, for all $k \in \mathcal{I}_K$. Hence, at low power budget, when $P_\mathrm{T} \to 0$, we have also $p_k \to 0$ so that only the first-order terms in (F.5) can be kept

$$\det\left\{\boldsymbol{I}_K + \frac{1}{\sigma_{n_\mathrm{r}}^2}\boldsymbol{K}_{\boldsymbol{g}_\mathrm{r}}\boldsymbol{D}_{\boldsymbol{p}}\right\} \underset{P_\mathrm{T}\to 0}{\approx} 1 + \sum_{k\in\mathcal{I}_K} a_k p_k. \tag{F.6}$$

Using $\log_2(1+\epsilon) \underset{\epsilon\to 0}{\approx} \log_2(e)\,\epsilon$, the objective function in (3.15) can be further approximated by

$$w_\mathrm{r}\log_2\det\left(\boldsymbol{I}_K + \sigma_{n_\mathrm{r}}^{-2}\boldsymbol{K}_{\boldsymbol{g}_\mathrm{r}}\boldsymbol{D}_{\boldsymbol{p}}\right) + w_\mathrm{c}\sum_{k\in\mathcal{I}_K}\log_2(1+c_k p_k) \underset{P_\mathrm{T}\to 0}{\approx} \log_2(e)\sum_{k\in\mathcal{I}_K}\underbrace{(w_\mathrm{r}a_k + w_\mathrm{c}c_k)}_{=\lambda_k^{\mathrm{th}}} p_k. \tag{F.7}$$

The optimization problem resulting from this approximation is a linear program with a simple solution [84, Sec. 4.3]. The J allocation activates only the subcarrier with the highest DFRC SNR. If two (or more) subcarriers share that SNR, the power is arbitrarily distributed among them, leading to an infinite number of allocations.

F.2.3 J allocation at very high power budget

At very high power budget, when $P_\mathrm{T} \to +\infty$, the equality constraint (3.16) indicates that the p_k's can be unbounded. Observing (F.5) jointly with (3.15), we see that all p_k's contribute in increasing the objective of Problem J, except for very specific cases (e.g., see Appendix F.3 with $w_\mathrm{r} = 1$). (We do not provide an exhaustive list of them.) Hence, in most cases, when $P_\mathrm{T} \to +\infty$, the objective will be maximized by equally distributing the power among the subcarriers.

F.3 J allocation for a radar-only waveform and a fully-correlated channel

In this section, we derive the J allocation when the radar channel is fully correlated. The covariance matrix $\boldsymbol{K}_{\boldsymbol{h}_\mathrm{r}}$ and, thus, $\boldsymbol{K}_{\boldsymbol{g}_\mathrm{r}}$ in (2.38) are of rank one. Let us denote the eigenvalue decomposition of the latter (including $\sigma_{n_\mathrm{r}}^{-2}$).

$$\sigma_{n_\mathrm{r}}^{-2}\boldsymbol{K}_{\boldsymbol{g}_\mathrm{r}} = \lambda\boldsymbol{u}\boldsymbol{u}^{\mathsf{H}} \tag{F.8}$$

with $\lambda > 0$ its unique nonzero eigenvalue and $\boldsymbol{u}$ the associated eigenvector. Using $\det(\boldsymbol{I} + \boldsymbol{AB}) = \det(\boldsymbol{I} + \boldsymbol{BA})$, the determinant of the radar objective in (3.15) becomes

$$\begin{aligned}\det\left\{\boldsymbol{I}_K + \frac{1}{\sigma_{n_\mathrm{r}}^2}\boldsymbol{K}_{\boldsymbol{g}_\mathrm{r}}\boldsymbol{D}_{\boldsymbol{p}}\right\} &= 1 + \lambda \boldsymbol{u}^{\mathsf{H}}\boldsymbol{D}_{\boldsymbol{p}}\boldsymbol{u} \\ &= 1 + \lambda \sum_{k\in\mathcal{I}_K} |u_k|^2 p_k \\ &= 1 + \sum_{k\in\mathcal{I}_K} a_k p_k\end{aligned}$$

since $\lambda|u_k|^2$ are the diagonal elements of (F.8).

When $w_\mathrm{c} = 0$, Problem J is thus tantamount to maximize the objective $\sum_{k\in\mathcal{I}_K} a_k p_k$ under the constraints (3.16) and (3.17). The J allocation activates thus only the subcarrier with the highest radar SNR. If two (or more) subcarriers share that SNR, the power is arbitrarily distributed among them, leading to an infinite number of allocations.

Appendix G

Jensen-Hadamard-based approximation and power allocation

This appendix derives and analyzes the Jensen-Hadamard approximation for the radar CMI under Gaussian symbol assumptions. By combining Jensen's and Hadamard's inequalities, we obtain a simplified expression that enables a closed-form power allocation strategy. We first prove the validity of this approximation and then derive the associated optimal power allocation using KKT conditions. Special cases and asymptotic behaviors are also discussed.

G.1 Application of Hadamard's inequality

Herein, we prove Lemma 3. Using a standard property of the determinant, the conditions of application of Hadamard's inequality hold for the determinant in (3.20), which leads to

$$\begin{aligned}
&\det\Big\{\boldsymbol{I}_K + \frac{1}{\sigma_{n_\mathrm{r}}^2}\boldsymbol{K}_{\boldsymbol{g}_\mathrm{r}}^{\frac{1}{2}}\boldsymbol{D}_{\boldsymbol{p}}\boldsymbol{K}_{\boldsymbol{g}_\mathrm{r}}^{\frac{1}{2}}\Big\} \\
&\quad= \det\left\{\boldsymbol{I}_K + \frac{1}{\sigma_{n_\mathrm{r}}^2}\boldsymbol{D}_{\boldsymbol{p}^{1/2}}\boldsymbol{K}_{\boldsymbol{g}_\mathrm{r}}\boldsymbol{D}_{\boldsymbol{p}^{1/2}}\right\} \\
&\quad\leq \prod_{k\in\mathcal{I}_K}\left(1 + \frac{1}{\sigma_{n_\mathrm{r}}^2}\left[\boldsymbol{D}_{\boldsymbol{p}^{1/2}}\boldsymbol{K}_{\boldsymbol{g}_\mathrm{r}}\boldsymbol{D}_{\boldsymbol{p}^{1/2}}\right]_{k,k}\right) \qquad \text{[using (3.18)]} \\
&\quad= \prod_{k\in\mathcal{I}_K}\left(1 + \frac{\left[\boldsymbol{K}_{\boldsymbol{g}_\mathrm{r}}\right]_{k,k}}{\sigma_{n_\mathrm{r}}^2}p_k\right). \qquad \text{(G.1)}
\end{aligned}$$

In the last line, we have used the diagonality of $\boldsymbol{D}_{\boldsymbol{p}}$ as

$$\operatorname{diag}\left\{\boldsymbol{D}_{\boldsymbol{p}^{1/2}}\boldsymbol{K}_{\boldsymbol{g}_\mathrm{r}}\boldsymbol{D}_{\boldsymbol{p}^{1/2}}\right\} = \operatorname{diag}\left\{\boldsymbol{D}_{\boldsymbol{p}}\odot\boldsymbol{K}_{\boldsymbol{g}_\mathrm{r}}\right\}$$

where $\odot$ is the Hadamard (element-wise) product. Applying the non-decreasing logarithm function to the inequality (G.1) yields Lemma 3.

G.2 Jensen-Hadamard's power allocation

In this section, we derive the closed-form solution to Problem JH.

G.2.1 Principle

Problem JH is a special case of Problem J, where $\boldsymbol{K}_{\boldsymbol{g}_\mathrm{r}}$ is a diagonal matrix. Hence, KKT conditions are necessary and sufficient for optimality. We show in what follows that a unique solution satisfies the KKT conditions of Problem JH; it is thus the unique solution.

G.2.2 Lagrangian and KKT conditions

To simplify the derivation of the Lagrangian and avoid repeated factors of $\log_2(e)$, we henceforth use natural logarithms, denoted $\log$, in place of base-2 logarithms. This is equivalent to dividing the objective function (3.20) by $\log_2(e)$, which does not affect the solution of the power allocation problem JH. Thus, the Lagrangian associated with Problem JH is [84, Ch. 5]

$$\begin{aligned}\mathcal{L}(\boldsymbol{p},\boldsymbol{\mu},\lambda) = w_\mathrm{r}\sum_{k\in\mathcal{I}_K}\log\left(1+a_k p_k\right) + w_\mathrm{c}\sum_{k\in\mathcal{I}}\log\left(1+c_k p_k\right)\\ + \sum_{k\in\mathcal{I}_K}\mu_k p_k - \lambda\left(\sum_{k\in\mathcal{I}_K} p_k - P_\mathrm{T}\right)\end{aligned} \tag{G.2}$$

where $\boldsymbol{\mu}\in\mathbb{R}^K$ and $\lambda\in\mathbb{R}$ are the Lagrange multipliers associated with the inequality and equality constraint functions, respectively. (Herein, log is the natural logarithm, to lighten the notation, the factor $\log 2 > 0$ of the objective function (3.20) is absorbed into the Lagrange multipliers.) The KKT conditions are [84, Sec. 5.5.3]

$$\begin{aligned}\sum_{k\in\mathcal{I}_K} p_k &= P_\mathrm{T}\\ k\in\mathcal{I}_K,\quad p_k &\geq 0\\ \mu_k &\geq 0\\ \mu_k p_k &= 0\\ \frac{w_\mathrm{r}a_k}{(1+a_k p_k)} + \frac{w_\mathrm{c}c_k}{(1+c_k p_k)} - \lambda + \mu_k &= 0.\end{aligned}$$

Since $\boldsymbol{\mu}$ acts as a slack variable, they can be reformulated as

$$\sum_{k\in\mathcal{I}_K} p_k = P_{\mathrm{T}} \tag{G.3a}$$

$$k \in \mathcal{I}_K, \quad p_k \geq 0 \tag{G.3b}$$

$$\lambda - \left(\frac{w_{\mathrm{r}} a_k}{1 + a_k p_k} + \frac{w_{\mathrm{c}} c_k}{1 + c_k p_k}\right) \geq 0 \tag{G.3c}$$

$$\left[\lambda - \left(\frac{w_{\mathrm{r}} a_k}{1 + a_k p_k} + \frac{w_{\mathrm{c}} c_k}{1 + c_k p_k}\right)\right] p_k = 0. \tag{G.3d}$$

G.2.3 Solution for a fixed λ

Let us consider a fixed λ and show, for each k, there is a unique p_k solution to (G.3b)–(G.3d). We denote $\lambda_k^{\mathrm{th}} \triangleq w_{\mathrm{r}} a_k + w_{\mathrm{c}} c_k \geq 0$. Given (G.3c), we deduce first that $\lambda > 0$; otherwise, we would have an irrelevant scenario where for all k, $\lambda_k^{\mathrm{th}} = 0$. Then, three cases arise according to the value of λ_k^{th}. To study them, let us denote ℓ the function

$$\begin{aligned} \ell : \mathbb{R}_+ &\to \mathbb{R}_+ \\ p_k &\mapsto \frac{w_{\mathrm{r}} a_k}{1 + a_k p_k} + \frac{w_{\mathrm{c}} c_k}{1 + c_k p_k}. \end{aligned}$$

ℓ is strictly decreasing if $\lambda_k^{\mathrm{th}} > 0$ and the zero function if $\lambda_k^{\mathrm{th}} = 0$, in addition $\ell(0) = \lambda_k^{\mathrm{th}}$.

1. If $\lambda_k^{\mathrm{th}} = 0$, we have necessarily $p_k = 0$. Otherwise, if $p_k > 0$, then condition (G.3d) imposes $\lambda = \ell(p_k) = 0$ which is not possible since $\lambda > 0$.

2. If $\lambda \geq \lambda_k^{\mathrm{th}} > 0$, we have necessarily $p_k = 0$. Otherwise, if $p_k > 0$, then $\ell(p_k) < \lambda_k^{\mathrm{th}} \leq \lambda$ meaning the condition (G.3d) cannot be fulfilled.

3. If $0 < \lambda < \lambda_k^{\mathrm{th}}$, then there is a unique $p_k > 0$ solution. Indeed, using (G.3c) we have $\ell(p_k) \leq \lambda < \lambda_k^{\mathrm{th}}$ which implies $p_k > 0$. To fulfill (G.3d), p_k must verify

$$\lambda = \frac{w_{\mathrm{r}} a_k}{1 + a_k p_k} + \frac{w_{\mathrm{c}} c_k}{1 + c_k p_k}. \tag{G.4}$$

   3.1) If $a_k > 0$ and $c_k > 0$, (G.4) can be rearranged as a quadratic equation

$$p_k^2 + \beta_k p_k + \gamma_k = 0 \tag{G.5}$$

   where

$$\begin{aligned} \beta_k &\triangleq -\lambda^{-1} + a_k^{-1} + c_k^{-1} \\ \gamma_k &\triangleq -\lambda^{-1}\left(w_{\mathrm{r}} c_k^{-1} + w_{\mathrm{c}} a_k^{-1}\right) + c_k^{-1} a_k^{-1}. \end{aligned} \tag{G.6}$$

The discriminant of (G.5) is given by

$$\begin{aligned}\Delta_k &\triangleq \beta_k^2 - 4\gamma_k \\ &= \left[\lambda^{-1}\left(w_\mathrm{r} - w_\mathrm{c}\right) + \left(c_k^{-1} - a_k^{-1}\right)\right]^2 \\ &\quad + 4\lambda^{-2} w_\mathrm{r} w_\mathrm{c}\end{aligned} \tag{G.7}$$

where the last line is obtained after straightforward manipulations. It becomes clear that $\Delta_k \geq 0$, and it cannot be zero. Otherwise, if $\Delta_k = 0$, (G.7) implies one of the two cases

$$\begin{cases} w_\mathrm{c} = 0 & \text{and } \lambda^{-1} = a_k^{-1} - c_k^{-1} \\ w_\mathrm{r} = 0 & \text{and } \lambda^{-1} = c_k^{-1} - a_k^{-1}. \end{cases}$$

In the first case, we have $\lambda_k^{\mathrm{th}} = a_k$, which results in the absurd inequality $a_k^{-1} < \lambda^{-1} < a_k^{-1}$. A similar inequality is obtained in the second case.
Since $\Delta_k > 0$, the quadratic equations (G.5) admits two real roots. The product (G.6) of these roots is easily reformulated as

$$\gamma_k = \left(-\lambda^{-1}\lambda_k^{\mathrm{th}} + 1\right) a_k^{-1} c_k^{-1} \tag{G.8}$$

so that $\gamma_k < 0$ since $\lambda < \lambda_k^{\mathrm{th}}$. Hence, the roots of (G.5) have opposite signs, and the unique strictly positive solution is

$$p_k^+(\lambda^{-1}) \triangleq \frac{1}{2}\left(-\beta_k + \Delta_k^{1/2}\right). \tag{G.9}$$

A similar expression is given in [17] without elements of proof.

3.2) If $a_k > 0$ and $c_k = 0$, it is straightforward to show that (G.4) has a unique solution

$$p_k^+(\lambda^{-1}) \triangleq \left(\lambda^{-1} w_\mathrm{r} a_k - 1\right) a_k^{-1}. \tag{G.10}$$

It is positive since, in that case, $\lambda_k^{\mathrm{th}} = w_\mathrm{r} a_k > \lambda$.

3.3) If $a_k = 0$ and $c_k > 0$, it is straightforward to show that (G.4) has a unique solution

$$p_k^+(\lambda^{-1}) \triangleq \left(\lambda^{-1} w_\mathrm{c} c_k - 1\right) c_k^{-1}. \tag{G.11}$$

It is positive since, in that case, $\lambda_k^{\mathrm{th}} = w_\mathrm{c} c_k > \lambda$.

Hence, there is a unique p_k solution to (G.3b)–(G.3d) defined by, for each $\lambda > 0$,

$$p_k(\lambda^{-1}) = \begin{cases} 0 & \text{if } \lambda_k^{\mathrm{th}} = 0 \\ \begin{cases} 0 & \text{if } \lambda^{-1} \leq \lambda_k^{\mathrm{th}\,-1} \\ p_k^+(\lambda^{-1}) & \text{if } \lambda^{-1} > \lambda_k^{\mathrm{th}\,-1} \end{cases} & \text{if } \lambda_k^{\mathrm{th}} > 0 \end{cases} \tag{G.12}$$

where

$$p_k^+(\lambda^{-1}) = \begin{cases} \frac{1}{2}\left(-\beta_k + \sqrt{\Delta_k}\right) & \text{if } a_k, c_k > 0 \\ \left(\lambda^{-1} w_\mathrm{r} a_k - 1\right) a_k^{-1} & \text{if } a_k > 0 \text{ and } c_k = 0 \\ \left(\lambda^{-1} w_\mathrm{c} c_k - 1\right) c_k^{-1} & \text{if } a_k = 0 \text{ and } c_k > 0. \end{cases}$$

It can be verified that, in all cases, $p_k^+(\lambda^{-1})$ is a continuous function with $p_k^+(\lambda_k^{\mathrm{th}\,-1}) = 0$ (a similar functional form appears in [17] when $a_k, c_k > 0$).

G.2.4 Unique solution and optimal $\lambda^\star$

Let us consider $\lambda_k^{\mathrm{th}} > 0$ and show $p_k^+(\lambda^{-1})$ is a strictly increasing function of λ^{-1} when $\lambda^{-1} > \lambda_k^{\mathrm{th}\,-1}$. The result is obvious from the expressions (G.10) and (G.11), if $a_k = 0$ and $c_k > 0$ or if $a_k = 0$ and $c_k > 0$, respectively. If $a_k, c_k > 0$, we obtain straightforwardly the derivative of (G.9) as

$$\begin{aligned} \frac{dp_k^+}{d\lambda^{-1}}(\lambda^{-1}) &= \frac{1}{2}\left[1 + \frac{-2\beta_k + 4\lambda_k^{\mathrm{th}} a_k^{-1} c_k^{-1}}{2\Delta_k^{1/2}}\right] \\ &= \frac{p_k^+(\lambda^{-1}) + \lambda_k^{\mathrm{th}} a_k^{-1} c_k^{-1}}{\Delta_k^{1/2}} > 0 \end{aligned}$$

where, to obtain the sign in the last line, we have used the previous result that $p_k^+(\lambda^{-1}) > 0$ if $\lambda^{-1} > \lambda_k^{\mathrm{th}\,-1}$.
From (G.12), we finally conclude that the function

$$\lambda^{-1} \mapsto \sum_{k \in \mathcal{I}_K} p_k(\lambda^{-1})$$

is zero for $\lambda^{-1} \leq \min_{k \in \mathcal{I}_K / \lambda_k^{\mathrm{th}\,-1} > 0} \{\lambda_k^{\mathrm{th}\,-1}\}$ and, otherwise, is strictly increasing and unbounded when $\lambda^{-1} \to +\infty$. Thus, a unique $\lambda^\star$ verifies the equality constraint (G.3a).

G.3 Asymptotic behavior of $p_k(\lambda^{-1})$

This section determines the asymptotic behavior of $p_k(\lambda^{-1})$ at the first order.

Let us consider the case $\lambda_k^{\mathrm{th}} > 0$ and $a_k, c_k > 0$. It is simple to show that the discriminant (G.7) asymptotically behaves as a linear function of λ^{-1} such as

$$\Delta_k^{1/2} \underset{\lambda^{-1} \to +\infty}{\sim} \lambda^{-1} + (w_\mathrm{r} - w_\mathrm{c})(c_k^{-1} - a_k^{-1})$$

and so the root (G.9)

$$p_k^+(\lambda^{-1}) \underset{\lambda^{-1}\to+\infty}{\sim} \lambda^{-1} - \left(w_\mathrm{r} a_k^{-1} + w_\mathrm{c} c_k^{-1}\right).$$

In addition, we obtain after straightforward manipulations (for all $\lambda^{-1} > 0$)

$$\begin{aligned}\Delta_k - &\left[\lambda^{-1} + (w_\mathrm{r} - w_\mathrm{c})(c_k^{-1} - a_k^{-1})\right]^2 \\ &= (c_k^{-1} - a_k^{-1})^2 (4 w_\mathrm{r} w_\mathrm{c}) \geq 0. \end{aligned} \tag{G.13}$$

From the sign of (G.13) and since the square-root is a non-decreasing function, we conclude the discriminant is above its asymptote for all $\lambda^{-1} > 0$ (and thus for $\lambda^{-1} > \lambda_k^{\mathrm{th}\,-1}$)

$$\Delta_k^{1/2} \geq \lambda^{-1} + (w_\mathrm{r} - w_\mathrm{c})(c_k^{-1} - a_k^{-1})$$

and so the root (G.9)

$$p_k^+(\lambda^{-1}) \geq \lambda^{-1} - \left(w_\mathrm{r} a_k^{-1} + w_\mathrm{c} c_k^{-1}\right). \tag{G.14}$$

In the other cases implied in (G.12), $p_k(\lambda^{-1})$ is already a linear function of λ^{-1}.

We conclude that, in all cases, $\sum_{k\in\mathcal{I}_K} p_k(\lambda^{-1})$ is above its linear asymptote yielding necessarily with (G.10), (G.11), and (G.14)

$$\lambda^{\star -1} \leq \lambda^{\infty -1}$$

where

$$\lambda^{\infty -1} \triangleq \frac{P_\mathrm{T} + \sum_{k\in\mathcal{I}_K^1} (w_\mathrm{r} a_k^{-1} + w_\mathrm{c} c_k^{-1}) + \sum_{k\in\mathcal{I}_K^2} a_k^{-1} + \sum_{k\in\mathcal{I}_K^3} c_k^{-1}}{n_1 + n_2 w_\mathrm{r} + n_3 w_\mathrm{c}} \tag{G.15}$$

with $n_i = \#\mathcal{I}_K^i$, for $i = 1, 2, 3$, and

$$\begin{aligned}\mathcal{I}_K^1 &= \{k \in \mathcal{I}_K | \lambda_k^{\mathrm{th}} > 0, a_k > 0, c_k > 0\} \\ \mathcal{I}_K^2 &= \{k \in \mathcal{I}_K | \lambda_k^{\mathrm{th}} > 0, a_k > 0, c_k = 0\} \\ \mathcal{I}_K^3 &= \{k \in \mathcal{I}_K | \lambda_k^{\mathrm{th}} > 0, a_k = 0, c_k > 0\}.\end{aligned}$$

G.4 Bisection search of $\lambda^\star$

Using results from Appendix G.3, we propose herein an interval to initiate the bisection search of $\lambda^{\star -1}$. Let us note $\lambda_{\min}^{\mathrm{th}\,-1} = \min_{k\in\mathcal{I}_K} \{\lambda_k^{\mathrm{th}\,-1}\}$ and $\lambda_{\max}^{\mathrm{th}\,-1} = \max_{k\in\mathcal{I}_K} \{\lambda_k^{\mathrm{th}\,-1}\}$. We propose

the interval $[{\lambda_{\min}^{\text{th}}}^{-1}, {\lambda_{\max}^{\text{th}}}^{-1}]$ if $\sum_{k\in\mathcal{I}_K} p_k({\lambda_{\max}^{\text{th}}}^{-1}) \geq P_{\text{T}}$ and, otherwise, $[{\lambda_{\min}^{\text{th}}}^{-1}, \lambda^{\infty-1}]$ with $\lambda^{\infty-1}$ defined in (G.15).

G.5 J and JH allocations for a radar-only waveform and an uncorrelated channel

In this section, we prove that when $w_{\text{r}} = 1$ and $\boldsymbol{K}_{\boldsymbol{h}_{\text{r}}}$ is diagonal, the unique solution to Problems J and JH is $\boldsymbol{p}^{(\text{EQ})}$.

When $\boldsymbol{K}_{\boldsymbol{h}_{\text{r}}}$ is diagonal, so is the matrix $\boldsymbol{\Lambda} \triangleq \sigma_{n_{\text{r}}}^{-2} K \boldsymbol{Q}_{\Delta_{\text{CP}}} \boldsymbol{V}_{\text{r}} \boldsymbol{K}_{\boldsymbol{h}_{\text{r}}} \boldsymbol{V}_{\text{r}}^{\mathsf{T}} \boldsymbol{Q}_{\Delta_{\text{CP}}}^{\mathsf{T}}$. Using Hadamard's inequality and the definition of $\boldsymbol{K}_{\boldsymbol{g}_{\text{r}}}$ in (2.38) yields [4, Th. 17.9.2]

$$\det\left\{\boldsymbol{I}_K + \frac{1}{\sigma_{n_{\text{r}}}^2}\boldsymbol{K}_{\boldsymbol{g}_{\text{r}}}\boldsymbol{D}_{\boldsymbol{p}}\right\} = \det\left\{\boldsymbol{I}_K + \boldsymbol{\Lambda}\boldsymbol{F}_K^{\mathsf{H}}\boldsymbol{D}_{\boldsymbol{p}}\boldsymbol{F}_K\right\} \tag{G.16}$$

$$\leq \prod_{k\in\mathcal{I}_K}\left(1 + [\boldsymbol{\Lambda}\boldsymbol{F}_K^{\mathsf{H}}\boldsymbol{D}_{\boldsymbol{p}}\boldsymbol{F}_K]_{k,k}\right). \tag{G.17}$$

By construction, $\boldsymbol{F}_K^{\mathsf{H}}\boldsymbol{D}_{\boldsymbol{p}}\boldsymbol{F}_K$ is circulant and its diagonal element is $K^{-1}\sum_{k\in\mathcal{I}_K} p_k$ [110]. Hence, the inequality (G.17) becomes with $\boldsymbol{\Lambda}$ a diagonal matrix

$$\det\left\{\boldsymbol{I}_K + \frac{1}{\sigma_{n_{\text{r}}}^2}\boldsymbol{K}_{\boldsymbol{g}_{\text{r}}}\boldsymbol{D}_{\boldsymbol{p}}\right\} \leq \prod_{k\in\mathcal{I}_K}\left(1 + [\boldsymbol{\Lambda}]_{k,k}K^{-1}\sum_{k\in\mathcal{I}_K} p_k\right).$$

Any solution $\boldsymbol{p}^{(\text{J})}$ to Problem J verifies the constraint $\sum_{k\in\mathcal{I}_K} p_k = P_{\text{T}}$ and thus the inequality

$$\det\left\{\boldsymbol{I}_K + \frac{1}{\sigma_{n_{\text{r}}}^2}\boldsymbol{K}_{\boldsymbol{g}_{\text{r}}}\boldsymbol{D}_{\boldsymbol{p}^{(\text{J})}}\right\} \leq \prod_{k\in\mathcal{I}_K}\left(1 + [\boldsymbol{\Lambda}]_{k,k}K^{-1}P_{\text{T}}\right) \tag{G.18}$$

$$= \det\left\{\boldsymbol{I}_K + \frac{1}{\sigma_{n_{\text{r}}}^2}\boldsymbol{K}_{\boldsymbol{g}_{\text{r}}}\boldsymbol{D}_{\boldsymbol{p}^{(\text{EQ})}}\right\}. \tag{G.19}$$

This proves that $\boldsymbol{p}^{(\text{EQ})}$ is a solution to Problem J (with $w_{\text{r}} = 1$). In addition, the Hadamard's inequality (G.19) becomes an equality if and only if $\boldsymbol{I}_K + \boldsymbol{\Lambda}\boldsymbol{F}_K^{\mathsf{H}}\boldsymbol{D}_{\boldsymbol{p}}\boldsymbol{F}_K$ in (G.17) is diagonal [4, Th. 17.9.2]. It happens if and only if $\boldsymbol{F}_K^{\mathsf{H}}\boldsymbol{D}_{\boldsymbol{p}}\boldsymbol{F}_K$ is diagonal. Since the latter is also circulant, it happens if and only if $\boldsymbol{D}_{\boldsymbol{p}} = K^{-1}P_{\text{T}}\boldsymbol{I}_K$. This proves that $\boldsymbol{p}^{(\text{EQ})}$ is the unique solution to Problem J.

When $\boldsymbol{K}_{\boldsymbol{h}_{\text{r}}}$ is diagonal, $\boldsymbol{K}_{\boldsymbol{g}_{\text{r}}}$ is circulant which implies that its diagonal elements are identical, i.e., $a_k = a_0$ for all $k \in \mathcal{I}_K$. Problem JH (with $w_{\text{r}} = 1$) is thus equivalent to a WF problem where all radar subcarriers have the same SNR. Hence, power is allocated evenly among the K subcarriers. This proves that $\boldsymbol{p}^{(\text{EQ})}$ is the unique solution to Problem JH.

Appendix H

Jensen gap analysis for radar CMI approximation

This appendix provides an analysis of the Jensen gap that arises when approximating the radar CMI using Jensen's inequality (3.14) (The Jensen gap is defined as the difference between the true radar CMI and its Jensen-approximated value). Specifically, we show that the error introduced by this approximation is bounded and grows linearly with the number of nonzero scatterers, independent of the number of subcarriers K.

Let $\boldsymbol{e}$ be a random variable and g a real-valued concave function. The *Jensen gap* Δ is defined as the difference between the concave transformation of the mean and the mean of the concave transformation:

$$\Delta = g\left(\mathcal{E}_{\boldsymbol{e}}\left\{\boldsymbol{e}\right\}\right) - \mathcal{E}_{\boldsymbol{e}}\left\{g(\boldsymbol{e})\right\}.$$

Definition H.0.1 (Jensen gap of the radar CMI)**.** The Jensen gap in the context of radar CMI is given by:

$$\Delta = \log_2 \det\left(\sigma_{n_\mathrm{r}}^{-2}\boldsymbol{K}_{\boldsymbol{g}_\mathrm{r}}^{1/2}\boldsymbol{D}_{\boldsymbol{p}}\boldsymbol{K}_{\boldsymbol{g}_\mathrm{r}}^{1/2} + \boldsymbol{I}_K\right) - \mathcal{E}_{\boldsymbol{x}}\left\{\log_2 \det\left(\sigma_{n_\mathrm{r}}^{-2}\boldsymbol{K}_{\boldsymbol{g}_\mathrm{r}}^{1/2}\boldsymbol{D}_{|\boldsymbol{x}|^2}\boldsymbol{K}_{\boldsymbol{g}_\mathrm{r}}^{1/2} + \boldsymbol{I}_K\right)\right\} \quad \text{(H.1)}$$

where $\boldsymbol{K}_{\boldsymbol{g}_\mathrm{r}}$ is the $K \times K$ radar covariance matrix, assumed Hermitian and of rank L_r corresponding to the number of nonzero radar scatterers.

Using the definition of the Jensen gap we establish a universal upper bound on Δ in terms of the radar channel rank L_r.

Theorem H.0.1 (Upper bound on Jensen gap for radar CMI)**.** *Let $\boldsymbol{K}_{\boldsymbol{g}_\mathrm{r}}$ be a Hermitian matrix of rank L_r. Then, the Jensen gap Δ in the radar CMI approximation satisfies:*

$$\Delta < L_\mathrm{r} \cdot \gamma \log_2(e) \quad \text{(H.2)}$$

where γ is the Euler–Mascheroni constant and e the base of the natural logarithm.
This implies that the gap value increases linearly with the number of active scatterers L_r, and is independent of the number of subcarriers K.

Proof. The proof proceeds in three steps:

- Step 1: Reformulate the radar CMI and lower bound it.
- Step 2: Apply Jensen's inequality and derive a lower bound.
- Step 3: Bound the Jensen gap Δ using properties of exponential integrals and the eigenvalues of the matrix $\boldsymbol{A}$.

Step 1: Lower bounding the radar CMI We aim to derive a lower bound on the radar CMI, expressed as a log-determinant involving an exponential random vector. To facilitate analysis, we reformulate the radar CMI in terms of a positive semi-definite matrix denoted $\boldsymbol{A}$, constructed from the radar covariance matrix $\boldsymbol{K}_{\boldsymbol{g}_\mathrm{r}}$ and the power allocation matrix $\boldsymbol{D}_{\boldsymbol{p}}$. This formulation allows us to apply eigenvalue-based inequalities, which are instrumental in bounding the Jensen gap.

As proved in Appendix F.1, the radar CMI can be rewritten in terms of an exponential random vector $\boldsymbol{e}$ (F.2):

$$\mathrm{CMI} = \mathcal{E}_{\boldsymbol{e}} \left\{ \log_2 \det \left(\boldsymbol{I}_K + \left(\sigma_{n_\mathrm{r}}^{-1} \boldsymbol{K}_{\boldsymbol{g}_\mathrm{r}}^{1/2} \boldsymbol{D}_{\boldsymbol{p}^{1/2}} \right) \boldsymbol{D}_{\boldsymbol{e}} \left(\sigma_{n_\mathrm{r}}^{-1} \boldsymbol{K}_{\boldsymbol{g}_\mathrm{r}}^{1/2} \boldsymbol{D}_{\boldsymbol{p}^{1/2}} \right)^{\mathsf{H}} \right) \right\} \tag{H.3}$$

where the elements of $\boldsymbol{e}$ are independent and follow an exponential distribution with a unitary rate parameter $e_k \sim \mathcal{E}xp\,(1)$. We recall that [70, p. 271]

$$\mathcal{E}_{\boldsymbol{e}} \left\{ \log_2 \det \left(\left(\sigma_{n_\mathrm{r}}^{-1} \boldsymbol{K}_{\boldsymbol{g}_\mathrm{r}}^{1/2} \boldsymbol{D}_{\boldsymbol{p}^{1/2}} \right) \boldsymbol{D}_{\boldsymbol{e}} \left(\sigma_{n_\mathrm{r}}^{-1} \boldsymbol{K}_{\boldsymbol{g}_\mathrm{r}}^{1/2} \boldsymbol{D}_{\boldsymbol{p}^{1/2}} \right)^{\mathsf{H}} + \boldsymbol{I}_K \right) \right\} = \mathcal{E}_{\boldsymbol{e}} \left\{ \log_2 \det \left(\boldsymbol{A} \boldsymbol{D}_{\boldsymbol{e}} + \boldsymbol{I}_K \right) \right\} \tag{H.4}$$

where

$$\boldsymbol{A} \triangleq \sigma_{n_\mathrm{r}}^{-2} \boldsymbol{D}_{\boldsymbol{p}}^{1/2} \boldsymbol{K}_{\boldsymbol{g}_\mathrm{r}} \boldsymbol{D}_{\boldsymbol{p}}^{1/2}. \tag{H.5}$$

Since $\boldsymbol{K}_{\boldsymbol{g}_\mathrm{r}}$ is Hermitian and $\boldsymbol{D}_{\boldsymbol{p}}$ is a positive real-valued diagonal matrix, it follows that $\boldsymbol{A}$ is Hermitian and positive semi-definite:

- Hermitian: $\boldsymbol{A}^{\mathsf{H}} = \boldsymbol{A}$;
- positive semi-definite: $\forall \boldsymbol{x} \in \mathbb{C}^K$, we have

$$\begin{aligned} \boldsymbol{x}^{\mathsf{H}} \boldsymbol{A} \boldsymbol{x} &= \boldsymbol{x}^{\mathsf{H}} \left(\sigma_{n_\mathrm{r}}^{-1} \boldsymbol{K}_{\boldsymbol{g}_\mathrm{r}}^{1/2} \boldsymbol{D}_{\boldsymbol{p}^{1/2}} \right)^{\mathsf{H}} \left(\sigma_{n_\mathrm{r}}^{-1} \boldsymbol{K}_{\boldsymbol{g}_\mathrm{r}}^{1/2} \boldsymbol{D}_{\boldsymbol{p}^{1/2}} \right) \boldsymbol{x} \\ &= (\boldsymbol{x}^{\mathsf{H}} \left(\sigma_{n_\mathrm{r}}^{-1} \boldsymbol{K}_{\boldsymbol{g}_\mathrm{r}}^{1/2} \boldsymbol{D}_{\boldsymbol{p}^{1/2}} \right)^{\mathsf{H}})(\boldsymbol{x}^{\mathsf{H}} \left(\sigma_{n_\mathrm{r}}^{-1} \boldsymbol{K}_{\boldsymbol{g}_\mathrm{r}}^{1/2} \boldsymbol{D}_{\boldsymbol{p}^{1/2}} \right)^{\mathsf{H}})^{\mathsf{H}} \\ &= \left\| \left(\sigma_{n_\mathrm{r}}^{-1} \boldsymbol{K}_{\boldsymbol{g}_\mathrm{r}}^{1/2} \boldsymbol{D}_{\boldsymbol{p}^{1/2}} \right)^{\mathsf{H}} \boldsymbol{x} \right\|^2 \geq 0. \end{aligned}$$

Then, using the eigendecomposition of a matrix, we can factorize $\boldsymbol{A}$ as follows

$$\boldsymbol{A} = \boldsymbol{Q} \boldsymbol{\Lambda} \boldsymbol{Q}^{\mathsf{H}} \tag{H.6}$$

where $\boldsymbol{Q}$ is unitary the matrix whose columns are the eigenvectors and $\boldsymbol{\Lambda} = \operatorname{diag}\{\lambda_0, \ldots, \lambda_{K-1}\}$ is a diagonal matrix whose diagonal elements are the corresponding eigenvalue λ_i.

We introduce the following theorem [111, Theorem 1. (a)].

Theorem H.0.2. *Let $\boldsymbol{D_e}$ be a $K \times K$ diagonal matrix whose diagonal entries $e_0, \ldots, e_{K-1}$ are identically distributed nonnegative random variable. Let $\boldsymbol{A}$ be a positive semi-definite Hermitian $K \times K$ matrix with eigenvalues $\lambda_0, \ldots, \lambda_{K-1}$ and let $\boldsymbol{\Lambda} = \operatorname{diag}\{\lambda_0, \ldots, \lambda_{K-1}\}$, then*

$$\mathcal{E}_{\boldsymbol{e}}\left\{\log_2 \det\left(\boldsymbol{A}\boldsymbol{D_e} + \boldsymbol{I}\right)\right\} \geq \mathcal{E}_{\boldsymbol{e}}\left\{\log_2 \det\left(\boldsymbol{\Lambda}\boldsymbol{D_e} + \boldsymbol{I}\right)\right\}.$$

Remark H.0.1. *This theorem was introduced and proved in [111, Theorem 1. (a)]. The authors used a nonnegative definite matrix to designate a positive semi-definite matrix.*

Applying this to (H.3) yields:

$$\begin{aligned} \mathrm{CMI} &\geq \mathcal{E}_{\boldsymbol{e}}\left\{\log_2 \det\left(\boldsymbol{\Lambda}\boldsymbol{D_e} + \boldsymbol{I}_K\right)\right\} \\ &\geq \sum_{k \in \mathcal{I}_K} \mathcal{E}_{\boldsymbol{e}}\left\{\log_2\left(\lambda_k e_k + 1\right)\right\}. \end{aligned} \tag{H.7}$$

We note that each λ_k depends on p_k.

Step 2: Expression of the Jensen approximation We derive the Jensen-based approximation of the radar CMI by expressing the log-determinant in terms of the eigenvalues of the matrix $\boldsymbol{A}$, obtained via its eigendecomposition. This yields a tractable upper bound on the radar CMI, expressed as a sum over scalar terms, which will be used to analyze and bound the Jensen gap in the following sections:

$$\begin{aligned} \log_2 \det\left(\boldsymbol{A} + \boldsymbol{I}_K\right) &= \log_2 \det\left(\boldsymbol{Q}\boldsymbol{\Lambda}\boldsymbol{Q}^{\mathsf{H}} + \boldsymbol{I}_K\right) \\ &= \log_2 \det\left(\boldsymbol{\Lambda} + \boldsymbol{I}_K\right) \\ &= \sum_{k \in \mathcal{I}_K} \log_2\left(\lambda_k + 1\right). \end{aligned} \tag{H.8}$$

Step 3: Jensen gap bound via exponential integrals We now establish an explicit upper bound on the Jensen gap Δ by expressing it in terms of the eigenvalues of the matrix $\boldsymbol{A}$ defined in (H.5). Let $\{\lambda_k\}_{k=0}^{K-1}$ denote its eigenvalues (only L_{r} elements of the eigenvalues

are nonzero). Then the Jensen gap Δ satisfies:

$$\begin{aligned}\Delta &= \log_2 \det\left(\boldsymbol{A} + \boldsymbol{I}_K\right) - \mathcal{E}_{\boldsymbol{e}}\left\{\log_2 \det\left(\boldsymbol{A}\boldsymbol{D}_{\boldsymbol{e}} + \boldsymbol{I}\right)\right\} \\ &\leq \sum_{k\in\mathcal{I}_K} \log_2\left(\lambda_k + 1\right) - \sum_{k\in\mathcal{I}_K} \mathcal{E}_{e_k}\left\{\log_2\left(\lambda_k e_k + 1\right)\right\} \\ &\leq \sum_{k\in\mathcal{I}_K} \delta(\lambda_k)\end{aligned}$$

where each term $\delta(\lambda_k)$ is defined as:

$$\delta(\lambda_k) \triangleq \log_2\left(\lambda_k + 1\right) - \mathcal{E}_{\boldsymbol{e}}\left\{\log_2\left(\lambda_k e_k + 1\right)\right\}.$$

This function admits a uniform upper bound:

$$\delta(x) \;<\; \gamma \log_2(e), \quad \forall x > 0,$$

where $\gamma \approx 0.57$ is the Euler–Mascheroni constant.
Since $\boldsymbol{A}$ has at most L_{r} non-zero eigenvalues—the rank of $\boldsymbol{K}_{\boldsymbol{g}_{\mathrm{r}}}$—it follows that:

$$\Delta < L_{\mathrm{r}} \cdot \gamma \log_2(e) \cdot$$

Proof. We express $\delta(x)$ in terms of the exponential integral $\mathrm{E}_1(1/x)$:

$$\begin{aligned}\delta(x) &\triangleq \log_2(x+1) - \mathcal{E}_{e_k}\left\{\log_2\left(xe_k + 1\right)\right\} && \text{(H.9)} \\ &= 1/\log(2)\left(\log(x+1) - \int_0^{+\infty} \log\left(xt+1\right) e^{-t} dt\right) && \text{(H.10)} \\ &= 1/\log(2)\left(\log(x+1) - e^{1/x}\,\mathrm{E}_1(1/x)\right) \quad \text{(integration by parts + change of variable)} && \text{(H.11)}\end{aligned}$$

where $\mathrm{E}_1()$ is the exponential integral such that $\mathrm{E}_1(z) = \int_z^{+\infty} \frac{e^{-t}}{t} dt, \quad |\arg(z)| < \pi$. We can also rewrite the exponential integral as follows [112, Eq. 5.1.11]

$$\mathrm{E}_1(z) = -\gamma - \log(z) + \mathrm{Ein}(z), \tag{H.12}$$

with $\gamma \approx 0.57$ the Euler–Mascheroni constant and $\mathrm{Ein}()$ the entire function such that $\mathrm{Ein}(z) = \sum_{k=1}^{\infty} \frac{(-1)^{k+1} z^k}{k k!}$.

We analyze the behavior of the function $\delta(x)$ to establish two key properties (1) it is strictly increasing for all $x > 0$, and (2) it is uniformly upper bounded by $\gamma \log_2(e)$.
To prove monotonicity, we compute the derivative $\frac{d\delta(x)}{dx}$. We recall the following identity from [112, Eqs. 5.1.24, 5.1.26]

$$\frac{d\,\mathrm{E}_1(x)}{dx} = -\,\mathrm{E}_0(x) = -\frac{e^{-x}}{x}. \tag{H.13}$$

Therefore, by the chain rule:

$$\frac{d}{dx}\left(e^{1/x}\,\mathrm{E}_1\left(1/x\right)\right) = -\frac{1}{x^2}\left(e^{1/x}\,\mathrm{E}_1\left(1/x\right) - x\right).$$

Substituting into the expression of $\delta(x)$, we obtain:

$$\frac{\partial\delta(x)}{\partial x} = \log_2\left(e\right)\left(\frac{1}{x+1} + \frac{1}{x^2}\left(e^{1/x}\,\mathrm{E}_1\left(1/x\right) - x\right)\right). \tag{H.14}$$

(H.15)

We used the inequality $e^{1/x}\,\mathrm{E}_1\left(1/x\right) > \frac{1}{1+1/x}$ [112, Eq. 5.1.19] to obtain

$$\frac{\partial\delta(x)}{\partial x} > \log_2\left(e\right)\left(\frac{1}{x+1} + \frac{\frac{1}{1+1/x} - x}{x^2}\right) = \log_2\left(e\right)\left(\frac{1}{x+1} + \frac{1-x-1}{x^2+x}\right) \tag{H.16}$$

$$= \log_2\left(e\right)\cdot\frac{x-x}{x^2+x} = 0. \tag{H.17}$$

Therefore, $\delta(x)$ is strictly increasing for all $x > 0$.

Asymptotic Upper Bound of $\delta(x)$ To find an upper bound for $\delta(x)$, we analyze its behavior as $x \to +\infty$. First, we use expansion of the exponential integral $\mathrm{E}_1\left(z\right)$ as explained in [112, Eq. 5.1.11]. Using (H.12), we rewrite

$$e^{1/x}\,\mathrm{E}_1\left(1/x\right) = e^{1/x}\left(-\gamma - \log\left(1/x\right) + \mathrm{Ein}\left(1/x\right)\right). \tag{H.18}$$

Substituting into the definition of $\delta(x)$, we obtain:

$$\delta(x) = \log_2\left(e\right)\cdot\left(\log\left(x+1\right) + e^{1/x}\gamma + e^{1/x}\log\left(1/x\right) - e^{1/x}\,\mathrm{Ein}\left(1/x\right)\right).$$

Now, taking the limit:

$$\begin{aligned}\lim_{x\to+\infty}\delta(x) &= \log_2\left(e\right)\cdot\lim_{x\to\infty}\left(\log\left(x+1\right) + e^{1/x}\gamma + e^{1/x}\log\left(1/x\right) - e^{1/x}\,\mathrm{Ein}\left(1/x\right)\right)\\ &= \log_2\left(e\right)\cdot\left(\underbrace{\lim_{x\to+\infty}\log\left(x+1\right) + e^{1/x}\log\left(1/x\right)}_{=0} + \underbrace{\lim_{x\to+\infty}e^{1/x}\gamma}_{=\gamma} - \underbrace{\lim_{x\to+\infty}e^{1/x}\,\mathrm{Ein}\left(1/x\right)}_{=0}\right)\\ &= \log_2\left(e\right)\gamma.\end{aligned}$$

Consequently, because δ is increasing; for all $x > 0$, we obtain the strict inequality:

$$\delta(x) < \lim_{x\to+\infty}\delta(x) = \log_2\left(e\right)\gamma. \tag{H.19}$$

□

Since the radar covariance matrix $\boldsymbol{K}_{\boldsymbol{g}_\mathrm{r}}$ has rank L_r, it follows that $\boldsymbol{A} = \sigma_{n_\mathrm{r}}^{-2} \boldsymbol{D}_{\boldsymbol{p}}^{1/2} \boldsymbol{K}_{\boldsymbol{g}_\mathrm{r}} \boldsymbol{D}_{\boldsymbol{p}}^{1/2}$ has rank at most L_r. Therefore, $\boldsymbol{A}$ has at most L_r non-zero eigenvalues.
Moreover, we established that the function $\delta(x)$ satisfies the uniform upper bound $\forall x > 0, \delta(x) < \frac{\gamma}{\log(2)}$. As a result, the Jensen gap Δ can be bounded as follows:

$$\Delta \leq \sum_{k \in \mathcal{I}_K} \delta(\lambda_k) \leq \sum_{l \in \mathcal{I}_{L_\mathrm{r}}} \delta(\lambda_l) < L_\mathrm{r} \cdot \log_2(e)\, \gamma. \tag{H.20}$$

□

Appendix I

Optimal allocation for Gaussian transmitted symbols at very low power budget

In this appendix, we solve Problem OPT-G in the regime of very low transmit power. As the transmitted symbols are Gaussian, we have $x_k \sim \mathcal{CN}(0, p_k)$ (2.9). The equality constraint (3.10) implies $p_k \to 0$ at very low P_{T}. Since the Gaussian distribution is short-tailed, we can also assume $|x_k| \to 0$ within any expectation $\mathcal{E}_{\boldsymbol{x}}\{\}$. Following the same reasoning as in (F.5)–(F.6), we approximate the radar CMI from (3.9) as:

$$\begin{aligned} I(\tilde{\boldsymbol{x}}_{\mathrm{r}}; \boldsymbol{h}_{\mathrm{r}}|\boldsymbol{x}) &\underset{P_{\mathrm{T}}\to 0}{\approx} \log_2(e)\, \mathcal{E}_{\boldsymbol{x}}\left\{\sum_{k\in\mathcal{I}_K} a_k |x_k|^2\right\} \\ &= \log_2(e) \sum_{k\in\mathcal{I}_K} a_k \mathcal{E}_{x_k}\left\{|x_k|^2\right\} \\ &= \log_2(e) \sum_{k\in\mathcal{I}_K} a_k p_k \end{aligned}$$

where we have used in the last line that $|x_k|^2/p_k \sim \mathcal{E}xp(1)$. Therefore, as for the J (cf. Appendix F.2) and JH allocations, the OPT-G waveform activates only the subcarrier with the highest DFRC SNR at very low power. If two (or more) subcarriers share that SNR, the power is arbitrarily distributed among them, leading to an infinite number of allocations.

Furthermore, when the radar channel is uncorrelated in range (i.e., $\boldsymbol{K}_{\boldsymbol{h}_{\mathrm{r}}}$ is diagonal), the a_k's are all equal (cf. Appendix G.5). The resulting radar CMI is thus

$$I(\tilde{\boldsymbol{x}}_{\mathrm{r}}; \boldsymbol{h}_{\mathrm{r}}|\boldsymbol{x}) = \log_2(e)\, a_0 \sum_{k\in\mathcal{I}_K} p_k = \log_2(e)\, \mathrm{Tr}\{\boldsymbol{K}_{\boldsymbol{h}_{\mathrm{r}}}\}\, P_{\mathrm{T}}.$$

Appendix J

Hadamard-based approximation and power allocation

This appendix presents the detailed derivation of the optimal solution to Problem H, which relies on a Hadamard-based approximation of the radar CMI. The objective function (3.37) is differentiable and the constraint set (3.39) is convex. Since Slater's condition is satisfied, the KKT conditions are both necessary and sufficient for global optimality [84, Sec. 5.5.3]. In this appendix, we derive the KKT conditions and show that they admit a unique solution. This guarantees that the resulting allocation is the unique global optimum of Problem H. The derivation follows a structure analogous to the MWF method but adapted to the modified objective induced by the Hadamard approximation.

J.1 Proof of Hadamard's inequality applied to radar CMI

Starting from the expression of the radar CMI (3.1), we note that for each realization of $\boldsymbol{x}$, the matrix $\boldsymbol{I}_K + \sigma_{n_\mathrm{r}}^{-2} \boldsymbol{K}_{\boldsymbol{g}_\mathrm{r}} \boldsymbol{D}_{|\boldsymbol{x}|^2}$ is Hermitian positive definite. By *Hadamard's inequality*, its determinant is bounded by the product of its diagonal entries, hence

$$\log_2 \det \left(\boldsymbol{I}_K + \sigma_{n_\mathrm{r}}^{-2} \boldsymbol{K}_{\boldsymbol{g}_\mathrm{r}} \boldsymbol{D}_{|\boldsymbol{x}|^2} \right) \leq \sum_{k \in \mathcal{I}_K} \log_2 \left(1 + a_k |x_k|^2 \right),$$

with a_k the per-subcarrier radar SNR from (2.39). The expectation is monotonic, hence substituting back into (3.1) gives

$$\mathrm{CMI} \leq \mathcal{E}_{\boldsymbol{x}} \left\{ \sum_{k \in \mathcal{I}_K} \log_2 \det \left(1 + a_k |x_k|^2 \right) \right\}.$$

Since the expectation is taken over a *finite constellation*, it reduces to a finite average, and linearity allows us to exchange the sum and expectation:

$$\mathrm{CMI} \leq \sum_{k \in \mathcal{I}_K} \mathcal{E}_{x_k} \left\{ \log_2 \det \left(1 + a_k |x_k|^2 \right) \right\}.$$

Writing $x_k = \sqrt{p_k}\, v_k$ with v_k unit-power, we arrive at

$$\mathrm{CMI} \leq \sum_{k \in \mathcal{I}_K} \mathcal{E}_{v_k} \left\{ \log_2 \left(1 + a_k |v_k|^2 p_k \right) \right\}.$$

J.2 Lagrangian and KKT conditions

To simplify the derivation of the Lagrangian and avoid repeated factors of $\log_2(e)$, we henceforth use natural logarithms, denoted $\log$, in place of base-2 logarithms. This is equivalent to dividing the objective function (3.37) by $\log_2(e)$, which does not affect the solution of the power allocation problem H. The Lagrangian associated with Problem H is given by [84, Ch. 5]:

$$\begin{aligned} \mathcal{L}(\boldsymbol{p}, \boldsymbol{\mu}, \lambda) = w_{\mathrm{r}} \sum_{k \in \mathcal{I}_K} \mathcal{E}_{v_k} \left\{ \log \left(1 + a_k |v_k|^2 p_k \right) \right\} \\ + w_{\mathrm{c}} \sum_{k \in \mathcal{I}_K} \frac{I_{\mathrm{c},k}(p_k)}{\log_2(e)} + \sum_{k \in \mathcal{I}_K} \mu_k p_k - \lambda \left(\sum_{k \in \mathcal{I}_K} p_k - P_{\mathrm{T}} \right) \end{aligned}$$

where $\boldsymbol{\mu} \in \mathbb{R}^K$ and $\lambda \in \mathbb{R}$ are the Lagrange multipliers associated with the inequality and equality constraints, respectively. The KKT conditions [84, Sec. 5.5.3] are:

$$\frac{d\mathcal{L}(\boldsymbol{p}, \boldsymbol{\mu}, \lambda)}{\boldsymbol{p}} = 0 \tag{J.1a}$$

$$\sum_{k \in \mathcal{I}_K} p_k = P_{\mathrm{T}} \tag{J.1b}$$

$$\forall k \in \mathcal{I}_K, \quad \mu_k \geq 0, \tag{J.1c}$$

$$\forall k \in \mathcal{I}_K, \quad p_k \mu_k = 0. \tag{J.1d}$$

Since the inequality constraints $p_k \geq 0$ are associated with slack variables μ_k, and using the expressions for the derivatives of the Lagrangian terms, namely the approximated radar CMI from Lemma 4, and the communication IR from Theorem 3.3.1, the KKT conditions simplify to the following system [84, Sec. 5.5.3]:

$$\sum_{k \in \mathcal{I}_K} p_k = P_{\mathrm{T}} \tag{J.2a}$$

$$k \in \mathcal{I}_K, \quad p_k \geq 0 \tag{J.2b}$$

$$\lambda - \left(w_{\mathrm{r}} \mathcal{E}_{v_k} \left\{ \frac{a_k |v_k|^2}{1 + a_k |v_k|^2 p_k} \right\} + w_{\mathrm{c}} c_k \mathrm{MSE}_{\mathrm{c},k}(p_k) \right) \geq 0 \tag{J.2c}$$

$$\left[\lambda - \left(w_{\mathrm{r}} \mathcal{E}_{v_k} \left\{ \frac{a_k |v_k|^2}{1 + a_k |v_k|^2 p_k} \right\} + w_{\mathrm{c}} c_k \mathrm{MSE}_{\mathrm{c},k}(p_k) \right) \right] p_k = 0. \tag{J.2d}$$

J.3 Solution for a fixed λ

We fix the Lagrange multiplier λ and show that, for any k, there exists a unique solution p_k satisfying (J.2b)–(J.2d). We define the threshold value $\lambda_k^{\text{th}} \triangleq w_{\text{r}} a_k + w_{\text{c}} c_k \geq 0$. From (J.2c), we deduce that $\lambda > 0$; otherwise, the scenario implies λ_k^{th} for all k and is thus irrelevant.

Let us define the function:

$$\begin{aligned} \ell_k : [0, +\infty) &\to [0, +\infty) \\ p_k &\mapsto w_{\text{r}} \mathcal{E}_{v_k} \left\{ \frac{a_k |v_k|^2}{1 + a_k |v_k|^2 p_k} \right\} + w_{\text{c}} c_k \text{MSE}_{\text{c},k}(p_k). \end{aligned}$$

with $\ell_k(0) = w_{\text{r}} a_k + w_{\text{c}} c_k$. We now analyze the monotonicity properties of ℓ_k, which are essential for identifying the solution.

Lemma 9. *Let $k \in \mathcal{I}_K$.*

- *If $\lambda_k^{th} = 0$, then $\ell_k(p_k) = 0$ for all $p_k \geq 0$.*
- *If $\lambda_k^{th} > 0$, then ℓ_k is strictly decreasing, continuous, and positive over $p_k \geq 0$ and we have*

$$\lim_{p_k \to 0} \ell_k(p_k) = \lambda_k^{th}, \quad \lim_{p_k \to \infty} \ell_k(p_k) = 0. \tag{J.3}$$

Proof. We use Lemma 5 and 6. □

Hence, three cases emerge according to the value of λ_k^{th}:

1. If $\lambda_k^{\text{th}} = 0$, we have necessarily $p_k = 0$. Otherwise, if $p_k > 0$, then condition (J.2d) imposes $\lambda = \ell_k(p_k) = 0$ which is not possible since $\lambda > 0$.
2. If $\lambda \geq \lambda_k^{\text{th}} > 0$, we have necessarily $p_k = 0$. Otherwise, if $p_k > 0$, then using that ℓ_k is strictly decreasing (cf.) $\ell_k(p_k) < \ell_k(0) = \lambda_k^{\text{th}} \leq \lambda$ meaning the condition (J.2d) cannot be fulfilled.
3. If $0 < \lambda < \lambda_k^{\text{th}}$, using (J.2c) we have $\ell_k(p_k) \leq \lambda < \lambda_k^{\text{th}}$ which implies $p_k > 0$. From Lemma 9 the intermediate value theorem ensures that there exists one $p_k > 0$ such that

$$\lambda = \ell_k(p_k) \tag{J.4}$$

Moreover, since ℓ_k is strictly decreasing, this solution is necessarily unique. That is,

$$\exists! \, p_k > 0 \text{ such that } \ell_k(p_k) = \lambda. \tag{J.5}$$

In other words, there is a one-to-one correspondence between each $\lambda \in (0, \lambda_k^{\text{th}})$ and a unique power allocation $p_k > 0$ satisfying the KKT condition (J.2d).

Hence, in this case, the optimal p_k is strictly positive and given by the inverse of ℓ_k:

$$p_k = \ell_k^{-1}(\lambda)$$

where $\ell_k^{-1} : (0, \lambda_k^{\text{th}}] \to [0, +\infty)$ is the inverse function of ℓ_k that is also strictly decreasing.

For any fixed $\lambda > 0$, the power allocation that satisfies the KKT conditions (J.2b)-(J.2d) is given in closed form by:

$$p_k(\lambda) \triangleq \begin{cases} 0 & \text{if } \lambda_k^{\text{th}} = 0 \\ \begin{cases} 0 & \text{if } \lambda \geq \lambda_k^{\text{th}} \\ \ell_k^{-1}(\lambda) & \text{if } \lambda < \lambda_k^{\text{th}} \end{cases} & \text{if } \lambda_k^{\text{th}} > 0 \end{cases} \tag{J.6}$$

J.4 Unique solution and optimal $\lambda^\star$

Let us consider $\lambda_k^{\text{th}} > 0$, we know that $p_k \to \ell_k(p_k)$ is strictly decreasing in p_k (see Lemma 9). Consequently, its inverse $\ell_k^{-1}(\lambda)$ is also strictly decreasing for $\lambda \in (0, \lambda_k^{\text{th}})$. Therefore, the function: $\lambda \mapsto \sum_{k \in \mathcal{I}_K} p_k(\lambda)$ is a finite sum of strictly decreasing nonnegative functions, each defined on its interval $\lambda < \lambda_k^{\text{th}}$, and equal to zero when $\lambda \geq \lambda_k^{\text{th}}$. This piecewise-defined function is strictly decreasing on the interval $(0, \lambda_{\max}^{\text{th}}]$, where $\lambda_{\max}^{\text{th}} \triangleq \max_{k \in \mathcal{I}_K} \{\lambda_k^{\text{th}}\}$, and satisfies:

$$\lim_{\lambda \to 0^+} \sum_{k \in \mathcal{I}_K} p_k(\lambda) = +\infty, \quad \text{and} \quad \sum_{k \in \mathcal{I}_K} p_k(\lambda) = 0 \text{ for } \lambda \geq \lambda_{\max}.$$

By the intermediate value theorem, there exists a unique $\lambda^\star > 0$ that verifies the equality constraint (J.2a) such that $\sum_{k \in \mathcal{I}_K} p_k(\lambda^\star) = P_{\text{T}}$.

Appendix K

MMSE estimator under a well-designed CP

This appendix details how a well-designed CP allows the MMSE estimator to be implemented efficiently in the frequency domain. We proceed step by step: first rewriting $\boldsymbol{A}_{\mathrm{r}}$ (2.29), then exploiting CP circularity, then diagonalizing via FFT.

K.1 Observation matrix under the range-unambiguous assumption

Recalling that the target is range-unambiguous (i.e., $\ell_{0,i} < L$, for $i \in \mathcal{I}_{L_{\mathrm{r}}}$), the matrix (2.29) can first be written as

$$\boldsymbol{A}_{\mathrm{r}} = \begin{pmatrix} e^{2j\pi f_d 0} \boldsymbol{F}_K \boldsymbol{D}_{\boldsymbol{w}_{f_d}} \boldsymbol{R}_{\Delta_{\mathrm{CP}}} \boldsymbol{S}_0 \boldsymbol{P}_{\mathrm{r},1} \\ \vdots \\ e^{2j\pi f_d (M-1)} \boldsymbol{F}_K \boldsymbol{D}_{\boldsymbol{w}_{f_d}} \boldsymbol{R}_{\Delta_{\mathrm{CP}}} \boldsymbol{S}_{M-1} \boldsymbol{P}_{\mathrm{r},1} \end{pmatrix} \tag{K.1}$$

with $\boldsymbol{P}_{\mathrm{r},1}$ and $\boldsymbol{w}_{f_d}$ defined in (2.37) and (5.7), respectively, and for $m \in \mathcal{I}_M$,

$$\boldsymbol{S}_m \triangleq [\boldsymbol{S}]_{mL \le i \le (m+1)L-1, 1 \le j \le L}. \tag{K.2}$$

K.2 Exploiting CP-induced circularity

Let $\boldsymbol{s}_m$ denote the mth L-length block of $\boldsymbol{s}$ in (2.5), i.e.,

$$\boldsymbol{s}_m = \boldsymbol{T}_{\Delta_{\mathrm{CP}}} \boldsymbol{F}_K^{\mathsf{H}} \boldsymbol{x}_m. \tag{K.3}$$

For a well-designed CP, the first and last Δ_{CP} elements of $\boldsymbol{s}_m$ are identical by construction. This yields, for $m \in \mathcal{I}_M$

$$\boldsymbol{R}_{\Delta_{\mathrm{CP}}} \boldsymbol{S}_m \boldsymbol{P}_{\mathrm{r},1} = \mathrm{circ}\left\{ \boldsymbol{R}_{\Delta_{\mathrm{CP}}} \boldsymbol{s}_m \right\} \boldsymbol{Q}_{\Delta_{\mathrm{CP}}} \boldsymbol{P}_{\mathrm{r},1} \tag{K.4}$$

with $\boldsymbol{Q}_{\Delta_{\mathrm{CP}}}$ defined in (2.36).
Injecting (K.3) in (K.4) and observing $\boldsymbol{R}_{\Delta_{\mathrm{CP}}}\boldsymbol{T}_{\Delta_{\mathrm{CP}}} = \boldsymbol{I}_K$ yields

$$\boldsymbol{R}_{\Delta_{\mathrm{CP}}}\boldsymbol{S}_m\boldsymbol{P}_{\mathrm{r},1} = \mathrm{circ}\left\{\boldsymbol{F}_K^{\mathsf{H}}\boldsymbol{x}_m\right\}\boldsymbol{Q}_{\Delta_{\mathrm{CP}}}\boldsymbol{P}_{\mathrm{r},1}. \tag{K.5}$$

K.3 Fourier diagonalization of circulant matrices

Since any circulant matrix is diagonal in the Fourier basis, (K.5) results in

$$\boldsymbol{R}_{\Delta_{\mathrm{CP}}}\boldsymbol{S}_m\boldsymbol{P}_{\mathrm{r},1} = \sqrt{K}\boldsymbol{F}_K^{\mathsf{H}}\boldsymbol{D}_{\boldsymbol{x}_m}\boldsymbol{F}_K\boldsymbol{Q}_{\Delta_{\mathrm{CP}}}\boldsymbol{P}_{\mathrm{r},1}. \tag{K.6}$$

Using the definition (2.35) of $\boldsymbol{B}_{\mathrm{r}}$ in (K.6), we can rewrite (K.1) as

$$\boldsymbol{A}_{\mathrm{r}} = \begin{pmatrix} e^{2j\pi f_d 0}\boldsymbol{F}_K\boldsymbol{D}_{\boldsymbol{w}_{f_d}}\boldsymbol{F}_K^{\mathsf{H}}\boldsymbol{D}_{\boldsymbol{x}_0}\boldsymbol{B}_{\mathrm{r}} \\ \vdots \\ e^{2j\pi f_d(M-1)}\boldsymbol{F}_K\boldsymbol{D}_{\boldsymbol{w}_{f_d}}\boldsymbol{F}_K^{\mathsf{H}}\boldsymbol{D}_{\boldsymbol{x}_{M-1}}\boldsymbol{B}_{\mathrm{r}} \end{pmatrix}. \tag{K.7}$$

Using (K.7), it is then straightforward to obtain for a well-designed CP

$$\boldsymbol{A}_{\mathrm{r}}^{\mathsf{H}}\boldsymbol{A}_{\mathrm{r}} = \boldsymbol{B}_{\mathrm{r}}^{\mathsf{H}}\boldsymbol{D}_{\sum_{m=0}^{M-1}|\boldsymbol{x}_m|^2}\boldsymbol{B}_{\mathrm{r}}$$

and with (2.28)

$$\boldsymbol{A}_{\mathrm{r}}^{\mathsf{H}}\tilde{\boldsymbol{x}}_{\mathrm{r}} = \boldsymbol{B}_{\mathrm{r}}^{\mathsf{H}}\sum_{m=0}^{M-1}\boldsymbol{D}_{\boldsymbol{x}_m}^{\mathsf{H}}\boldsymbol{F}_K\boldsymbol{D}_{\boldsymbol{w}_{f_d}}^{\mathsf{H}}\boldsymbol{R}_{\Delta_{\mathrm{CP}}}\boldsymbol{y}_{\mathrm{r},m}e^{-2j\pi f_d m}$$

where $\boldsymbol{y}_{\mathrm{r},m}$ is the mth L-length block of $\boldsymbol{y}_{\mathrm{r}}$.

Using the simplified expressions for $\boldsymbol{A}_{\mathrm{r}}^{\mathsf{H}}\boldsymbol{A}_{\mathrm{r}}$ and $\boldsymbol{A}_{\mathrm{r}}^{\mathsf{H}}\tilde{\boldsymbol{x}}_{\mathrm{r}}$, the implementation of the MMSE estimator can be simplified.

Bibliography

[1] A. Hassanien et al. "Dual-Function Radar Communication Systems: A Solution to the Spectrum Congestion Problem." In: *IEEE Signal Process. Mag.* 36.5 (Sept. 2019), pp. 115–126. DOI: 10.1109/MSP.2019.2900571 (cit. on pp. 1, 7, 8).

[2] Y. L. Sit et al. "Extension of the OFDM joint radar-communication system for a multipath, multiuser scenario." In: *Proc. IEEE Radar Conf.* 2011, pp. 718–723. DOI: 10.1109/RADAR.2011.5960632 (cit. on p. 1).

[3] C. Sturm, T. Zwick, and W. Wiesbeck. "An OFDM system concept for joint radar and communications operations." In: *Proc. IEEE Veh. Technol. Conf.* 2009, pp. 1–5. DOI: 10.1109/VETECS.2009.5073387 (cit. on pp. 1, 6, 12).

[4] T. M. Cover and J. A. Thomas. *Elements of Information Theory*. Wiley, Hoboken, NJ, USA, 2006. ISBN: 0471241954 (cit. on pp. 1, 14, 15, 34, 38, 46–48, 50, 55, 68, 137).

[5] M. R. Bell. "Information theory and radar waveform design." In: *IEEE Trans. Inf. Theory* 39.5 (1993), pp. 1578–1597. DOI: 10.1109/18.259642 (cit. on pp. 1, 16, 35).

[6] Y. Cui et al. "Integrating sensing and communications for ubiquitous IoT: Applications, trends, and challenges." In: *IEEE Netw.* 35.5 (2021), pp. 158–167. DOI: 10.1109/MNET.010.2100152 (cit. on p. 5).

[7] U.S. Government Accountability Office. *Spectrum management: Key practices could help address challenges to improving receiver performance*. Report to Congressional Committees GAO-24-106325. U.S. Government Accountability Office, July 2024. URL: https://www.gao.gov/assets/gao-24-106325.pdf (cit. on p. 6).

[8] H. Griffiths et al. "Radar Spectrum Engineering and Management: Technical and Regulatory Issues." In: *Proc. IEEE* 103.1 (2015), pp. 85–102. DOI: 10.1109/JPROC.2014.2365517 (cit. on p. 6).

[9] Defense Advanced Research Projects Agency (DARPA). *Shared Spectrum Access for Radar and Communications (SSPARC)*. 2017. URL: https://www.darpa.mil/research/programs/shared-spectrum-access-for-radar-and-communications (visited on 08/26/2025) (cit. on p. 6).

[10] National Telecommunications and Information Administration (NTIA). *NTIA, FCC and Navy work to expand innovative 3.5 GHz spectrum sharing framework*. Nov. 2024. URL: https://www.ntia.gov/press-release/2024/ntia-fcc-navy-work-expand-innovative-35-ghz-spectrum-sharing-framework (visited on 08/26/2025) (cit. on p. 6).

[11] *Technical Interference Mitigation Measures to Protect the Radio Astronomy Service (RAS) Against Interference from Ground-Based Vehicular Radars in the 77 GHz to 81 GHz Frequency Band*. Technical Report ETSI TR 104 098 V1.1.1. European Telecommunications Standards Institute (ETSI), May 2025. URL: https://www.etsi.org/deliver/etsi_tr/104000_104099/104098/01.01.01_60/tr_104098v010101p.pdf (cit. on p. 6).

[12] *Wireless Communication Technologies and Signal Processing – Standardisation and Follow-up/PoCs*. HORIZON-JU-SNS-2025-01-STREAM-B-02, Horizon Europe, Smart Networks and Services Joint Undertaking (SNS JU). Ministère de l'Enseignement Supérieur et de la Recherche (France). May 2025. URL: https://www.horizon-europe.gouv.fr/wireless-communication-technologies-and-signal-processing-standardisation-and-follow-uppocs-39426 (cit. on p. 6).

[13] B. Paul, A. R. Chiriyath, and D. W. Bliss. "Survey of RF Communications and Sensing Convergence Research." In: *IEEE Access* 5 (Dec. 2016), pp. 252–270. DOI: 10.1109/ACCESS.2016.2639038 (cit. on p. 6).

[14] F. Liu et al. "Joint Radar and Communication Design: Applications, State-of-the-Art, and the Road Ahead." In: *IEEE Trans. Commun.* 68.6 (June 2020), pp. 3834–3862. DOI: 10.1109/TCOMM.2020.2973976 (cit. on p. 6).

[15] J. A. Zhang et al. "An overview of signal processing techniques for joint communication and radar sensing." In: *IEEE J. Sel. Top. Signal Process.* 15.6 (Nov. 2021), pp. 1295–1315. DOI: 10.1109/JSTSP.2021.3113120 (cit. on p. 6).

[16] N. C. Luong et al. "Radio Resource Management in Joint Radar and Communication: A Comprehensive Survey." In: *IEEE Commun. Surv. Tutor.* 23.2 (2021), pp. 780–814. DOI: 10.1109/COMST.2021.3070399 (cit. on p. 6).

[17] Y. Liu et al. "Adaptive OFDM integrated radar and communications waveform design based on information theory." In: *IEEE Commun. Lett.* 21.10 (Oct. 2017), pp. 2174–2177. DOI: 10.1109/LCOMM.2017.2723890 (cit. on pp. 7, 14, 17, 134, 135).

[18] A. Martone and M. Amin. "A view on radar and communication systems coexistence and dual functionality in the era of spectrum sensing." In: *Digit. Signal Process.* 119 (2021), p. 103135 (cit. on p. 7).

[19] R. Saruthirathanaworakun, J. M. Peha, and L. M. Correia. "Opportunistic Sharing Between Rotating Radar and Cellular." In: *IEEE J. Sel. Areas Commun.* 30.10 (2012), pp. 1900–1910. DOI: 10.1109/JSAC.2012.121106 (cit. on p. 7).

[20] F. Liu et al. "Interfering Channel Estimation in Radar-Cellular Coexistence: How Much Information Do We Need?" In: *IEEE Trans. Wireless Commun.* 18.9 (2019), pp. 4238–4253. DOI: 10.1109/TWC.2019.2921556 (cit. on p. 7).

[21] N. Parveen et al. "Coexistence in wireless networks: Challenges and opportunities." In: *Telecom* 6.2 (2025), p. 23. DOI: 10.3390/telecom6020023 (cit. on p. 7).

[22] S. Parvin et al. "Cognitive radio network security: A survey." In: *J. Netw. Comput. Appl.* 35.6 (2012), pp. 1691–1708. DOI: 10.1016/j.jnca.2012.06.006. URL: https://www.sciencedirect.com/science/article/pii/S1084804512001518 (cit. on p. 8).

[23] X. Hu et al. *MIMO-OFDM Dual-Functional Radar-Communication Systems: Low-PAPR Waveform Design*. Sept. 2021. arXiv: 2109.13148 [eess.SP] (cit. on p. 9).

[24] X. Hu et al. "Low-PAPR DFRC MIMO-OFDM Waveform Design for Integrated Sensing and Communications." In: *Proc. IEEE Int. Conf. Commun.* May 2022, pp. 1599–1604. DOI: 10.1109/ICC45855.2022.9838548 (cit. on p. 9).

[25] A. Hanif et al. "Exploring the Synergy: A Review of Dual-Functional Radar Communication Systems." In: *IEEE Aerosp. Electron. Syst. Mag.* (2025), pp. 1–26. DOI: 10.1109/MAES.2025.3551690 (cit. on p. 9).

[26] M. A. Richards, J. A. Scheer, and W. A. Holm. *Principles of Modern Radar*. Raleigh, NC: SciTech Publishing, 2010. ISBN: 978-1-891121-52-4 (cit. on pp. 10, 11, 24, 25).

[27] R. M. Mealey. "A Method for Calculating Error Probabilities in a Radar Communication System." In: *IEEE Trans. Space. El. Tel.* 9.2 (1963), pp. 37–42. DOI: 10.1109/TSET.1963.4337601 (cit. on p. 11).

[28] M. Roberton and E. R. Brown. "Integrated radar and communications based on chirped spread-spectrum techniques." In: *Proc. IEEE MTT-S Int. Microw. Symp. Dig.* Vol. 1. 2003, 611–614 vol.1. DOI: 10.1109/MWSYM.2003.1211013 (cit. on p. 11).

[29] S. D. Blunt, P. Yatham, and J. Stiles. "Intrapulse radar-embedded communications." In: *IEEE Trans. Aerosp. Electron. Syst.* 46.3 (2010), pp. 1185–1200. DOI: 10.1109/TAES.2010.5545182 (cit. on p. 11).

[30] M. Jamil, H.-J. Zepernick, and M. I. Pettersson. "On integrated radar and communication systems using Oppermann sequences." In: *Proc. IEEE Mil. Commun. Conf.* 2008, pp. 1–6. DOI: 10.1109/MILCOM.2008.4753277 (cit. on p. 11).

[31] K. V. Mishra et al. "Toward millimeter-wave joint radar communications: A signal processing perspective." In: *IEEE Signal Process. Mag.* 36.5 (2019), pp. 100–114. DOI: 10.1109/MSP.2019.2913173 (cit. on p. 11).

[32] P. Kumari et al. "IEEE 802.11ad-Based Radar: An Approach to Joint Vehicular Communication-Radar System." In: *IEEE Trans. Veh. Technol.* 67.4 (2018), pp. 3012–3027. DOI: 10.1109/TVT.2017.2774762 (cit. on p. 11).

[33] S. Mazahir, Sajid S. Ahmed, and M. S. Alouini. "A Survey on Joint Communication-Radar Systems." In: *Frontiers in Commun. and Netw.* 1 (2021), p. 9. ISSN: 2673-530X. DOI: 10.3389/frcmn.2020.619483 (cit. on p. 11).

[34] D. Li, B. Tang, and L. Xue. "Waveform design for MIMO DFRC systems: Finer sensing and safer communications." In: *IEEE Trans. Signal Process.* 72 (2024), pp. 4509–4524. DOI: 10.1109/TSP.2024.3470219 (cit. on p. 12).

[35] Z. Xiao and Y. Zeng. "Integrated sensing and communication with delay alignment modulation: Performance analysis and beamforming optimization." In: *IEEE Trans. Wireless Commun.* 22.12 (2023), pp. 8904–8918. DOI: 10.1109/TWC.2023.3266758 (cit. on p. 12).

[36] L. Dai et al. "FBMC-chirp waveforms for joint wireless communication and SAR imaging." In: *IEEE Trans. Veh. Technol.* (2025), pp. 1–14. DOI: 10.1109/TVT.2025.3571915 (cit. on p. 12).

[37] G. Liu et al. "Joint radar communication system design based on filter bank multicarrier modulation scheme." In: *IET Radar Sonar Navig.* 17.1 (2023), pp. 47–62. DOI: 10.1049/rsn2.12323. URL: https://ietresearch.onlinelibrary.wiley.com/doi/abs/10.1049/rsn2.12323 (cit. on p. 12).

[38] C. D. Ozkaptan et al. "OFDM pilot-based radar for joint vehicular communication and radar systems." In: *Proc. IEEE Veh. Netw. Conf.* 2018, pp. 1–8. DOI: 10.1109/VNC.2018.8628347 (cit. on p. 13).

[39] G. Song, J. Bai, and G. Wei. "An OTFS-DFRC waveform design method based on phase perturbation." In: *IEEE Commun. Lett.* 27.10 (2023), pp. 2578–2582. DOI: 10.1109/LCOMM.2023.3303538 (cit. on p. 13).

[40] R. Hadani et al. "Orthogonal time frequency space modulation." In: *Proc. IEEE Wireless Commun. Netw. Conf.* 2017, pp. 1–6. DOI: 10.1109/WCNC.2017.7925924 (cit. on p. 13).

[41] G. D. Surabhi, R. M. Augustine, and A. Chockalingam. "Peak-to-average power ratio of OTFS modulation." In: *IEEE Commun. Lett.* 23.6 (2019), pp. 999–1002. DOI: 10.1109/LCOMM.2019.2914042 (cit. on p. 13).

[42] L. Gaudio et al. "Performance analysis of joint radar and communication using OFDM and OTFS." In: *Proc. IEEE Int. Conf. Commun. Workshops*. 2019, pp. 1–6. DOI: 10.1109/ICCW.2019.8757044 (cit. on p. 13).

[43] M. F. Munir et al. "Next-gen solutions: Deep learning-enhanced design of joint cognitive radar and communication systems for noisy channel environments." In: *Comput. Electr. Eng.* 120 (2024), p. 109663. DOI: 10.1016/j.compeleceng.2024.109663. URL: https://www.sciencedirect.com/science/article/pii/S0045790624005901 (cit. on p. 13).

[44] A. Ahmed et al. "OFDM-based joint radar-communication system: Optimal subcarrier allocation and power distribution by exploiting mutual information." In: *Proc. Asilomar Conf. on Signals, Syst., and Comput.* Nov. 2019, pp. 559–563. DOI: 10.1109/IEEECONF44664.2019.9049009 (cit. on pp. 14, 17).

[45] X. Yuan et al. "Spatio-Temporal Power Optimization for MIMO Joint Communication and Radio Sensing Systems With Training Overhead." In: *IEEE Trans. Veh. Technol.* 70.1 (Jan. 2021), pp. 514–528. DOI: 10.1109/TVT.2020.3046438 (cit. on pp. 14, 17).

[46] A. Lozano, A. M. Tulino, and S. Verdú. "Optimum power allocation for parallel Gaussian channels with arbitrary input distributions." In: *IEEE Trans. Inf. Theory* 52.7 (July 2006), pp. 3033–3051. DOI: 10.1109/TIT.2006.876220 (cit. on pp. 15, 41, 57, 59, 82).

[47] J. G. Proakis and M. Salehi. *Digital Communications*. 5th ed. Boston, MA, USA: McGraw-Hill Education, 2007. ISBN: 978-0-07-295716-7 (cit. on pp. 15, 81).

[48] D. Tse and P. Viswanath. *Fundamentals of Wireless Communication*. Cambridge, U.K.: Cambridge Univ. Press, 2005 (cit. on pp. 15, 28).

[49] A. Lozano, A. M. Tulino, and S. Verdu. "Optimum power allocation for multiuser OFDM with arbitrary signal constellations." In: *IEEE Trans. Commun.* 56.5 (2008), pp. 828–837. DOI: 10.1109/TCOMM.2008.060211 (cit. on p. 15).

[50] D. Guo, S. Shamai, and S. Verdu. "Mutual information and minimum mean-square error in Gaussian channels." In: *IEEE Trans. Inf. Theory* 51.4 (Apr. 2005), pp. 1261–1282. DOI: 10.1109/TIT.2005.844072 (cit. on pp. 16, 57).

[51] D. P. Palomar and S. Verdu. "Gradient of mutual information in linear vector Gaussian channels." In: *IEEE Trans. Inf. Theory* 52.1 (Jan. 2006), pp. 141–154. DOI: 10.1109/TIT.2005.860424 (cit. on p. 16).

[52] Y. Yang and R. S. Blum. "MIMO radar waveform design based on mutual information and minimum mean-square error estimation." In: *IEEE Trans. Aerosp. Electron. Syst.* 43.1 (Jan. 2007), pp. 330–343. DOI: 10.1109/TAES.2007.357137 (cit. on p. 16).

[53] Y. Yang and R. S. Blum. "Minimax robust MIMO radar waveform design." In: *IEEE J. Sel. Top. Signal Process.* 1.1 (June 2007), pp. 147–155. DOI: 10.1109/JSTSP.2007.897056 (cit. on p. 16).

[54] B. Tang, J. Tang, and Y. Peng. "MIMO radar waveform design in colored noise based on information theory." In: *IEEE Trans. Signal Process.* 58.9 (Sept. 2010), pp. 4684–4697. DOI: 10.1109/TSP.2010.2050885 (cit. on p. 16).

[55] X. Song et al. "The MIMO radar and jammer games." In: *IEEE Trans. Signal Process.* 60.2 (Feb. 2012), pp. 687–699. DOI: 10.1109/TSP.2011.2169251 (cit. on p. 16).

[56] W. Zhang and L. Yang. "Communications-Inspired Sensing: A Case Study on Waveform Design." In: *IEEE Trans. Signal Process.* 58.2 (Feb. 2010), pp. 792–803. DOI: 10.1109/TSP.2009.2028941 (cit. on p. 16).

[57] A. Leshem, O. Naparstek, and A. Nehorai. "Information-theoretic adaptive radar waveform design for multiple extended targets." In: *IEEE J. Sel. Top. Signal Process.* 1.1 (June 2007), pp. 42–55. DOI: 10.1109/JSTSP.2007.897047 (cit. on pp. 16, 51).

[58] R. A. Romero, J. Bae, and N. A. Goodman. "Theory and application of SNR and mutual information matched illumination waveforms." In: *IEEE Trans. Aerosp. Electron. Syst.* 47.2 (Apr. 2011), pp. 912–927. DOI: 10.1109/TAES.2011.5751234 (cit. on p. 16).

[59] Y. Gu and N. A. Goodman. "Information-theoretic waveform design for Gaussian mixture radar target profiling." In: *IEEE Trans. Aerosp. Electron. Syst.* 55.3 (June 2019), pp. 1528–1536. DOI: 10.1109/TAES.2018.2881365 (cit. on p. 16).

[60] A. De Maio and M. Lops. "Design principles of MIMO radar detectors." In: *IEEE Trans. Aerosp. Electron. Syst.* 43.3 (July 2007), pp. 886–898. DOI: 10.1109/TAES.2007.4383581 (cit. on p. 16).

[61] A. De Maio, M. Lops, and L. Venturino. "Diversity-integration tradeoffs in MIMO detection." In: *IEEE Trans. Signal Process.* 56.10 (Oct. 2008), pp. 5051–5061. DOI: 10.1109/TSP.2008.928693 (cit. on p. 16).

[62] M. M. Naghsh et al. "Unified optimization framework for multi-static radar code design using information-theoretic criteria." In: *IEEE Trans. Signal Process.* 61.21 (Nov. 2013), pp. 5401–5416. DOI: 10.1109/TSP.2013.2278154 (cit. on p. 16).

[63] M. M. Naghsh et al. "An information-theoretic approach to robust constrained code design for MIMO radars." In: *IEEE Trans. Signal Process.* 65.14 (July 2017), pp. 3647–3661. DOI: 10.1109/TSP.2017.2692747 (cit. on p. 16).

[64] L. Zheng et al. "Joint design of overlaid communication systems and pulsed radars." In: *IEEE Trans. Signal Process.* 66.1 (Jan. 2018), pp. 139–154. DOI: 10.1109/TSP.2017.2755603 (cit. on p. 17).

[65] J. Qian et al. "Joint system design for coexistence of MIMO radar and MIMO communication." In: *IEEE Trans. Signal Process.* 66.13 (July 2018), pp. 3504–3519. DOI: 10.1109/TSP.2018.2831624 (cit. on p. 17).

[66] M. Bică and V. Koivunen. "Multicarrier radar-communications waveform design for RF convergence and coexistence." In: *Proc. IEEE Int. Conf. Acoust., Speech, Signal Process.* May 2019, pp. 7780–7784. DOI: 10.1109/ICASSP.2019.8683655 (cit. on p. 17).

[67] S. H. Dokhanchi et al. "Multi-constraint Spectral Co-design for Colocated MIMO Radar and MIMO Communications." In: *Proc. IEEE Int. Conf. Acoust., Speech, Signal Process.* May 2020, pp. 4567–4571. DOI: 10.1109/ICASSP40776.2020.9054680 (cit. on p. 17).

[68] Y. Liu, G. Liao, and Z. Yang. "Robust OFDM integrated radar and communications waveform design based on information theory." In: *Signal Process.* 162 (Sept. 2019), pp. 317–329. ISSN: 0165-1684. DOI: https://doi.org/10.1016/j.sigpro.2019.05.001 (cit. on p. 17).

[69] C. Shi et al. "Joint Optimization Scheme for Subcarrier Selection and Power Allocation in Multicarrier Dual-Function Radar-Communication System." In: *IEEE Syst. J.* 15.1 (Mar. 2021), pp. 947–958. DOI: 10.1109/JSYST.2020.2984637 (cit. on p. 17).

[70] C. Pozrikidis. *An Introduction to Grids, Graphs, and Networks*. New York, NY, USA: Oxford Univ. Press, 2014. ISBN: 9780199996728 (cit. on pp. 20, 140).

[71] G. Matz, H. Bölcskei, and F. Hlawatsch. "Time-frequency foundations of communications: Concepts and tools." In: *IEEE Signal Process. Mag.* 30.6 (2013), pp. 87–96. DOI: 10.1109/MSP.2013.2269702 (cit. on p. 21).

[72] S. Weinstein and P. Ebert. "Data Transmission by Frequency-Division Multiplexing Using the Discrete Fourier Transform." In: *IEEE J. Sel. Areas Commun.* 19.5 (Oct. 1971), pp. 628–634. DOI: 10.1109/TCOM.1971.1090705 (cit. on p. 22).

[73] A. Peled and A. Ruiz. "Frequency domain data transmission using reduced computational complexity algorithms." In: *Proc. IEEE Int. Conf. Acoust., Speech, Signal Process.* Vol. 5. Apr. 1980, pp. 964–967. DOI: 10.1109/ICASSP.1980.1171076 (cit. on p. 22).

[74] E. Telatar. "Capacity of multi-antenna Gaussian channels." In: *Eur. Trans. Telecommun.* 10.6 (1999), pp. 585–595 (cit. on pp. 23, 46).

[75] J. Villares and G. Vazquez. "The Gaussian Assumption in Second-Order Estimation Problems in Digital Communications." In: *IEEE Trans. Signal Process.* 55.10 (2007), pp. 4994–5002. DOI: 10.1109/TSP.2007.897872 (cit. on pp. 23, 46).

[76] V. C. Chen et al. "Micro-Doppler effect in radar: phenomenon, model, and simulation study." In: *IEEE Trans. Aerosp. Electron. Syst.* 42.1 (2006), pp. 2–21. DOI: 10.1109/TAES.2006.1603402 (cit. on p. 24).

[77] H. L. Van Trees. *Detection, Estimation, and Modulation Theory, Part III: Radar-Sonar Signal Processing and Gaussian Signals in Noise*. Wiley Series in Telecommunications and Signal Processing. Wiley, 2001. ISBN: 9780471093909 (cit. on p. 26).

[78] Z. Wang and G. B. Giannakis. "Wireless multicarrier communications." In: *IEEE Signal Process. Mag.* 17.3 (2000), pp. 29–48 (cit. on p. 28).

[79] C. M. Bishop. *Pattern Recognition and Machine Learning*. New York, NY, USA: Springer, 2006 (cit. on p. 36).

[80] S. M. Kay. *Fundamentals of Statistical Signal Processing: Estimation Theory*. Englewood Cliffs, NJ, USA: Prentice Hall, 1993 (cit. on pp. 37, 115, 116).

[81] S. Haykin. *Communication Systems*. 4th ed. Hoboken, NJ, USA: Wiley & Sons, Inc., 2001 (cit. on p. 38).

[82] A. T. Asyhari. "New bounds on the mutual information for discrete constellations and application to wireless channel estimation." In: *Digit. Commun. Netw.* 6.4 (2020), pp. 542–546. DOI: 10.1016/j.dcan.2020.04.001. URL: https://www.sciencedirect.com/science/article/pii/S2352864819300185 (cit. on p. 40).

[83] F. J. García-Gómez. *Numerically Computing Achievable Rates of Memoryless Channels*. Tutorial note mediaTUM 1533663. Technical University of Munich, Institute for Communications Engineering (LNT), Jan. 2020. URL: https://mediatum.ub.tum.de/doc/1533663/file.pdf (visited on 09/22/2025) (cit. on p. 40).

[84] S. Boyd and L. Vandenberghe. *Convex Optimization*. Cambridge, U.K.: Cambridge Univ. Press, 2004. ISBN: 0521833787 (cit. on pp. 47, 49, 52, 58, 68, 126, 128, 132, 147, 148).

[85] N. Bekkali et al. "Mutual Information-Driven Power Allocation in OFDM Dual-Function Radar-Communication Systems." In: *IEEE Trans. Radar Syst.* 1 (2023), pp. 605–622. DOI: 10.1109/TRS.2023.3322961 (cit. on pp. 47, 63, 77, 87).

[86] N. Bekkali et al. "Optimal Power Allocation in Monostatic OFDM Joint Radar Communications Systems." In: *Proc. IEEE Radar Conf.* Mar. 2022, pp. 1–6. DOI: 10.1109/RadarConf2248738.2022.9764299 (cit. on p. 48).

[87] W. Rudin. *Principles of Mathematical Analysis*. 3rd ed. New York, NY, USA: McGraw-Hill (Inc.), 1976 (cit. on p. 49).

[88] M. Grant and S. Boyd. *CVX: Matlab Software for Disciplined Convex Programming, version 2.1*. http://cvxr.com/cvx. Mar. 2014 (cit. on pp. 49, 99).

[89] M. Grant and S. Boyd. "Graph implementations for nonsmooth convex programs." In: *Recent Adv. in Learn. and Control*. Ed. by V. Blondel, S. Boyd, and H. Kimura. Lecture Notes in Control and Information Sciences. http://stanford.edu/~boyd/graph_dcp.html. Springer-Verlag Limited, 2008, pp. 95–110 (cit. on pp. 49, 99).

[90] R. P. Brent. *Algorithms for Minimization without Derivatives*. Englewood Cliffs, NJ, USA: Prentice Hall, 1973. ISBN: 0-13-022335-2 (cit. on pp. 52, 59).

[91] N. Bekkali et al. "Mutual Information-Driven Power Allocation in OFDM-DFRC Systems with Discrete Signaling." In: *IEEE Trans. Radar Syst.* (2026). Under review (cit. on pp. 54, 63).

[92] N. Bekkali et al. "The Price of Information in OFDM-DFRC Systems." In: *Proc. IEEE Radar Conf.* 2024, pp. 1–6. DOI: 10.1109/RadarConf2458775.2024.10548514 (cit. on pp. 63, 76).

[93] C. P. Robert and G. Casella. *Monte Carlo Statistical Methods*. 2nd ed. New York, NY, USA: Springer, 2004 (cit. on p. 67).

[94] D. P. Palomar and J. R. Fonollosa. "Practical algorithms for a family of waterfilling solutions." In: *IEEE Trans. Signal Process.* 53.2 (Feb. 2005), pp. 686–695. DOI: 10.1109/TSP.2004.840816 (cit. on p. 68).

[95] P. Setlur, N. Devroye, and M. Rangaswamy. "Radar waveform design with the two step mutual information." In: *Proc. IEEE Radar Conf.* May 2014, pp. 1317–1322. DOI: 10.1109/RADAR.2014.6875803 (cit. on p. 69).

[96] F. Liu et al. "Deterministic-random tradeoff of integrated sensing and communications in Gaussian channels: A rate-distortion perspective." In: *Proc. IEEE Int. Symp. Inf. Theory*. 2023, pp. 2326–2331. DOI: 10.1109/ISIT54713.2023.10206462 (cit. on p. 79).

[97] Y. Xiong et al. "On the fundamental tradeoff of integrated sensing and communications under Gaussian channels." In: *IEEE Trans. Inf. Theory* 69.9 (2023), pp. 5723–5751. DOI: 10.1109/TIT.2023.3284449 (cit. on pp. 79, 88).

[98] N. Bekkali, S. Bidon, and D. Roque. "OFDM-DFRC waveform design based on mutual information in presence of Doppler." In: *Proc. Int. Radar Conf.* 2024, pp. 1–6. DOI: 10.1109/RADAR58436.2024.10993945 (cit. on p. 94).

[99] G. Goertzel. "An algorithm for the evaluation of finite trigonometric series." In: *Amer. Math. Monthly* 65.1 (Jan. 1958), pp. 34–35 (cit. on p. 97).

[100] S. Haykin. "Cognitive radar: A way of the future." In: *IEEE Signal Process. Mag.* 23.1 (2006), pp. 30–40. DOI: 10.1109/MSP.2006.1593335 (cit. on p. 108).

[101] J. Barnard, R. McCulloch, and X.-L. Meng. "Modelling covariance matrices in terms of standard deviations and correlations, with application to shrinkage." In: *Statist. Sinica* 10 (Oct. 2000), pp. 1281–1311 (cit. on p. 108).

[102] L. Wang and C. Tellambura. "A simplified clipping and filtering technique for PAR reduction in OFDM systems." In: *IEEE Signal Process. Lett.* 12.6 (2005), pp. 453–456. DOI: 10.1109/LSP.2005.847886 (cit. on p. 109).

[103] C. Chen et al. "Wi-Fi Sensing Based on IEEE 802.11bf." In: *IEEE Communications Magazine* 61.1 (2023), pp. 121–127. DOI: 10.1109/MCOM.007.2200347 (cit. on p. 121).

[104] C. Tellambura. "Computation of the continuous-time PAR of an OFDM signal with BPSK subcarriers." In: *IEEE Commun. Lett.* 5.5 (2001), pp. 185–187. DOI: 10.1109/4234.922754 (cit. on p. 121).

[105] Tao Jiang et al. "Derivation of PAPR Distribution for OFDM Wireless Systems Based on Extreme Value Theory." In: *IEEE Trans. Wireless Commun.* 7.4 (2008), pp. 1298–1305. DOI: 10.1109/TWC.2008.060862 (cit. on p. 121).

[106] H. Ochiai and H. Imai. "On the distribution of the peak-to-average power ratio in OFDM signals." In: *IEEE Trans. Commun.* 49.2 (2001), pp. 282–289. DOI: 10.1109/26.905885 (cit. on p. 122).

[107] S. H. Han and J. H. Lee. "An overview of peak-to-average power ratio reduction techniques for multicarrier transmission." In: *IEEE Wireless Commun.* 12.2 (2005), pp. 56–65. DOI: 10.1109/MWC.2005.1421929 (cit. on p. 122).

[108] G. Wunder et al. "The PAPR Problem in OFDM Transmission: New Directions for a Long-Lasting Problem." In: *IEEE Signal Process. Mag.* 30.6 (2013), pp. 130–144. DOI: 10.1109/MSP.2012.2218138 (cit. on p. 122).

[109] D. Poole. *Linear Algebra: A Modern Introduction*. Boston, MA: Brooks/Cole, 2005 (cit. on p. 127).

[110] P. J. Davis. *Circulant Matrices*. NY, USA: Wiley, 1979 (cit. on p. 137).

[111] M. Dörpinghaus et al. "A log-det inequality for random matrices." In: *SIAM J. Matrix Anal. Appl.* 36.3 (2015), pp. 1164–1179. DOI: 10.1137/140954647 (cit. on p. 141).

[112] M. Abramowitz and I. A. Stegun. *Handbook of Mathematical Functions with Formulas, Graphs, and Mathematical Tables*. Vol. 55. Applied Mathematics Series. Reprinted by Dover Publications, 1972. Washington, D.C.: National Bureau of Standards, 1964 (cit. on pp. 142, 143).

Abstract — English and French versions

Abstract — This PhD thesis investigates the design of Dual-Function Radar-Communication (DFRC) waveforms based on Cyclic Prefix (CP)-Orthogonal Frequency Division Multiplexing (OFDM). The principal methodological difficulty is conceptual: radar systems typically assume deterministic transmitted signals, whereas communication requires random, information-bearing symbols. To reconcile these views, we propose an information-theoretic framework that pairs radar Conditional Mutual Information (CMI), which is the radar Mutual Information (MI) averaged over all possible realizations of the transmitted symbols, with the communication Information Rate (IR). These formulations preserve the randomness of the transmitted symbols required for communication while yielding a radar metric that is well-defined and interpretable.

Within this framework, we formulate waveform design as a subcarrier power allocation optimization problem under a total power constraint, maximizing a weighted CMI–IR objective. Because the exact problem is analytically intractable, we develop tractable approximations: Jensen and Hadamard relaxations for Gaussian inputs, with corresponding formulations for practical discrete constellations. These yield efficient numerical or closed-form solutions that may exhibit Waterfilling (WF)-like behavior in specific regimes.

We therefore analyze the "price of information", i.e., the radar estimation loss induced by conveying data in DFRC systems. We conclude that in radar-only settings, constant-modulus constellations match deterministic waveforms; in DFRC, randomness induces loss, with a constant-modulus constellation degrading radar performance less than a non-constant-modulus constellation. Conversely, the communication IR in DFRC prefers higher-randomness modulations. We further study how constellation choice, each channel's Signal-to-Noise Ratio (SNR), the degree of competition between radar and communication functions, and CMI/IR weights, shift the operating point along the DFRC trade-off frontier.

We further extend the framework to a multi-block (multi-sweep) scenario in the presence of Doppler (a constant Doppler shift induced by target motion), under the narrowband assumption. We show that the radar CMI remains invariant to Doppler shifts: the Doppler manifests as transformations that do not alter the value of the CMI. In the radar-only case, the power allocation follows from a convex optimization problem derived via Jensen's inequality.

Throughout this work, simulations consistently corroborate the analysis. The proposed power-allocation strategies induced by the CMI–IR objective illustrate interpretable trade-offs and quantitatively reveal how the operating point shifts in different scenarios. These results endorse an MI-based allocation formulation that is clear and practical to implement.

Keywords: Waveform, radar, communication, OFDM, mutual information, power allocation, optimization

Résumé — Ces travaux de thèse portent sur la conception de formes d'onde à double fonction radar–communication (DFRC) pour des systèmes basés sur le multiplexage par répartition orthogonale de la fréquence à préfixe cyclique (CP-OFDM). Le premier défi méthodologique tient au fait que les radars privilégient des signaux émis déterministes, tandis que les communications exigent des symboles aléatoires porteurs d'information. Pour unifier ces points de vue, nous nous appuyons sur la théorie de l'information en utilisant l'information mutuelle conditionnelle (CMI) côté radar (l'information mutuelle (MI) radar moyennée sur toutes les réalisations possibles des symboles émis) et le débit d'information (IR) côté communication. Cette formulation préserve l'aléa des symboles émis indispensable aux communications tout en fournissant une métrique radar bien définie et interprétable.

Dans ce cadre, la synthèse de la forme d'onde DFRC se formule comme un problème d'allocation de puissance par sous-porteuse, sous contrainte de puissance totale, visant à maximiser une somme pondérée CMI–IR. Le problème d'optimisation exact étant intraitable analytiquement, nous proposons des relaxations analytiques résolubles basées sur les inégalités de Jensen et d'Hadamard pour des symboles émis gaussiens, puis nous étendons ces approches aux constellations discrètes usuelles. Ces approximations conduisent à des solutions numériques efficaces ou à des solutions en forme analytique explicite (*closed form*) révélant un comportement de type *waterfilling* dans certains régimes.

Nous quantifions ensuite le « prix de l'information » qui est la dégradation de l'estimation de la réponse impulsionnelle de la cible induite par la transmission de données. Nos résultats montrent qu'en mode radar seul (poids de l'IR nul), les constellations à module constant égalent les performances des formes d'onde déterministes usuelles pour les radars. En DFRC, l'aléa requis par les communications introduit une perte d'estimation radar ; toutefois, les constellations à module constant le dégradent moins que les constellations à module non constant. À l'inverse, l'IR bénéficie de constellations à plus fort aléa. Nous analysons également comment le choix de la constellation, le rapport signal sur bruit (SNR) par sous-porteuse de chaque canal (radar et communication), le degré de compétition entre les deux fonctions, et les pondérations CMI/IR influencent le compromis entre radar et communication.

Ensuite, nous étendons le cadre à des scénarios multi-blocs (multi-balayages) sous l'hypothèse de bande étroite en présence du décalage Doppler (constant) dû au mouvement de la cible. Dans ces conditions, nous démontrons que la CMI radar est invariante au décalage Doppler : celui-ci n'altère pas sa valeur dans le modèle retenu. Dans le cas radar seul, l'allocation de puissance résulte d'une optimisation convexe obtenue via l'inégalité de Jensen.

Tout au long de ce travail, des simulations corroborent l'analyse. Les stratégies d'allocation de puissance induites par l'objectif CMI–IR proposées mettent en évidence des compromis interprétables et révèlent la manière dont le point de fonctionnement se déplace, selon les scénarios, le long de la frontière de compromis DFRC. Ces résultats valident une formulation d'allocation fondée sur la MI, à la fois claire et pratique à mettre en œuvre.

Mots clés : Forme d'onde, radar, communication, OFDM, allocation de puissance, information mutuelle, optimisation.